Universitat Autònoma de Barcelona
Departament de Física
Grup de Física de les Radiacions

Neutron spectrometry in complex $n - \gamma$ fields: Application to LINAC and PET facilities

María José García Fusté

PhD Thesis
Supervised by Dr. Carles Domingo and Dr. Khalil Amgarou

July 2010

A l'Ilyas Amgarou, sempre pensarem en tu
A l'Angel
A la meva família
i que soni sempre "The Pink Panther!"

Acknowledgements

El procés que ha portat a l'elaboració d'aquesta tesi ha estat llarg i ple d'experiències, de manera que tinc la sort d'haver de fer una llista d'agraïments multilingüe i ben llarga, tingueu paciència, ...

El proceso que ha llevado a la elaboración de esta tesis ha sido largo y lleno de experiencias, de modo que tengo la suerte de tener que hacer una lista de agradecimientos multilingüe y bien larga, tened paciencia, ...

Il processo che ha portato all'elaborazione di questa tesi è stato lungo e pieno di esperienze, quindi sono fortunata ad avere una lista multilingue e molto lunga di riconoscimenti, essere paziente ...

Gràcies a / Gracias a / Grazie a / Thanks to ...

Dr. Francisco Fernández, primer director y punto de partida de lo que tenéis entre manos. Quisiera agradecerte Paco las oportunidades, el apoyo, la paciencia y la motivación. Esta tesis es fruto de todo lo cultivado por ti en nuestro grupo, sin tu tutela no estaríamos aquí.

Dr. Carles Domingo y al Dr. Khalil Amgarou, directors de la tesi i tantes altres coses més. Estimats caça-neutrons, després de tants kilòmetres recorreguts i experiències compartides per fi la tenim entre les mans, sense vosaltres no ho hauria pogut fer. Us he d'agrair que aquestes 180 planes tinguin sentit i aportin alguna cosa, però també us he d'agrair "las oportunidades, el apoyo, la paciencia y la motivación". No només he après física amb vosaltres, també he après a viure el món al vostre costat (i a fer-li una volta completa!).

Dr. Adolfo Esposito, per essere il presidente del tribunale di questa Tesi, per decidere di parlarmi in italiano dal momento che ci abbiamo incontrato e per correggimi se sbaglio, per avermi permesso di participare al loro lavoro e alla loro vita quotidiana. E 'un piacere averti incontrato e compartire con te tanti momenti.

Dra. Carmen Baixeras, por haber aceptado ser la secretaria del tribunal. Pero no sólo por eso, Carmen, sino también por todo lo vivido y por todo lo compartido durante estos 7 años. Eres una luchadora, gracias por compartir el día a día conmigo y por haberme acogido con tanta calidez.

Dr. Francisco Sánchez-Doblado, por formar parte del tribunal y por todo lo demás, empezando por todo lo que hay escrito en estas páginas que proviene de NEUTOR y que si no fuera por tu ímpetu, tu preocupación por el paciente y tu visión de futuro, Paco, seguramente no hubiera visto la luz.

Dr. Roberto Bedogni. Gracias por ayudarme Rob siempre que te he necesitado, por haberme acogido tan cálidamente la primera vez que vine a Italia y por todas las demás veces. Y sobretodo gracias por ofrecerme tu amistad, por permitirme aprender de tus experiencias de "joven católico" y por tu español interpolado. Al fin y al cabo gracias por dejarme formar parte de tu vida. Y preguntále a Rocío si nos vemos en la casa de Andalucía...

A todos aquellos con los que he participado en alguna campanya de medida (y son unas cuantas) cuyos resultados se reflejan en este texto. / To the people that participated with me in any of the measurement campaigns(and they are a few) that appear in this thesis: ... los de NEUTOR, los radiofísicos catalanes (Ernesto Luguera y Alberto Sánchez-Reyes), the Irish people (Louise Bowden, Dr. Lluís Vintró and the M2i staff), the Cadarache staff, ...

A todos aquellos con los que he participado en alguna campanya de medida cuyos resultados no se reflejan en este texto (y son unas cuantas más). / To the people that participated

with me in any of the measurement campaigns that do not appear in this thesis (and they are a few more)

I no, no m'oblido de la resta de companys, no. Menció especial per en Javier Castelo, en Lluís Font, i la meva Carolina. També a la Victòria Moreno, a en Marc de San Pedro i és clar, a tota la colla de Radiofísica Ambiental. Sense vosaltres la meva vivència del Grup de Física de les radiacions no seria la mateixa. Gràcies per les converses i per compartir amb mi les vostres experiències.

Als meus amics de l'ànima. Al Joan, la Patri i la Candela que són com la meva segona família, sabeu que us porto ben endins del cor i que us estimo moltíssim. A l'Eva i la Felisa us sento molt a prop cuques i sapigueu que, tot i les distàncies físiques i temporals, ens tindrem tota la vida, res em farà més feliç que poder seguir al vostre costat. Per cert ladies, saludeu-me els vostres "currutacus". A la Marcel.la, tant aprop i tan lluny de vegades, espero que siguis feliç en tot allò que facis. A tots plegats, i com ja us vaig dir a la tesina, sou un tresor que espero no perdre mai. Gràcies!!, per tantes i tantes coses ...

A la meva mare per ser com és i per estar en constant evolució. Sóc molt feliç de tenir una persona com tu de la que aprendre.

Al meu pare, per ensenyar-me per la via de l'exemple que les coses s'han de viure amb intensitat. Sóc molt feliç per compartir amb tu la vida. A tots dos pel seu amor i per ser bellíssimes persones.

A la meva família sencera, especialment a les meves àvies (lluitadores sense fi), al Marc i l'Ana (i ara el Roc) per que sé que sempre puc comptar amb ells, i als meus avis que sé que serien molt feliços per compartir aquest moment amb mi.

A l'Angel, per regalar-me el seu amor i ajudar-me a ser millor persona. Per fer junts el camí...

Contents

List of Figures

List of Tables

CHAPTER 1.

Introduction

1.1. Outline

One of the research subjects of the Grup de Física de les Radiacions (GFR) at the Physics Department of the Universitat Autònoma de Barcelona, where the present work has been developed, is the study of neutron interactions with matter in order to perform their spectrometry and dosimetry through their detection. Neutrons are electrically neutral, so that they are not affected by electromagnetic forces and they are unable to directly ionize matter. Due to the complexity of the neutron interaction mechanisms, neutron dosimetry and spectrometry are, generally, complicated problems that need to be solved with the required precision. In fact, interaction of neutrons with matter is only possible through nuclear processes like scattering, capture and fission, which can produce charged particles that at the same time originate ionisation. This ionisation is what dosemeters or spectrometers are able to detect, and is responsible of the biological effects of neutron irradiation on life beings. Moreover, neutrons are usually present in the form of radiation mixed fields, with gamma radiation, and with an energy spectrum covering a range between 0.01 eV and several GeV, a total of 14 energy decades. In practice, difficulties arise when an instrument must respond adequately to such an extended energy range. Only multisphere systems (Bonner spheres) are able to detect neutrons in energy ranges wide enough, from thermal to some hundreds of MeV.

On the other hand, radiation dosimetry deals with the effect of a certain radiation over living beings and it consists on the definition of a series of dosimetric quantities by the International Commission of Radiological Protection (ICRP). Physical or measurable quantities (fluence, absorbed dose, kerma,...) characterize the radiation field, whilst limiting quantities (equivalent dose in an organ or tissue, effective dose, ...) are defined to take into account the biological effects of radiation. The limiting quantities are, by definition, impossible to measure in practice, so their values are estimated from operational quantities (like ambient dose equivalent or personal dose equivalent). The conversion from one type of quantity to another is performed through weighting factors and conversion coefficients, which values depend on the type

of radiation and its energy. In the case of neutrons, these factors and coefficients are strongly dependent on the incident neutron energy, so that it is required to have spectrometric information about the incoming neutron radiation field to correctly evaluate the adequate quantities.

As a consequence, in order to measure and characterize correctly a neutron field, several points must be taken into account:

1. The knowledge of the physical mechanisms of neutron interaction with matter in a broad energy range, from the thermal region (around 0.01 eV) to high energy neutrons (in the order of GeV).

2. The knowledge of neutron interaction cross sections, which will provide information on the production probabilities of secondary charged particles as a function of their energy and emission angle.

3. The knowledge of the mechanisms through which the secondary charged particles interact with matter and deliver their energy, generating a measurable signal in a certain detector or producing damage in an alive being.

4. The importance of obtaining the detector response as a function of the incident neutron energy (response function), which relates the value of the measured signal with the neutron fluence or with a given operational dosimetric quantity to which the detector is calibrated.

5. The adequate calibration of the detector in neutron reference fields that allow validating the response function matrix, usually obtained from Monte Carlo simulations.

Measurement campaigns have been undertaken by the GFR for characterising neutron fields of different kinds, like those encountered inside of the containment building of nuclear power plants, around containers of spent nuclear fuel or those produced in high energy accelerators. This work deals with the development and characterisation of a new Bonner spheres neutron spectrometer based on the activation of gold foils as thermal neutron detector. This new spectrometer is especially useful when mixed neutron-gamma fields or pulsed neutron fields are to be measured. The immediate application of this spectrometer is to characterise neutron fields originated in linear electron accelerators (LINACs) used for radiotherapy and in cyclotrons used for the production of the positron emitting radionuclides needed in positron emission tomography (PET). The particularities of neutron production in these types of facilities are discussed below.

1.2. Neutron production and transport in radiotherapy linear accelerators

Radiotherapy treatments with electron linear accelerators (LINACs) are currently extended worldwide and based on well-established techniques. In a typical LINAC, the primary electron beam collides with a high Z target (Pb or W typically) to produce a bremsstrahlung photon beam used to treat the cancerous tissue. The shape of the photon beam is conformed to match the shape of the volume to be irradiated with the help of collimating jaws and filters

made of high Z materials. Both electrons and gamma rays can produce neutrons when interacting with the accelerator shielding and collimators materials. This neutron production can result in doses to patients and to operating personnel from direct exposure both to neutrons and to the resulting residual radioactivity. The constant improvement and evolution of the methodology used in radiotherapy because of the advances of Physics and Engineering has the outcome of a better confinement of the radiation dose around the clinical target. In this way, techniques like Radiosurgery, Intensity Modulated Radiation Therapy (IMRT) or hadron therapy have an increasing role in the treatment of cancer.

The photon field produced at radiotherapy LINACs is very intense, collimated, pulsed and accompanied by high-frequency microwaves. This type of environment usually limits the use of active systems inside the treatment room and passive detectors must be used. A brief introduction on neutron production and transport associated to LINACs facilities is provided below.

1.2.1. Physics of neutron production in LINACs

At present, medical electron accelerators operate at energies between 6 MeV and 25 MeV. They generate a photon bremsstrahlung beam when electrons hit a heavy target. Both the generated electrons and photons can be absorbed in the materials constituting the accelerator head. Neutron emission is possible if the energy of these electrons or photons exceeds the minimum energy required to remove a neutron from the nuclides they encounter. For the majority of stable nuclei heavier than C, the minimum energy necessary to remove a neutron from the nucleus lies between 6 and 16 MeV. Thus, neutron emission is a possible process in typical materials composing a LINAC head if the accelerator operates above ~ 8 MeV.

The production of neutrons resulting from the interaction of photons and electrons with various nuclides is governed by the properties of the giant resonance of the photonuclear interaction [1]. The giant resonance appears as a large peak in the plot of the nuclear photon absorption cross section as a function of the photon energy. In fact, the photonuclear reaction cross section in most light elements has a maximum around 20 MeV to 25 MeV, while for heavier elements the maximum appears at lower photon energies, down to about 13 MeV in uranium. The narrowest resonances appear in nuclides with closed shells, while the broadest ones appear for nuclides, like ^{165}Ho, that have large permanent deformations. To a very good approximation, the sum of the neutron producing cross sections is the total nuclear absorption cross section for photons. This effect implies that heavier nuclides are much more efficient photoneutron producers than are the lighter nuclides. For photon energies below 35 MeV, i.e. in the giant resonance energy range, the photonuclear cross section is dominated by the (γ, n) reaction, with very few exceptions.

The same nuclear reaction that can be induced by a photon can also be induced by the interaction of an electron with a nuclide. Two processes can take place for electrons as shown in figure 1.1:

i) An electron scatters through a certain angle in the Coulomb field of a radiator, nuclide R, to produce a photon of energy $E_\gamma = E_i - E_f$. This photon then induces a photonuclear reaction in a second nuclide A, for example a (γ, n) reaction.

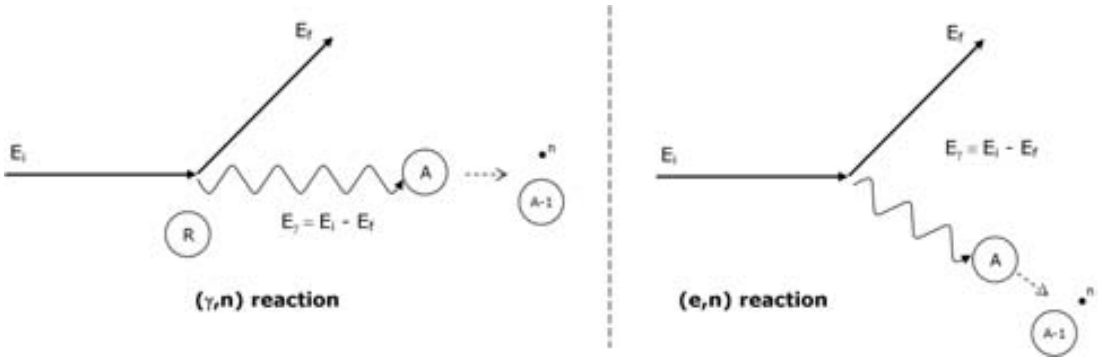

Figure 1.1. Schematic representation of neutron production processes. On the left a (γ, n) reaction, on the right an (e, n) reaction. From [1].

ii) Instead of creating a real photon, a virtual photon of energy $E_\gamma = E_i - E_f$ interact directly with nuclide A to initiate a reaction, for example $e + A \rightarrow (A-1) + n + e'$.

The second process is known as electrodisintegration. Its cross section is analogous to the bremsstrahlung-weighted photodisintegration cross section that would be measured using a bremsstrahlung spectrum generated by an electron. The electrodisintegration cross section is expected to be of the order of the fine structure constant, $\alpha = 1/137$, times the corresponding bremsstrahlung-weighted cross section and may be neglected, except for accelerators where direct electron irradiation is used. Thus, at the typical operating energy range of LINACs, neutron emission is possible and explained by the photoneutron reactions, (γ, n), induced by the photon bremsstrahlung beam on the nuclides present in the several structures where they impact.

Primary photoneutron spectra

In a LINAC, the neutron spectrum produced in the accelerator's target by photon absorption is called *primary neutron spectra*. The absorption reaction of a photon of energy E_γ by a nuclide (A, Z) in the giant dipole resonance (GDR) regime is usually described with Bohr's compound-nucleus hypothesis, [2]. The main idea is to split the nuclear reaction in two steps: the formation of a compound nucleus and its decay after a time much greater than the interaction time (10^{-16} to 10^{-18} s). With the exception of a few quantities, which are subject to conservation laws (energy, angular momentum, parity), the compound nucleus loses memory on the way it was formed. Consequently, the spectrum of neutrons emitted following the absorption of a photon of energy E_γ by a nuclide (A, Z) is determined by the spectrum of states of the daughter nuclide, $(A-1, Z)$, up to an excitation energy given by $E_{\max} = E_\gamma - S_n - \Delta_R$, where S_n is the neutron separation energy for (A, Z) and $\Delta_R \simeq E_\gamma^2/2AMc^2$ is the center-of-mass recoil energy. The Weisskopf's statistical treatment of nuclear level densities [3] is used to describe the energy distribution of photoneutrons. Weisskopf considered a nucleus $(A-1, Z)$ and a neutron with energy E_n enclosed in a volume V. Assuming that the neutron moved in a random way like a molecule of a gas, Weisskopf derived the mean probability of the neutron being captured by the nucleus $(A-1, Z)$. From this he obtained the probability of the reverse process, i.e. the evaporation of a neutron from a nucleus (A, Z). This probability has an energy-dependent factor

that defines the shape of the energy spectrum of the emitted neutrons. The resulting expression of this neutron evaporation energy spectrum is:

$$\frac{dN\left(E_n\right)}{dE_n} = K_w \sigma_c \left(A-1, Z : E_n\right) E_n e^{-\frac{E_n}{T}} \tag{1.1}$$

where $\sigma_c \left(A-1, Z : E_n\right)$ is the capture cross section of nuclide $(A-1, Z)$ for a neutron of energy E_n; K_w is a constant that normalises the spectrum to contain a specific number of neutrons; and T is the "nuclear temperature" associated with the daughter nucleus that remains after the neutron has been emitted. Over the portion of the spectrum where this expression is valid, σ_c is a slowly varying function of E_n, so the evaporation spectrum displays a Maxwell-Boltzmann distribution, being the angular distribution of the emitted neutrons isotropic. For the materials of interest, the nuclear temperature lies typically between 0.5 and 1.5 MeV and is a mild function of the excitation energy. The average energy of the Maxwell-Boltzmann distribution, $2T$, which corresponds to its maximum, ranges between $1 < E_{av} < 3\,\mathrm{MeV}$.

Mainly three possibilities have to be considered which violate the compound-nucleus hypothesis [4]:

1. Direct reactions, which are nuclear reactions that occur in a time (about $10^{-22}\,\mathrm{s}$) comparable to the interaction time.

2. Fast processes or pre-equilibrium reactions leading to particle emission with a time scale longer than the very rapid direct reactions but much shorter than the slower compound nucleus reactions.

3. Slow dynamic evolution of shape, density or other global degrees of freedom, which create time-dependent global conditions for the intrinsic degrees of freedom.

These three processes produce deviations from the spectrum given by equation (1.1) in the high energy range, being the contribution of direct reactions the most important in our case. The direct spectrum of photoneutrons produced by a monoenergetic photon beam would consist of a series of discrete lines. In contrast to the isotropic angular distribution of the "statistical decay" neutrons described by equation (1.1), the angular distribution of the "direct" neutrons is usually anisotropic with respect to the photon beam direction. The consequence of all these possible reactions is that photoneutron spectrum can be approximated by assuming that, for monoenergetic photons, E_γ, it is given by an evaporation spectrum plus a discrete peak at an energy $E_n = E_\gamma - S_n$ and containing $10 - 20\%$ of the neutrons in the evaporation spectrum, [1] and [5]. The spectrum of neutrons produced by a bremsstrahlung spectrum, as in a LINAC accelerator, with a maximum energy E_b is then given by integrating over the photon energy the spectrum produced at each photon energy weighted with the bremsstrahlung spectrum. Because of the assumption that the direct-neutron spectrum consists of ground-state neutrons only, the resulting spectrum errs on the side of having somewhat higher-energy neutrons that will be found in a measured spectrum.

1.2.2. Neutron transport in LINACs

Transport in the accelerator head

The typical linear accelerator for radiotherapy purposes has massive photon shielding (collimator, flattening filter, fixed and/or mobile jaws) around the target, which, when the accelerator is energised, produces a collimated beam of X-rays. Neutrons originated inside the head are approximately isotropic and penetrate the shielding in all directions. The photon shielding material is usually some heavy metal such as W or Pb; the head also contains a certain amount of iron and copper in bending magnets. Although these materials provide good photon shielding, the only significant mechanisms of neutron energy loss in these materials are inelastic scattering and $(n, 2n)$ reactions, as for the energies involved reactions giving more than two neutrons are highly improbable. The inelastic scattering dominates energy losses at lower energies and the $(n, 2n)$ reactions dominate at higher energies. The energy loss in any inelastic collision cannot be determined or predicted exactly, but there is a minimum energy loss which equals the energy of the lowest excited state of the shielding material. In the $(n, 2n)$ reaction, the minimum energy loss is equal to the binding energy of a neutron, and, since the energies of the two emerging neutrons tend to be similar, this reaction produces large number of low energy neutrons. Therefore, a typical primary neutron penetrating the photon shielding material undergoes several collisions. In addition, a large amount of elastic scattering takes place in these materials at these energies. The elastic scattering results in negligible energy loss but has the effect of increasing the path length of the neutrons in the shielding material and offering greater opportunity for the inelastic and $(n, 2n)$ reactions to occur. All these reactions produce a degraded neutron spectrum, quite different from the primary neutron spectrum produced at the target.

Two effects of the head shielding on the primary neutron spectrum can be identified:

i) The average energy of the neutron spectrum decreases almost exponentially with increasing shielding thickness. The slope of this exponential decrease is much steeper for W than for Pb, and it becomes steeper with increasing spectral energy, see 1.2 and 1.3. Since these materials become very transparent to neutrons with energy below that of the first excited state of the nucleus, the exponential decrease will eventually begin to level off and the average energy will remain almost constant for transmission through further thicknesses of Pb or W. Therefore, once the neutron energy has been reduced by the shielding to values below that of the first excited state of the nucleus, increasing shielding thicknesses will not be able to further reduce the neutron average energy. However, for the thicknesses encountered in medical accelerators, the exponential decrease is a reasonable approximation. It should be noticed, that the decrease in the average energy also produces a decrease in the absorbed dose or the dose equivalent to the patient.

ii) A small attenuation of the neutron fluence in the accelerator head should be expected, since capture cross sections for the heavy metals are small except at thermal neutron energies. In fact, there may be a small build up of neutron fluence due to the multiplying effect of $(n, 2n)$ reactions. Considerable attenuation of the neutron fluence can be achieved by adding some borated hydrogenous shielding outside the photon shielding.

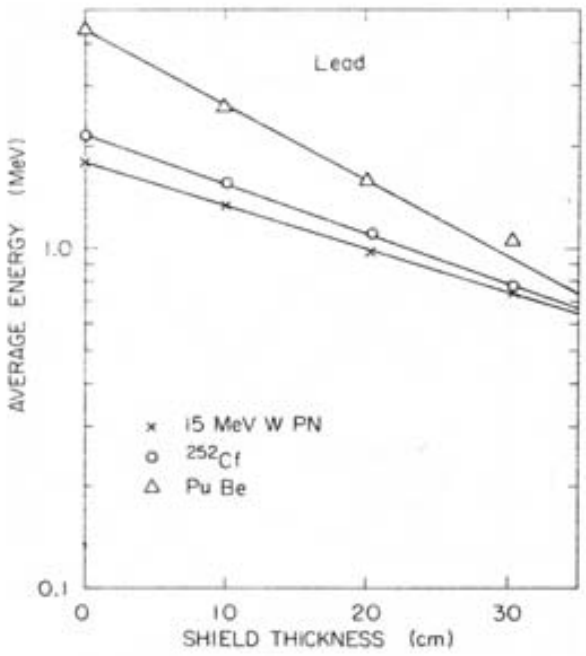

Figure 1.2. The average energy of various neutron spectra as a function of the thickness of a spherical shield of lead surrounding the source, from [1].

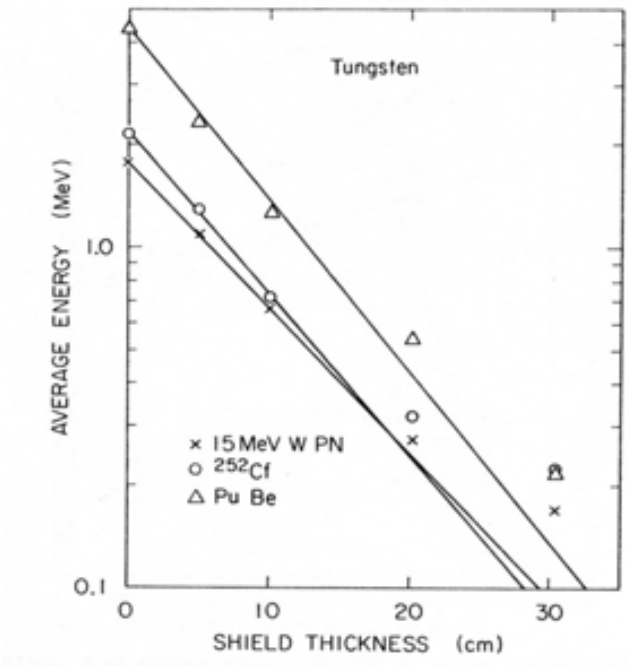

Figure 1.3. The average energy of various neutron spectra as a function of the thickness of a spherical shield of tungsten surrounding the source, from [1].

Transport in the concrete room

Linear accelerator machines are placed inside shielded rooms, most made of concrete, with the access door separated from the accelerator by a maze. Neutrons striking the concrete undergo mostly elastic scattering. Hydrogen in the concrete thermalises the neutrons rapidly and are captured, usually with accompanying gamma ray emission. Many of the neutrons may backscatter out of the walls and traverse the room several times before being captured. Eisenhauer et al. [6] were able to deduce that the typical neutron traverses ~ 2.4 times the room before it is captured or its energy falls below the Cd cut-off energy (0.4 eV). The resulting neutron spectrum everywhere in the room has a low energy scattered component, which is almost constant. The total neutron fluence will then consist of a direct component, given by the fast neutrons produced in the LINAC head, summed with a scattered constant component from the walls and a thermal component:

$$\Phi_{total} = \Phi_{dir} + \Phi_{sc} + \Phi_{th} \tag{1.2}$$

McCall et al. [5] provided an empirical method of estimating Φ_{dir}, Φ_{sc} and Φ_{th}. They studied the effects of a concrete room on the neutron spectrum with Monte Carlo techniques and obtained the following empirical relationships:

$$\Phi_{dir} = \frac{a\mathfrak{Q}}{4\pi d^2} \tag{1.3}$$

$$\Phi_{sc} = 5.4\frac{a\mathfrak{Q}}{S} \tag{1.4}$$

$$\Phi_{th} = 1.26\frac{\mathfrak{Q}}{S} \tag{1.5}$$

where the quantity a is the transmission factor for neutrons that penetrate the LINAC head shielding ($a = 1$ for Pb, $a = 0.85$ for W). The quantity S refers to the treatment room inner surface area in cm^2, and $\mathfrak{Q}$ is the neutron strength in neutrons from the head per X-ray dose (Gy) delivered at isocenter. Finally, d is the distance in cm from the target to the point where the direct fluence is evaluated. A complete study of $\mathfrak{Q}$ values for several LINAC models and operating energies can be found in [7]. From this expressions, it can be seen that the direct component is expected to follow the inverse square distance law, and that both the scattered and thermal components depend on the inner surface of the treatment room and not on its exact geometry.

We can conclude that a typical neutron spectrum inside a LINAC treatment room will display a peak around 1 MeV (direct or primary component), another peak around 0.025 eV (thermal component) and a much less abundant epithermal component of neutrons with intermediate energies (scattered component). All these neutrons will contribute to the unwanted dose delivered to the patient outside the treated organ (peripheral dose). As doses deliverd by neutrons depend highly on their energy, a correct estimation of this contribution can only be achieved if spectral information is available.

1.3. Neutron production in positron emission tomography cyclotrons

1.3.1. Overview

Radioisotopes of different types are commonly used in medicine for therapeutic and diagnostic purposes. For diagnose they have become a standard method of noninvasive exploration and of study of a patient's condition [8]. There are two different production processes, depending on the usage of reactors or accelerators to induce radioactivity from stable elements. The invention of the cyclotron by Ernest Lawrence in 1934, a machine able to accelerate deuterons to very high speeds, showed that the production of the nuclear instability necessary to generate radioactivity was possible. During the years from 1935 to the end of World War II, particle accelerators and in particular cyclotrons became very important in the preparation of radioisotopes. Immediately after World War II, almost all the radioisotopes in use were made in reactors, and the use of accelerators became less important. In the 1950s, the discovery that ^{201}Tl could be used as an ideal tracer for detecting myocardial perfusion and other improvements in radiotracing techniques generated a growing demand of radionuclides to which reactors could not answer. Consequently, the production of radioisotopes in cyclotrons for medical applications revived. The preparation of fluorodeoxyglucose (^{18}FDG) in the mid-1970s and its use for studying glucose metabolism was a major breakthrough, leading to the development of the now widely used imaging modality called Positron Emission Tomography (PET), in which β^+ emitter radioisotopes are used. The use of ^{18}FDG along with a PET camera yields excellent quality images of the brain (for studying functional abnormalities), heart (for studying viability function) and tumors (for detection of metastases). A large number of other ^{18}F and ^{11}C labelled radiopharmaceuticals were developed subsequently, and the quest for newer and more effective ones continues at present.

The applications of isotopes produced in cyclotrons have been expanding at a much faster pace in the last 15 years, as indicated by the large number of new machines being installed for isotope production. Some cyclotrons are dedicated to the production of a single isotope such as ^{18}F or ^{103}Pd. In Spain, a total of 5 (out of 262 in the world) cyclotrons for production of PET radioisotopes where operative in November 2005, when the International Atomic Energy Agency (IAEA) compiled an updated cyclotron directory between all the 39 Member States of the Agency [9].

In order to be used in diagnosis, radionuclides and compounds to which they are attached must obey some criteria [10]:

1. Radionuclides must have suitable physical properties: for example emission energies related to high detection efficiencies, compatible with the lowest possible radiation dose delivered to the patient.

2. Compunds must also have suitable biochemical properties like interacting with the system to be probed in a known and reproducible way and not altering or perturbing the system in any measurable manner.

Moreover, most of the radioisotopes used in vivo should have relatively short half-lives (less than a few hours to at most a few days) and the decay should occur preferably via IT, EC or

Table 1.1. Routine methods of prouction of some commonly used positron-emitting isotopes in PET studies, data adapted from cite Qaim and cite Vega-Carrillo

Production data				β^+ emitter data	
Nuclear reaction	**Q − value** (MeV)	Energy range (MeV)	Thick target yield MBq (mCi) / μA h	Radionuclide	$\mathbf{T}_{1/2}$ (min)
$^{14}N(p,\alpha)$	−2.922	3 − 13	3820	^{11}C	20.4
$^{16}O(p,\alpha)$	−5.217	7 − 16	1665	^{13}N	10.0
$^{15}N(p,n)$	−3.536	0 − 10	2220	^{15}O	2.0
$^{14}N(d,n)$	+5.073	0 − 8	2368	^{15}O	2.0
$^{18}O(p,n)$	−2.437	3 − 16	2960	^{18}F	109.8
$^{20}Ne(d,\alpha)$	+2.792	0 − 14	1110	^{18}F	109.8

β^+ emission. There are definite advantages in using short lived radionuclides; for example, there is a low radiation dose associated with each study, serial studies are possible and radioactive waste disposal problems are minimized if not eliminated. The disadvantages are the need for an accelerator nearby or within easy shipping distance for the longer lived species (a few hours), and for rapid chemical procedures, especially for formation of more complex compounds.

As shown in table 1.1, PET radionuclides are produced from either proton or deuteron nuclear reactions. Since most PET research was performed at major research laboratories having accelerators capable of proton or deuteron production, these reactions were the standard. However, in the early 1980s, small compact proton-only cyclotrons became available, and cyclotrons specifically designed for producing PET radionuclides were installed in many hospitals.

Cyclotron technology has improved significantly since the 1980s. Cyclotrons are now stable machines, controlled by computers, which can produce a wide variety of radioisotopes. Hospital based machines, which are generally dedicated to the production of the standard PET radioisotopes (^{11}C, ^{13}N, ^{15}O and ^{18}F), accelerate protons in the $10 - 19$ MeV range, and some also produce deuterons with an energy of about half that of the protons ($5 - 9$ MeV) [10].

1.3.2. Neutron fields around PET cyclotrons

Cyclotron machines accelerate charged particles (protons or deuterons mainly) that follow circular trajectories, originating bremsstrahlung radiation. In addition, as a consequence of the interactions between the charged particle beam and surrounding media radiation is produced. Thus, bremsstrahlung and characteristic X-rays, prompt γ-rays, neutrons and delayed radiation (β and γ) are produced making the radiation fields around cyclotron machines complex, mixed and very intense. In particular, neutrons are produced as secondary particles and their contribution, in the operation of biomedical cyclotrons, is generally the most important one to the radiation field around the accelerator, driving shield calculations [11]. Neutrons are produced in nuclear reactions involving several materials and components of the cyclotron system:

- in the isotope of interest from the cyclotron target material, through the reaction channel producing the desired radioisotope;
- in the isotope of interest from the cyclotron target material, from concurrent reaction channels that do not produce the desired radioisotope, i.e. from non useful nuclear reactions;

- in isotopes from the cyclotron target material other than the isotope of interest;
- in the components of the target assembly, like the body enclosing the target material, or the target foils insulating it from the vacuum chamber of the cyclotron;
- in the collimator system, purposely hit by the beam to delimit its shape during irradiation;
- in other structures of the cyclotron that may be hit by tails of the beam or by stray ions.

The energy and angular distributions of the neutrons produced are consequence of all these reactions, which are initiated by charged particles, unlike the LINAC case. Although the exact mechanism of nuclear reactions is not yet completely understood, the compound nucleus reaction model is applicable if one takes into account that, from classical mechanics, a reaction between a charged particle and a nucleus cannot take place if the centre-of-mass energy of the two bodies is less than the Coulomb barrier. In fact, these reactions take place at energies well below this barrier due to the effects of quantum tunnelling. Because the compound nucleus model is valid, one expects the neutron field to be characterised by the decay of the compound nuclei created. At the low energies of interest in PET cyclotrons, deexcitations of compound nuclei take place mainly through evaporation processes, so the neutron energy spectrum can be described by a Maxwellian distribution with a peak in the MeV order, like in the LINAC case. These primary neutrons will then undergo scattering reactions in the target, in the structural cyclotron materials and in the bunker walls, so a thermal neutron component will also exist. The experimental determination of neutron fields around PET cyclotron facilities is a difficult task due to complexity of the radiation fields encountered.

1.4. Scope of the study

The present work deals with the need of characterising experimentally the neutron fields generated in LINAC and PET medical facitilties. These fields may be pulsed, intense and mixed with high energy predominant photon component, where active instruments may experiment some limitations such as pulse pile-up, dead-time and radiofrequency interferences. To overcome these difficulties, a passive Bonner sphere spectrometer (BSS), using pure gold foils as central detectors, has been recently developed in the laboratory of the Grup de Física de les Radiacions at the UAB. This spectrometer should tolerate exposures in extreme environment conditions of temperature and humidity, and should be able to measure neutron spectra in such environments independently on their direction of incidence and over a wide energy range (from 1 meV up to 20 MeV).

The present manuscript describes the design, characterisation and application of the new UAB neutron passive Bonner sphere spectrometer, and is structured in 9 chapters and 4 appendixes:

- Chapter 1 gives an introduction about the neutron production in LINACs and PET facilities and the scope of the study is presented.
- Chapter 2 is dedicated to review neutron properties and their interaction mechanisms and to summarise the different types of neutron workplace fields. Radiation protection

quantities are introduced and the need of neutron spectrometry to estimate correctly limiting quantities is discussed.

- Chapter 3 provides an overview of neutron spectrometry techniques. Special attention is dedicated to Bonner sphere spectrometers and their response functions and a review of unfolding techniques is given. The parameters affecting measurements in real irradiatons, like all parasitic effects of neutron scattering and the geometric features due to source and/or instrument dimensions, are presented.

- In chapter 4 the major limitations of the UAB active BSS in presence of LINACs neutron fields are analysed. An introduction to Bonner spectrometry with activation detectors as central thermal neutron detectors is given and the criteria needed to design a passive BSS are outlined. The last part of the chapter is dedicated to describe the design of the new UAB passive BSS developed in this thesis.

- In chapter 5, the calculation procedure used to obtain the UAB passive BSS response matrix is explained. The dependence of the response functions on several factors, such as the neutron incidence direction, the mass density of the polyethylene spheres and the gold foil geometry is also studied.

- Chapter 6 is dedicated to the experimental characterisation of the UAB passive BSS. The calibration factor and the overall uncertainty of the response functions are determined. The results obtained from validation to monoenergetic neutron beams are also presented.

- In chapter 7 the performance of the UAB passive BSS in the neutron fields for which it has been designed, has been tested in various measurement campaigns. This chapter presents the neutron spectra obtained from measurements with the UAB passive BSS in several LINAC and PET facilities, under a wide variety of irradiation conditions.

- The conclusions and perspectives derived from the present work are given in chapter 8.

Complementary information is given in the appendixes.

CHAPTER 2.

General concepts

2.1. Neutron physics and interactions

2.1.1. General properties

Neutrons, together with protons, play a fundamental role in the study of nuclear forces and the formation of the atomic nucleus [12]. Their existence was predicted by Ernest Rutherford in 1920. However, the first experimental evidence came a decade after, when Walther Bothe and Herbert Becker bombarded berylium (and also boron and lithium) with α-particles from a ^{210}Po radioactive source. They observed the emission of a very penetrating but nonionizing radiation, which they assumed to be high-energy photons. Around 1931, Irène Joliot-Curie and Fréderic Joliot-Curie noticed that, when this radiation fell on a paraffin target, energetic (5.3 MeV) protons were emitted. They estimated, using the Compton scattering formula, that the photons originating these protons would be at least 52 MeV. However, the emission of such photon energy seemed extremely unlikely at that time. One year later, James Chadwick repeated the same experiment with other recoil nuclei and he provided the correct explanation, identifying the mysterious radiation as electrically neutral with nearly the same mass as that of the proton. Chadwick named this particle "neutron" and he is credited until today with being its discoverering father.

Neutrons are composed of three quarks (uud), so that they interact through strong nuclear forces. They have a rest mass of 939.573 MeV/c^2, slightly greater than that of protons, and have no net electric charge and spin 1/2. However, the inner distribution of positive and negative charges gives rise to electromagnetic momenta. Extremely weak electromagnetic forces may appear when these momenta are coupled with the charge and spin of atomic orbital electrons. Therefore, neutrons can travel appreciable distances in matter until a "collision" or interaction takes place with a surrounding nucleus due to nuclear forces leading to scattering or capture processes [13]. Generally, neutrons are stable when they are well bounded within the atomic nucleus, but they can decay sometimes into a proton, an electron and an electron anti-neutrino. The lifetime of free neutrons outside the atomic nucleus is about 886 s.

Table 2.1. Energy classification for neutrons.

Neutron Type	Energy Range
Thermal	$10^{-3}\,\mathrm{eV} - 1\,\mathrm{eV}$
Intermediate	$1\,\mathrm{eV} - 100\,\mathrm{keV}$
Fast	$100\,\mathrm{keV} - 20\,\mathrm{MeV}$
High-energy	$> 20\,\mathrm{MeV}$

The probability that an interaction takes place between an incident neutron and a target nucleus is expressed through the concept of the cross-section, σ, of this particular type of interaction, which has the dimensions of area and is commonly expressed in barns ($1\,\mathrm{b} = 10^{-24}\,\mathrm{cm}^2$). If a large number of neutrons of the same energy are directed into a given material layer, some of them may pass through with no effects, others may have interactions that change their directions and energies, and the last portion may be fully captured. On the other hand, they do not produce primary ionization when passing through matter due the their lack of Coulomb interactions with atoms and molecules of the medium. The only way to detect them is through the secondary charged particles released from nuclear interactions in a given material. These secondary particles are able to produce electrical signals or pulses, which can, then, be easily processed by practically any of the available radiation detectors or measurement instruments [14].

2.1.2. Classification

Neutrons are usually classified on the basis of their kinetic energies but without clear established limits. As these limits depend on the application field considered, table 2.1 lists the main categories that are commonly used in neutron dosimetry and spectrometry.

Relativistic neutrons with energies above 10 MeV [15] interact mainly through inelastic scattering (n, n') with high Z (atomic number) materials and are able to induce spallation reactions like (n, xn) or (n, np). In the range between 10 MeV and 100 keV, they may undergo elastic scattering (n, n) with low Z materials like hydrogen, carbon and oxygen, transferring part of their energy to the recoil nuclei. However,.inelastic interactions could become important for the higher energies of this range or for materials with high Z. Neutrons may therefore be slowed down, via multiple and/or successive elastic collisions with the nuclei of the medium, becoming intermediate neutrons with an energy distribution or spectrum proportional to $1/E_n$ (being E_n the neutron energy). At this stage, neutron resonance processes, due mainly to (n, γ), (n, p) , (n, α) and $(n, \text{fission})$ reactions, may also take place. Below 1 eV, neutrons reach thermal equilibrium with the surrounding atoms or molecules of the medium, displaying a Maxwellian energy distribution. The most probable energy for these thermal neutrons is given by:

$$E_0 = k_B \cdot T \tag{2.1}$$

where k_B is the Boltzmann constant and T the medium absolute temperature. At a room temperature of 20 °C, the most probable energy for thermal neutrons is:

$$E_0 \sim 25.3\ \mathrm{m\,eV} \tag{2.2}$$

which corresponds to a velocity $v_0 \sim 2200\ \mathrm{m\,s^{-1}}$. A single thermal neutron is able to gain and lose small amounts of energy through many elastic scatterings until it is absorbed by a neighbour

nucleus. For almost all stable elements absorption takes place through radiative capture (n,γ) reactions, whereas for some low Z nuclei nuclear reactions like (n,p) or (n,α) are also possible. In most nuclei, the (n,γ) cross-section is inversely proportional to the neutron velocity. In which follows, we describe in detail all the neutron interaction mechanisms with nuclei.

2.1.3. Neutron interactions with matter

As stated above, the interaction of neutrons with matter is quite different from that of charged particles or gamma radiation because of the absence of electric charge. Electromagnetic interaction is negligible and neutrons must enter the nucleus or come sufficiently close to it to interact via nuclear forces, so neutron interactions are always at a nuclear scale. Many processes are involved and depend highly on the neutron energy; but two main categories can be established: scattering and capture processes [16], [14], [17], [13].

a) Scattering processes

- Elastic scattering (n,n)**:** This process, which is the major responsible for neutron moderation or thermalization, occurs when part of the incident neutron energy is transfered to a nucleus that recoils without acquiring any excited state. After interaction, the recoil nucleus may cause atomic ionization and excitation in the surrounding material, until it finally stops. The relationships between the energies and the scattering angles for the emitted neutron $(E_n^{'},\theta_n)$ and those of the recoil nucleus (E_A,θ_A), in the laboratory (LAB) reference system, can be obtained through basic kinematics:

$$E_n' = \frac{\alpha m_n}{4m_A} E_n \left(\cos\theta_n + \sqrt{\left(\frac{m_A}{m_n}\right)^2 - \sin\theta_n} \right)^2 \tag{2.3}$$

$$E_A = \alpha E_n \cos^2\theta_A \qquad \text{where} \quad \alpha = \frac{4m_A m_n}{(m_A+m_n)^2} \tag{2.4}$$

$$\sin\theta_n = \sqrt{\frac{\alpha}{1-\alpha\cos^2\theta_A}\frac{m_A}{m_n}}\cos\theta_A \sin\theta_A \tag{2.5}$$

It can be observed, according to these expressions, that in the case of an hydrogen nucleus ($\alpha \simeq 1$) and scattering angle $\theta_A = 0$, the recoil nucleus or proton is ejected with the same energy ($E_n' = E_n$) as that of the incident neutron. In general, the average energy transferred to a recoil proton is 50% that of the incident neutron, which is enough to break the chemical bonds and to ionize the medium. Moreover, it is an experimental fact that below 10 MeV all neutrons are scattered following an isotropic angular distribution in the centre-of-mass (CM) reference system, which means that the number of emitted neutrons is proportional to the solid angle $d\Omega$ and that the scattering probability inside a certain solid angle, $P(\Omega)$, is:

$$P(\Omega) = \frac{d\Omega}{4\pi} = \frac{1}{2}\sin\phi d\phi \tag{2.6}$$

being ϕ the scattering angle of the emitted neutrons in the CM reference system.

The recoil nucleus energy depends on the atomic mass number of the target, on the incident neutron energy and also on the scattering angle. In fact, the energy tranferred from

an incident neutron as well as the elastic scattering cross-section decrease when the mass of the target nucleus increases. Neutrons of any energy can interact by elastic scattering as no threshold is needed for this reaction.

- Inelastic scattering (n, n')**:** In this process, the incident neutron is captured by the target nucleus and a new unstable compound nucleus is immediately formed. This compound nucleus releases rapidly another neutron of less energy than that of the incident neutron, leaving the residual nucleus in a given excited state, which subsequently returns to its ground state after liberating one or more γ rays. All these steps last less than 10^{-14} s. Applying the conservation laws for energy and momentum, the following relationship for the energy of the emitted neutron is obtained:

$$E'_n = \frac{1}{(1+\mathcal{A})^2}\left[\omega\sqrt{E_n} \pm \sqrt{E_n\left(\omega^2+\mathcal{A}^2-1\right)-\mathcal{A}\left(\mathcal{A}+1\right)E_i}\right]^2 \tag{2.7}$$

$$\omega = \frac{1}{2}\left(\left(\mathcal{A}+1\right)\sqrt{\frac{E'_n}{E_n}} - \left(\mathcal{A}-1\right)\sqrt{\frac{E_n}{E'_n}} + \frac{\mathcal{A}E_i}{\sqrt{E_n E'_n}}\right) \tag{2.8}$$

where E_i is the energy of the i-th excited level of the residual nucleus and $\mathcal{A}$ represents the quotient between the target nucleus mass and the neutron mass. For E'_n to be real and positive, the next condition should be imposed:

$$E_n\left(\omega^2+\mathcal{A}^2-1\right)-\mathcal{A}\left(\mathcal{A}+1\right)E_i \geq 0 \tag{2.9}$$

This puts into evidence that inelastic scattering processes only occurs if the incident neutron energy is above a given threshold, which must be at least equal to the energy of the excited state of the residual nucleus formed. It should be point out that the energy level of the excited state of the residual nucleus decrease with increasing mass number. This is why neutron inelastic scattering is more probable for heavier nuclei than for lighter ones. As a consequence, the cross-sections of inelastic scatterings increase with the incident neutron energy and their threshold values are between some MeV for light nuclei and some keV for heavy ones.

b) Capture reactions

- Radiative capture reaction (n, γ)**:** In this process, the target nucleus absorbs the incident neutron and becomes a compound nucleus at an excited state. The compound nucleus does not take longtime to reach its ground state with the subsequent release of the corresponding γ rays. However, the newly formed nucleus is normally a radioactive isotope able to decay afterwards mostly with the emission of γ- rays and/or β-particles. Radiative capture reactions are always exothermic (positive $\mathcal{Q}$-values) since the binding energy of the newly formed isotope is larger than the sum of the binding energy of the original target nucleus and the energy of the incident neutron. The radiative capture cross-section is quite high for the majority of nuclei, showing most of them a $1/v$ dependence (being v the neutron velocity) for thermal neutrons, whereas others display very pronounced resonances at intermediate energies.

- Non-elastic or Non-radiative capture reaction: A non-elastic capture reaction occurs when the result of a neutron absorption by a target nucleus is the emission of

Table 2.2. Some exoenergetic capture reactions.

Capture reaction	Q**-value** (MeV)	σ_0 (barns)*
${}^{3}_{2}\mathrm{He}(n,p){}^{3}_{1}\mathrm{H}$	0.7637	5400 ± 300
${}^{14}_{7}\mathrm{N}(n,p){}^{14}_{6}\mathrm{C}$	0.626	1.76 ± 0.05
${}^{35}_{17}\mathrm{Cl}(n,p){}^{35}_{16}\mathrm{S}$	0.62	0.79 ± 0.05
${}^{6}_{3}\mathrm{Li}(n,\alpha){}^{3}_{1}\mathrm{H}$	4.785	945 ± 5
${}^{10}_{5}\mathrm{B}(n,\alpha){}^{7}_{3}\mathrm{Li}$	2.791	4017 ± 32

* For the most probable thermal neutron energy 25.3 meV

protons, deuterons, alpha particles, tritons, etc. In principle, the emission of any charged particle ($p,\ \alpha,\ d,\ t, ...$) would only be possible if it acquires enough energy to overcome the Coulomb barrier of the compound nucleus, but these reactions take place at energies below this barrier due to the effects of quantum tunnelling. As $\mathcal{Q}$-values for these reactions are commonly negative, the processes are usually endoenergetic. However, the capture reaction could be exoenergetic for some specific nuclei like ^{3}He, ^{6}Li and ^{10}B, and for these nuclei capture is possible even for thermal incident neutrons, see table 2.2.

c) Spallation reaction (n, xn) **or** (n, np)

Spallation is a nuclear reaction in which the initial collision between the incident neutron and the target nucleus leads to a series of direct reactions (intranuclear cascade). During interaction, individual nucleons or small groups of them are fully ejected from the compound nucleus. After this intranuclear cascade phase, the residual nucleus is left in an excited state and it subsequently relaxes to its ground state by "evaporating" nucleons, mostly neutrons. As stated before, spallation reactions are predominant for relativistic neutrons, i.e., with energies above 10 MeV.

d) Fission reaction $(n, \mathbf{fission})$

Interactions of neutrons with heavy nuclei ($Z > 90$) may originate compound nuclei that split into two fission unequal fragments. This process, which takes place to avoid the high Coulomb repulsion force between protons of the nucleus, is always accompanied by prompt emission of one or more neutrons that may lead to further fissions of other nuclei resulting in a chain reaction. Fission reaction are likely for several isotopes of thorium, uranium, neptunium, plutonium, and higher mass actinides. It is possible for all incident neutron energies, although the cross-section is considerably greater for thermal neutrons in the case of ^{233}U, ^{235}U and ^{239}Pu. For ^{232}Th and ^{238}U, the fission reaction only takes place above 1 MeV and they are commonly used in dosimetry to separate the fast neutron component form the thermal one.

2.2. Neutron fields in workplaces

On 2^{nd} december 1942 and under Fermi's direction, the first man-made nuclear reactor went onto criticality. Since then, many techniques of profiting neutrons have been developed for different purposes, although sometimes neutrons are presented as an unwanted radiation. A great variety of neutron fields, generally mixed with photons, can be found in nuclear technology,

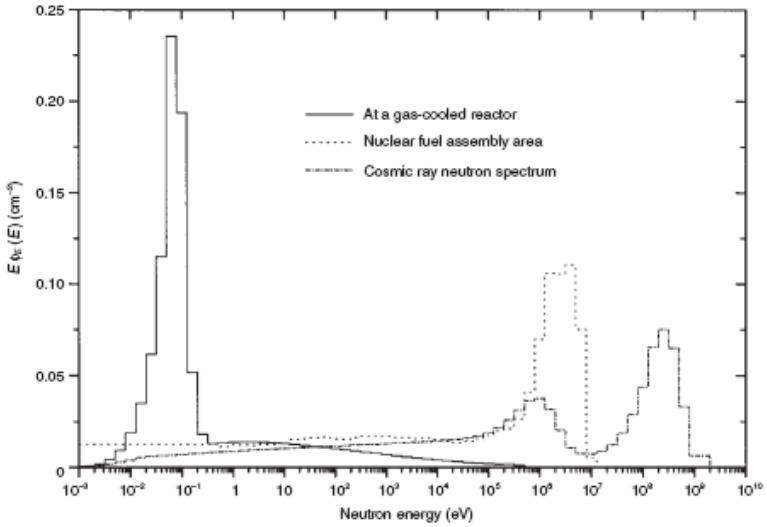

Figure 2.1. Examples of neutron spectra in workplace environments [18].

at research laboratories, at medical facilities, at places where radionuclide sources are used for testing and process control, and in the environment, particularly at high altitudes [18]. Clearly, all these different types of sources produce neutrons that cover a wide energy range, from 1 meV (or less) to hundreds of MeV (or more). Neutrons are always accompanied by γ radiation, leading to $n-\gamma$ mixed fields, due to the photon emissions from most of their nuclear interactions with nuclei of the medium. As an example, several neutron spectra are shown in figure 2.1. Neutron fields can be divided into several categories, related to their production mechanisms.

2.2.1. Neutron fields in the nuclear power industry

Neutrons originated from spontaneous or neutron-induced fission and from (α, n) sources could be found at fuel production and reprocessing plants, power plants, around nuclear fuel transport containers as well as at their intermediate and final storage sites. As these neutrons may be shielded with many absorbing and moderating materials (water, polyethylene, heavy water, graphite, iron, concrete, etc.), their spectra outside the shields consist commonly of thermal, intermediate and fast components. These spectra may reach up to a few MeV and they often have a fast component with a maximum located at several hundreds of keV.

2.2.2. Neutron fields based on radioactive sources

Radioactive neutron sources have to be manufactured in specialist plants and are used for a number of applications (moisture gauging, geological prospection, material activation analysis, instrument calibration in radiation protection, etc.). They are based mainly on spontaneous fission (such as the ^{252}Cf and ^{244}Cm source) and (α, n) processes. Although they are physically small, the total neutron emission rate can range from less than $1\,\mathrm{s}^{-1}$ to $10^{10}\,\mathrm{s}^{-1}$. The location of their primary high-energy peak may vary between 500 keV and 5 MeV depending on the considered radionuclide and, in the case of (α, n) sources, on the target used.

2.2.3. Neutron fields at nuclear research laboratories

Charged particle accelerators are widely used in both fundamental and applied research laboratories. They typically operate at high energy (up to GeV) and neutrons may be generated from (p, n) or (d, n) reactions. Behind the shielding of beam dumps, or in the vicinity of neutron-producing targets, neutron fields are encountered with energies from the keV region up to 100 MeV or even GeV. A special mention should be paid to the plasma fusion experiments (for example the ITER thermonuclear experimental reactor), which may yield excessive neutron fluxes with energies around 2.5 MeV in the case of deuterium-deuterium discharge reaction and around 14 MeV for that of triton-deuterium.

2.2.4. Neutron fields in medical facilities

As stated in chapter 1., neutrons may be generated by positron emission tomography (PET) cyclotrons and linear electron accelerators (LINACs). In the first type of facilities, protons (up to 40 MeV) or deuterons (up to 20 MeV) hit label organic compounds to produce short half-life positron emitting radionuclides, which are used to diagnose physiologically active compounds within the human body. LINACs are mostly utilised in radiotherapy for cancer treatment, producing high-energy (up to 25 MeV) electron or Bremsstrahlung photon beams. Primary neutrons may be scattered within the PET cyclotron vault or within the LINAC treatment room, giving rise to a broad energy distribution ranging from thermal to a few MeV. Neutron production is also observed in hadron and ion therapy facilities.

2.2.5. Cosmic neutron fields in the atmosphere

Earth is continually exposed to high-energy ionizing radiation that arises from sources outside the solar system. It consist of about 87% protons, 12% helium, 2% electrons and 1% heavier ions. The majority of these nuclei have kinetic energies between 100 MeV and 10 GeV. These energies are enough to penetrate the magnetic fields of the Earth and to initiate secondary particle showers in the atmosphere, mainly with nitrogen and oxygen, producing neutrons, protons, pions, photons, electrons and muons. The neutron field originated is complex and isotropic and varies with many environmental factors such as geomagnetic latitude, altitude, atmospheric pressure and solar activity.

Cosmic neutron fields in atmosphere generally present a broad spectrum with two peaks around 1 MeV and 100 MeV. The former is attributed to neutrons emitted by the evaporation process, whereas the latter is attributed to those produced by the pre-equilibrium and intranuclear cascade processes. The thermal component can be found only in spectra at ground level, since it is due predominantly to the Earth's albedo neutrons.

2.3. Radiation protection quantities

The aim of radiological protection is to control exposure to ionising radiation for preventing acute damage and for limiting the risk of long term effects in humans to acceptable levels. This can be achieved only through the establishment of a protection system, able to

allow the quantification of the extent of exposure to ionising radiation from both whole and partial body external irradiation and from intakes of radionuclides.

It was the International Commission on Radiation Protection (ICRP) who defined, in its Publication 60 [19] (ICRP60), a radiation protection system that has been implemented in almost all national regulations and which contemplates three main objectives:

- The characterisation of the radiation fields and their interactions with matter from physical and measurable quantities; the so-called **primary quantities**.
- The definition of **limiting quantities,** able to estimate the biological risk due to radiation exposures at low doses and from which legal limits to the public and professional radiation exposures can be created.
- The establishment of a series of **operational quantities,** to be used in practical measurements, as limiting quantities can not be applied directly since they are not directly measurable.

All these quantities are related with each other and define a clear hierarchy, as it can be seen in figure 2.2, being the effective dose the limiting quantity in terms of which dose limits for workers and population are defined, playing then a central role in radiological protection. Some of the ICRP60 recommendations as well as the radiation and tissue weighting factors were replaced and updated recently by the Commission in its publication 103 [20] (ICRP103). This publication also gives an additional guidance on the control of exposure from ionising radiation.

2.3.1. Primary standard quantities

A radiation field is completely described by the number of particles, their energy and directional distribution, and their spatial and temporal distribution defined through scalar and vectorial quantities. The three quantities most widely used for dosimetric applications are: **fluence**, **kerma** and **absorbed dose**, all of them scalar quantities. These quantities characterize the radiation fields and their interaction with matter. They are also defined as physical quantities without considering any specific aspect of radiation protection. The vector quantities providing information on direction distributions concern only the radiation transport theory and calculations.

Fluence

Radiation field quantities are defined at any point in a radiation field. There are two classes of radiation field quantities referring either to the number of particles, such as fluence Φ, or to the energy transported by them, such as fluence energy distribution or spectrum $\Phi_E = \frac{d\Phi}{dE}$.

Fluence, Φ, is the quotient of the number of particles dN incident upon a small sphere of cross-sectional area dS, thus

$$\Phi = \frac{dN}{dS} \tag{2.10}$$

The SI unit of fluence is cm^{-2} and is independent of the direction distribution of the particles entering the sphere. In calculations, fluence is often alternatively expressed in terms of the length of trajectories of particles passing through a small volume dV as follows

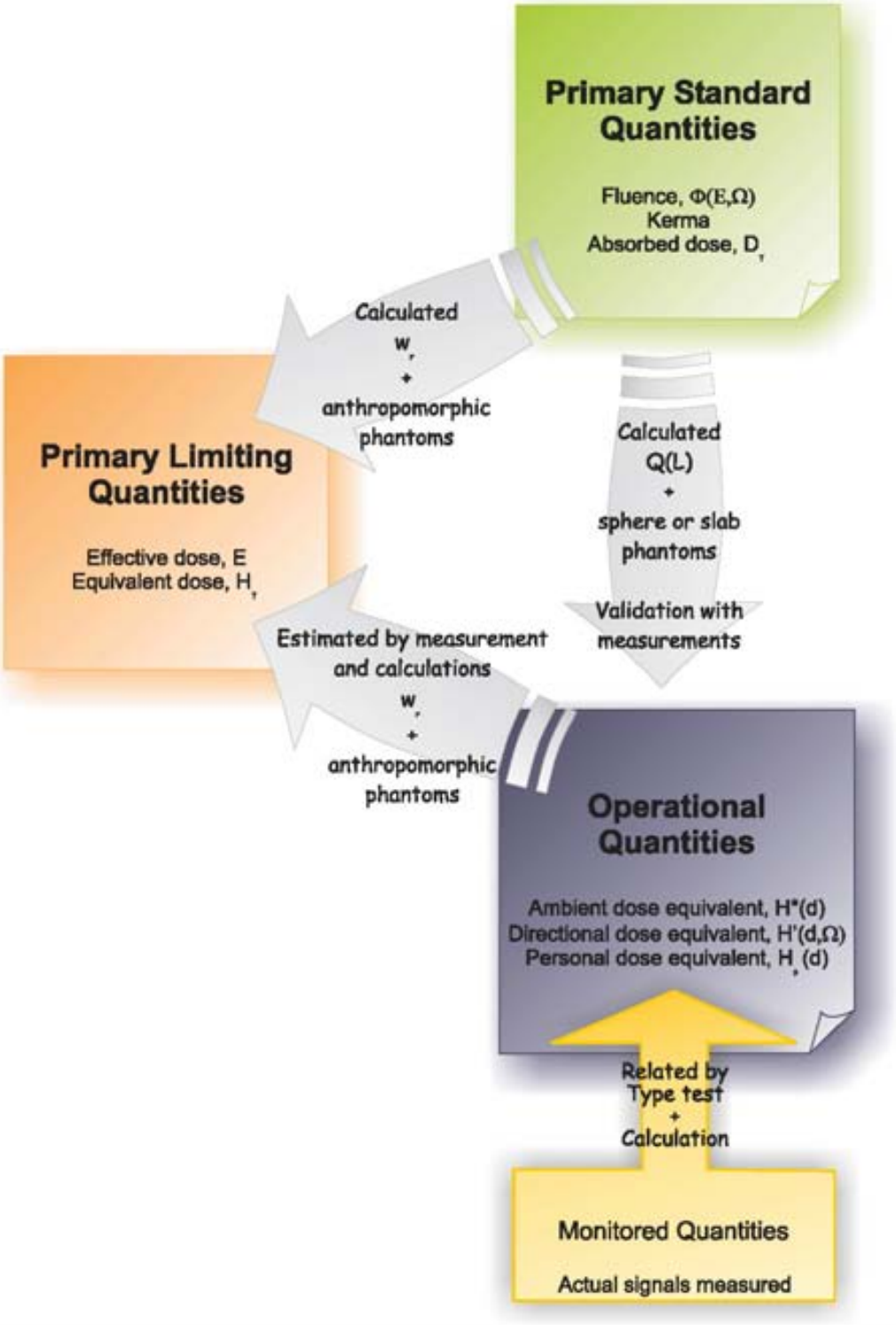

Figure 2.2. Hierarchy of radiation protection quantities [21].

$$\Phi = \frac{dl}{dV} \tag{2.11}$$

where dl is the sum of the lengths of trajectories through this volume dV.

Fluence is a quantity used to describe external radiation fields. It is not, however, practicable for general use in radiological protection and the definition of limits. Fluence always needs the additional specification of the particle and particle energy as well as direction distributions. Its correlation with the radiation detriment is very complex.

Kerma

The transfer of energy from uncharged particles (indirectly ionising particles, e.g., photons or neutrons) to matter is performed by the subsequent liberation and slowing down of secondary charged particles in this matter. This leads to the definition of the quantity kerma, K, which is the quotient of the sum of the kinetic energies, dE_{tr}, of all charged particles liberated by uncharged particles in a mass dm of material, and the mass dm. It is given by:

$$K = \frac{dE_{tr}}{dm} \tag{2.12}$$

The SI unit of kerma is $\mathrm{J\,kg^{-1}}$ and its special name is Gray (Gy). It is a non-stochastic quantity in which dE_{tr} is seen to be the expectation value of the sum of the energies of the liberated charged particles.

Absorbed dose

In radiation biology, clinical radiology and radiological protection the absorbed dose, D, is the fundamental physical quantity and it is used for all types of ionising radiation and any irradiation geometry. It is defined as the quotient of the mean energy, $d\bar{\varepsilon}$, imparted by ionising radiation to matter of mass dm, and the mass dm:

$$D = \frac{d\bar{\varepsilon}}{dm} \tag{2.13}$$

Similarly to kerma, the SI unit of the absorbed dose is the Gray (Gy). The value of kerma depends only on the local interactions in the material of mass element dm, but the value of absorbed dose also takes into account the secondary charged particles which are released in the surroundings of the mass element dm and which enter this element. Absorbed dose is derived from the mean value of the stochastic quantity of energy imparted, ε, and does not reflect the random fluctuations of the interaction events in tissue. While it is defined at any point in matter, its value is obtained as an average over a mass element dm and hence over many atoms or molecules of matter.

The definition of absorbed dose has the scientific rigor required for a basic physical quantity. It implicitly takes account of the radiation field as well as of all of its interactions with matter inside and outside the specified volume. It does not, however, take account of the atomic structure of matter and the stochastic nature of the interactions. Absorbed dose is a measurable quantity and primary standards exist to allow its determination by measurement.

2.3.2. Limiting quantities

In practical protection applications, absorbed doses are often averaged over larger tissue volumes. The mean absorbed dose, $D_{\mathbf{T},\mathbf{R}}$, due to a radiation type $\mathbf{R}$ and averaged over a specific organ or tissue $\mathbf{T}$ is defined by

$$D_{\mathbf{T},\mathbf{R}} = \frac{\int_{\mathbf{T}} D_{\mathbf{R}}(x,y,z)\rho(x,y,z)dV}{\int_{\mathbf{T}} \rho(x,y,z)dV} \tag{2.14}$$

where V is the volume of the organ or tissue region, $D_{\mathbf{R}}(x,y,z)$ the absorbed dose at a point (x,y,z) in that region and $\rho(x,y,z)$ the mass density at this point.

Nevertheless, this quantity is unable to estimate, by definition, the radiation risk due to induced stochastic health effects. It also depends both on the type of organ or tissue and on the different radiation fields. For that reason, additional quantities have been defined to take into account variations in the biological effectiveness of radiations as well as the different sensitivities of organs and tissues of the human body to each ionising radiation.

Equivalent dose

The protection quantity *equivalent dose* in an organ or tissue, $H_{\mathbf{T}}$, is defined by

$$H_{\mathbf{T}} = \sum_{\mathbf{R}} w_{\mathbf{R}} D_{\mathbf{T},\mathbf{R}} \tag{2.15}$$

where $w_{\mathbf{R}}$ is the radiation weighting factor for radiation $\mathbf{R}$. The sum is performed over all types of radiations involved. The SI unit of equivalent dose is $\mathrm{J\,kg^{-1}}$ and has the special name Sievert (Sv).

The values of $w_{\mathbf{R}}$ were defined largely on the basis of the relative biological effectiveness (RBE) of the different radiations. They are specified in terms of type and, in the case of neutrons, in terms of energy of radiation either incident on the human body or emitted by radionuclides residing in the body, see table 2.3. The following continuous function in neutron energy is recommended for the calculation of their weighting factors [20]:

$$w_{\mathbf{R}} = \begin{cases} 2.5 + 18.2\exp(-\frac{[\ln(E_n)]^2}{6}), & E_n < 1\,\mathrm{MeV} \\ 5.0 + 17.0\exp(-\frac{[\ln(2E_n)]^2}{6}), & 1\,\mathrm{MeV} \leq E_n \leq 50\,\mathrm{MeV} \\ 2.5 + 3.25\exp(-\frac{[\ln(0.04E_n)]^2}{6}), & E_n > 50\,\mathrm{MeV} \end{cases} \tag{2.16}$$

Figure 2.3 displays the $w_{\mathbf{R}}(E)$ function defined in ICRP103 compared to those defined in ICRP60.

Effective dose

The relationship between equivalent dose and the probability of stochastic effects is found to vary also with the organ or tissue irradiated. For that purpose, ICRP60 introduced the notion of effective dose, $\mathbf{E}$, which is defined by weighted sum of tissue equivalent doses as:

$$\mathbf{E} = \sum_{\mathbf{T}} w_{\mathbf{T}} H_{\mathbf{T}} = \sum_{\mathbf{T}} w_{\mathbf{T}} \sum_{\mathbf{R}} w_{\mathbf{R}} D_{\mathbf{T},\mathbf{R}} \tag{2.17}$$

where $w_{\mathbf{T}}$ is the tissue weighting factor for tissue $\mathbf{T}$ with $\sum_{\mathbf{T}} w_{\mathbf{T}} = 1$. The sum is performed over all organs and tissues of the human body considered to be sensitive to the induction of

Table 2.3. Radiation weighting Factors, from [20].

Type and energy range	**Radiation weighting factor, $w_{\mathbf{R}}$**
Photons	1
Electrons	1
Muons	1
Protons	2
Charges pions	2
Alpha particles	20
Fission fragments	20
Heavy ions	20
Neutrons	$w_{\mathbf{R}}(E)$ (see Eq. 2.16)

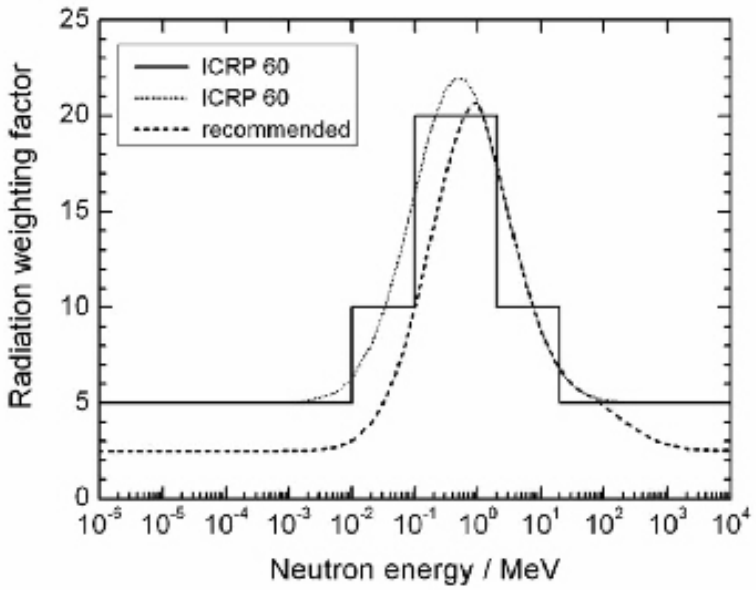

Figure 2.3. Radiation weighting factor, $w_{\mathbf{R}}$, for neutrons versus neutron energy. Step function and continuous function given in ICRP60 [19] and function adopted in ICRP103 [20].

Table 2.4. Recommended tissue weighting factors [20].

Tissue	$w_{\mathbf{T}}$	$\sum_{\mathbf{T}} w_{\mathbf{T}}$
Bone-marrow (red), Colon, Lung, Stomach, Breast, Remainder tissues*	0.12	0.72
Gonads	0.08	0.08
Bladder, Oesophagus, Liver, Thyroid	0.04	0.16
Bone surface, Brain, Salivary glands, Skin	0.01	0.04
	Total	1.00

* Remainder tissues: Adrenals, Extrathoracic (ET) region, Gall bladder, Heart, Kidneys, Lymphatic nodes, Muscle, Oral mucosa, Pancreas, Prostate (#), Small intestine, Spleen, Thymus, Uterus/cervix ($).

Table 2.5. Specified Q(L) relationships, from [19].

$L\ \left(\mathrm{K\,eV\cdot}\mu\mathrm{m}^{-1}\right)$	$Q(L)$
< 10	1
$10 - 100$	$0.32L - 2.2$
> 100	$300/\sqrt{L}$

stochastic effects. The $w_{\mathbf{T}}$ values are chosen to represent the contributions of individual organs and tissues to overall radiation detriment from stochastic effects. The unit of effective dose is the Sievert ($1\ \mathrm{Sv} = 1\ \ \mathrm{J\,kg}^{-1}$). This unit is the same for equivalent dose and effective dose as well as for operational dose quantities (see Section 2.3.3.). Therefore, care must be taken to ensure that the quantity being used is clearly stated.

The new recommended $w_{\mathbf{T}}$ values for different organs and tissues are given in ICRP103 [20] and shown in table 2.4. They are based on the last epidemiological data for cancer induction.

2.3.3. Operational quantities

Neither the effective dose $\mathbf{E}$ nor the equivalent dose $H_{\mathbf{T}}$ are quantities that can be measured in a straight forward manner and therefore cannot be used directly in radiation monitoring. This circumstance has forced the development of operational quantities, which are measurable and traceable to metrology standards.

Operational quantities are defined for radiation monitoring in situations of external exposure, with the goal of providing an estimate or upper limit for the value of the protection quantities related to an exposure or potential exposure of persons under most irradiation conditions. They are often used in practical regulations or guidance. In general, the quantity dose equivalent, H, is defined by

$$H = Q\ D \tag{2.18}$$

where D is the absorbed dose at the point of interest in tissue and Q the corresponding quality factor at this point, the value of which is determined by the type and energy of the charged particles passing a small volume element at this point. It is well known that the biological effectiveness of a radiation is correlated with the ionisation density along the track of charged particles in tissue. Therefore, Q is defined as a function of the unrestricted linear energy transfer, L_∞ (often denoted as L or LET), of charged particles in water (table 2.5).

Table 2.6. Operational quantities for different radiation protection tasks.

Task	**Operational quantities**	
	Area monitoring	Individual monitoring
Control of effective dose	*Ambient dose equivalent* $H^*(10)$	*Personal dose equivalent* $H_p(10)$
Control of doses to skin, hand, feet and eye lenses	*Directional dose equivalent* $H'(0.07, \Omega)$	*Personal dose equivalent* $H_p(0.07)$

The functions given in this table are the outcome of judgements taking account of results of radiobiological investigations on cellular and molecular systems as well as on the results of animal experiments. The quality factor Q at a point in tissue is then given by:

$$Q = \frac{1}{D} \int_{L=0}^{\infty} Q(L) D_L dL \tag{2.19}$$

where $D_L = \frac{dD}{dL}$ is the distribution of the absorbed dose in the linear energy transfer for the charged particles contributing to absorbed dose at the point of interest. This function is particularly important for neutrons because various types of secondary charged particles are produced in tissue by neutron interactions.

Different operational dose quantities are required for different tasks in radiological protection. These include area monitoring for controlling the radiation in workplaces and for defining controlled or restricted areas, and individual monitoring for the control and limitation of individual exposures. While measurements with an area monitor are preferably performed free in air, personal dosimeters are worn on the body. As a consequence, in a given situation, the radiation field 'seen' by an area monitor free in air differs from that 'seen' by a personal dosimeter worn on the body where the radiation field is strongly influenced by the backscatter and absorption of radiation in the body.

The use of different operational dose quantities reflects these differences. To describe the application of the different operational dose quantities for the different tasks of monitoring of external exposures, three operational quantities are defined, see table 2.6. Using the scheme of this table, it is not necessary to use the terms 'strongly penetrating radiation' (also called 'penetrating radiation') and 'low-penetrating radiation' (also called 'weakly penetrating radiation') in specifying the range of application of the operational quantities. The International Commission on Radiation Units and Measurements (ICRU) in its Report 51 (ICRU51) stated that $H^*(10)$ and $H_p(10)$ are designed for monitoring strongly penetrating radiation, e.g., photons (above about 12 keV) and neutrons, while $H'(0.07, \Omega)$ and $H_p(0.07)$ are applied for monitoring low-penetrating radiation, e.g., beta particles [22]. Furthermore, $H_p(0.07)$ is also used for monitoring the doses to the hands and feet from all ionising radiation.

There are situations in which individual monitoring is not used and where area monitoring or computational methods are applied to assess individual exposures. These situations include the assessment of doses to aircrew, prospective dose assessments and assessment of doses in workplaces and the natural environment.

Operational quantities for area monitoring

Two operational quantities are considered for area monitoring to assess effective dose; the ambient dose equivalent, $H^*(10)$, which is appropriate for strongly penetrating radiation

(photons above 12 keV, neutrons) and the directional dose equivalent, $H'(d,\Omega)$, only suitable for weakly penetrating radiation (α or β particles). Their definitions are as follows [20]:

- **Ambient dose equivalent,** $H^*(10)$, at a point in a radiation field, is the dose equivalent that would be produced by the corresponding expanded and aligned field in the ICRU sphere at a depth, 10 mm, on the radius opposing the direction of the aligned field.
- **Directional dose equivalent,** $H'(d,\Omega)$, at a point in a radiation field, is the dose equivalent that would be produced by the corresponding expanded field in the ICRU sphere at a depth d, on a radius in a specified direction Ω . For low-penetrating radiation the recommended depth is 0.07 mm and the directional dose equivalent must be $H'(0.07,\Omega)$.

For a complete understanding of these definitions, two concepts have to be clarified:

i) ICRU sphere phantom:

For all types of external radiation, the operational quantities for area monitoring are defined on the basis of a dose equivalent value at a point in a simple phantom, the ICRU sphere. It is as a sphere of tissue-equivalent material that adequately approximates the human body as regards the scattering and attenuation of the radiation fields under consideration. It has 30 cm in diameter, a density of 1 g cm^{-3} and a mass composition of: 76.2% oxygen, 11.1% carbon, 10.1% hydrogen and 2.6% nitrogen.

ii) Aligned and expanded radiation field:

The operational quantities for area monitoring defined in the ICRU sphere should retain their character of a point quantity and the property of additivity. This is achieved by introducing the terms *"expanded"* and *"aligned"* radiation field in the definition of these quantities. An *expanded* radiation field, defined as a hypothetical field, is a radiation field in which the spectral and the angular fluence have the same value in all points of a sufficiently large volume equal to the value in the actual field at the point of interest. The expansion of the radiation field ensures that the whole ICRU sphere is thought to be exposed to a homogeneous radiation field with the same fluence, energy distribution and direction distribution as in the point of interest of the real radiation field.

If all radiation is aligned in the expanded radiation field so that it is opposed to a radius vector Ω specified for the ICRU sphere, the aligned and expanded radiation field is obtained. In this hypothetical radiation field, the ICRU sphere is homogeneously irradiated from one direction, and the fluence of the field is the integral of the angular differential fluence at the point of interest in the real radiation field over all directions. In the expanded and aligned radiation field, the value of the dose equivalent at any point in the ICRU sphere is independent of the direction distribution of the radiation in the real radiation field. Conversion coefficients relating radiation field quantities to the operational quantities are usually calculated assuming vacuum outside of the phantom considered.

Operational quantities for individual monitoring

Individual monitoring of external exposure is usually performed with personal dosimeters worn on the body, and the operational quantity defined for this application takes this

situation into account. The true value of the operational quantity is determined by the irradiation situation near the point where the dosimeter is worn. The operational quantity for individual monitoring is the personal dose equivalent, $H_p(d)$.

- **Personal dose equivalent,** $H_p(d)$, is the dose equivalent in ICRU (soft) tissue at an appropriate depth, d, below a specified point on the human body. The specified point is usually given by the position where the individual dosimeter is worn. For the assessment of effective dose a depth $d = 10\,\text{mm}$ is recommended, and for assessing equivalent dose to the skin, and to the hands and feet, the recommended depth is $d = 0.07\,\text{mm}$. In special cases of monitoring the dose to the lens of the eye, it has been proposed that a depth $d = 3\,\text{mm}$ would be appropriate.

An operational quantity for individual monitoring should allow the effective dose to be assessed or should provide a conservative estimate under nearly all irradiation conditions. This, however, requires that the personal dosimeter be worn at a position on the body which is representative with respect to the exposure. For a dosimeter position in front of the trunk, the quantity $H_p(10)$ mostly furnishes a conservative estimate of the effective dose even in cases of lateral or isotropic radiation incidence on the body. In cases of exposure from the back only, however, a dosimeter worn at the front side and correctly measuring $H_p(d)$ will not appropriately assess **E**. Also in cases of partial body exposures the reading of a personal dosimeter may not provide a representative value for the assessment of effective dose.

2.3.4. Relationship between quantities

The relationships between all the quantities introduced so far were evaluated by a joint ICRP/ICRU task and published in ICRU Report 57 [23] and ICRP Report 74 [21]. They were obtained from Monte Carlo calculations, which simulated the behaviour of particles in a human body phantom in order to determine the spatial distribution of the limiting and operational quantities. In the case of neutrons, the conversion coefficients (up to 200 MeV for neutrons and up 10 MeV to for photons) to be used in practice are normalised to unit fluence or unit air kerma, and they are much more well defined for primary standard quantities and for area monitoring operational quantities ($H^*(d)$, $H'(d)$) than for $H_p(d)$. As an example, and as in this work we are concerned with area monitoring, the $H^*(10)/\Phi$ conversion factors for neutrons as a function of the particle energy, usually named h^*_Φ, are given in figure 2.4 and the $H^*(10)/K_{air}$ conversion factors for photons are given in figure 2.5.

2.4. Need of neutron spectrometry

Neutrons with which we are concerned cover a wide energy range that extends from below 1 meV to more than hundreds of MeV. Independently of the fact that neutrons may come from natural sources or be produced by human activities and that, for particular applications, the neutron energy range can be restricted to few orders of magnitude, instrumentation used for neutron dosimetry should cover the whole range of energies. This fact has clear implications in the performance of a good neutron dosimetry, which is always a complex radioprotection task due to several factors, starting with the definition of the operational quantities themselves, and ending in instrument design and calibration.

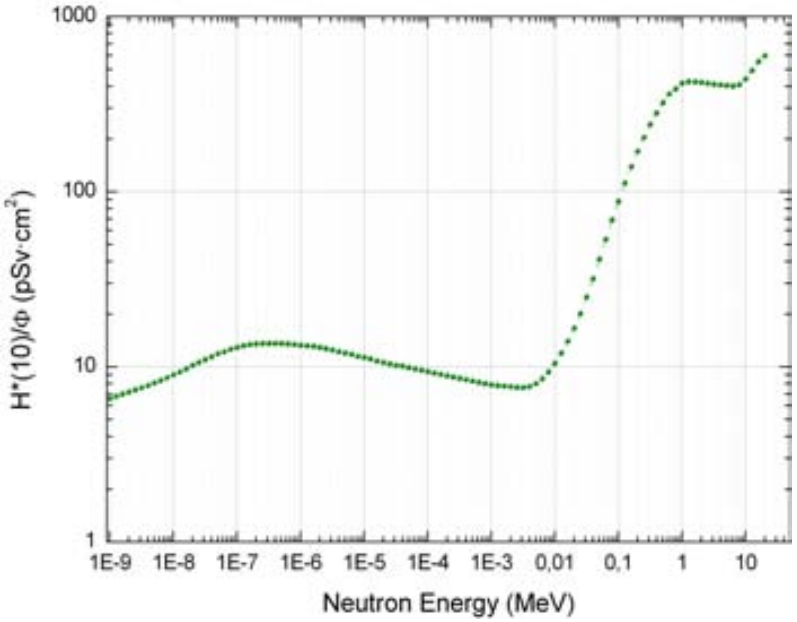

Figure 2.4. Neutron energy dependence of the $H^*(10)/\Phi$ conversion factor for neutrons [21].

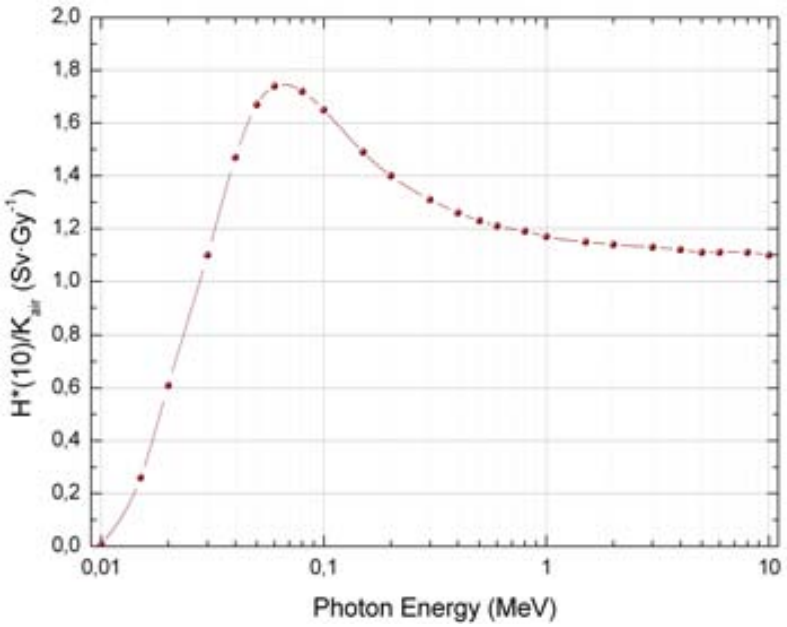

Figure 2.5. Photon energy dependence of the $H^*(10)/K_{air}$ conversion factor [21].

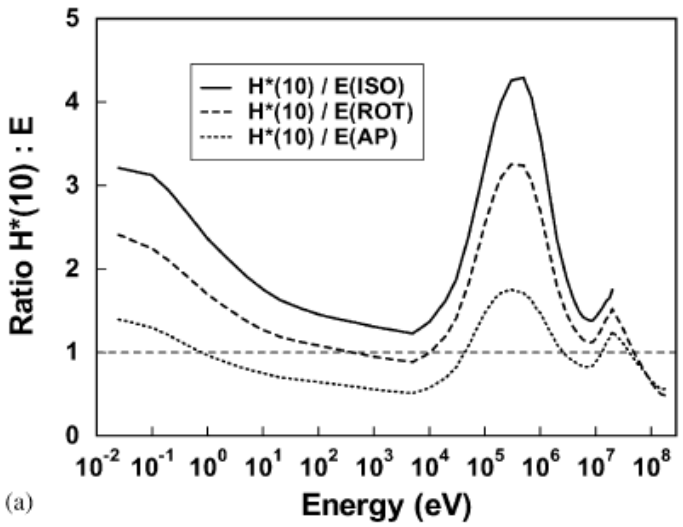

Figure 2.6. The ratio $H^*(10)/\mathbf{E}$ for several irradiation geometries as a function of neutron energy [21].

2.4.1. The role of operational quantities

Operational quantities were designed to provide an adequate approximation of the limiting quantities for irradiation from external sources, while avoiding underestimation or excessive overestimation of the quantity. The performance of the operational quantities as predictors of the limiting quantities can be dine by examining the relationships between operational and limiting quantities, particularly with respect to effective dose **E** for area monitoring. Figure 2.6 shows the $H^*(10)/\mathbf{E}$ ratio as a function of neutron energy.

It can be seen that in general **E** is overestimated by $H^*(10)$, except in few energy ranges mainly for the AP irradiation geometry. Although these different regions and, as in practice, irradiation by monoenergetic neutrons rarely occurs, the ambient dose equivalent is usually a conservative estimate for the effective dose. Accordingly, knowledge of the neutron spectrum is always recommended in situations where the operational quantities approach or exceed the limits.

2.4.2. The role of instrumentation

The analysis of the instrumentation and its performance clearly show another main problem in neutron dosimetry, i.e. the impossibility of designing instruments able to correctly estimate doses from their readings for all incident neutron energies and angles [24]. Two main factors contribute to this fact: the complexity of neutron interactions with matter and the dramatic dependence of the fluence to dose conversion coefficients, which vary a factor 40 for neutron energies ranging from 1 keV to 1 MeV. The responses in terms of dose equivalent of personal and area dosemeters are highly energy dependent. In addition, the detection mechanisms are very different than the processes of energy deposition in tissue. As a consequence, neutron instrumentation is usually able to respond with a *flat* response only within a restricted energy

interval. In fact, the reading M from a given neutron monitor having a response function $R(E)$ as a function of the incident neutron energy, when exposed to a given neutron field with fluence distribution $\Phi_E(E)$, is given by:

$$M = \int R(E)\,\Phi_E(E)\,dE \tag{2.20}$$

The instrument response function is called *flat* when it is proportional to h^*_Φ conversion coefficients, i.e. $R(E) = kh^*_\Phi, \forall E$. If this is the case, the instrument reading would be proportional to the ambient dose equivalent $H^*(10)$ as:

$$M = \int kh^*_\Phi \Phi_E(E)\,dE = k\int h^*_\Phi \Phi_E(E)\,dE = k\,H^*(10) \tag{2.21}$$

and an adequate instrument calibration would allow to determine the k proportionality constant value between the reading and the value of $H^*(10)$. In any other case, no simple relationship exists between M and $H^*(10)$, and an adequate methodology should be used to infer $H^*(10)$ from M, with the need of determining $\Phi_E(E)$ and, therefore, to perform neutron spectrometry.

Frequently used area monitors, such as rem counters with spherical (Leake type) or cylindrical (Anderson-Braun type) moderators, or tissue equivalent proportional counters (TEPC), show satisfactory responses in the MeV region, but their performances in the intermediate energy region are very poor. This can be observed for several neutron monitors in figure 2.7, where the readings per unit fluence as a function of the neutron energy are plotted to be compared with the h^*_Φ conversion coefficients [25].

The suitability of a neutron monitor will consequently depend on the specific environment where it is to be used; for example Berthold LB6411 and Leake 0949 have similar responses in the fast region, but LB6411 would give smaller overestimations if the workplace spectrum lays mainly on the intermediate range. That is why that the variability of the response with neutron energy becomes a key factor in the performance of any neutron monitor. Usually some **spectrometric** information and calibration in front of sources representative of the workplace spectra are needed for a correct estimation of the different quantities. As the response functions of neutron survey instruments do not behave like $h^*_\Phi(E)$ in all the neutron energy range, important over/underestimations of $H^*(10)$ may be obtained if instruments are calibrated in neutron fields that do not represent the workplace fields.

Notwithstanding, as the available instrumentation used for neutron dosimetry is not able to cover all the energy range of interest due to the large variability of neutron fields (see figure 2.1), a reliable $H^*(10)$ value may be derived from the spectrometric measurements using the following relation:

$$H^*(10) = \int_{E_{\min}}^{E_{\max}} h^*_\Phi(E)\,\Phi_E(E)\;\;dE \tag{2.22}$$

where $\Phi_E(E) = \frac{d\Phi}{dE}$ is the energy distribution of the neutron fluence (usually called neutron spectrum) and $h^*_\Phi(E)$ the fluence to ambient dose equivalent conversion coefficient for neutron of energy E. In cases where an accuracy higher than that achievable by these instruments is required, $H^*(10)$ must be evaluated via the determination of the spectrum $\Phi_E(E)$.

Finally, it is clear that a good neutron spectrometer for radiation protection purposes should accomplish as many of the following features as possible [26]:

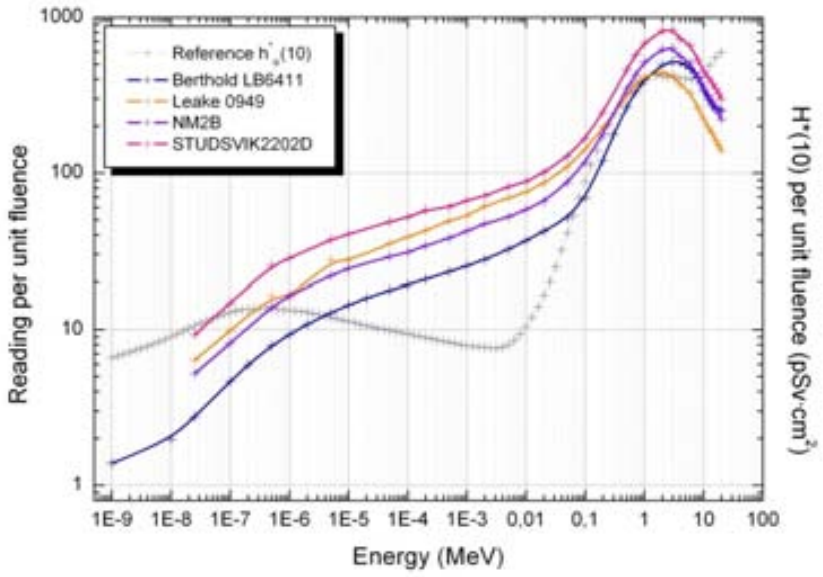

Figure 2.7. Ambient dose equivalent to fluence conversion coefficients as a function of neutron energy compared with the readings per unit fluence of different types of neutron monitors; (blue line) Berthold LB6411; (orange line) Leake 0949; (violet line) NM2B; (pink line) STUDSVIK22202D. Data from [25].

- It must be portable, or at least *transportable*.
- It should cover an energy range as wide as possible.
- It should have an isotropic or nearly isotropic response.
- It must be able to provide reliable results even under extreme environmental conditions.
- It must be insensitive to gamma radiation, or at least able to distinguish effectively between neutron- and photon-induced events.
- It has to maintain its accuracy in intense neutron fields (few mSv/ h) but also under very low exposures (a few nSv/ h).

CHAPTER 3.

Neutron spectrometry

3.1. Overview

Neutron spectrometry is as old as the famous Chadwick experiments in which *the neutron revealed itself to us* [27]. In those experiments, the neutron energies were obtained from the scattering recoil experiments in hydrogen and nitrogen. All neutron spectrometry techniques are based on the detection of secondary particles, charged particles or photons, created through the interaction of neutrons with matter. Methods of neutron spectrometry can be classified into seven groups based on the principle used to detect or measure the neutron energy [28]:

1. Neutron scattering and measurement of the energies of recoil nuclei.
2. Measurement of the energies of charged particles released in neutron-induced nuclear reactions.
3. Methods in which the velocity of neutrons is measured.
4. Threshold methods, in which the appearance of a neutron-induced effect such as radioactivity or other effects indicates that the neutron energy is, at least, at a given value.
5. Methods in which the neutron energy distribution is determined by unfolding a set of readings of several detectors that differ in the energy-dependence of their response to neutrons.
6. Neutron diffraction.
7. Measurement of the time-distribution of the slowing down of a short burst of high energy neutrons in a suitable medium.

Groups 6 and 7 and some methods in group 3 are pulsed-beam methods that need the use of a pulsed neutron source, whereas the remaining methods measure continuous neutron beams.

Many neutron spectrometers used today are based on methods introduced before 1960, like nuclear emulsions, recoil telescopes, proportional counter, organic scintillators and cloud chambers [28]. At that time, methods based on measuring energies of reaction products included ^{3}He proportional counter spectrometers and ^{6}LiI(Eu) scintillation crystals. Also time-of-flight and threshold radioactivation methods were used.

In 1960 notable developments were introduced with the Bonner sphere spectrometer method (BSS, group 5) and with the advances made in techniques based on gaseous ionization detectors and scintillation detectors. The Bonner sphere method is based on a thermal neutron sensor placed at the center of polyethylene spheres of different diameters. Iterative unfolding methods were introduced for the inference of the neutron spectrum from the readings of the different spheres during these years. Semiconductor based spectrometers were introduced in 1963, and superheated drop detectors were firstly used by Apfel in 1979.

Since the 80's, considerable technological progress was achieved but probably, the most important improvement was the impact of computers in neutron dosimetry: Monte Carlo codes were used to generate the response functions of the detectors, and iterative algorithms were applied to unfold the neutron spectra from the spectrometer readings.

3.1.1. Current techniques

In addition to the BSS technique, which will be reviewed in the following section, several techniques are widely used at present:

a) Spectrometry of recoil nuclei

Recoil spectrometers are detectors based on the production of secondary charged particles by the incident neutrons in the spectrometer material and collect the recoil particles emerging at all angles from it. On the other hand, recoil telescopes collect only recoil particles emerging at a particular angle. Typical energy ranges are from 50 keV to 4 MeV; peak-energy resolution is typically about 10% for 1 MeV neutrons. Wider energy ranges, up to 200 MeV, can be achieved with telescope detectors or organic scintillator based instruments. Reviews of spectrometers based on proportional counters and liquid scintillators are given in [29] and [30].

b) Nuclear reaction based spectrometers

This type of spectrometers is used to determine the neutron energy by measuring the energies of charged reaction products originated by neutron induced nuclear reactions (exo- and endothermic). The main candidates for use in this type of spectrometers are $^{3}\mathrm{He}(n,p)^{3}\mathrm{H}$ ($\mathcal{Q} = 0.764\,\mathrm{MeV}$), $^{6}\mathrm{Li}(n,\alpha)^{3}\mathrm{H}$ ($\mathcal{Q} = 4.79\,\mathrm{MeV}$), $^{10}\mathrm{B}(n,\alpha)^{7}\mathrm{Li}$ ($\mathcal{Q} = 2.79\,\mathrm{MeV}$) and $^{12}\mathrm{C}(n,\alpha)^{9}\mathrm{Be}$ ($\mathcal{Q} = -5.70\,\mathrm{MeV}$) and $^{28}\mathrm{Si}(n,\alpha)^{25}\mathrm{Mg}$ ($\mathcal{Q} = -1.65\,\mathrm{MeV}$). The most popular reaction is $^{3}\mathrm{He}(n,p)^{3}\mathrm{H}$, which allows to cover an energy range from 50 keV to 5 MeV with energy resolutions of $15 - 40$ keV.

c) Time-of-flight (TOF) methods

In this method, the neutron energy is determined by measuring the neutron flight time over a known distance [28]. When the neutron source is not pulsed, start and termination signals

Table 3.1. Some of the elements used for threshold spectrometry with the relevant reactions and threshold energies. Source: ENDF/B-VI.8 [33]

Element	**Reaction**	$T_{1/2}$ (s)	$E_{\min}$ (MeV)
F	$^{19}\mathrm{F}(n,2n)^{18}\mathrm{F}$	6586.2 ± 2.9	11.5
Mg	$^{24}\mathrm{Mg}(n,p)^{24}\mathrm{Na}$	52772 ± 14	4.9
Al	$^{27}\mathrm{Al}(n,\alpha)^{24}\mathrm{Na}$	52772 ± 14	3.2
Al	$^{27}\mathrm{Al}(n,p)^{27}\mathrm{Mg}$	567.72 ± 0.66	1.9
Fe	$^{56}\mathrm{Fe}(n,p)^{56}\mathrm{Mn}$	9282.6 ± 2.2	3.0
Co	$^{59}\mathrm{Co}(n,\alpha)^{56}\mathrm{Mn}$	9282.6 ± 2.2	3.9
Ni	$^{58}\mathrm{Ni}(n,2n)^{57}\mathrm{Ni}$	$(1283.4 \pm 1.8) \times 10^2$	12.4
Cu	$^{63}\mathrm{Cu}(n,2n)^{62}\mathrm{Cu}$	584.4 ± 1.2	11.0
Cu	$^{65}\mathrm{Cu}(n,2n)^{64}\mathrm{Cu}$	45723.6 ± 7.2	10.0
In	$^{115}\mathrm{In}(n,n')^{115m}\mathrm{In}$	16150 ± 14	0.3
I	$^{127}\mathrm{In}(n,2n)^{126}\mathrm{In}$	$(1124.9 \pm 6.0) \times 10^3$	9.2
Au	$^{197}\mathrm{Au}(n,2n)^{196}\mathrm{Au}$	$(53421.0 \pm 8.6) \times 10^2$	8.7
Li	$\mathrm{Li}(n,\alpha n')\mathrm{t}$	$(389.1 \pm 1.9) \times 10^6$	2.8

have to be provided. Two methods are used to generate the *start* signal. In the first method, the neutron is scattered in a start detector, for example an organic scintillator, and the time of flight to a second detector at a known distance and the angle is measured. In the second method, the start signal is provided by an associated particle or quantum that is emitted from the neutron source at the same time as the neutron. Typical energy range is from 1 to 15 MeV, with a 5% peak-energy resolution at 2.5 MeV.

d) Threshold methods

Radioactivation methods based on endoenergetic neutron-induced nuclear reactions ($\mathcal{Q} < 0$) are known as threshold methods. Neutrons with energies above the reaction threshold are detected by the presence of radioactive products or daughters. An appropriate set of nuclear reactions with well known threshold energies can be used for neutron spectrometry. See table 4.4 for a relation of the most common threshold reactions [31]. Activation foil techniques and superheated drop detectors spectrometry [32] are based on this principle. Superheated drop detectors spectrometry can be used in energy ranges from 0.1 to 20 MeV.

3.2. Bonner sphere spectrometers

3.2.1. Overview

Forty years after its first description by Bramblett et al. in 1960, the multi-sphere, or the Bonner sphere spectrometer (BSS), remains widely used in the field of neutron spectrometry and dosimetry by more laboratories than any other method [34]. Its almost isotropic response, its wide energy range from thermal to GeV neutrons when compared to other spectrometer instruments, see figure 3.1, and its easy operation make this type of spectrometer still being useful [35].

Any Bonner sphere spectrometer consists of a thermal neutron sensor placed at the center of a number of moderating spheres with different diameters and which may contain

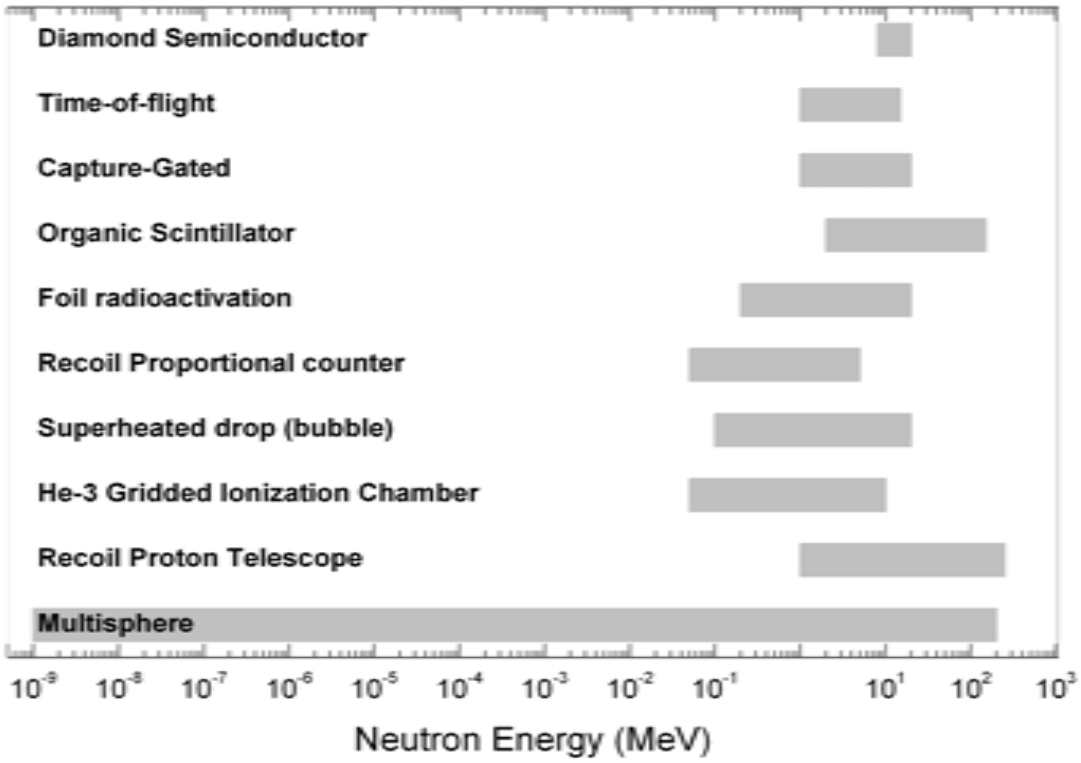

Figure 3.1. Neutron energy range of applicability of different neutron spectrometers [28].

different materials. Thermal sensors are used to detect moderated neutrons as direct fast neutron detection is complex and the related cross sections show lower values than those of thermal neutrons. Moreover, there is a considerable number of thermal neutron detectors with high sensitivity and good gamma rejection. As the size of the sphere increases, thermalisation is more effective for higher incident neutron energies, so that the maximum response of the sphere-detector assembly is shifted to upper energies. The neutron spectrum can be derived from the detector readings obtained with a given set of spheres, although this derivation is not a straight-forward process (see Section 3.3.).

The response of a given sphere-detector assembly i to an incident neutron of energy E is generally defined as the ratio of the instrument reading to the neutron fluence that induced the reading, is known as the *fluence response*, $R_i(E)$

$$R_i(E) = \frac{M_i}{\Phi(E)} \tag{3.1}$$

where M_i is the instrument reading (given in counts) and $\Phi(E)$ is the neutron fluence (in neutrons cm^{-2}) at the point where the center of the sphere is placed, *but in the abscence of the sphere*. This definition includes the requirement that the sphere must be uniformly *illuminated* by neutrons. This requierement is obviously fullfilled for measurements in a homogeneous *plane-parallel* neutron field. As the diameter of the sphere may be large, the homogeneity of the illumination is an important condition not easy to satisfy in certain experimental situations, as in irradiations with a point neutron source placed at small distances. The fluence response defined in equation 3.1 can be equally calculated if M_i is given as a count rate, using neutron fluence rates in the denominator.

The main operating principle of a BSS is the moderation of neutrons within the spheres, mainly via elastic scattering with hydrogen nuclei. Figure 3.2 illustrates the most frequent interactions of neutrons entering a Bonner sphere. According to this figure, neutron 1 escapes the sphere after its first elastic interaction. Neutron 2 escapes the sphere after being slowed down by several elastic collisions. Neutron 3 undergoes many interactions within the sphere and it is finally thermalised, but it is captured by a hydrogen nucleus before reaching the central detector. The resulting 2.2 MeV gamma ray may escape the sphere or produce an ionization electron in the central detector itself or in its walls and mounting structure. Finally, neutron 4 is thermalised inside the sphere and enters the detector sensitive volume, where the probability of detection approaches unity [36]. The proportion in which the four types of neutron interactions occur depends on the incident neutron energy and on the sphere diameter. For small spheres, low-energy neutrons produce a great number of processes leading to detection, whereas high-energy neutrons generally escape. For larger spheres, there is a considerable moderation, so low-energy neutrons are basically of type 3 and the detector response is low. However, high-energy neutrons have a great probability of being thermalised and detected.

Several well documented BSSs are actually in use in Europe with sets of spheres that go from 2 in (or even bare detector) to 12 in (or 18 in in the case of PTB) [37], [38], [39], [31] and [40]. These diameters allow to measure neutrons from thermal to $20 - 30$ MeV, although the energy resolution in the keV region is particularly poor because the few spheres having a response maximum in this region show very broad peaks. Including outer shells of different thickness of thermal neutron-absorbing materials (B, Li or Cd) has the effect of moving the peak in the response function to increasingly higher energies as the absorber thickness is increased. Several

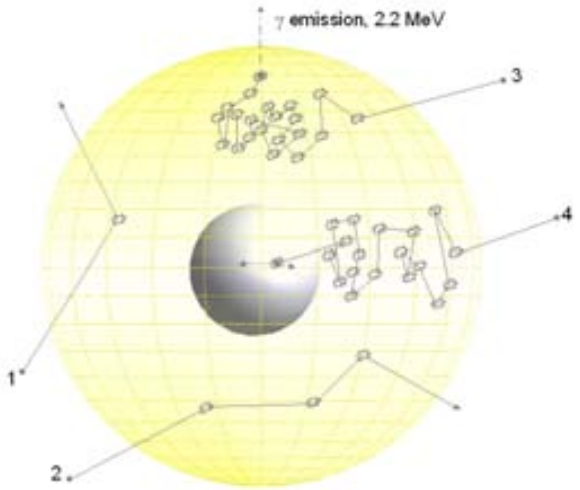

Figure 3.2. Neutron interactions in a Bonner sphere. The grey sphere represents the central thermal neutron sensor which is surrounded by a polyethylene sphere (yellow) [35].

authors have investigated this approach ([41], [42]) and have produced sphere configurations with response functions that peak in the low- and intermediate-energy range, although their overall sensitivity is unfortunately reduced.

High energy neutron fields ($> 20\,\mathrm{MeV}$) can be found at high energy particle accelerators or in cosmic rays. This fact leads to the need of improving the BSS response functions at higher energies. A possible solution is to include, into the polyethylene spheres, some high atomic number materials (Pb, Cu, Fe, W, etc.) that exhibit high (n, xn) reaction cross sections (see figure 3.3) [43]. The idea was theoretically developed by Kryuchkov et Semenova [44] and Hsu *et al.* [45] and experimentally tested by Birattari *et al.* [46] for a commercial extended range rem counter.

3.2.2. BSS response function

As it has been stated above, each sphere-detector combination i has a unique response function, R_i, that is a continous function of the neutron energy, E. When exposing the BSS in a neutron field with a fluence spectrum $\Phi_E(E) = \frac{d\Phi}{dE}$, the reading M_i of the sphere-detector combination i is related to its response $R_i(E)$ and to $\Phi_E(E)$, through their adequate *folding*

$$M_i = \int R_i(E)\,\Phi_E(E)\,dE \tag{3.2}$$

The inverse process, known as *unfolding*, allows to derive the neutron spectrum from the readings, provided that the corresponding response functions are well known. Mathematically, equation 3.2 is formally known as linear Fredholm integral of the first kind. As it is difficult to evaluate continuous functions from a finite number of measurements, for calculation purposes the following discretisation approach is applied

$$M_i = \sum_{i=1}^{n_E} R_{i,j}\Phi_j \tag{3.3}$$

Figure 3.3. Parts of the set of modified spheres extending the PTB 'C' BSS to measurements in high energy neutron fields, taken from [36]

where $\Phi_j = \Phi_E(E_j)\,\Delta E_j$ is the neutron fluence rate in the j-th energy group of width ΔE_j centered on E_j and $R_{i,j} = R_i(E_j)$ is the response function (calculated by Monte Carlo or other techniques) of the sphere-detector combination i for an energy E_j of the incident neutron. The number of energy groups, n_E, must be large enough to cover the entire energy range and to allow a reasonable description of $\Phi_E(E)$ without affecting the accuracy of the results. E_j and ΔE_j are usually defined in a logarithmic scale.

The information related with the neutron spectrum is contained in a vector $\vec{\Phi}$ with n_E components Φ_j $(i = 1, 2, \ldots, n_E)$. If measurements are taken with n_D spheres, n_D readings are obtained that can be written as a vector $\vec{M}$. This set of n_D equations form a matrix equation:

$$\vec{M} = \mathbf{R}\,\vec{\Phi} \tag{3.4}$$

where the $n_D \times n_E$ rectangular matrix $\mathbf{R}$ is the fluence response matrix of the BSS set. Therefore, it should be possible to determine, from the BSS measurement data, the n_E components of $\vec{\Phi}$ if the response matrix $\mathbf{R}$ is well known and if an appropriate unfolding procedure is used.

3.3. Unfolding procedures

In general, the problem of unfolding in Bonner sphere spectrometry is that the number of individual measurements, n_D, is largely smaller that the number of unknowns, n_E. In addition, BSS individual measurements cannot be considered as truly independent since, as shown in figure 3.4, the sphere response functions are broad smooth curves which overlap in extended neutron energy intervals. Such an under-determined problem has an infinite number of mathematical solutions, many of them without an acceptable physical meaning. As a consequence, to obtain a meaningful solution from BBS measurements, one must restrict the space of solutions by including some *a priory* information about the sought neutron spectrum. This information

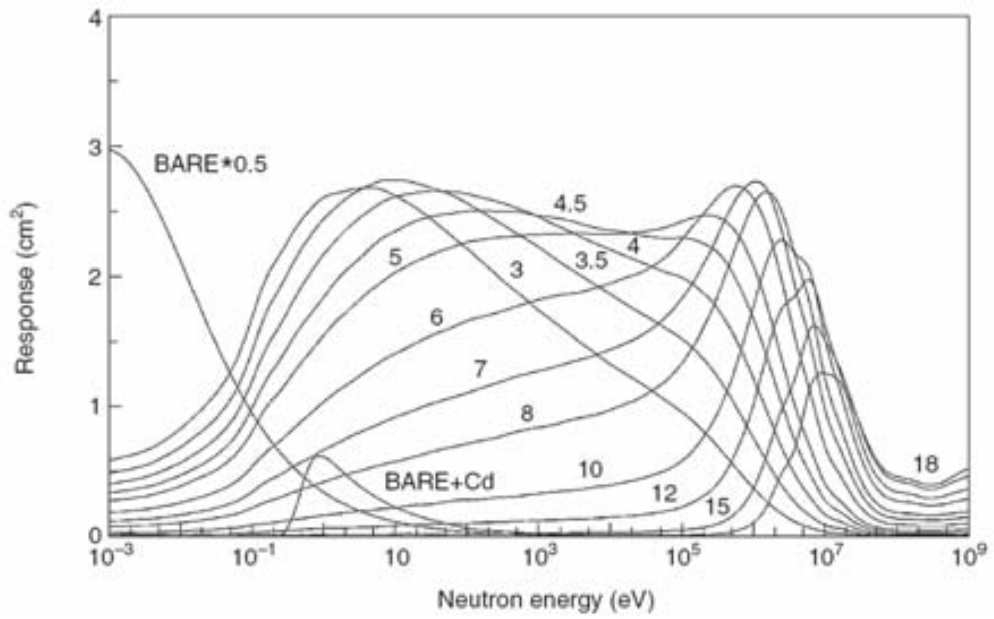

Figure 3.4. Fluence response matrix of the PTB Bonner sphere spectrometer [35].

is usually related to the laws governing the production of neutrons and their subsequent interactions with the surrounding materials. In general, there are two ways of implementing the a priori information about the measured neutron spectrum for almost all the unfolding codes:

1. By taking an initial guess or default spectrum, with non-negative values Φ_j^{DEF} at each of the chosen neutron energy bins E_j, to start the iteration process.

2. By representing the unknown spectrum with a parameterized function based on physical meaning.

For the first case, the initial guess spectrum can be obtained from Monte Carlo simulations of the given situation or from previous measurements performed in limited energy ranges with complementary neutron spectrometry systems. In the second case, the chosen parameters must not exceed the number of available meaurements, n_D, and should be enough to describe correctly the main features of the neutron spectrum.

To date, the problem of the neutron spectrum unfolding from the BSS measurements has been extensively studied, giving rise to a number of independent methods, based on least-square, Monte Carlo, maximum entropy and Bayesian approach procedures as well as on genetic and neutral network algorithms. Examples of unfolding codes using these techniques can be found in [47], [48], [49], [50], [51], [52], [53] and [54].

Many attempts were carried out in our group to develop our own unfolding codes, namely MITOM [55], CDM [56] and FRUIT [57]. The latter, which was developed in the framework of a collaboration with the Frascati (INFN-LNF) laboratory, is specifically designed for spectrometric measurements in workplaces, where detailed a priori information about the neutron fields is often unavailable. Among its main features, we should highlight the following aspects:

- It models any neutron spectrum as the superposition of up to four elementary (thermal, epithermal, fast and high energy) components, fully described by a set of positive parameters with physical meaning.
- It needs a limited amount of a priori information to obtain meaningful solutions. The user is only asked to provide qualitative information on the type of *radiation environment*. No default spectrum is asked to the user because the code generates it itself on the basis of the radiation environment selected by the user.
- Its iterative convergence procedure is based on Monte Carlo method to vary the above parameters and to derive the final spectrum according to pre-established convergence criteria.
- It has an user-friendly and visual operation, under the Labview environment, which continuously displays all quantities involved in the unfolding process and their variations together with a plot of the sought spectrum.
- It is equipped with a tool to evaluate the probability distribution for the estimated parameters, such as the neutron fluence and the peak energy. Uncertainties are evaluated from 16% to 84% interval of the cumulative probability [58].

Relevant achievements of the FRUIT code are: *i)* a high level of interactivity, allowing the user to follow and modify the convergence process, *ii)* the possibility to modify the convergence tolerances during the run, allowing a rapid achievement of meaningful solutions, and *iii)* the reduced dependence of the results from the initial hypothesis.

When using FRUIT one must provide the response matrix of the system used, the BSS measurements and their relative uncertainties. Then, the type of radiation environment must be selected among the following options:

1. Fission-like fields, like those in the vincinity of nuclear reactors or fuel elements.
2. Radionuclide neutron sources.
3. Fields produced by evaporation processes; such those produced in medical linear electron accelerators (LINACs) or accelerators producing radioisotopes for Positron emission tomography (PET cyclotrons).
4. High-energy electron accelerators.
5. High-energy hadron accelerators.
6. Monoenergetic Gaussian fields.
7. User-defined field providing other parameters than the ones defining the former cases.

According to the specified radiation environment, the code selects the appropiate physical model: fission $(1, 2)$, evaporation (3), evaporation and high-energy components $(4, 5)$, Gaussian (6). In case (7), the user choses the model. Thereafter, the code normalises the sphere readings to their weighted average, using their relative uncertainties as weighting factors. This allows working only with unit spectra.

The iterative process starts when the code generates automatically an initial parameter array depending on the radiation environment chosen. From this array, the code derives a first *trial* unit spectrum. Then, the measured count rates are compared with those calculated by folding the trial unit spectrum with the BSS response matrix to obtain a set of convergence indexes. In each iteration, the code generates a new spectrum by randomly changing one of the parameters used to model the neutron spectrum on the basis of a *variable tolerance*. This tolerance may be changed by the user according to the progress of the run. If the new parameter set fulfills the acceptance criteria defined in FRUIT, the new spectrum is accepted as a new solution. The user can, at any moment, interrupt the process and re-start it using this accepted solution, increasing or decreasing the tolerance. This allows to rapidly restrict the whole *parameter space* to a meaningful subspace containing the final solution. After few interventions, the solution is found and the user can stop the code and get the results. The code provides three output files, containing the final spectrum parameters, the numerical unit spectrum and the summary of all results. The latter contains:

- The sphere counts and their relative uncertainties.
- The physical model adopted, the spectrum parameters and their meaning according to the model used.
- The numerical unit spectrum in the specified energy binning.
- The sphere responses per unit fluence, R_i.
- The fluence estimated from each single spheres Φ_i.
- The best estimation of the fluence Φ and its uncertainty.
- The best estimation of the ambient dose equivalent $H^*(10)$ and its uncertainty.
- The final value of the deviation between measured and calculated normalized readings.
- The mean fluence to ambient dose equivalent conversion coefficient $\bar{h}^*_\Phi$ and its uncertainty, calculated using the following expression:

$$\bar{h}^*_\Phi = \frac{\int_0^{E\,\max} \Phi_E(E)\, h^*_\Phi(E)\, dE}{\int_0^{E\,\max} \Phi_E(E)\, dE} \tag{3.5}$$

- The fluence or dose equivalent averaged mean energy, $\bar{E}_\Phi$ or $\bar{E}_H$ respectively, characterising the hardness of the measured neutron spectrum. These quantities are defined as:

$$\bar{E}_\Phi = \frac{\int_0^{E\,\max} \Phi_E(E)\, E dE}{\int_0^{E\,\max} \Phi_E(E)\, dE} \tag{3.6}$$

$$\bar{E}_H = \frac{\int_0^{E\,\max} h^*_\Phi(E)\, E dE}{\int_0^{E\,\max} h^*_\Phi(E)\, dE} \tag{3.7}$$

In this work, neutron spectra from different neutron production methods (radionuclide neutron sources, quasi mono-energetic neutron beams, neutrons present in medical linear electron accelerators, and those produced at Positron Emision Tomography dedicated cyclotrons) were used or studied. All of them were obtained by unfolding the sphere readings with the FRUIT code by selecting the adequate radiation environment in each case.

3.4. Experimental validation at known neutron fields

Calibration procedures always consist of the irradiation of a measurement device under very precise and reproducible conditions in order to determine a correction factor f that relates the system reading with the reference value for that measurement position. This factor should depend only on the measurement instrument and the neutron spectrum but not on any other aspect characterising the irradiation device.

Compatibility with standard irradiation conditions, used in the definition of operational magnitudes, would mean to irradiate in vacuum and with plane-parallel beams. These conditions can never be satisfied because of the use of extended sources inside irradiation rooms with finite dimensions and scattering walls. Moreover, the presence of air inside these rooms and the unavoidable use of supports, to conveniently fix the source and the instrument at the considered positions, leads to the fact that gross readings provided by instruments are generally very dependent on irradiation conditions. In order to minimise the effect of all these factors a series of recommendations have been developed by the International Organization for Standardization (ISO) [59].

3.4.1. Deviation from the inverse square law

The reading of a given instrument must be corrected for all parasitic effects of neutron scattering and the geometric features due to source and/or instrument dimensions which deviate the behaviour instrument readings from the inverse square distance law. In fact, any instrument reading in presence of a field composed of direct and scattered neutrons, after linearity corrections are introduced, can be expressed as [59]:

$$M_T = \frac{B\, R_\Phi F_1(\theta)}{4\pi l^2}\left[\frac{F_1(l)}{F_A(l)} + F_2(l) - 1\right] \tag{3.8}$$

where

l is the distance between the source center and the reference point where the measurement is done

B is the total emission rate of the source (in 4π sr)

$F_1(\theta)$ is source anisotropy correction factor

R_Φ is the instrument response or sensitivity in terms of neutron fluence

$F_1(l)$ is the geometric factor

$F_A(l)$ is the air outscatter and/or attenuation correction factor

$F_2(l)$ is the correction function that represents the additional contribution of the inscattered neutrons

The geometric factor $F_1(l)$ takes into account the detector finite dimensions that induce its readings to be above the $1/l^2$ expected behaviour. It is clear that plane-parallel beam geometries can only be achieved for long distances between the source and the detector. However, as l increases scattering and times needed for irradiation also increase. In practice, if $l > 2r_D$, being r_D the detector radius, $F_1(l)$ is close to 1. The neutron fluence at the point of measurement decreases almost linearly as l increases due to outscatter interactions and/or nuclear reactions

with the surrounding air. This effect is accounted for by the term $F_A(l)$. However, the most important correction factor is $F_2(l)$, as the major deviations from the $1/l^2$ behaviour are given by the presence of *inscatter* neutrons. Inscatter neutrons are those that are not initially emitted towards the detector but can return back due to scattering in the room walls, floor and air volume. Again, the additional contribution of these neutrons to the instrument readings increases linearly as l increases. The inscatter neutron contribution to instrument readings can be determined experimentally under controlled specific irradiation conditions, with the shadow-cone or polynomial techniques.

3.4.2. Methods of evaluation of the scattered radiation

The shadow-cone procedure

In the shadow cone procedure, one or several shadow-cones able to remove any direct radiation are positioned between the neutron source and the detector for the experimental determination of the inscattered contribution. In the case of Bonner sphere spectrometers, each sphere is exposed in both "total spectrum" and "shadowed" configuration. The contribution of the direct fluence to the reading of the i^{th}-sphere can be calculated as:

$$M_i = M_i^{tot} - M_i^s \tag{3.9}$$

being M_i^s the inscattered reading behind the shadow cone (assumed to completely remove direct radiation), and M_i^{tot} the total reading obtained with no shadow-cone.

According to [59], shadow-cones consist of two sections; a 20 cm iron front part followed by a 30 cm polyethylene block (plus $\geq 5\%$ of Boron) in their rear part. To correctly apply this technique, the following requirements should be fullfilled:

- Large irradiation rooms, where the increase in instrument readings due to scattered radiations do not exceed 40%.
- The source-to-detector distance should be greater than twice the shadow-cone length.
- The obscured area at the reference point should ideally be equal to that of the considered sphere. In practice, an over-obscuration up to a factor two is acceptable. Higher values are not recommended since in over-shadowed geometries scattered radiation is underestimated and direct radiation overestimated.
- The distance between the source and the cone's front face should be accurately and experimentally optimised.

The polynomial procedure

When the shadow-cone technique cannot be used, a second approach can be applied to estimate the contribution of the scattered radiation. The polynomial procedure relies on the hypothesis that the total reading M_i^{tot} for any given sphere deviates from the $1/l^2$ behaviour as:

$$\frac{M_i^{tot} \cdot l^2}{F_1(l)} = M_i^{1m}\left(1 + Al + Sl^2\right) \tag{3.10}$$

where $F_1(l)$ is the geometric factor defined in section 3.4.1. and where M_i^{1m} represents the reading of the sphere due only to the direct contribution of the field at 1 m from the source. This reading obviously decreases with distance following the inverse square law. The terms Al and Sl^2 represent air scatter and room scatter contributions respectively.

If a series of measurements of the "total field" are performed at different source-to-detector distances and the left term of equation 3.10 is calculated for each sphere and distance, then M_i^{1m}, A and S can be derived by second degree interpolations as function of l.

CHAPTER 4.

Development of the passive Bonner sphere spectrometer

4.1. The UAB active neutron spectrometer

From the late 90's, one of the projects of the Grup de Física de les Radiacions of the Universitat Autònoma de Barcelona was characterizing neutron spectra at several Spanish nuclear power plants [60], [61] by means of Bonner sphere spectrometry. A new BSS was designed for that purpose which uses an active[1] detector [31] able to work in extreme environmental conditions. In what follows, the main features of this spectrometer are described.

4.1.1. Main features

Polyethylene spheres

As stated in section 3.2., a Bonner sphere spectrometer consists of a thermal neutron detector placed in the center of a set of moderating spheres. For the BSS developed by the GFR-UAB, a set of 11 polyethylene or polyethylene/cadmium spheres with diameters 2.5 in, 3 in, 4.2 in, 5 in, 6 in, 8 in, 10 in, 12 in, 2.5 in + 1.5 mm Cd, 3 in + 1.5 mm Cd, 4.2 in + 1.5 mm Cd, were precisely manufactured with high quality polyethylene (density $0.920\,\mathrm{g\,cm^{-3}}$). The complete set of spheres and their associated polyethylene holders, used to place the detector at the center of each sphere, are shown in figure 4.1. The cadmium shell is used because cadmium presents a heavy cut in its neutron cross section at 0.4 eV and allows to obtain information about the thermal component of the neutron spectrum.

Central neutron detector

The central thermal neutron detector is a ^{3}He proportional counter, 0.5NH1/1KI type, manufactured by Eurisys Measures [62]. The High Voltage tension is supplied by a HV source model 556 from EG&ORTEC, which allows to connect two detectors at the same time. This

[1] An active detection system is that requiring some kind of external electronic conexion and power supply to operate.

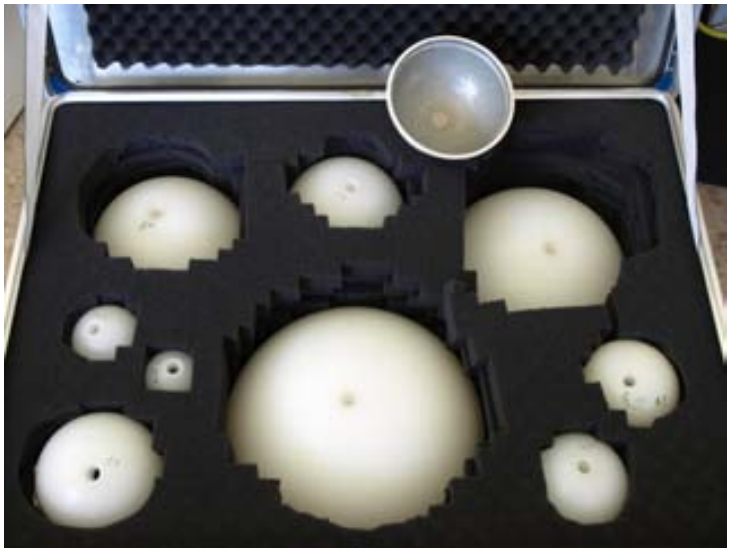

Figure 4.1. Set of polyethylene spheres and Cd shell to be used as neutron moderators with the UAB active Bonner sphere system

feature is used in facilities where it is important to monitor the neutron production rate by connecting a second ^{3}He detector with an additional single 4.2 in sphere. As it can be seen in figure 4.2, the 0.5NH1/1KI proportional counter is a cylinder of Monel^{TM} (a metal alloy, primarily composed of nickel, up to 67%, and copper, with some iron and other trace elements) of 4.4 cm height and 1 cm diameter. The sensible volume is on top of the Monel cylinder and it is also cylindric in shape (1 cm height and 0.9 cm diameter), as it can be seen in the detailed internal schema shown in figure 4.2. It consists of a mixture of ^{3}He (99, 7% in isotopic composition at 8 bar), Krypton (2 bar) and a small quantity of CO_2 at 100 mbar to avoid discharge and, theoretically, it is sensible enough to provide 0.5 pulses per detected thermal neutron. Experimental calibrations with the SIGMA neutron source at IRSN Cadarache (France) allowed to obtain an experimental sensitivity of 0.36 pulses/n cm^2 which agrees with calculations made by Caizergues and Poulot [63].

It should be mentioned that gamma radiation associated to neutron beams may induce a parasitic signal of electronic origin when interacting with the detector heavy materials (cathode) leading to a "wall effect" [14]. In order to avoid the wall effect without interfering with neutron detection, one takes into account that the total absorption cross section for photons decreases rapidly with photon energy and with atomic number of the medium. In our case, a lead cap (1 mm thick) is placed inside the polyethylene holders used to center the detector inside the spheres, shielding the detector from the unwanted secondary gamma radiation.

Electronics

The environmental conditions in which the spectrometer was to be used implied that, many times, the operator could not stay near the measuring point but had to move behind shieldings, several meters away from the measuring point. The electronics was consequently chosen to be able to amplify the ^{3}He proportional counter signal and to transport it to distances

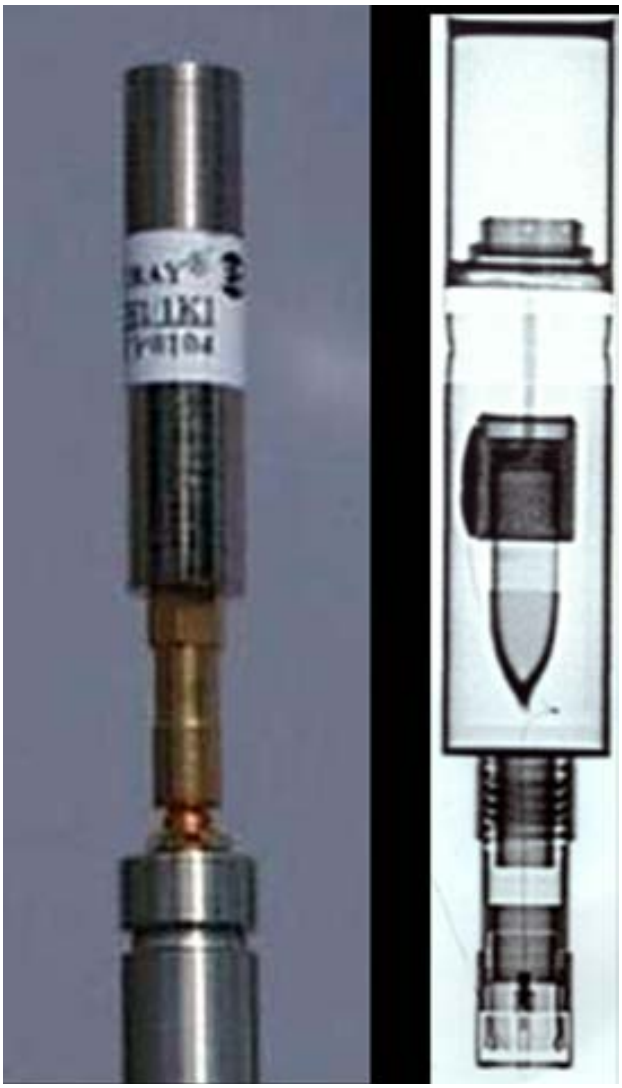

Figure 4.2. The ^{3}He proportional counter, 0.5NH1/1KI type, and its internal details used as neutron detector for the UAB active Bonner sphere spectrometer.

Figure 4.3. The electronics with its inputs and outputs and the proportional counter fixed on top.

up to 100 m, where the acquisition system was placed. It can be used both as a simple counter or as a signal treatment unit as it consists of:

- a charge amplifier ACHMC98 type, specially conceived for Bonner sphere neutron spectrometry,
- a high voltage filter,
- a preamplifier,
- an amplification section,
- a shape circuit with discriminator,
- and a height pulse discriminator.

This set of electronic components is placed inside an aluminium box to ensure electromagnetic shielding, see figure 4.3, with a metal screw below that allows to fix it in a tripod. The ^{3}He proportional counter is fixed in top of this aluminium box. The voltage for the electronics is provided by a home made $+12\,\mathrm{V}/-12\,\mathrm{V}$ source.

Data acquisition system

A logical pulse counter from Novelec, model E720, is normally used during measurement campaigns to count the number of pulses provided by the detector in a specified time interval. This counter has up to 8 inputs which allow to monitorise simultaneously several units. A multichannel analyzer (MCA) is also used when analogic pulses must be analysed.

Discrimination of photon pulses

The electronics described above contains a height pulse discriminator that sets a threshold level below which pulses are rejected. Neutron detection with an ^{3}He proportional counter takes place through the capture reaction $^3\mathrm{He}(n,p)\mathrm{T}$ with a $\mathcal{Q}$ value of 764 keV whereas gamma particles leave very few energy inside the detector. These facts, together with the *wall effect*, explain the typical height pulse distribution in figure 4.4 [14]. This distribution contains two main parts separated by a valley that can be used as discrimination level in order to avoid gamma induced pulses to be counted.

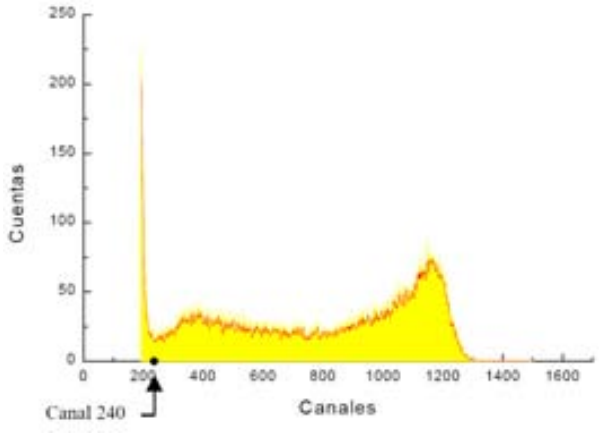

Figure 4.4. Typical pulse height distribution obtained with the UAB active BSS spectrometer

4.1.2. Response functions

It has been said in section 3.2.2. that each sphere-detector combination has a unique response, $R_i\,(E)$, which is a continous function of the neutron energy. The response functions for the UAB active Bonner sphere spectrometer were calculated by Monte Carlo techniques with the MCNP4B code [64] considering a realistic representation of the detection system, which was achieved by a radiography examination with X-rays and the information provided by the manufacturer. A total of 31 cells have been defined as it can be seen in figure 4.5 [31].

The influence of the polyethylene density in the response functions was also studied using the 6 in sphere and introducing 3% variations in the density value [31]. The variations obtained in the sphere response were less than 11% in the whole energy range. As a consequence, the tolerance on the nominal density provided by the manufacturer, which was 0.4%, was considered to have no effect on the response functions.

The response functions obtained for all the spheres and for neutrons with energies ranging from thermal to fast regions can be seen in figure 4.6.

4.1.3. Experimental validation

The response functions are usually obtained by simulation. Consequently, the results obtained by calculation may not coincide with those obtained experimentally. The most used

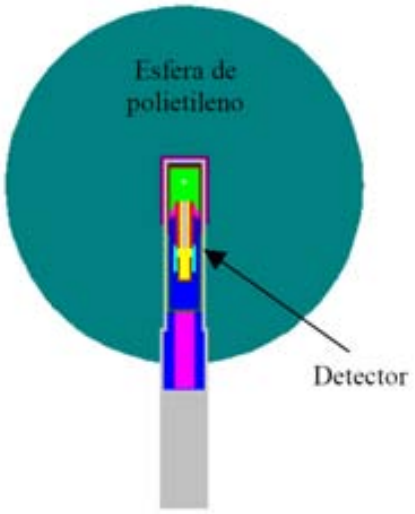

Figure 4.5. Representation of the active BSS detection system used for simulation of the response functions with MCNP4B

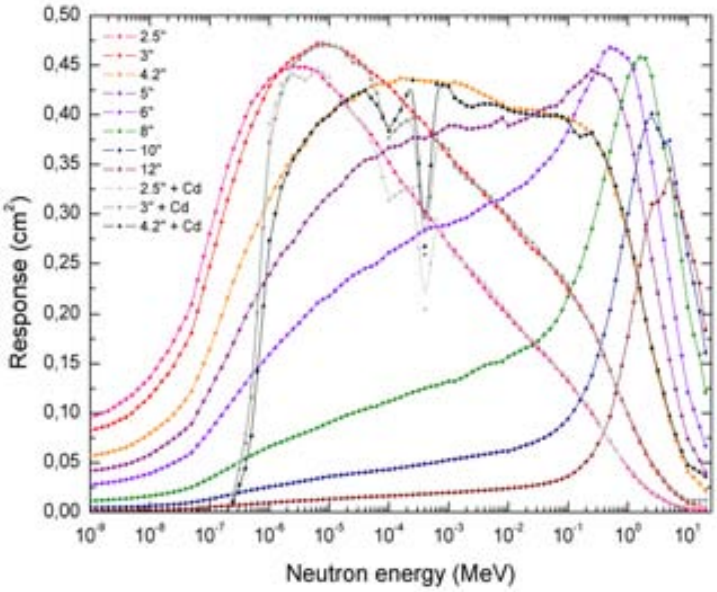

Figure 4.6. Response functions for the whole set of spheres used as Bonner sphere system active neutron spectrometer

method to adjust these discrepancies is to apply a scale factor to the response functions, allowing to minimize the differences between the calculated values and the experimental ones. The ideal situation is to find a common multiplicative factor for the complete set of response functions.

The performance of the active Bonner sphere spectrometer was tested with neutron reference fields at IRSN (Institut de Radioprotection et de Sûreté Nucléaire, France), and with monoenergetic neutron beams at Physikalisch-Technische Bundesanstalt (PTB, Germany) [31].From a comparison of the measured BSS measurement data and those calculated by folding the reference spectra with the BSS response matrix, a calibration factor of 0.99 ± 0.03 was obtained for all the sphere-detector combinations and reference spectra. However, the sensitivity of the ^{3}He proportional counters must be checked from time to time, specially because little variation on the ^{3}He pressure may lay to significant variations on the measurements. Periodic checks of the calibration factor have taken place, the last one in March 2010.

4.1.4. Limitations of the active BSS in intense and pulsed γ-neutron mixed fields

The performance of the UAB active Bonner sphere spectrometer in intense and pulsed γ-neutron mixed fields was tested with a Varian 2100CD radiotherapy LINAC of 18 MV nominal acceleration potential at the *Germans Trias i Pujol* hospital, in the area of Barcelona. The spheres were centered at 50 cm distance from the isocenter[2] and at its same height. The output signal of the central ^{3}He proportional counter was monitored with a multichannel analyser. Pulse height distributions like those presented in figure 4.4 were expected.

Nonetheless, the measured pulse height distributions, as shown in figure 4.7, presented many alterations related to the own characteristics of the LINAC environment field. Two unexpected phenomena were observed: the photons wall effect and pulse pile-up. Both phenomena may be explained by the following reasons:

- The primary photon field is very intense and pulsed in time, so that a large number of pulses are generated inside the ^{3}He proportional counter with a time separation below its dead time. The ^{3}He proportional counter is unable to separate these pulses and counts them as a unique golbal pulse, with a total energy equivalent to the sum of the delivered energies. This finally distorts the output pulse-heigh distribution. Many times, the corresponding energy of the global pulse is so high that it is not processed at all and a final sum peak appears in the last MCA channel.

- The detector wall effect phenomenon becomes important if the photon rate and energy increases, as is the case.

- A small amount of undesirable photonuclear reactions like $^3\mathrm{He}(\gamma, n)^2\mathrm{H}$ and $^3\mathrm{He}(\gamma, 2p)\, n$ may also take place within the detector and may affect its readings.

- The radiofrequency waves generated in the klystrons that guide the electron beam may interfere with the associated detector electronics leading to its incorrect working.

[2] A reference position located along the LINAC beam axis at 100 cm distance from the target and around which the gantry can rotate completely.

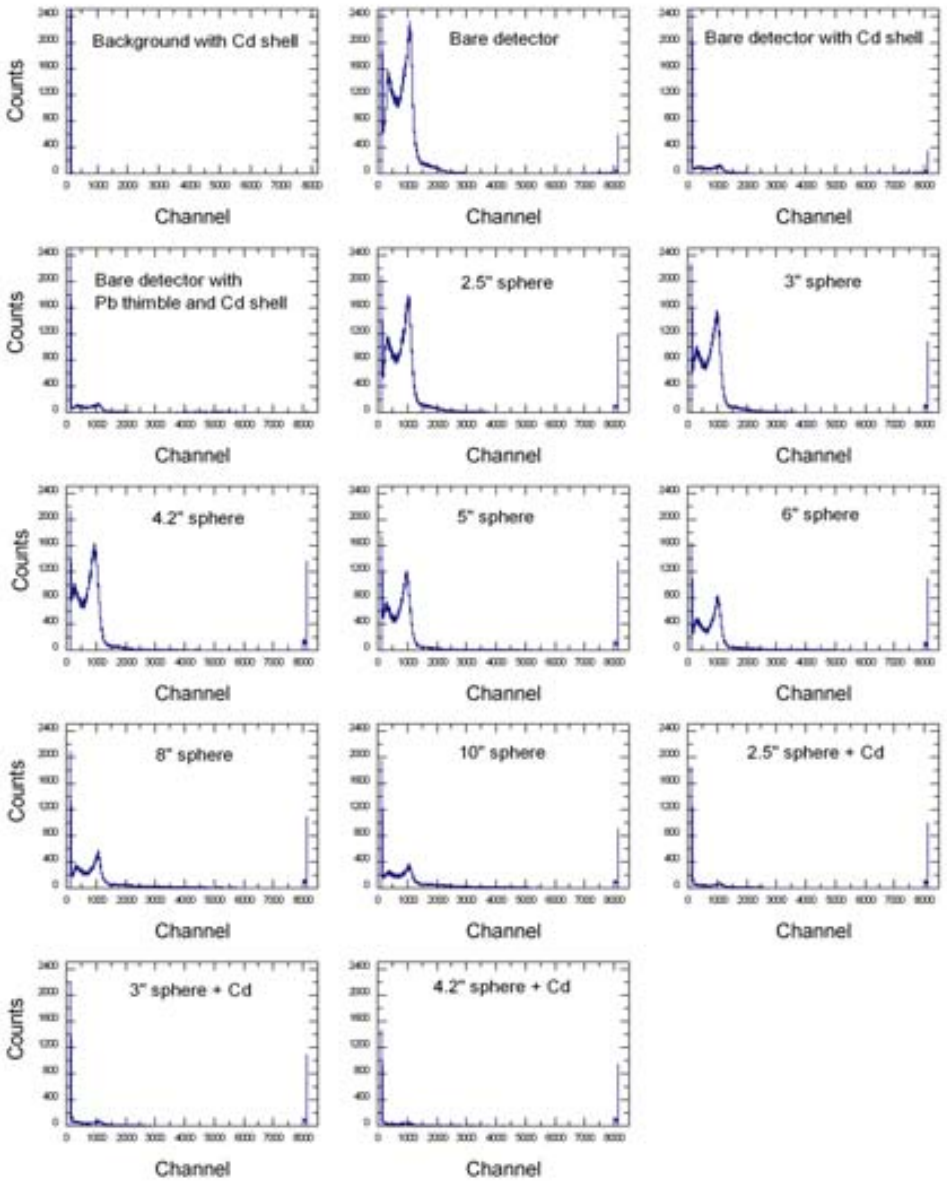

Figure 4.7. Output signals obtained with a multichannel analyser when the UAB active BSS was tested with an 18MV medical LINAC at 50cm distance from isocenter and at its same height.

All these limitations discourage the use of the active BSS in such severe irradiation environments. There were many attemps to unfold the active BSS readings but all of they completly failed.

4.2. Passive neutron spectrometry

Determination of neutron spectra with BSS in presence of very important gamma fields becomes specially difficult when active detectors are used. One way to overcome all the associated difficulties in these cases is using passive[3] detectors able to detect thermal neutrons together with the set of polyethylene spheres. An overview of neutron passive detectors, their implications on spectrometry and the selection of an adequate passive detector ([14], [65] and [66]) are developed in the following subsections.

4.2.1. Neutron passive detectors

Several types of passive neutron detectors exist with clear different characteristics.

Nuclear emulsion films

Related to the discovery of X-rays, at the end of 19^{th} century, nuclear emulsion films remain a widespread technique for neutron personal dosimetry. These films consist of an emulsion of silver bromide grains suspended in a gelatine matrix, supported in turn with a backing of glass or cellulose acetate polymers. The action of ionising radiation (charged particles or photons) in the emulsion is similar to that of visible light. Hence, neutrons can be registered only if an appropriate converter originating charged particles is used.

The nuclear emulsion films are divided into two categories: those in which a general darkening of the emulsion is recorded due to the cumulative effects of many interactions, and those in which trajectories of single ionising radiation particles are individually recorded. However, the main drawbacks of these detectors are that they are highly sensitive to photons, they may present problems of emulsion saturation and their precision is not enough to be used in neutron spectrometry with the Bonner sphere method.

Thermoluminescent crystals

Thermoluminescent crystals are based on the properties of some inorganic materials doped by inherent impurities to trap all the electron-hole pairs created as a result of irradiation to ionising radiation. If the TLD material is heated thereafter, all trapped electrons may return to the conduction band and they may migrate to the nearest trapped hole, where they can recombine with the emission of photons in the form of prompt fluorescence. The intensity of photon emission can be measured with a photomultiplier tube and is proportional to the number of electrons liberated. This process provides a measure of the energy delivered to the TLD crystal by the ionising radiation. ^{6}LiF is the most popular thermoluminescence crystal used to measure thermal neutrons. Since this crystal is sensitive to photons, pairs of ^{6}LiF and ^{7}LiF must be used

[3] A detection system is passive when it does not require any external external electronic conexion or power supply.

in mixed $n - \gamma$ fields, as ^{7}LiF only measures the photon component. It must be said that the method is reliable only when the neutron/gamma ratio is high enough, which is not the case in LINAC and PET workplaces fields.

Superheated drop liquids

A superheated drop liquid detector consists of a pocket-size tube filled with a transparent gel, equivalent to tissue in composition, containing tiny dichlorodifluoromethane (halocarbon, CCl_2F_2) droplets. When one of these droplets is hit by a neutron, it immediately vaporises and a visible gas bubble is trapped inside the gel. The number of bubbles trapped inside the gel is directly countable and provides a measure of the neutron fluence. Their main advantages are the low detection limit for the neutron dose, the zero sensitivity to photons, the isotropic angular response and good energy dependence and the fact that they are reusable. However their are not sensitive to thermal neutrons and can be easily affected by ambient temperature variations.

Solid state nuclear track detectors

In most dielectric materials – including minerals, crystals and plastics – the passage of a heavily charged particles creates damage zones, on an atomic scale, along their paths called latent tracks. In the case of plastics, an eventual treatment of these latent tracks using chemical or electrochemical etching allows their visualisation under optical microscopes or by a naked eye, respectively. Polyallyl di-glycol carbonate (PADC) polymers are the most popular since they are used in combination with a ^{6}Li, ^{10}B and ^{14}N converter for thermal neutrons and a hydrogenated one for fast neutrons. Being insensitive to photons, they are particularly suitable for use in mixed $n - \gamma$ fields. In each configuration, the counted track density can be related to the number of incident neutrons if a proper calibration is conveniently performed. Nonetheless, they have some negative aspects, as for instance the high variability of the number of tracks due to background effects, poor statistics and the existence of a critical angle that limits the registration of incident particles. Moreover, they reveal track saturation problems when using electrochemically etched plastics and, similarly to nuclear emulsion films, the analysis of chemically etched tracks is very tedious and complicated.

Activation materials

Thermal neutron detection is also possible by measuring the radioactivity induced in some materials as a result of their nuclear reactions. The resulting activation products are α, β and γ emitters which activities can be measured with conventional instruments. A key point for this technique is to choose materials with high cross sections but with small thicknesses to avoid perturbation of the neutron flux. The main advantage of this technique is that measurements are not severely affected by the presence of photons and it can be used in pulsed and/or very intense fields.

From all the types of passive neutron detectors described above, activation detectors can be considered the most adequate for the Bonner sphere technique.

4.2.2. Bonner sphere spectrometry with activation detectors

The principle of Bonner sphere spectrometry was introduced in section 3.2., where it was stated that the neutron spectrum can be derived from measurements, provided the response matrix of the BSS is well known. Neutron exposure originates a given radionuclide of interest when the activation detector is irradiated. Measurement of the radioactivity of this induced radionuclide allows to derive the incident neutron spectrum. In fact, if an activation foil is thin enough to avoid unwanted perturbation of the neutron fields, the formation rate r (s^{-1}) of the radionuclide products at a given incidence energy is given by:

$$r = V\Sigma_{\mathrm{act}}\dot{\Phi} = V\rho_{\mathrm{at}}\sigma_{\mathrm{act}}\dot{\Phi} \tag{4.1}$$

where $\dot{\Phi}\left(\mathrm{cm}^{-2}\,\mathrm{s}^{-1}\right)$ is the neutron fluence rate averaged over the foil surface, Σ_{act} $\left(\mathrm{cm}^{-1}\right)$ is the macroscopic cross-section of the radiative capture (n,γ) reaction, V is the foil volume, ρ_{at} $\left(\mathrm{cm}^{-3}\right)$ is the foil atomic density and $\sigma_{\mathrm{act}}(\mathrm{cm}^2)$ is the radiative capture microscopic cross-section.

When exposing the foil to a uniform neutron field with spectral energy distribution $\dot{\Phi}_E(E) = \frac{d\dot{\Phi}}{dE}$, the formation rate becomes

$$r = V\rho_{\mathrm{at}}\int \sigma_{\mathrm{act}}(E)\dot{\Phi}_E(E)\,dE \tag{4.2}$$

In the case that the activation foil is put in the centre of a given sphere-detector combination i, we must consider only the energy distribution of the neutrons inside this sphere, $\dot{\Phi}^i_E(E)$, that reach this central position after moderation within the sphere volume.

$$r = V\rho_{\mathrm{at}}\int \sigma_{\mathrm{act}}(E)\dot{\Phi}^i_E(E)\,dE \tag{4.3}$$

As it is not possible to have information about $\dot{\Phi}^i_E(E)$, a connection between the formation rate of the induced radionuclides in the central activation foil and the energy distribution of the external incident neutrons, $\dot{\Phi}_E(E)$, is used instead in the following form:

$$r = \int R_i(E)\,\dot{\Phi}_E(E)\,dE \tag{4.4}$$

where $R_i(E)$ (cm^2) has the same meaning as in equation 3.2.

On the other hand, whilst the activation material is irradiated, the radionuclide product that is formed undergoes radioactive decay. The total number of radioactive nuclei, N, present in the sample varies in time and is given by the difference between the formation and decay rates (r and λN, respectively, bieng λ the decay constant of the radionuclide product). Thus,

$$\frac{dN}{dt} = r - \lambda N \tag{4.5}$$

If the neutron flux does not vary during exposure, the activity of the foil (assuming $N = 0$ at $t = 0$) is :

$$A(t) = r\left(1 - e^{-\lambda t}\right) \tag{4.6}$$

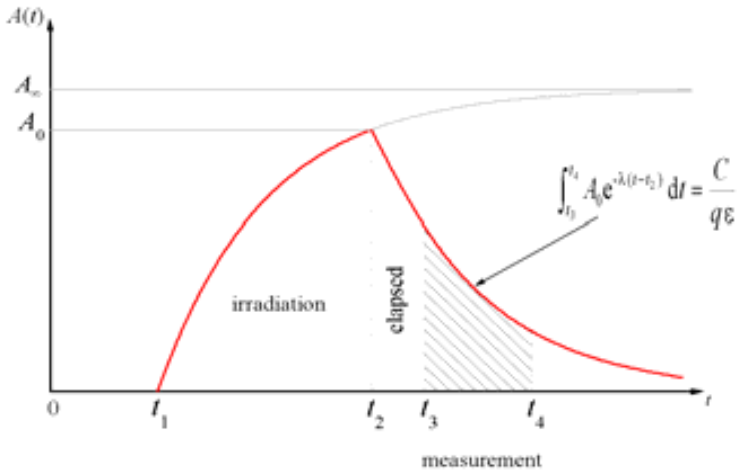

Figure 4.8. Time variation of the radioactivity induced in the activation material after being exposed to a neutron flux.

As shown in figure 4.8, this induced activity builds up with time and approaches asymptotically a saturation activity, A_∞, which is equal to the formation rate (equation 4.4), such that

$$A_\infty = r = \int R_i(E)\,\dot{\Phi}_E(E)\,dE \tag{4.7}$$

Comparing this equation with equation 3.2 allows to identify the reading of the sphere-detector combination i with the saturation activity of its corresponding gold foil. Discretasing equation 4.7 leads to an equation equivalent to 3.3

$$A^i_\infty = \sum_{i=1}^{n_E} R_{i,j}\dot{\Phi}_j \tag{4.8}$$

where it becomes apparent that for an activation based BSS the response matrix $R_{i,j}$ gives the relationship between the incident neutron fluence rate and the gold foil saturation activity.

Usually, irradiation takes place during a time interval $t_i = t_2 - t_1$ after which the foil is removed from the sphere with an activity:

$$A_0 = A(t_2) = A_\infty\left(1 - e^{-\lambda t_i}\right) \tag{4.9}$$

that is measured with an appropriate radiation counter. As the activity is continuously decaying during measurement, careful recording of times is needed. In fact, if the counting is carried out between t_3 and t_4 (measurement time, $t_m = t_4 - t_3$), the number of the net counts will be:

$$C = q\varepsilon\int_{t_3}^{t_4} A_0 e^{-\lambda(t-t_2)}dt \tag{4.10}$$

where q is the production yield of the decay channel and ε the overall counting efficiency. A convenient change of variable can be introduced by defining the time between the end of irradiation and the end of counting as $t' = t_4 - t_2$. Doing so, the net count rate can be approximated by:

$$\dot{C} \simeq \frac{C}{t_4 - t_3} = \frac{q\varepsilon}{t_4 - t_3} \int_{t_3 - t_2}^{t_4 - t_2} A_0 e^{-\lambda t'} dt' = \frac{q\varepsilon}{t_m} \int_{t_e}^{t_e + t_m} A_0 e^{-\lambda t'} dt' \tag{4.11}$$

where $t_e = t_3 - t_2$ is the time elapsed between the end of exposure and the beginning of counting and $t_m = t_4 - t_3$ is the measurement time interval. By substituting A_∞ with its value calculated from equation 4.9 and solving the integral, we find:

$$A_\infty \,(\,\mathrm{Bq}) = \frac{\lambda t_m \dot{C}}{q\varepsilon} \frac{e^{\lambda t_e}}{(1 - e^{-\lambda t_i})\,(1 - e^{-\lambda t_m})} \tag{4.12}$$

Finally, if we divide by the foil mass m, we obtain:

$$A_\infty \left(\,\mathrm{Bq\,mg^{-1}}\right) = \frac{\lambda t_m \dot{C}}{mq\varepsilon} \frac{e^{\lambda t_e}}{(1 - e^{-\lambda t_i})\,(1 - e^{-\lambda t_m})} \tag{4.13}$$

4.2.3. Selection of an activation material

A theoretical research study was performed, in collaboration with the IRSN laboratory [66], to choose the most appropriate activation material to be used as a thermal neutron detector within the passive BSS. The summary of the criteria considered in the subsequent selection is given as follows:

1. **Shape and magnitude of the cross section**

   Thermal neutrons are able to activate almost any stable element through radiative capture reactions, but the selection was limited only to those with the largest cross-sections and with a definite $1/v$ dependence behaviour in the region of interest (from 10^{-3} to 1 eV).

2. **Decay constant of the induced activity**

   The half-life of the induced species should be neither too short nor too long. Half-lives between several hours and few days are near the optimum. Long half-lives require the use of long irradiation times in order to approach saturation. Very short half-lives compared to the time needed to transfer the foil to the counter or to the counting time lead to difficulties.

3. **Purity and interfering activities**

   Very high purity of the material is often required to avoid interference from other neutron-induced reactions due to the presence of impurities. It should contain one unique stable isotope or, at least, should have a dominating isotope so that nuclear reactions with other family members can be neglected.

4. **Nature of the induced activity**

   Only activation materials, which neutron induced radionuclide products emit γ radiation, were chosen because the penetrating nature of this radiation minimises the self-absorption

effect within the sample. Furthermore it is far easier to perform gamma spectroscopy, so that interfering activities and background can be discriminated easily. The decay scheme of the induced species must also be as simple as possible.

5. **Physical properties**

   The activation material should be solid, preferably in form of metallic disc or wires easy to handle and to adapt to the Bonner spheres in use with the active spectrometer. It should be also commercially available at reasonable prices and it must be not toxic for human health.

Taking into account all these criteria, ^{197}Au was selected from the 120 stable nuclear species that can be activated through radiactive capture processes by thermal neutrons. Other relevant characteristics of ^{197}Au are its high chemical stability, its good mechanical resistance and its commercially availability, with almost any desirable shape, at an acceptable cost. The radiative capture reaction involved is $^{197}\mathrm{Au}(n,\gamma)^{198}\mathrm{Au}$. The main induced activation product, ^{198}Au, has a simple and well defined γ spectrum and has a very adequate half-life value $\left(T_{1/2} \simeq 2.7\,\mathrm{days}\right)$.

4.3. The new passive BSS

A new UAB passive neutron spectrometer based on the Bonner sphere technique has been designed in this work after selecting ^{197}Au as the best passive activation detector for this particular purpose. The polyethylene spheres in use with the active UAB BSS neutron spectrometer have been adapted to allocate the gold foils in their central position as thermal neutron detectors. Figure 4.9 shows the appropriate polyethylene holders and the metallic support used to place the spheres at the measurement point. The same set of 11 polyethylene or polyethylene/cadmium spheres with diameters 2.5 in, 3 in, 4.2 in, 5 in, 6 in, 8 in, 10 in, 12 in, 2.5 in + 1.5 mm Cd, 3 in + 1.5 mm Cd, 4.2 in + 1.5 mm Cd is used for this passive spectrometer.

A total of 60 disc foils of ^{197}Au where acquired from Goodfellow® with 99.99% purity, 0.10 mm thickness, 15 mm diameter and an approximate mass of 0.35 g. When the gold foils are exposed to a thermal neutron field an activation process takes place through radiative capture (n,γ) reactions with a cross-section value of 98.88 b for the thermal neutron reference energy of 0.025 eV. Activation gives rise to formation of ^{198}Au, which is a β^- emitter with a half-life of (2.6956 ± 0.0003) d and has a decay scheme that is given in figure 4.10. ^{198m}Au may also be formed with extremely small probability, which leads to emission of a non detectable amount of 312.2 keV γ rays with $T_{1/2} = 124$ ns. Beta decay of ^{198}Au leads to the formation of the ground state and 2 excited states of ^{198}Hg with the branching ratios shown in the figure, and the subsequent emission of γ rays of energy 411.8 keV, with a production yield of 95.5%, 675.9 keV, with a production yield of 0.8%, and 1087.7 keV, with a production yield of 0.16%. The production of 675.9 keV and of 1087.7 keV gamma rays can be neglected due to their small yields.

For each irradiation point where the neutron spectrum is to be obtained, the 11 sphere-detector combinations of the BSS are irradiated sequentially. After irradiation of each configuration, the 411.8 keV γ-ray photopeak emitted by the corresponding gold foil is measured using a

Figure 4.9. Polyethylene holders and methalic support adapted for the new gold foils

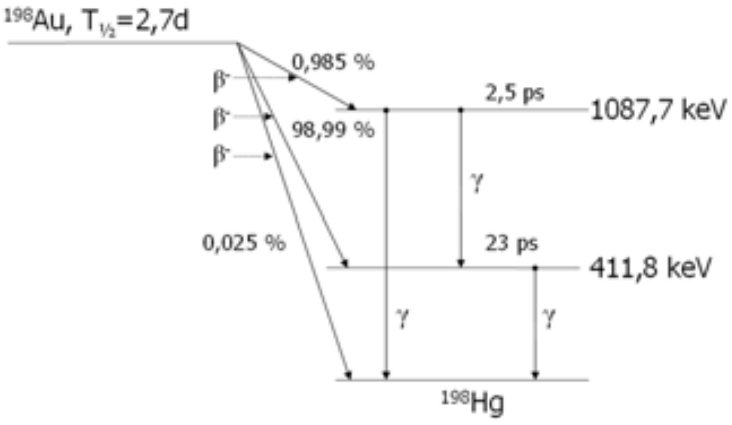

Figure 4.10. Decay scheme of ^{198}Au produced by thermal neutron activation from ^{197}Au. Source: wikipedia.

NaI(Tl)[4] detector in order to determine the subsequent saturation activity. This detector, even having a moderate energy resolution when compared to HPGe semiconductors, has in contrast the extra benefits of being sensitive, cheap, rugged, and does not need cryogenic cooling with liquid nitrogen.

Two NaI(Tl) detectors, fixed and portable, are currently in use for this purpose.

- **Fixed NaI(Tl) detector**

  The fixed NaI(Tl) detector, see figure 4.11, is a Canberra® unit (model 802) with an integrated photomultiplier tube and a preamplifier. This unit is connected to a standard PC via a 2 kBits memory ORTEC® plug-in multi-channel analyzer (MCA) board, model AccuSpec/NaI plus, which provides the high-voltage power supply as well as the pulse shaping amplification, gain stabilization and analog-to-digital conversion. The scintillation crystal, of cylindrical shape (diameter = height = 7.62 cm), has a nominal relative energy resolution of $\sim 7.5\%$ for the ^{137}Cs 661.66 keV γ-ray emissions.

  The NaI(Tl) detector is placed vertically, head up, inside a cylindrical heavy (450 kg) lead shield (60 cm height, 30 cm outer diameter and 10 cm thick) that provides an efficient reduction of the environment radiation. Between the Pb shield and the detector, graded Z plates, made successively of Zn and Cu, of respective thicknesses of 1.5 mm and 1 mm, are added to suppress the emissions of the Pb K-shell fluorescence X-rays that result from the photoelectric interactions of incident photons with the Pb shield inner walls.

- **Portable NaI(Tl) detector**

  The portable NaI(Tl), model Nanospec provided by MGI®, has also an identical cylindrical scintillation crystal (diameter = height = 7.62 cm) covered with a 7 mm thick protective plastic material of 7 mm, see figure 4.12. Its nominal energy resolution is $\sim 8.0\%$ for the ^{137}Cs 661.66 keV γ-ray emissions. All the associated electronic components (photomultiplier tube, HV power supply, preamplifier, shaping amplifier, gain stabilizer, analog-to-digital converter and multi-channel analyzer) are incorporated into a compact module that can be connected to a PC using a serial interface. It includes also a microprocessor that permits stand-alone measurements. The complete unit is placed vertically, head down, inside a 30 kg Pb shield box (30 cm height and 3 cm thick) that may be transported outside our laboratory wherever it is convenient to perform in situ measurements.

Energy calibrations of both NaI(Tl) were performed using four certified standard sources (^{137}Cs, ^{60}Co, ^{22}Na and ^{133}Ba). Monte Carlo simulations with MCNPX 2.5.0 and subsequent validation with the above standard sources were the basis of efficiency calibration [67]. The general characteristics of both detectors are summarised in table 4.1.

Gold foils are used for activation in the passive BSS under study, therefore the saturation activity obtained from a given sphere-detector combination i is calculated from expression 4.13:

$$A_{\infty}^{i} = \frac{\lambda t_m \dot{C}_i}{mq\varepsilon} \frac{e^{\lambda t_e}}{\left(1 - e^{-\lambda t_i}\right)\left(1 - e^{-\lambda t_m}\right)} \left(\mathrm{Bq\,mg^{-1}}\right) \tag{4.14}$$

[4] Sodium iodide doped with thallium

Figure 4.11. The fixed NaI(Tl) gamma-ray detector inside the Pb shield

Figure 4.12. The portable NaI(Tl) gamma-ray detector inside its transport suitcase. On the left, its portable Pb shielding.

Table 4.1. Summary of characteristics for both NaI(Tl) in use for the determination of gold foil specific saturation activities at the GFR-UAB

	Fixed	**Portable**
HV	1000 V	555 V
# channels	2048	1024
$R_{^{137}Cs}$	$\sim 7.5\%$	$\sim 8.0\%$
$\varepsilon_{412\,keV}$	0.2412 ± 0.0010	0.1918 ± 0.0009
$\varepsilon_{333\,keV}$	0.2833 ± 0.0013	0.2247 ± 0.0010
$\varepsilon_{356\,keV}$	0.2698 ± 0.0012	0.2139 ± 0.0010
$\varepsilon_{426\,keV}$	0.2335 ± 0.0011	0.1852 ± 0.0008

with $\lambda = 2.97 \times 10^{-6}\,s^{-1}$ the ^{198}Au decay constant, m the gold foil mass in mg, q (0.9550) the production yield of the emitted γ-rays (412 keV) of interest, ε the corresponding NaI(Tl) detector efficiency and $\dot{C}_i$ the net count rate of the 411.8 keV ^{198}Au photo-peak, after background continuum subtraction and dead time correction.

4.3.1. Correction for photonuclear (γ, n) reactions

Additional photoneutron production on the gold foil

Although gold can be qualified as being generally insensitive to photons, it should be noticed that in presence of photon fields with energies above 8.07 MeV, the photoneutron absorption reaction ^{197}Au $(\gamma, n)^{196}$Au can also take place [67]. In this case, the subsquent disintegration of ^{196}Au, with $T_{1/2} = 6.18$ d, results in the emission of 66 keV, 76 keV, 333 keV, 356 keV and 426 keV γ-rays with different production yields (0.59300, 0.16310, 0.22855, 0.86900 and 0.07213, respectively). The photo-peaks originated by these $\gamma-$rays can overlap the ^{198}Au photo-peak at 412 keV when using NaI(Tl) detectors. Figure 4.13 gives an example of the ^{198}Au photo-peak contamination by ^{196}Au radionuclides when measured with the NaI detector, after background continuum subtraction. Consequently, if no corrections are taken into account, the saturation activities of ^{198}Au will be overestimated in presence of intense gamma fields above 8.07 MeV.

To overcome this possible overestimation, the contamination due to ^{196}Au 412 keV γ-ray emissions must be quantified. This can be done if a method of peak separation is available. In our case, Origin©, a data analysis software, allows to separate between two main peaks, P_I and P_{II}, as shown in figure 4.14, by performing a multi-Gaussian fit of the measured pulse-height distribution. If one compares figure 4.13 with figure 4.14, it can be asumed that P_I is formed by the 333 keV and 356 keV $\gamma-$ray emissions of ^{196}Au, and that the 426 keV (^{196}Au) and 412 keV (^{198}Au) $\gamma-$rays contribute to the peak P_{II}; so that:

$$P_{II} = \dot{C}_3 + \dot{C}_4 \tag{4.15}$$

$$P_I = \dot{C}_1 + \dot{C}_2 \tag{4.16}$$

where $\dot{C}_1, \dot{C}_2, \dot{C}_3$ and $\dot{C}_4$ are the net count rates originated from the 333 keV (^{196}Au), 356 keV (^{196}Au), 426 keV (^{196}Au) and 412 keV (^{198}Au) $\gamma-$ray emissions, respectively. Besides, $\dot{C}_1, \dot{C}_2$ and $\dot{C}_3$ are related to each other as they depend on the same number of ^{196}Au radionuclides created during irradiation. The relationship between them can be determined by equaling the ^{196}Au saturation activities derived from the eventual individual net count rates of its emitted

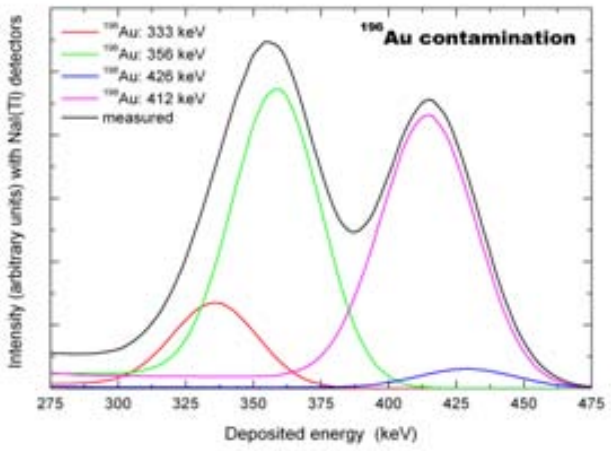

Figure 4.13. The ^{198}Au 412 keV photo-peak contaminated by the presence of ^{196}Au in the measured gold foil when using NaI(Tl) detectors after background continuum subtraction.

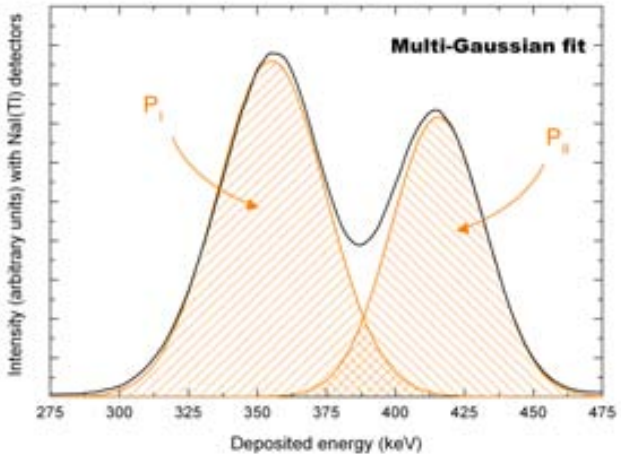

Figure 4.14. Multi-Gaussian fit of the pulse-height distribution obtained with NaI(Tl) detectors and performed by Origin© after background and Compton subtraction

$\gamma-$ray energies. Then, by using an identical expression to equation 4.13, the saturation activity of ^{196}Au can be estimated from each of the emitted γ-rays as:

$$A_{\infty}\left(^{196}\mathrm{Au}\right) = \frac{\lambda t_m \dot{C}_1}{m q_1 \varepsilon_1} \frac{e^{\lambda t_e}}{\left(1-e^{-\lambda t_i}\right)\left(1-e^{-\lambda t_m}\right)} \tag{4.17}$$

$$A_{\infty}\left(^{196}\mathrm{Au}\right) = \frac{\lambda t_m \dot{C}_2}{m q_2 \varepsilon_2} \frac{e^{\lambda t_e}}{\left(1-e^{-\lambda t_i}\right)\left(1-e^{-\lambda t_m}\right)} \tag{4.18}$$

$$A_{\infty}\left(^{196}\mathrm{Au}\right) = \frac{\lambda t_m \dot{C}_3}{m q_3 \varepsilon_3} \frac{e^{\lambda t_e}}{\left(1-e^{-\lambda t_i}\right)\left(1-e^{-\lambda t_m}\right)} \tag{4.19}$$

where q_i and ε_i are the production yield and the detection efficiency of the i^{th} γ ray. From these equations the relationship between the individual net count rates can be written as:

$$\dot{C}_1 = \frac{q_1 \varepsilon_1}{q_2 \varepsilon_2} \dot{C}_2 \tag{4.20}$$

$$\dot{C}_3 = \frac{q_3 \varepsilon_3}{q_2 \varepsilon_2} \dot{C}_2 \tag{4.21}$$

Combining these last expressions with equation 4.16, and taking into acount the efficiency values given in table 4.1 for the fixed NaI(Tl) detector, we obtain:

$$\dot{C}_3 = \frac{q_3 \varepsilon_3}{q_1 \varepsilon_1 + q_2 \varepsilon_2} P_I = 0.0563 P_I \tag{4.22}$$

which means that the contribution of ^{196}Au 426 keV γ-rays to the ^{198}Au photo-peak (P_{II}) when measured with the fixed or portable NaI detector is related to the net area of the first peak P_I (see figure 4.14) and represents 5.63% of this peak. Therefore, for a correct estimation of the saturation activity of ^{198}Au in presence of photon fields above 8.07 MeV, the net count rate due to ^{198}Au emissions must be estimated as:

$$\dot{C}_4 = P_{II} - 0.0563 P_I \tag{4.23}$$

Similar results are obtained for the portable NaI(Tl), using the adequate detection efficiencies from table 4.1.

Additional photoneutron production in the Cd shell

In neutron measurements, cadmium is normally used to absorb all neutrons with energies below its characteristic cut-off value of 0.4 eV. In our case, a 1.5 mm Cd shell is additionally used with the small spheres (2 in, 3 in and 4.2 in). Nevertheless, due to its photonuclear (γ, n) reaction in presence of photon fields with energies above 8.07 MeV, the Cd filter may generate extra neutrons. Hence, there is a possibility that the saturation activities of the gold foils placed at the center of the small spheres covered with cadmium are higher than expected.

Efforts have been made recently [68] to evaluate the cadmium contribution to the saturation activities when these sphere-detector combinations are used to measure the neutron spectrum at the isonceter of a 18 MV Varian 2100CD radiotherapy LINAC machine operating in photon mode. Firstly, taking into account the geometrical details of the LINAC head, the photon spectrum at the isocenter was estimated with the MCNPX code, starting from a primary 18 MeV electron pencil beam. Secondly, the photon energy distribution obtained was used as input to

simulate the photoneutron production in the Cd shell and its contribution to the response of each of the small polyethene spheres (2 in, 3 in and 4.2 in). These computed contributions (expressed in units of activity saturation in, $\mathrm{Bq\,mg^{-1}}$) from the eventual photonuclear reactions in the Cd shell were normalised to the LINAC beam yield.

CHAPTER 5.

Simulation of the passive BSS response matrix

5.1. Introduction

The knowledge of the energy dependence of the response function for each of the UAB passive BSS sphere-detector combinations is essential for characterising correctly the neutron fields measured, as it was commented in 3.2.2.. In fact, as the neutron spectrum is derived with an unfolding process that relies on a set of different sphere readings, an indetermination affecting a single response function would propagate over the whole unfolding process. Variations up to ±15% for the neutron fluence and up to ±40% for the mean neutron energy have been found when evaluating the same set of BSS readings with 5 different response functions that where independently determined [69].

As we advanced in 3.2.2., good approximations of the response functions of the passive BSS can be obtained by Monte Carlo calculations and experimental validations at ISO radioactive neutron sources and/or monoenergetic neutron fields.

In this chapter, the calculation procedure used to obtain the UAB passive BSS response functions by means of the MCNPX^{TM} code [70] is explained. The dependence of the response functions on several factors, such as the neutron incidence direction, the mass density of the polyethylene spheres and the gold foil geometry is also studied. Results of the experimental validation of the calculated response matrix will be shown in the following chapter.

5.2. Calculation procedure

5.2.1. Overview

In the early work with Bonner sphere spectrometers (1960s, 1970s and even the 1980s), when a lot of work was done, computing speed was a severe restriction on the use of Monte Carlo techniques and they could not be effectively used for the calculation of the response functions. These calculations were, therefore, performed using one-dimensional neutron transport codes,

which provided an approximate solution to the neutron transport equation and which ran much faster. The most commonly used one-dimensional code in those years was ANISN [71]. This code uses the discrete ordinates, or S_n, method to solve the steady state one-dimensional Boltzmann transport equation which relates losses of neutrons to gains within volumes in space. Although a one-dimensional code, it can treat problems with spherical symmetry such as Bonner spheres. ANISN became for a number of years the most used code for calculating BSS response functions because *i)* the method is computationally fast and reasonably reliable and *ii)* it can be run in adjoint mode, where the source term is not an external neutron fluence but the cross section for the reaction, occurring in the central sensor, which gives rise to neutron detection. The calculation can almost be thought of as a conventional transport calculation run in reverse, and it represented a considerable reduction in overall computing time.

The results of these calculations were used without experimental checks, but gradually the importance of validation was realised. The combination of measurement and ANISN calculations provided much more reliable response functions than those that could be obtained from either approach separately. With improved experimental accuracy and more detailed comparisons, certain discrepancies were revealed between measurement and calculation, particularly in the thermal energy region. These discrepancies were never fully resolved and, as computing speeds improved rapidly in the 1980s and 1990s, the use of Monte Carlo codes, which performed point energy calculations and enabled the geometry to be modelled in detail, gradually took over as the standard approach for calculating response functions.

In contrast to the discrete ordinate transport codes, Monte Carlo codes do not solve an explicit transport equation but rather simulate the statistical process of interactions with matter and are useful for solving complex problems that cannot be modelled using deterministic methods. The fast development of computers meant that by the 1990s complete sets of BSS responses could be calculated with adequate accuracy.

5.2.2. MCNPX™ simulation code

The MCNPX™ simulation code is a general purpose Monte Carlo transport code which, quoting version 2.4.0. manual, *tracks all particles at all energies*. It comes from a series of Monte Carlo transport codes that began at Los Alamos during the 50's [72], and it is constantly developing more accurate and complete versions. One of its main advantages, besides the big number of particle types that it tracks, is its capability to work with 3D complex geometries in a very user friendly way.

In MCNPX™, each space region defined by a given material constitutes a cell. Cells are defined by intersections, unions and complementary space regions, which are limited by surfaces. These limiting surfaces can be defined by fixing their analytical equation coefficients or by establishing points belonging to them. A plotting routine is available to check geometries easily. Each particle is tracked from the emission source by sampling all the possible random-walk interactions until it interacts with a terminal event (such as absorption, escaping from the geometry boundaries, capture, etc.). Cross section tables and physical models are used in order to sample all generated particles random-walk interactions according to the probabilities of different mechanisms.

The code permits to specify which type of information is to be gained from the Monte Carlo calculation through the definition of tally cards. Several types of tallies can be defined

such as current across a surface, flux at a point, heating in a region, track length over a cell volume, etc. Tally events can be classified into subgroups like, for example, energy intervals or incidence angle over a specified surface. The result of a tally is estimated as a mean value of the scored quantity x with a relative standard uncertainty σ_x/x (of statistical origin only) averaged over the N tally values obtained from the N individual starting stories. It is also usually normalised per unit of source emitting particle.

In order to run MCNPX^{TM} Monte Carlo code, the user must provide an input file with the geometry specifications of the problem, the source characteristics and the quantities that are to be determined. A detailed description of MCNPX^{TM} input files can be found in the code manual [70] and only the most relevant aspects related to the UAB passive BSS simulation files are commented below.

5.2.3. The UAB passive BSS input file

In order to correctly simulate the real spectrometer, the system must be modelled as accurately as possible. This can be achieved by throughout knowledge of the system geometry, from its materials to the physics involved in the detection mechanism.

The input MCNPX files to simulate the UAB passive Bonner sphere system can be found in appendix B. The model geometry is defined in the first 36 lines for Cd uncovered spheres and 45 for those covered with the Cd shell. A total of up to 10 cells and 25 surfaces were defined matching the exact dimensions of the gold foil and the sphere (with or without the Cd shell) as well as the hollow steel support. Each cell was defined by intersections and/or unions of different surfaces and was associated with a given material and a density value. The chemical composition and densities of the different materials used in the simulation are shown in table 5.1, together with the cross-section parameters for each element. The polyethylene density provided by the manufacturer was comprehended between 0.918 and 0.922 g cm^{-3}. However, this density was verified from a representative sample at our laboratory and a nominal value of 0.920 g cm^{-3} was considered for simulation [31]. The influence of the polyethylene density on the response functions will be discussed later.

The neutron source was modeled as an expanded and aligned beam emerging from a plane disk perpendicular to the neutron beam direction and to the plane defined by the gold foil, in a *parallel irradiation geometry*. Its diameter matches that of the sphere and the neutron starting positions were sampled uniformly over the disk surface. As it can be seen in table 5.3, a total of 104 logarithmic equidistant energy values (10 per decade) were selected for the incident mono-energetic neutron beams ranging from 10^{-9} to 20 MeV. The space between the neutron source and the sphere were defined as void, consequently no neutron interactions occur before neutrons reach the polyethylene sphere.

Cross-section libraries for neutron interaction with the elements composing the sphere, the gold foil, the Cd shell and the steel support were extracted from the evaluated nuclear data file, ENDF/B-VI release 8, and are detailed in table 5.1. In order to take into account the hydrogen binding energy in polyethylene, that affects thermal neutron scattering, the S(α, β) treatment option was activated and the corresponding cross-section poly.01t table used.

The response, $R_{i,j}$ in cm^2 mg^{-1}, for each sphere-detector combination i to an incident neutron energy E_j, was estimated as the number of ^{197}Au$(n,\gamma)^{198}$Au radiative capture reactions inside the gold foil cell per unit of mass and neutron fluence. To obtain the number of ^{197}Au

Table 5.1. Detailed decription of the materials used for the simulation of the BSS spectrometer response functions. Isotopic compositions, densities and cross section libraries employed are shown. The temperature indicated in the last column corresponds to the temperature at which each cross section is given.

Material	Density	Isotopic composition		Cross-section parameters			
	($\mathrm{g\,cm^{-3}}$)	Element	%	Element Id	Library	Year	T (K)
Dry Air	1.293×10^{-3}	^{16}O	24.21	8016.60c	ENDF60	1990	293.6
		^{14}N	75.53	7014.60c	ENDF60	1992	293.6
		^{12}C	0.21	6012.50c	DRMCCS	1977	293.6
		Ar$^{\mathrm{NAT}}$	0.05	18000.35c	RMCCSA	< 1985	0
Polyethylene	0.920	^{1}H	67	1001.60c	ENDF60	1989	293.6
		^{12}C	33	6012.50c	DRMCCS	1977	293.6
		$\mathrm{S}(\alpha,\beta)$	treatment→	poly.01t	TMCCS1	1985	300
Steel	7.960	^{50}Cr	0.8	24050.60c	ENDF60	1989	293.6
		^{52}Cr	15.1	24052.60c	ENDF60	1989	293.6
		^{53}Cr	1.7	24053.60c	ENDF60	1989	293.6
		^{54}Cr	0.4	24054.60c	ENDF60	1989	293.6
		^{54}Fe	3.9	26054.60c	ENDF60	1989	293.6
		^{56}Fe	63.4	26056.60c	ENDF60	1989	293.6
		^{57}Fe	1.5	26057.60c	ENDF60	1989	293.6
		^{58}Fe	0.2	26058.60c	ENDF60	1989	293.6
		^{58}Ni	6.7	28058.60c	ENDF60	1989	293.6
		^{60}Ni	2.7	28060.60c	ENDF60	1989	293.6
		^{61}Ni	0.1	28061.60c	ENDF60	1989	293.6
		^{62}Ni	0.4	28062.60c	ENDF60	1989	293.6
		^{64}Ni	0.1	28064.60c	ENDF60	1989	293.6
		Monel	3	42000.60c	ENDF60	1979	293.6
Pure Gold	19.300	^{197}Au	100	79197.60c			
Cadmium	8.640	Cd$^{\mathrm{NAT}}$	100	48000.51c	RMCCS	1974	293.6

Table 5.2. Multiplication factors to be used to obtain the fluence response, per unit of gold foil mass, from the MCNPX tally for the UAB passive BSS

Sphere-detector combination	Source radii (cm)	Multiplication factor $\pi r^2 \frac{n}{\rho}$ in Eq. 5.1
2.5 in	3.175	9.683×10^{-5}
3 in	3.810	1.394×10^{-4}
4.2 in	5.334	2.733×10^{-4}
5 in	6.350	3.873×10^{-4}
6 in	7.620	5.577×10^{-4}
8 in	10.160	9.915×10^{-4}
10 in	12.700	1.549×10^{-3}
12 in	15.240	2.231×10^{-3}
2.5 in + Cd	6.800	4.441×10^{-4}
3 in + Cd	6.800	4.441×10^{-4}
4.2 in + Cd	6.800	4.441×10^{-4}

radiative capture reactions inside the gold foil from the MCNPX simulation a track length estimate tally (tally type F4) is defined for the gold foil cell. The tally provides the estimated values of the energy distribution of neutrons reaching the gold foil normalised to one source particle, $\dot{\Phi}^i_E$, from which the response can be obtained as:

$$R_{i,j} = \pi r_i^2 \frac{n}{\rho} \int_0^{Ej} \dot{\Phi}^i_E(E) \sigma_{\text{act}}(E) dE \tag{5.1}$$

where r_i (cm) is the neutron source radius chosen to match that of the sphere or the Cd shell, σ_{act} is the microscopic radiative capture cross section (labelled by MCNPX with an identifier number 102) for gold, and n and ρ are the gold foil atomic and mass densities, respectively. The term $\pi r^2 \frac{n}{\rho}$ is a multiplication factor which values for the different sphere-detector combinations are given in table 5.2. This values are provided as input using a FM card [70].

A total of 11×104 simulation files were prepared, one for each sphere-detector combination i and neutron incident energy E_j. The results of the simulations using these files provided the response matrix values for the UAB passive BSS, which are presented in the following section. In all cases, the number of histories simulated was set to obtain statistical uncertainties below 1%.

5.3. Results

5.3.1. Response matrix of the UAB passive BSS

The response values obtained from simulation for each sphere-detector combination and neutron energy are shown in figure 5.1 as a 3-dimensional graph. This figure does not include the three configurations with the Cd shell, which will be commented later. The values of the fluence response were tabulated for all 11 configurations and can be found in appendix C, they are expressed in $\text{cm}^2\,\text{mg}^{-1}$.

In figure 5.2, the same fluence responses are shown as a function of the neutron energy, in a 2-dimensional plot. Data are available for the 104 discrete energy values used for simulation and are represented by sphere symbols. Curves obtained by cubic spline interpolation between

Table 5.3. The 104 energy groups (in MeV) equi-spaced in a logarithmic scale and used in the MCNPX simulation of the UAB passive Bonner sphere spectrometer. The values given correspond to the center of each energy bin.

1.000E-09	1.259E-09	1.585E-09	1.995E-09	2.512E-09	3.162E-09	3.981E-09	5.012E-09	6.310E-09	7.943E-09
1.000E-08	1.259E-08	1.585E-08	1.995E-08	2.512E-08	3.162E-08	3.981E-08	5.012E-08	6.310E-08	7.943E-08
1.000E-07	1.259E-07	1.585E-07	1.995E-07	2.512E-07	3.162E-07	3.981E-07	5.012E-07	6.310E-07	7.943E-07
1.000E-06	1.259E-06	1.585E-06	1.995E-06	2.512E-06	3.162E-06	3.981E-06	5.012E-06	6.310E-06	7.943E-06
1.000E-05	1.259E-05	1.585E-05	1.995E-05	2.512E-05	3.162E-05	3.981E-05	5.012E-05	6.310E-05	7.943E-05
1.000E-04	1.259E-04	1.585E-04	1.995E-04	2.512E-04	3.162E-04	3.981E-04	5.012E-04	6.310E-04	7.943E-04
1.000E-03	1.259E-03	1.585E-03	1.995E-03	2.512E-03	3.162E-03	3.981E-03	5.012E-03	6.310E-03	7.943E-03
1.000E-02	1.259E-02	1.585E-02	1.995E-02	2.512E-02	3.162E-02	3.981E-02	5.012E-02	6.310E-02	7.943E-02
1.000E-01	1.259E-01	1.585E-01	1.995E-01	2.512E-01	3.162E-01	3.981E-01	5.012E-01	6.310E-01	7.943E-01
1.000E+00	1.259E+00	1.585E+00	1.995E+00	2.512E+00	3.162E+00	3.981E+00	5.012E+00	6.310E+00	7.943E+00
1.000E+01	1.259E+01	1.585E+01	1.995E+01	2.000E+01					

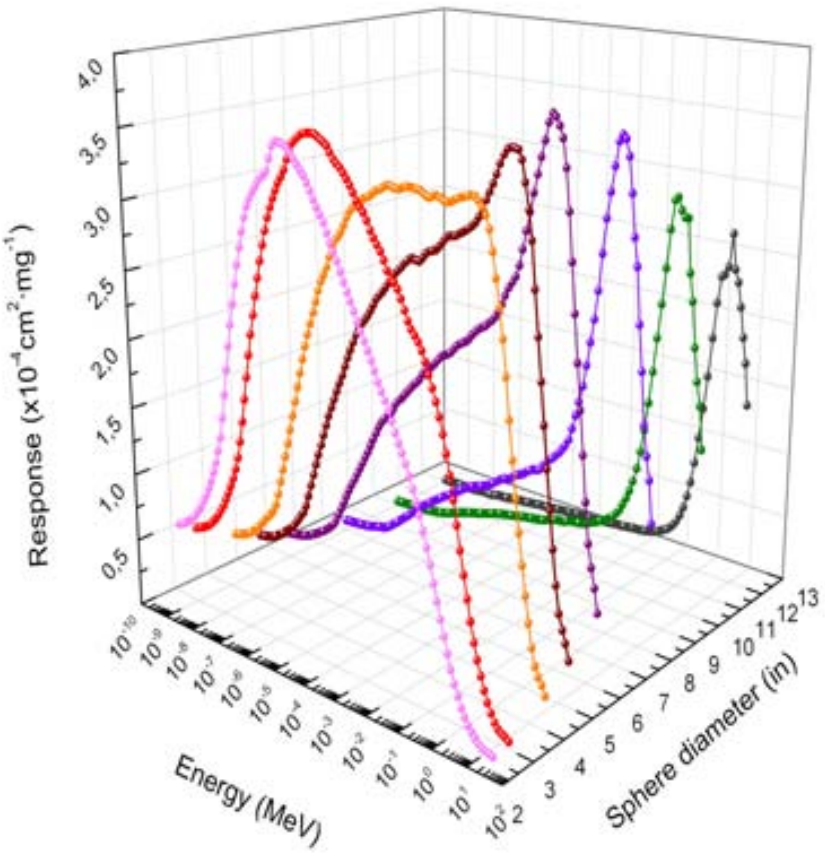

Figure 5.1. Calculated response matrix for the UAB passive BSS in a 3D representation, as a function of neutron energy and sphere diameter

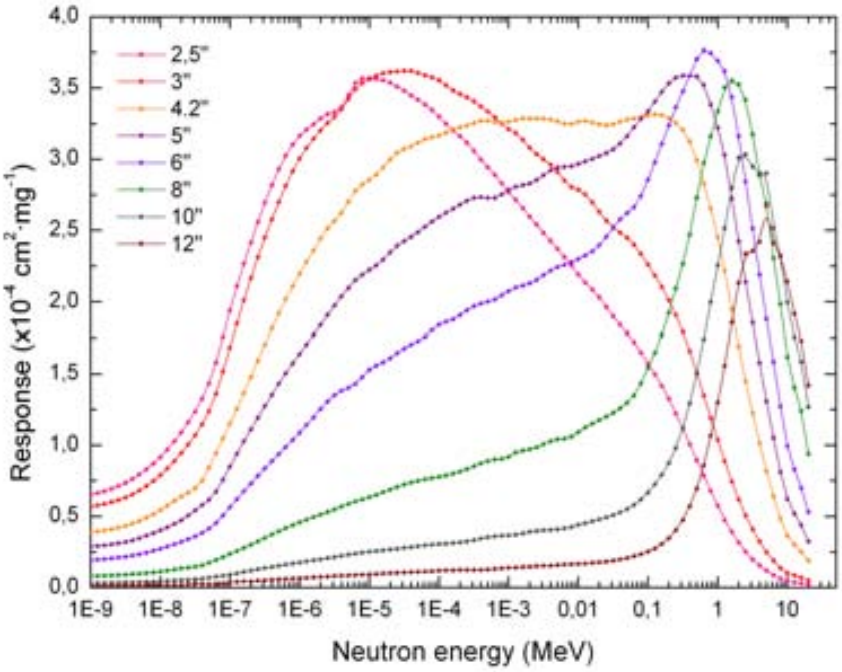

Figure 5.2. UAB passive BSS response matrix ina 2-dimensional plot. Simulated values are represented as spheres and cubic spline interpolations for each sphere are also shown as continuous lines.

points are also indicated. It is observed that the energy dependence of the fluence response is different for each sphere and that responses shift to higher energies when increasing the sphere diameter. It can be also seen that from the thermal energy range up to 20 MeV there is always at least one sphere having high response, so that the BSS is able to cover a wide energy range, extending over 9 energy decades. Most of the responses shown in figure 5.2 present maximum values which lie somewhere between 2.5×10^{-4} and 4×10^{-4} cm^{-2} mg^{-1}. The detection efficiency, understood as the ratio between the reading of the detector and the incident neutron fluence, decreases systematically with increasing sphere diameter, as indicated by fact that areas below the curves decrease with increasing sphere diameter [36].

Another interesting way of plotting the response matrix values can be seen in figure 5.3, where response is plotted as continuous functions of sphere diameter, for several values of neutron energy. Data available for the 8 discrete values of the sphere diameter are indicated by solid circle symbols and cubic spline interpolations between them allow to plot continuous curves. Cubic spline interpolation in diameter seems to produce correct response values for sphere diameters not available from calculations or experiment [36].

The fluence response values for the 3 configurations including the Cd shell (2.5 in+Cd, 3 in+Cd and 4.2 in+Cd) are shown in the bottom part of figure 5.4. The response values for the same sphere without the Cd shell are also plotted for comparison. Cadmium presents a high

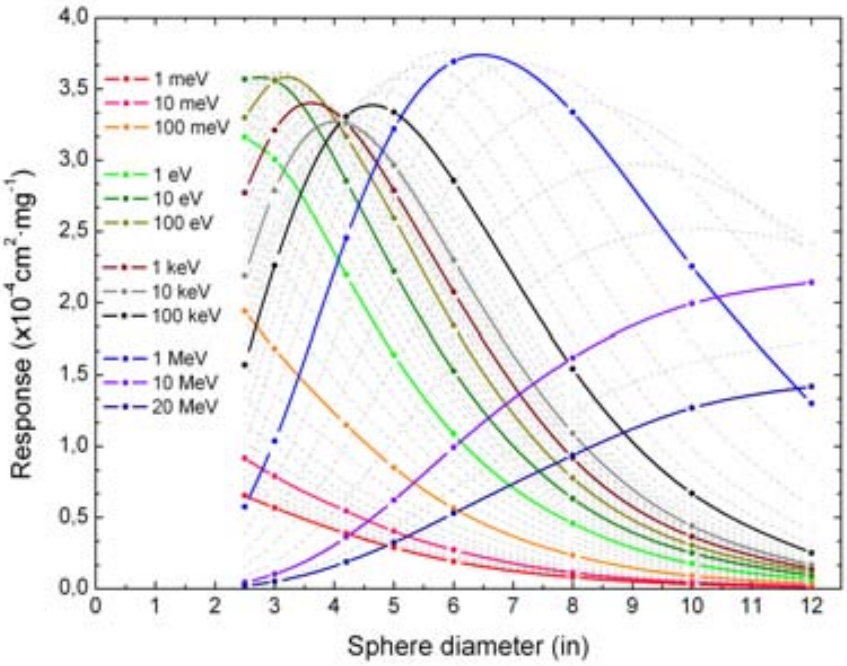

Figure 5.3. The simulated fluence response matrix of the UAB passive Bonner spectrometer. The responses are represented as functions of the sphere diameter for different neutron energies.

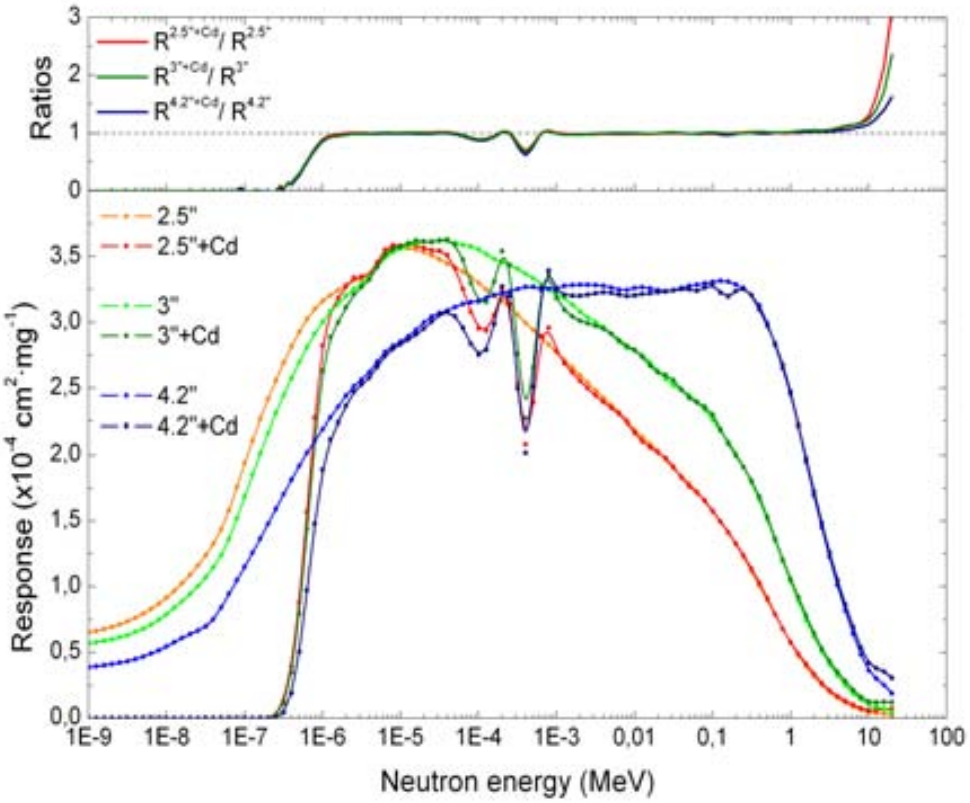

Figure 5.4. Response matrix of the sphere used with the Cd shell. Below, the simulated fluence respose values of 2.5", 3" and 4.2" spheres are shown with and without the Cd shell as spheres with cubic splines interpolations shown as lines. Above, the ratio between the response values with and without Cd for each sphere is represented

capture cross section for neutrons below 0.4 eV making the response fall dramatically for thermal neutrons. In the upper part of figure 5.4, the ratios between the Cd covered and the uncovered spheres with equal diameter are shown. These ratios are nearly equal to 1 for neutrons energies above 0.4 eV and for all the 3 configurations. The oscillations around the keV region can be explained by resonance peaks in the Cd capture cross section. The increase present above 1 MeV can be related to the $(n, 2n)$ spallation nuclear reactions in Cd, which cross-sections increase at these energies.

5.3.2. Influence of the neutron incidence direction

One of the most important characteristics of any Bonner sphere spectrometer is that its response should be isotropic. Isotropy of the moderation process of neutrons that reach the center of the polyethylene spheres is granted from spherical symmetry. Nevertheless, the fact that gold foils have plane-cylindrical geometry breaks this spherical symmetry compromising the isotropy of the whole system. The validity of using response matrixes to unfold measurements

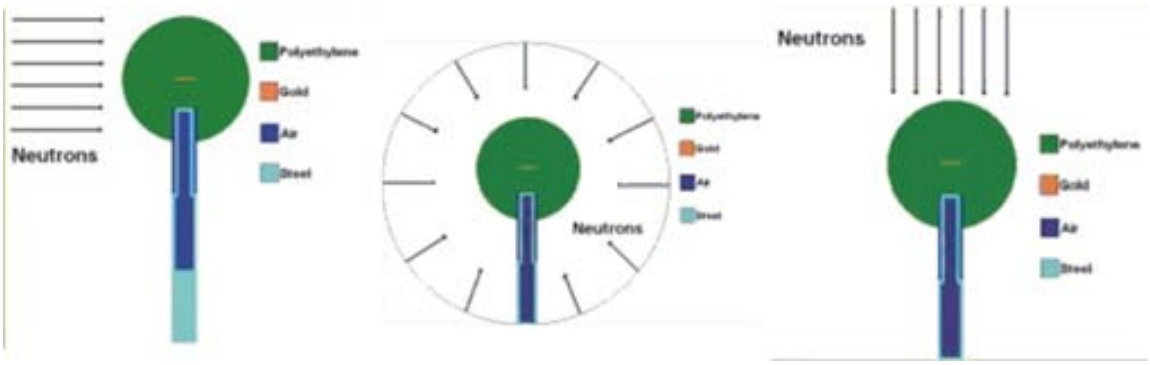

Figure 5.5. Schematic representation of the irradiation geometries calculated. On the left, the *parallel beam* geometry, on the right, the *normal beam* irradiation geometry, and between them, the *isotropic* irradiation geometry.

may be questioned when a real irradiation is carried out with neutron beam geometries different from those specified when calculating the response matrixes.

To check the validity of the isotropic behaviour of the UAB passive BSS and the independence of the response functions from the incident neutron beam irradiation geometry, an *isotropy study* was performed. For this study, the response functions for different incident neutron beam geometries were calculated for the 10 in, 4.2 in and the 2.5 in. The *worst*, most asymmetric possible conditions are reached when the smallest sphere available (2.5 in) is directionally irradiated. Figure 5.5 gives a schematic representation of the irradiation geometries calculated: *isotropic* irradiation, *normal beam* irradiation and the *parallel beam* irradiation, which is the irradiation geometry used for calculating the response matrix, as described in section 5.2.3..

No appreciable difference is found between the results for the three irradiation geometries of the incident neutron beam, even for the smallest (2.5 in) sphere, as they present deviations smaller than the combined uncertainties. Figure 5.6 shows the response functions for the 2.5 in sphere calculated for the three irradiation conditions, as well as the ratios between parallel and isotropic responses and between normal and isotropic responses. The most important deviations are found for the energies where the response function has its smallest values, although these deviations are comparable to uncertainties.

These results confirm that the passive UAB passive BSS response functions do not depend on the irradiation geometry of the the incident neutron beam and present an isotropic behaviour. This corroborates that thermalisation of neutrons inside the spheres eliminates the anisotropies given by any incidence privileged direction.

5.3.3. Other aspects

Influence of the polyethylene density

As Alevra and Thomas indicate [36], changes in polyethylene mass density (PEMD) produce considerable changes in responses, which depend on both sphere diameter and energy. One should expect that the largest effects appear for diameters and energies where the response values are low. Nevertheless relative changes in response, which are three times larger than

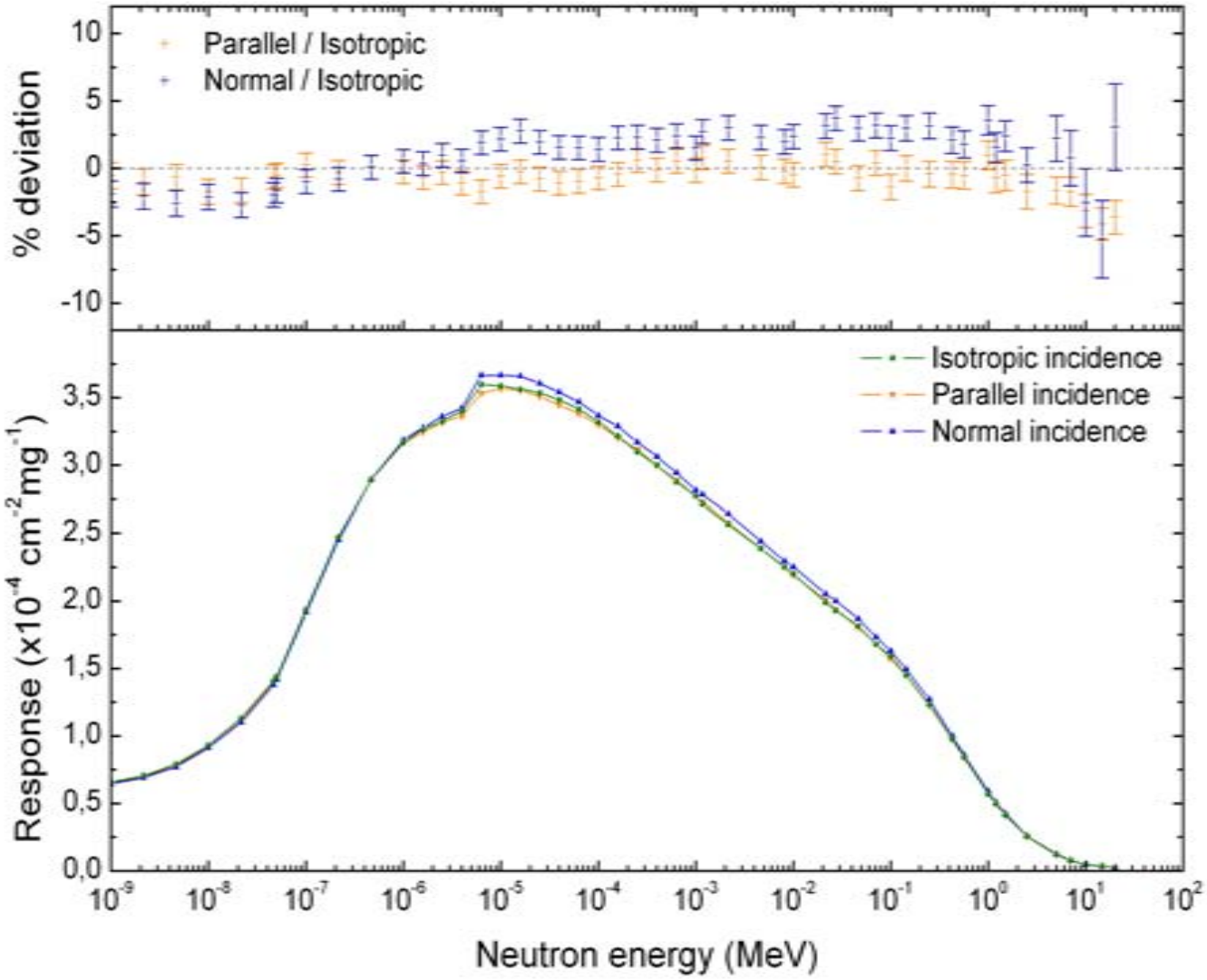

Figure 5.6. Response function values for the 2.5 in sphere with neutron beams of different geometry. Below: response functions for isotropic, parallel and normal neutrom beams incidence. Above: the quotients between isotropic response and parallel and normal response, respectively, expressed as per cent deviation.

the relative changes in PEMD, are still observed in regions where the response values are high enough.

Many authors have used Monte Carlo techniques to evaluate the changes in response values for BSS very similar to ours, when PEMD varies. Amgarou [73], considered 0.5% variations in PEMD for different sphere diameters (3 in, 6 in, 8 in and 12 in) and found that the overall influence of these changes could be neglected in the energy regions where response values reached their maximum. In agreement with Alevra and Thomas, Amgarou also found that for the biggest sphere, severe discrepancies (up to ±5%) appeared in the energy regions with low response values even when applying a variation of only 0.5% to the nominal PEMD value.

The influence of PEMD variations for the polyethylene sphere set used with the UAB passive and active spectrometers was studied by Bakali [31] with Monte Carlo techniques and for the 6 in sphere. The results obtained showed that a 3% deviation on the PEMD value produced variations below 11% in the response function values of this sphere. It was concluded that the 0.4% relative uncertainty in the nominal PEMD value provided by the manufacturer could be considered negligible. Consequently, no corrections due to PEMD variations have been included in this work.

Influence of the gold foil geometry

One could expect that for a fixed gold foil shape variations in diameter and thickness may have an influence in the response functions. The influence of these variations have been studied by Amgarou [73] for gold foils from the same manufacturer and shape as those used for the UAB passive BSS, with equal diameter but 2.5 times thicker. It was shown that diameter variations up to ±1 mm can be completely neglected. It was also observed that increasing the gold foil thickness an amount equal to the tolerance given by the manufacturer (10%) will lead to an overall shifting of −3% of the passive BSS response functions. Conversely, a 10% thickness diminishing will have the contrary consequence (i.e., a +3% shift of the response matrix). However, although this dependence is included within the overall uncertainty of the passive BSS response functions, this parameter should always be well controlled for each of the gold foils used to better ascertain the neutron spectra measurements.

CHAPTER 6.

Experimental validation of the passive BSS response matrix

6.1. Introduction

The term quality assurance, when applied to measurements of spectral and directional distributions of radiation fields, covers all the activities undertaken to validate the performance of the devices used for measurements and to ensure that the final results are of adequate quality, i.e. they are reliable (correct) and of the required accuracy. Quality assurance, which is a hard and time-consuming process, is thus closely linked to the estimation of the uncertainties in the measurements including both the experimental calibration of the device response function and determination of the requested field quantity. Comparisons of Bonner sphere spectrometry [74] and simulation studies [75] have highlighted the very significant errors introduced by using incorrect response functions. It is thus mandatory to have an accurate knowledge of the response matrix to obtain accurate results in terms of neutron spectra and dosimetric quantities.

As it has been seen in the previous chapter, greatest efforts have been needed to calculate the full response matrix of the UAB passive BSS and it is vital for the evaluated response functions to be as near correct as possible. Some general comments can be made about the factors influencing these calculations:

1. Cross sections: all spectrometer response function calculations require access to good cross-section data and these are available for the majority of materials used in neutron spectrometers. In our case, responses were calculated using a modern Monte Carlo code such as MCNPX, which uses up-to-date evaluated cross sections. It is, however, very important to ensure that molecular binding effects at thermal energy are included.

2. Materials: when calculating response functions, the complete instrument, and not just the radiation-sensitive part, should be included in the computational model to allow sampling all the possible random-walk interactions. Therefore, it is important that material compositions of all the material constituents are known and that accurate drawings of their geometry details are available. However, simulated geometries are always an approach to reality.

3. Critical parameters: it is important to know accurately those parameters on which the response function depends strongly, in our case the mass and shape of the gold foils or the polyethylene density.

With modern computing speeds the statistical uncertainties can be small, but it is difficult to estimate the realistic uncertainties in calculations. A way of doing it is to verify the response matrix ([36], [38]) through irradiation in reference neutron fields as those specified in ISO Standard 8529-1 [76], for which irradiation conditions are reproducible and well controlled. Since the response matrix of a BSS is defined as a function of the neutron energy, a way to verify it is to expose the BSS to a known neutron fluence in well-characterized mono-energetic beams. The advantage of this test is the possibility to evaluate the accuracy of the response matrix in the same condition of the simulation (monochromatic energy and uniform irradiation of the sphere), allowing a punctual verification of the Monte Carlo model of the BSS. The disadvantage is that this test can be carried out on a very limited number of energies. By contrast, the same test performed with continuous spectra, as those of the ISO recommended sources (^{241}Am-Be, ^{241}Am-B, ^{252}Cf or D_2O moderated ^{252}Cf), allows checking the response matrix, even if in integral form, over a rather large energy interval. Whilst the test with radionuclide sources is probably the most suited to estimate the overall uncertainty of the response matrix, that performed in monochromatic energies is useful to understand whether this overall uncertainty is adequate for a more restricted energy range.

The validation of any set of response functions can be achieved by comparing the response in terms of fluence of each sphere-detector combination with a reference spectrum with known fluence and energy distribution. The calibration factor, f_i, for a given sphere-detector combination is defined as:

$$f_i = \frac{A^i_\infty\big|_{\text{meas}}}{A^i_\infty\big|_{\text{cal}}} \tag{6.1}$$

where $A^i_\infty\big|_{\text{meas}}$ is the saturation activity obtained from the measured induced activity (equation 4.14) for the sphere-detector combination i after being exposed to a reference field with total fluence Φ_{ref}, and $A^i_\infty\big|_{\text{cal}}$ is the calculated saturation activity for the same combination obtained by folding the corresponding response function with the reference neutron spectrum (equation 4.7). In general, a given unit neutron spectrum $\varphi(E)$ is obtained as the corresponding absolute neutron spectrum, $\Phi(E)$, divided by the total neutron fluence, Φ:

$$\varphi(E) = \frac{\Phi(E)}{\Phi} = \frac{\Phi(E)}{\int \Phi(E)\, dE} \tag{6.2}$$

Consequently, the calculated saturation activity $A^i_\infty\big|_{\text{cal}}$ for a given reference field with total fluence Φ_{ref} and unit fluence spectrum $\varphi^{\text{ref}}(E)$, can be written from equations 4.7 and 4.8 as:

$$A^i_\infty\big|_{\text{cal}} = \Phi_{\text{ref}} \int R_i(E)\, \varphi^{\text{ref}}(E)\, dE \simeq \Phi_{\text{ref}} \sum_{j=1}^{n_E} R_{i,j} \varphi^{\text{ref}}_j \Delta E_j \tag{6.3}$$

Therefore:

$$f_i = \frac{A^i_\infty\big|_{\text{meas}}}{\Phi_{\text{ref}} \sum\limits_{j=1}^{n_E} R_{i,j} \varphi^{\text{ref}}_j \Delta E_j} \tag{6.4}$$

Ideally, all f_i values corresponding to a given BSS should be equal to 1 if the calculated response functions represent exactly the real responses of the spectrometer. In the real case, f_i may take any value, as response functions are calculated approximating and scaling reality. In addition, f_i for the different sphere-detector combinations of a given BSS may fluctuate. To account for this fluctuation, an average value f_{best} and its associated standard deviation are calculated to estimate the overall calibration factor of a given BSS and its uncertainty.

A value of measured fluence Φ_{meas} is obtained from unfolding the measured saturation activities $A^i_\infty\big|_{\text{meas}}$. Equation 6.4 can then be written as

$$f_i = \frac{\Phi_{\text{meas}} \sum_{j=1}^{n_E} R_{i,j}\varphi_j^{\text{meas}}\Delta E_j}{\Phi_{\text{ref}} \sum_{j=1}^{n_E} R_{i,j}\varphi_j^{\text{ref}}\Delta E_j} \tag{6.5}$$

As φ_j^{meas} and φ_j^{ref} are both unit spectra and f_{best} is an average of all f_i values, this equation can be approximated as

$$f_{best} \simeq \frac{\Phi_{\text{meas}}}{\Phi_{\text{ref}}} \tag{6.6}$$

Once the overall calibration factor f_{best} for a given BSS has been obtained, the true value of any unknown neutron fluence can be estimated from the measured (unfolded) fluence $\Phi_{\text{meas}}$by substituting Φ_{ref} with Φ_{est} in equation 6.6, so that

$$\Phi_{\text{est}} = \frac{\Phi_{\text{meas}}}{f_{best}} \tag{6.7}$$

The accuracy of the response function for a given sphere-detector combination i, in a given reference field, with a total (integrated) neutron fluence Φ_{ref}, can be evaluated as:

$$r_{i,\text{ref}} = \left.\frac{\Phi_{\text{est}}}{\Phi_{\text{ref}}}\right|_i = \left.\frac{\Phi_{\text{meas}}}{f_{best}\Phi_{\text{ref}}}\right|_i \tag{6.8}$$

The average of all $r_{i,\text{ref}}$ values obtained for a BSS should be 1 if calibration has been done correctly and the standard deviation of all $r_{i,\text{ref}}$ values can be associated to the overall uncertainty of the response matrix.

In our case, the calibration factor and the overall uncertainty of the response functions of the UAB passive BSS were obtained from irradiations at the Cadarache ^{252}Cf standard neutron source. The response functions were later validated at the Cadarache AMANDE facility, which provides monoenergetic neutron beams. Results obtained for the calibration factor and for the overall uncertainty of the response functions are presented in the following section. Experimental validation to monoenergetic neutron beams are presented in the second section of this chapter.

6.2. Exposure to an ISO ^{252}Cf standard source

6.2.1. Irradiation conditions

The ^{252}Cf ISO standard source at IRSN Cadarache center (France) was used to obtain the UAB passive BSS calibration factor and the overall uncertainty of the response functions.

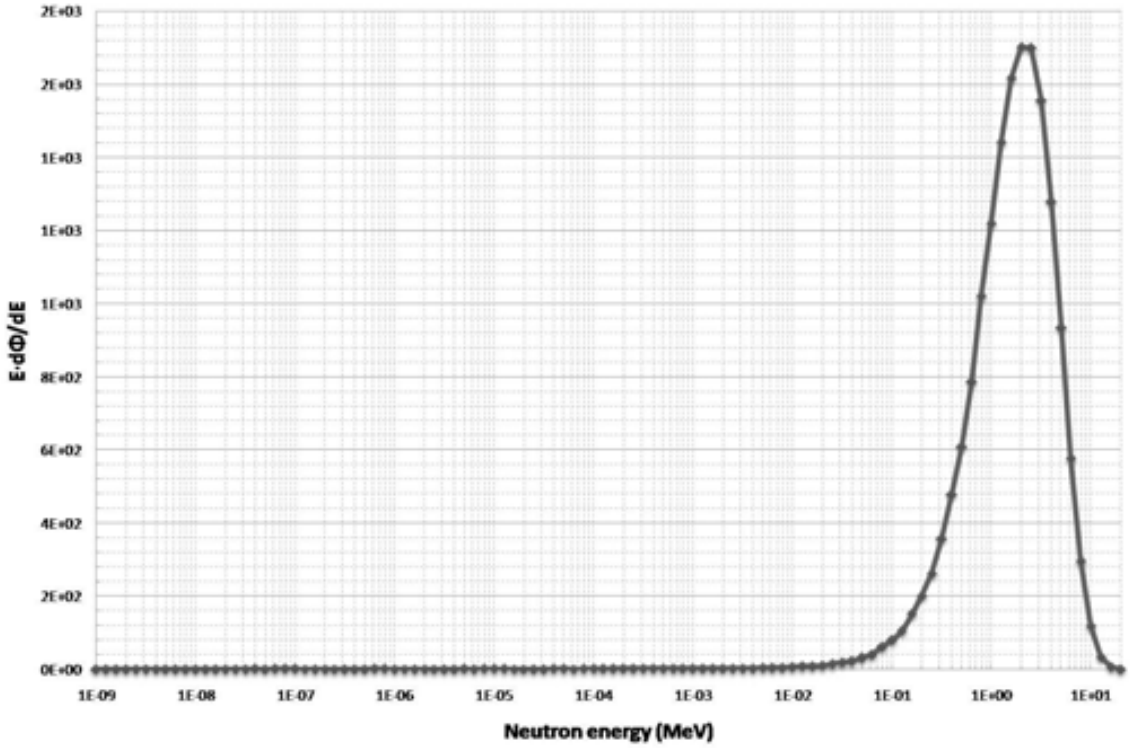

Figure 6.1. Neutron spectrum at the measurement point for calibration to ^{252}Cf at IRSN Cadarache (France).

The irradiation room (25 m × 12 m × 8 m) has been conceived to minimise scattered radiation and built with aluminium walls for this purpose. Monte Carlo simulations and experimental measurements confirmed the negligible neutron scattering effect in the room [77]. Therefore, no corrections for irradiation geometry and for the scattered contribution have been applied to the measurements. The source was placed at the reference irradiation point, at 3.2 m height, with a remote control device. The measurement point was at 75 cm from the source and at the same height. The reference neutron spectrum at the measurement point was provided by the IRSN Cadarache, see figure 6.1, with a total reference fluence rate $\dot{\Phi}_{\mathrm{ref}} = 3868 \pm 128\,\mathrm{cm}^{-2}\,\mathrm{s}^{-1}$ ($\pm 3.3\%$).

Eleven sphere-detector combinations were exposed to the ^{252}Cf field. The induced radioactivity for each gold foil was measured with our portable NaI(Tl) detector and the corresponding saturation activities were derived after background continuum subtraction and dead time correction.

6.2.2. Results

The calibration factor of the spectrometer was estimated for each sphere-detector combination i using equation 6.4 with the reference ^{252}Cf unit neutron spectrum and fluence rate.

Table 6.1. Evaluation of the accuracy of the repsonse matrix with the ^{252}Cf reference neutron field. Specific saturation activities uncertainties are calculated at 1σ level.

Sphere	A^i_∞ $\left(\mathrm{Bq\,mg^{-1}}\right)$			$R_i^{^{252}\mathrm{Cf}}$ $\left(\mathrm{cm^2\,mg^{-1}}\right)$	$\dot{\Phi}_{\mathrm{est}}$ $\left(\mathrm{cm^{-2}\,s^{-1}}\right)$	f_i	$r_{i,\mathrm{ref}}$
2.5 in	0.1789	±	0.0038	4.81×10^{-5}	3763	0.961	0.973
3 in	0.3099	±	0.0078	8.39×10^{-5}	3736	0.955	0.966
4.2 in	0.763	±	0.014	1.91×10^{-4}	4041	1.032	1.045
5 in	0.964	±	0.016	2.53×10^{-4}	3854	0.985	0.997
6 in	1.174	±	0.019	3.01×10^{-4}	3949	1.009	1.021
8 in	1.150	±	0.017	3.03×10^{-4}	3835	0.980	0.992
10 in	0.942	±	0.015	2.43×10^{-4}	3928	1.004	1.016
12 in	0.659	±	0.012	1.73×10^{-4}	3864	0.987	0.999
2.5 in+ Cd	0.1757	±	0.0031	4.90×10^{-5}	3625	0.926	0.937
3 in+ Cd	0.3375	±	0.0080	8.60×10^{-5}	3970	1.014	1.026
4.2 in+ Cd	0.761	±	0.014	1.93×10^{-4}	3990	1.019	1.032

The results are summarised in table 6.1, where $R_i^{^{252}\mathrm{Cf}} = \sum_{j=1}^{n_E} R_{i,j}\varphi_j^{^{252}\mathrm{Cf}}\Delta E_j$, represents the expected response of each sphere-detector combination in presence of the ^{252}Cf reference neutron spectrum.

The best estimation of the calibration factor for the UAB passive spectrometer, f_{best}, was obtained as a weighted average of the f_i values derived from all sphere-detector combinations. The inverse square of the uncertainties was used as weighting factor. The result obtained is:

$$f_{\mathrm{best}} = 0.988 \pm 0.033 \tag{6.9}$$

The uncertainty, ±3.4% at 1σ level, is estimated as the quadratic sum of two terms: the statistical contribution from the weighted average process (which only takes into account the saturation activity uncertainties with a total contribution of ±0.5%) and the systematic uncertainty arising from the reference neutron fluence (±3.3%). In figure 6.2 the measured fluence from each sphere is compared to the reference value Φ_{ref}. It is observed that the measured fluences obtained fluctuate around the reference.value with amplitudes comparable to the uncertainties.

The distribution of the $r_{i,\mathrm{ref}}$ values presented in table 6.1 has a mean value and standard deviation of 1.000 ± 0.032. Consequently, the uncertainty contribution due to the Monte Carlo modeling and simulation of the response matrix can be estimated to be ±3.2%. In the worst case, the discrepancy between Φ_{est} and Φ_{ref} is 6.3% for the 12 in sphere.

6.3. Validation with monoenergetic reference neutron beams

6.3.1. Irradiation conditions

AMANDE is a tandem accelerator able to accelerate protons and deuterons in an energy range from 100 keV up to 4 MeV, located at the IRSN Cadarache center in France. Neutrons can be produced through nuclear interactions of these charged particles with adequate target materials. At AMANDE, thin targets of scandium, lithium, deuterium or tritium in titanium are used for this purpose. Targets are placed at the end of the beamline and neutrons are produced

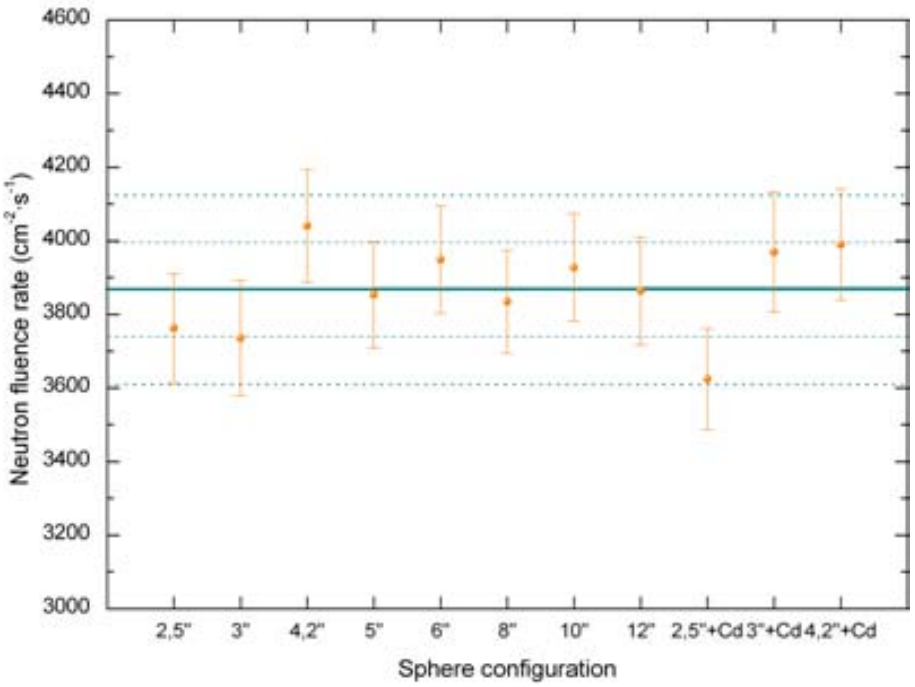

Figure 6.2. Comparison between the measured neutron fluences obtained with every sphere-detector combination and the reference value provided by IRSN Cadarache. The reference value is shown by the straight dark cyan line, also $\pm 1\sigma$ and $\pm 2\sigma$ deviations are shown by the dark cyan dashed and dot lines respectively.

Table 6.2. Targets used at AMANDE accelerator during the UAB passive BSS irradiations with monoenergetic neutron beams

Target Composition	**Thickness** ($\mathrm{mg\,cm^{-2}}$)	**Nuclear reaction**	**Neutron energy** (MeV)	**Peak FWHM** (MeV)
LiF	0.1568	$^{7}\mathrm{Li}(p,n)^{7}\mathrm{Be}$	0.144	0.021
LiF	0.1568	$^{7}\mathrm{Li}(p,n)^{7}\mathrm{Be}$	0.565	0.014
TiT	1.974	$^{3}\mathrm{H}(p,n)^{3}\mathrm{He}$	1.2	0.15
TiD	0.8252	$^{2}\mathrm{H}(d,n)^{3}\mathrm{He}$	5.0	0.11

in all directions. The neutron energy and emission angle depends on the charged particle energy, which was selected with appropriate magnets.

A total of two weeks have been scheduled for the UAB to validate the UAB passive BSS with 144 keV, 565 keV, 1.2 MeV and 5 MeV neutron monoenergetic beams. Experimental conditions allowing the maximum possible fluence rate were needed, so thickest targets and the maximum authorised current on each target were chosen.

Targets used during the irradiations are described in table 6.2. Neutron energy distributions, obtained with the TARGET code and measured with the SP2 and BC501A detectors, were provided by Cadarache.

As comented in 3.4.1., several constraints have to be applied to irradiation conditions to perform a correct validation. For example, the reading of a given instrument must be corrected for the geometric effects due to source and/or instrument dimensions which deviate the instrument readings from the inverse square law behaviour. In our case, maximal fluences were needed due to the low efficency of the UAB passive BSS, so the target-to-sphere distance was reduced down to which is reasonably possible:

1. To irradiate in a *incident parallel neutron beam*.
2. To keep the geometric factor $F_1\,(l)$ as close to 1 as possible.

The *incident parallel neutron beam* irradiation geometry was ensured by keeping the half apex angle of the solid angle subtended by each sphere to an arbitrary value of 10^o. The second condition can be achieved if the source-to-detector distance is kept above $2r_D$, being r_D the sphere radius in our case [59]. Two different target-to-sphere distances were finally chosen; 50.0 ± 0.2 cm for 2.5 in, 3 in, 4.2 in, 5 in, 6 in and 8 in spheres; and 75.0 ± 0.2 cm for the 10 in and 12 in spheres, ensuring both conditions 1 and 2 are preserved. The three Cd configurations were not used due to irradiation time limitations.

Another important question is the existence of scattered neutrons in the measurement point. Two main origins of scattered neutrons can be identified:

- Neutron scattering in the target holder and backing,
- Neutron scattering in the air and in all the other elements constituting the experimental hall.

The experimental hall can be seen in 6.3. It is a 20 m × 20 m × 16 m room surrounded mostly by metallic walls to minimize neutron scattering. A floor grating is placed at 6 m above the ground, over the entire hall surface with the exception of a 6 m radius hole where the

Figure 6.3. AMANDE accelerator experimental hall.

experimental area is. The neutron-producing target is centered in this hole at the end of the beamline, 7.2 m above the experimental hall ground. An automated transportation system with 3 arms is dedicated to place the detector and moveable access platforms are also available.

It was not necessary to estimate experimentally the scattered contribution because of the room configuration. Instead, Cadarache provided us the total neutron fluence rate and the reference spectrum at the place of measurement.

6.3.2. Results for the 144 keV neutron beam

Only the small spheres, placed at 50 cm, were tested with this monoenergetic beam due to the very long times needed for irradiation of the bigger spheres at 75 cm. As the total current varied for each sphere, the total reference fluence rate in each case is given in table 6.3, together with the experimental value determined with our passive BSS. When uncertainties are taken into account, all experimental values agree correctly with the corresponding reference fluence.

The neutron spectrum per unit total fluence obtained by unfolding the measurements from our BSS can be seen in figure 6.4 in lethargic representation, together with the reference spectrum provided for the AMANDE 144 keV neutron beam at 50 cm. The total neutron fluence, given as fluence per monitor unit (MU), associated to the unfolded spectrum is $\Phi_{\mathrm{est}}^{144\,\mathrm{keV}} = (6.001 \pm 0.086)\ \mathrm{cm}^{-2}\,\mathrm{MU}^{-1}$, in agreement with the corresponding reference value, $\mathbf{\Phi}_{\mathrm{ref}}^{144\,\mathrm{keV}} = (5.79 \pm 0.32)\ \mathrm{cm}^{-2}\mathrm{MU}^{-1}$.

Table 6.3. Validation of the repsonse matrix with the AMANDE 144 keV reference neutron field. Saturation activities uncertainties are calculated at 1σ level

Sphere	A^i_∞ $\left(\mathrm{Bq\,mg^{-1}}\right)$	$R_i^{144\,\mathrm{keV}}$ $\left(\mathrm{cm^2\,mg^{-1}}\right)$	$\dot{\Phi}_{\mathrm{ref}}$ $\left(\mathrm{cm^{-2}\,s^{-1}}\right)$	$\dot{\Phi}_{\mathrm{est}}$ $\left(\mathrm{cm^{-2}\,s^{-1}}\right)$
2.5 in	0.2904 ± 0.0058	1.48×10^{-4}	$(2.73 \pm 0.15) \times 10^7$	$(2.86 \pm 0.14) \times 10^7$
3 in	0.4372 ± 0.0075	2.16×10^{-4}	$(2.14 \pm 0.12) \times 10^7$	$(2.21 \pm 0.11) \times 10^7$
4.2 in	0.6824 ± 0.0097	3.30×10^{-4}	$(2.13 \pm 0.12) \times 10^7$	$(2.26 \pm 0.11) \times 10^7$
5 in	0.785 ± 0.012	3.42×10^{-4}	$(2.17 \pm 0.12) \times 10^7$	$(2.26 \pm 0.11) \times 10^7$
6 in	0.7610 ± 0.0069	3.01×10^{-4}	$(2.27 \pm 0.13) \times 10^7$	$(2.30 \pm 0.11) \times 10^7$
8 in	0.3188 ± 0.0036	1.68×10^{-4}	$(2.73 \pm 0.15) \times 10^7$	$(2.76 \pm 0.13) \times 10^7$

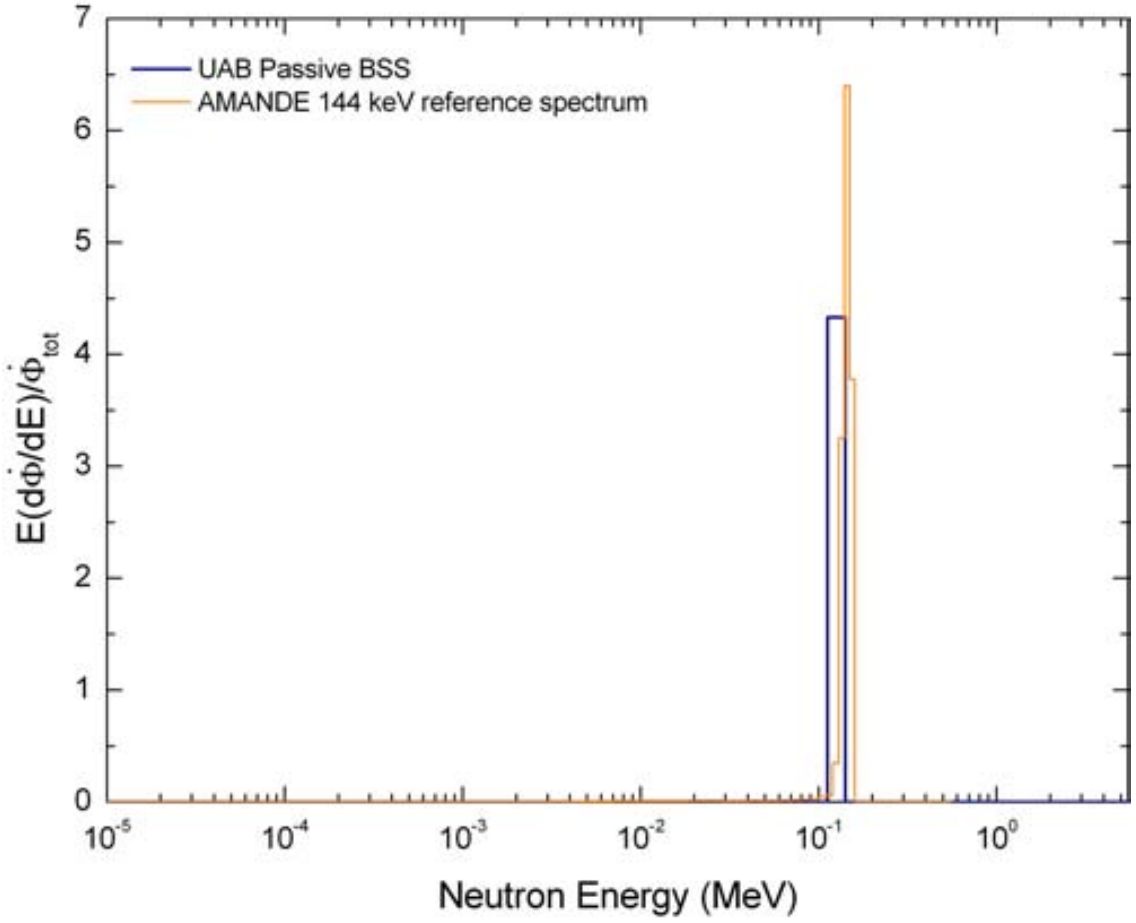

Figure 6.4. Comparison between the reference spectrum and that obtained by unfolding the UAB passive BBS readings for the AMANDE 144 k eV monoenergetic beam. Spectra are given in equilethargic representation and per unit total fluence.

Table 6.4. Validation of the repsonse matrix with the AMANDE 565 keV reference neutron field. Saturation activities uncertainties are calculated at 1σ level

Sphere	A^i_∞ $\left(\mathrm{Bq\,mg^{-1}}\right)$	$R_i^{565\,\mathrm{keV}}$ $\left(\mathrm{cm^2\,mg^{-1}}\right)$	$\dot{\Phi}_{\mathrm{ref}}$ $\left(\mathrm{cm^{-2}\,s^{-1}}\right)$	$\dot{\Phi}_{\mathrm{est}}$ $\left(\mathrm{cm^{-2}\,s^{-1}}\right)$
2.5 in	0.2688 ± 0.0061	8.52×10^{-5}	$(2.98 \pm 0.16) \times 10^7$	$(2.30 \pm 0.15) \times 10^7$
3 in	0.4771 ± 0.0094	1.44×10^{-4}	$(2.67 \pm 0.14) \times 10^7$	$(2.41 \pm 0.16) \times 10^7$
4.2 in	1.130 ± 0.018	2.92×10^{-4}	$(2.77 \pm 0.15) \times 10^7$	$(2.82 \pm 0.18) \times 10^7$
5 in	1.508 ± 0.020	3.54×10^{-4}	$(3.13 \pm 0.17) \times 10^7$	$(3.10 \pm 0.20) \times 10^7$
6 in	1.409 ± 0.020	3.71×10^{-4}	$(2.76 \pm 0.15) \times 10^7$	$(2.77 \pm 0.18) \times 10^7$
8 in	1.312 ± 0.020	2.83×10^{-4}	$(3.31 \pm 0.18) \times 10^7$	$(3.38 \pm 0.22) \times 10^7$
10 in	0.313 ± 0.0059	1.61×10^{-4}	$(1.630 \pm 0.086) \times 10^7$	$(1.421 \pm 0.096) \times 10^7$

6.3.3. Results for the 565 keV neutron beam

In the case of the 565 keV neutron beam, spheres 2.5 in, 3 in, 4.2 in, 5 in, 6 in and 8 in were placed at 50 cm from the target and the 10 in sphere was placed at 75 cm. As the total current varied for each sphere, the total reference fluence rate for each sphere is given in table 6.4, together with the corresponding experimental value determined with our passive BSS. If uncertainties are taken into account, all experimental values agree with their corresponding reference fluence rate, with the exception of the 2.5 in sphere. The experimental value calculated from this sphere is below the reference one. The deviation may be explained by the fact that the saturation activity obtained for this sphere was close to its associated detection limit (defined in Section 6.4.).

For all the spheres exposed at 50 cm the unfolded spectrum per unit of total fluence was obtained with the FRUIT code and it is presented in 6.5 in lethargic representation, together with the reference spectrum for the AMANDE 565 keV neutron beam. In this case, the total neutron fluence, given as fluence per monitor unit (MU), associated to the unfolded spectrum is $\Phi_{\mathrm{est}}^{565\,\mathrm{keV}} = (6.84 \pm 0.47)\ \mathrm{cm^{-2}\,MU^{-1}}$, in agreement with the 565 keV neutron beam reference value, $\Phi_{\mathrm{ref}}^{565\,\mathrm{keV}} = (6.99 \pm 0.37)\ \mathrm{cm^{-2}\,MU^{-1}}$.

6.3.4. Results for the 1.2 MeV neutron beam

All sphere configurations were exposed to the 1.2 MeV neutron beam. The biggest spheres (10 in and 12 in) were exposed at 75 cm from the target. In table 6.5, the saturation activities, A^i_∞, the response for the 1.2 MeV neutron beam, $R_i^{1.2\ \mathrm{MeV}}$, the total fluence rate reference value, $\dot{\Phi}_{\mathrm{ref}}$, and the fluence rate determined experimentally, $\dot{\Phi}_{\mathrm{est}}$, for each sphere are presented. As for the 565 keV neutron beam, all sphere configurations provide correct estimations of the total fluence rate when uncertainties are taken into account, except the 2.5 in configuration. This may be explained because of the low response that this sphere has for 1.2 MeV neutron energy spectrum.

The unfolded spectrum per unit of total fluence obtained is presented in figure 6.6, as a lethargy plot, together with the reference spectrum provided by AMANDE for the 1.2 MeV neutron beam. The total neutron fluence, given as fluence per monitor unit (MU), associated to the unfolded spectrum is $\Phi_{\mathrm{est}}^{1.2\,\mathrm{MeV}} = (6.93 \pm 0.75)\ \mathrm{cm^{-2}\,MU^{-1}}$, in agreement with the 1.2 MeV neutron beam reference value, $\Phi_{\mathrm{ref}}^{1.2\,\mathrm{MeV}} = (6.67 \pm 0.34)\ \mathrm{cm^{-2}\,MU^{-1}}$.

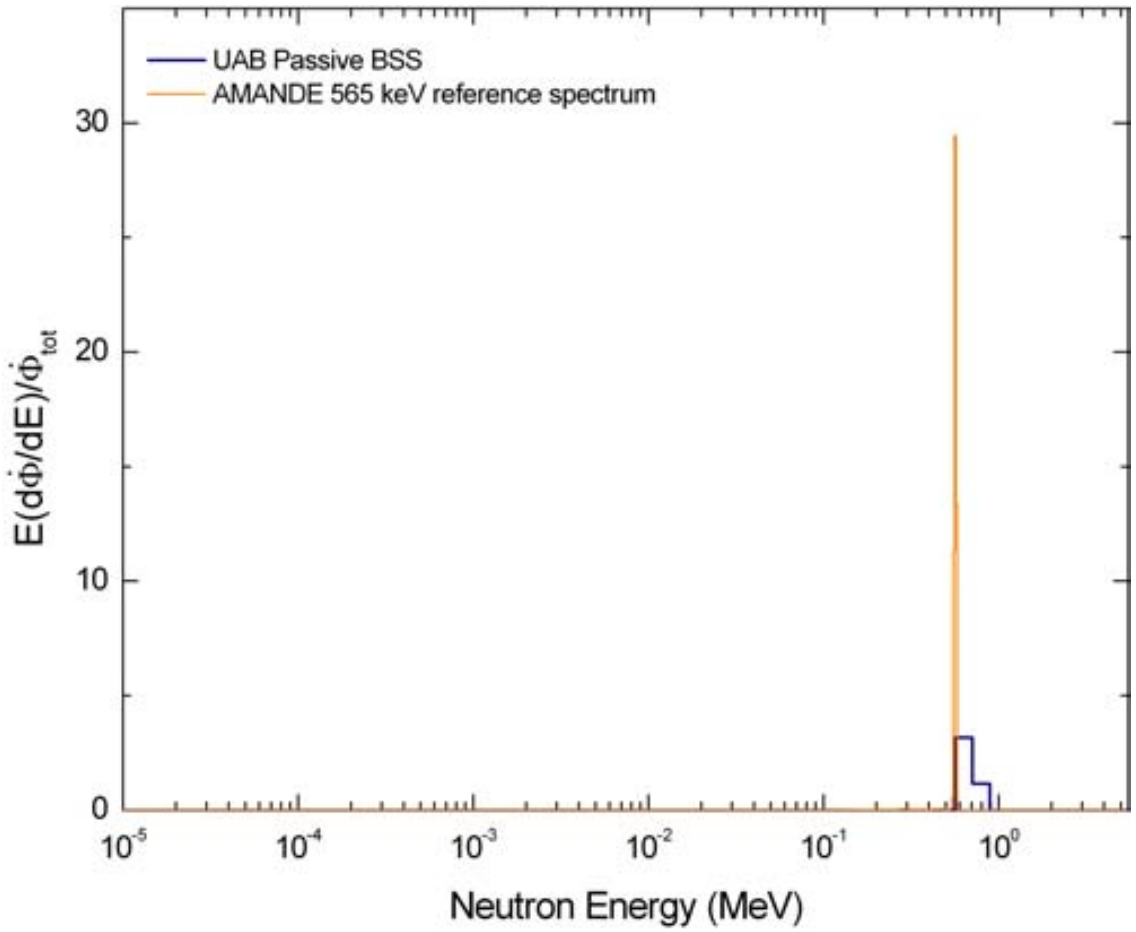

Figure 6.5. Comparison between the reference spectrum and that obtained by unfolding the UAB passive BBS readings for the AMANDE 565 k eV monoenergetic beam. Spectra are given in equilethargic representation per unit total fluence.

Table 6.5. Validation of the repsonse matrix with the AMANDE 1.2 MeV reference neutron field. Saturation activities uncertainties are calculated at 1σ level

Sphere	A^i_∞ $\left(\mathrm{Bq\,mg^{-1}}\right)$	$R_i^{1.2\,\mathrm{MeV}}$ $\left(\mathrm{cm^2\,mg^{-1}}\right)$	$\dot{\Phi}_{\mathrm{ref}}$ $\left(\mathrm{cm^{-2}\,s^{-1}}\right)$	$\dot{\Phi}_{\mathrm{est}}$ $\left(\mathrm{cm^{-2}\,s^{-1}}\right)$
2.5 in	0.887 ± 0.018	5.33×10^{-5}	$(4.89 \pm 0.25) \times 10^7$	$(3.74 \pm 0.24) \times 10^7$
3 in	2.046 ± 0.036	9.71×10^{-5}	$(7.34 \pm 0.37) \times 10^7$	$(7.68 \pm 0.49) \times 10^7$
4.2 in	5.691 ± 0.074	2.33×10^{-4}	$(8.41 \pm 0.43) \times 10^7$	$(8.91 \pm 0.56) \times 10^7$
5 in	7.345 ± 0.083	3.10×10^{-4}	$(8.00 \pm 0.41) \times 10^7$	$(8.64 \pm 0.54) \times 10^7$
6 in	8.674 ± 0.084	3.63×10^{-4}	$(7.99 \pm 0.41) \times 10^7$	$(8.72 \pm 0.54) \times 10^7$
8 in	7.947 ± 0.090	3.40×10^{-4}	$(7.85 \pm 0.40) \times 10^7$	$(8.53 \pm 0.53) \times 10^7$
10 in	1.914 ± 0.038	2.38×10^{-4}	$(3.00 \pm 0.16) \times 10^7$	$(2.94 \pm 0.20) \times 10^7$
12 in	1.483 ± 0.028	1.43×10^{-4}	$(3.57 \pm 0.19) \times 10^7$	$(3.77 \pm 0.25) \times 10^7$

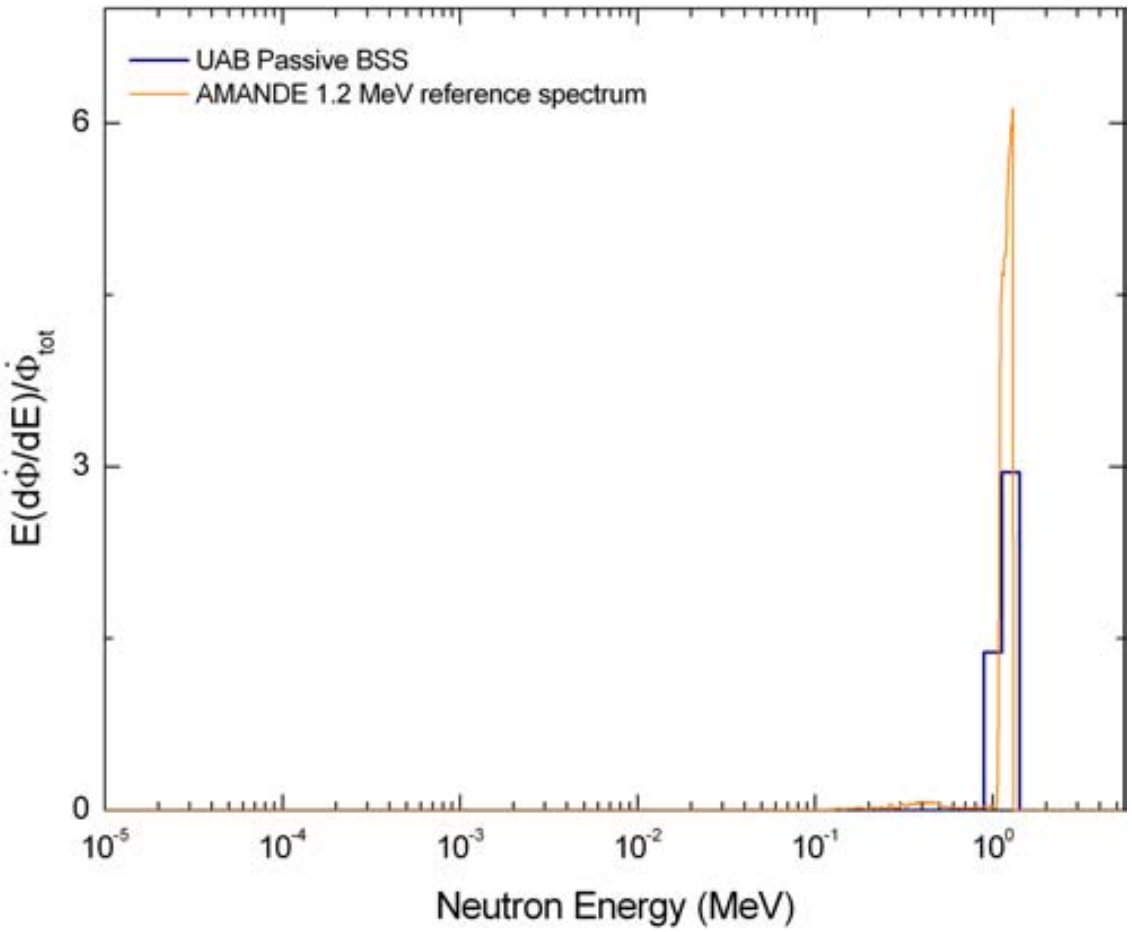

Figure 6.6. Comparison between the reference spectrum and that obtained by unfolding the UAB passive BBS readings for the AMANDE 1.2 MeV monoenergetic beam. Spectra are given in equilethargic representation per unit total fluence.

Table 6.6. Validation of the repsonse matrix with the AMANDE 5 MeV reference neutron field. Saturation activities uncertainties are calculated at 1σ level

Sphere	A^i_∞ $\left(\mathrm{Bq\,mg^{-1}}\right)$	$R_i^{5\,\mathrm{MeV}}$ $\left(\mathrm{cm^2\,mg^{-1}}\right)$	$\dot{\Phi}_{\mathrm{ref}}$ $\left(\mathrm{cm^{-2}\,s^{-1}}\right)$	$\dot{\Phi}_{\mathrm{est}}$ $\left(\mathrm{cm^{-2}\,s^{-1}}\right)$
4.2 in	0.425 ± 0.010	8.26×10^{-5}	$(4.35 \pm 0.15) \times 10^7$	$(3.75 \pm 0.20) \times 10^7$
5 in	0.792 ± 0.016	1.32×10^{-4}	$(4.49 \pm 0.15) \times 10^7$	$(4.38 \pm 0.23) \times 10^7$
6 in	1.153 ± 0.019	1.89×10^{-4}	$(6.90 \pm 0.23) \times 10^7$	$(6.70 \pm 0.34) \times 10^7$
8 in	1.649 ± 0.011	2.68×10^{-4}	$(4.64 \pm 0.16) \times 10^7$	$(4.48 \pm 0.22) \times 10^7$
10 in	0.815 ± 0.013	2.88×10^{-4}	$(2.473 \pm 0.094) \times 10^7$	$(2.06 \pm 0.11) \times 10^7$
12 in	0.919 ± 0.017	2.64×10^{-4}	$(2.482 \pm 0.094) \times 10^7$	$(2.53 \pm 0.14) \times 10^7$

6.3.5. Results for the 5.0 MeV neutron beam

The highest energy neutron reference beam used to validate the response function was a 5 MeV neutron beam. The two smallest spheres (2.5 in and 3 in) were not used due to the long times needed to activate the gold foils with these configurations. The results obtained for this beam are presented in table 6.6. Experimental values of the total fluence rate are similar to the reference ones, although 4.2 in and 10 in spheres provide values smaller than expected.

The unfolded spectrum per unit of total fluence is presented in lethargy terms in figure 6.7, together with the reference spectrum. The total neutron fluence, given as fluence per unit monitor (MU), associated to the unfolded spectrum was $\Phi_{\mathrm{est}}^{5\,\mathrm{MeV}} = (12.34 \pm 0.59)\ \mathrm{cm^{-2}MU^{-1}}$, in agreement with the 5 MeV neutron beam reference value, $\Phi_{\mathrm{ref}}^{5\,\mathrm{MeV}} = (11.38 \pm 0.39)\ \mathrm{cm^{-2}MU^{-1}}$.

6.4. Detection limit of the UAB passive neutron spectrometer

6.4.1. Introduction

The minimum detectable neutron fluence rate needs to be estimated to characterise fully the spectrometer. However, the definition of such a limit is not obvious when a complex procedure, involving unfolding, is required. Several factors need to be carefully taken into account for obtaining a reliable estimation.

In the particular case of the UAB passive Bonner sphere spectrometer, neutron fluence rate is derived from an unfolding procedure using the FRUIT code, which takes into account the saturation activities obtained for each sphere-detector combination (up to 11 values) and the system response matrix. It should be noticed that these saturation activities are determined from the net count rates of the corresponding ^{198}Au 412 keV photo-peaks for each sphere configuration. These count rates are obtained with a NaI(Tl) detector. Hence, the minimum detectable fluence or ambient dose equivalent rates are related with the ability of the NaI(Tl) detector to discriminate the ^{198}Au photo-peak from background contribution.

A clear conclusion arise: although the minimum detectable net count rate for a given NaI(Tl) detector is a quantity that only depends on the detector background level, different saturation activities can be derived if different irradiation, t_i, elapsed, t_e, and measurement, t_m, times are considered. Low neutron fluence rates will produce small saturation activities, which will be better determined with long irradiation and measuring times as well as small elapsed times.

With all these considerations, several steps were undertaken to estimate the minimum detectable neutron fluence rates for the UAB passive BSS;

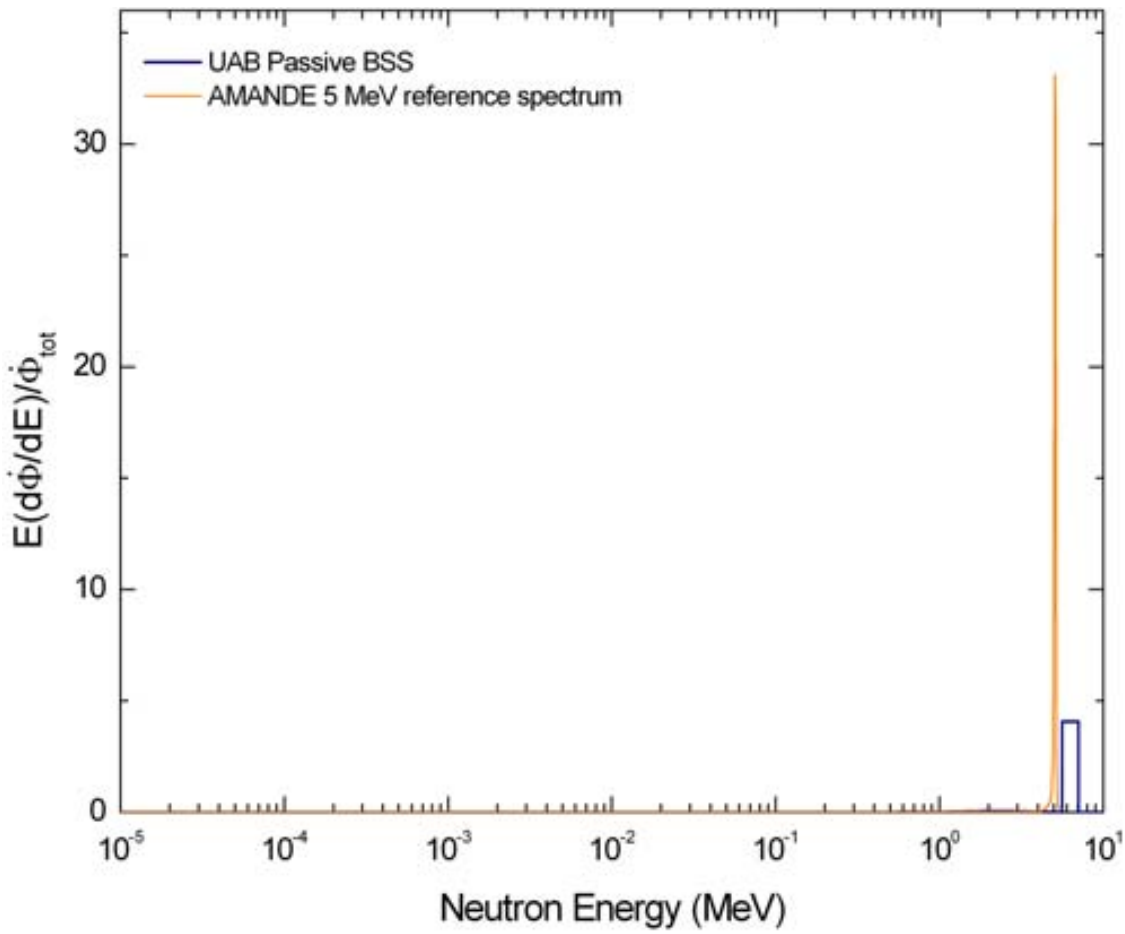

Figure 6.7. Comparison between the reference spectrum and that obtained by unfolding the UAB passive BBS readings for the AMANDE 5 MeV monoenergetic beam. Spectra are given in equilethargic representation per unit total fluence.

1. The background count rate, $\dot{B} \pm \sigma_{\dot{B}}$, for the ROI (region-of-interest) channels where the ^{198}Au photo-peak is always present, was evaluated with a long measurement time.

2. A set of several hypothetical irradiation times, t_i, elapsed times, t_m, and counting times, t_m, were chosen to study how the detection limit depends on them.

3. The detection limit, expressed as the minimum net count rate, $\dot{L}_D$, needed from an hypothetical ^{198}Au source to ensure a *false-negative* rate not larger than 5% and with a *false-positive* rate not greater than 5%, is estimated for the different sets of counting times chosen, according to Currie's equation [78]:

$$\dot{L}_D = \frac{1}{t_m}\left(4.653\sigma_{N_B} + 2.706\right) \tag{6.10}$$

   where σ_{N_B} stands for the standard deviation of the background counts, estimated in practice from a known background count rate $\dot{B}$ assuming Poisson counting statistics, that would be obtained during the counting time, t_m. It should be noticed that Currie's equation is obtained under *the null hypothesis*, i.e. that the true value of the estimated quantity is equal to zero.

4. A set of minimum detectable saturation activities, $\mathbf{A}_{\infty}^{\mathrm{MD}}$, is derived, according to equation 4.14, from all the minimum net count rate $\dot{L}_D$ values taking into account the different irradiation and elapsed times chosen.

5. Assuming that the $\mathbf{A}_{\infty}^{\mathrm{MD}}$ value obtained for a given combination of times would not depend on the sphere-detector combination, the minimum measurable neutron fluence rate, $\dot{\Phi}^{\mathrm{MD}}$, is derived by unfolding with the FRUIT code. Thus, the same minimum detectable saturation activity is associated to the 11 sphere-detector combinations.

6. The unfolding procedure is repeated for all sets of saturation activities obtained in step 4, and a set of minimum detectable neutron fluence rates is derived for the different irradiation conditions considered.

This procedure was applied for both (fixed and portable) NaI(Tl) detectors in use at our laboratory, as they present different background count rates.

6.4.2. Results

Pulse height distributions were obtained with a month reading time using as blank samples two gold foils, which have never been previously irradiated, for determining the background for both NaI(Tl) detectors. Several photo-peaks can be identified for both NaI(Tl) detectors, as it can be seen in figures 6.8 and 6.9, consequence of naturally occurring radioactive decay of ^{40}K as well as of ^{238}U and ^{232}Th series present as impurities in almost all the materials surrounding the two NaI detectors [79].

The background count rate in the channels corresponding to ^{198}Au photo-peak obtained with the fixed NaI(Tl) detector was $\dot{B}_{\mathrm{Fixed}} = 0.57933 \pm 0.00043$ cps, whereas with the portable detector it was $\dot{B}_{\mathrm{Portable}} = 2.13488 \pm 0.00082$ cps. The big difference between both background levels is explained by the particular Pb shielding used for each NaI(Tl) detector.

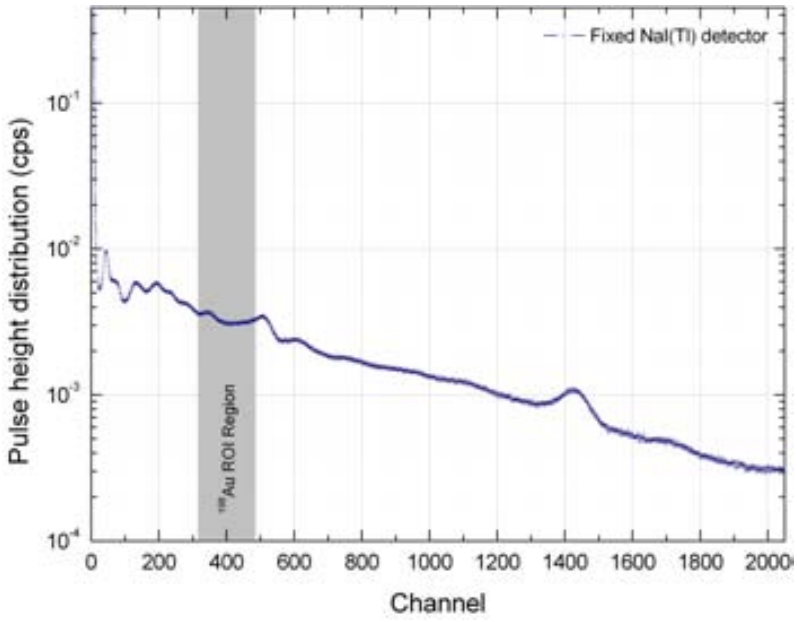

Figure 6.8. Pulse height distribution obtained with the fixed NaI(Tl) gamma-ray detector in use at our laboratory from a blank sample of ^{197}Au. The Region of Interest (ROI) defined for the determination of the ^{198}Au photo-peak is shown in grey.

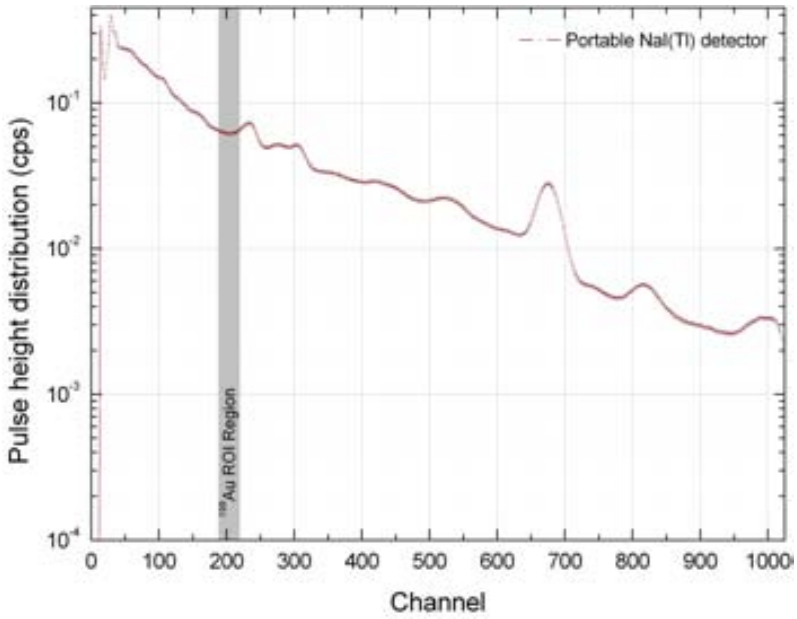

Figure 6.9. Pulse height distribution obtained with the portable NaI(Tl) gamma-ray detector in use at our laboratory from a blank sample of ^{197}Au. The Region of Interest (ROI) defined for the determination of the ^{198}Au photo-peak is shown in grey.

As explained above, several irradiation, elapsed and measurement times were chosen to estimate the detection limit of the spectrometer. According to the short half-life of gold and from previous experience in different measurement campaigns, it is recommend that, for low neutron fluences, irradiation and measurement times to be as large as possible and elapsed times to be as short as possible. Following this criteria three different scenarios were studied:

- Best scenario: with an irradiation time of 12 h (a complete night irradiation since longer times are not usual), a short elapsed time of 1 h and a long measuring time of 7 d.
- An average scenario, representing the most common irradiation conditions, with t_i = 10 min, t_e = 1 h and a measuring time t_m = 1 h.
- Worst scenario, defined by very short irradiation times and long elapsed times, with t_i = 5 min, t_e = 7 d and t_m = 1 h.

The detection limit in terms of net count rates for both NaI(Tl) detectors and for the three scenarios are shown in table 6.7. The differences between the minimum detectable saturation activities associated to the three scenarios (up to a factor 1000) reflect the importance of the irradiation and measurement conditions in presence of low fluence rates.

The unfolding code FRUIT was used to obtain the minimum detectable neutron fluence rates for all scenarios. As described in 3.3., the code is able to parametrise the neutron spectra with different physical models. However the minimum detectable neutron fluence rates should not depend on the physical model used for unfolding. In order to verify this independence, three different radiation environments (nuclear power plant, medical LINAC and narrow spectrum) were tested for the NaI(Tl) fixed detector for the best and average irradiation conditions. The results obtained are presented in table 6.8 and allow to conclude that the detection limit does not depend on the physical model used for unfolding.

Finally, the minimum detectable fluence rates for both NaI(Tl) detectors and for all scenarios are summarised in table 6.9. The evaporation physical model was used for unfolding. For a given detector clear differences arise between different irradiation conditions as expected. Variations between detectors for a given irradiation scenario are due to background contributions.

6.5. Conclusion

The results of the experimental validation of the response functions were presented in this chapter. The sphere-detector combinations of the UAB passive BSS, developed in this work, were exposed to a reference ^{252}Cf ISO standard source at IRSN Cadarache (France). From these measurements, an overall calibration factor was calculated for the spectrometer as the average of the f_i values for the all different sphere-detector combinations used. The best estimation of the calibration factor for the UAB passive spectrometer is $f_{\text{best}} = 0.988 \pm 0.033$.

The uncertainty of the response function matrix for the UAB passive BSS was also estimated to be ±3.2%. To do this, the accuracy of the response factors, $r_{i,\text{ref}}$, were calculated from the measurements of the ISO ^{252}Cf neutron field at IRSN Cadarache for each sphere-detector combination. An average value 1.000±0.032 was derived for all of them and its standard deviation is assumed to be the uncertainty associated to the contribution of the response matrix of the UAB passive BSS.

Table 6.7. Detection limit values, expressed as net count rates, for the three irradiation scenarios for both NaI(Tl) detectors in use at our laboratory. The saturation activities derived from these detection limits are also given.

NaI(Tl) detector	**Scenario**	$\mathbf{t}_i$	$\mathbf{t}_e$	$\mathbf{t}_m$	$\dot{\mathbf{L}}_D$ (**cps**)	$\mathbf{A}_\infty^{\mathrm{MD}}$ $\left(\mathrm{Bq\,mg^{-1}}\right)$
Fixed	Best	12 h	1 h	168 h	4.6×10^{-3}	1.0×10^{-3}
	Average	10 min	1 h	1 h	6.0×10^{-2}	0.43
	Worst	5 min	7 d	1 h	6.0×10^{-2}	5.1
Portable	Best	12 h	1 h	168 h	8.8×10^{-3}	2.5×10^{-3}
	Average	10 min	1 h	1 h	0.11	1.0
	Worst	5 min	7 d	1 h	0.11	12

Table 6.8. Detection limit fluence rates derived by unfolding with different physical models for the fixed NaI(Tl) detector in the best and average scenarios.

Irradiation conditions	**FRUIT Unfolding**		$\dot{\Phi}^{MD}$ $\left(cm^{-2}\,s^{-1}\right)$
	Radiation environment	**Physical model**	
Best	Nuclear power plant	Fission	8.3
	Medical LINAC	Evaporation	8.4
	Narrow spectrum	Gaussian	7.3
Average	Nuclear power plant	Fission	3.3×10^3
	Medical LINAC	Evaporation	3.3×10^3
	Narrow spectrum	Gaussian	2.9×10^3

Table 6.9. Minimum detectable fluence rates for the three sets of irradiation conditions studied and for both NaI(Tl) detectors in use at our laboratory

NaI(Tl) detector	**Irradiation conditions**	$\dot{\Phi}^{MD}$ $\left(cm^{-2}\,s^{-1}\right)$
Fixed	Best	8.4
	Average	3.3×10^3
	Worst	3.9×10^4
Portable	Best	20
	Average	8.3×10^3
	Worst	9.8×10^4

The monoenergetic neutron beams available at the AMANDE facility (IRSN Cadarache, France) were used to validate the UAB passive BSS response matrix. A total of 4 different energy beams were tested: 144 keV, 565 keV, 1.2 MeV and 5 MeV. In general, the experimental results obtained with our spectrometer agree with the reference spectra provided by AMANDE for all sphere configurations and neutron energies. Consequently, the response function is considered to be correctly validated.

The last section of the chapter is dedicated to the estimation of the minimum detectable fluence rate of the UAB passive BSS. A procedure to obtain this detection limit was defined taking into account the complex procedure, involving unfolding, required to obtain fluence rate estimations from the BSS measurements. Three different scenarios reflecting different irradiation, elapsed and measurement times were considered. The minimum detectable net count rates, for both NaI(Tl) detector in use at our laboratory, were determined and different minimum detectable saturation activities, $\mathbf{A}_{\infty}^{MD}$, were estimated for the three scenarios. The $\mathbf{A}_{\infty}^{MD}$ value obtained for a given scenario was associated to the 11 sphere-detector combinations of the UAB passive BSS and the minimum measurable neutron fluence rate, $\dot{\Phi}^{MD}$, was derived by unfolding with FRUIT. The independence of the results from the physical model used for unfolding has been proved. For a given detector clear differences arise between different irradiation conditions as expected, showing the influence of the conditions of irradiation and measurement in presence of low fluence rates. The minimum detectable fluence rate, $\dot{\Phi}^{MD}$, obtained for the average scenario condition is $3.3 \times 10^3\,cm^{-2}\,s^{-1}$ for fixed NaI(Tl) detector and $8.3 \times 10^3\,cm^{-2}\,s^{-1}$ for the portable one.

CHAPTER 7.

Application at LINAC and PET workplaces

The aim of this work is to develop a passive BSS useful in intense and pulsed neutron fields, even in presence of an important photon component. Examples of this type of workplace fields are those produced in facilities containing radiotherapy LINACs and PET dedicated cyclotrons. This chapter is dedicated to present the results obtained with the UAB passive BSS in these type of facilities. The neutron spectra and global dosimetric quantities that have been measured at three points inside a LINAC treatment room for comparison of the results obtained between 3D and IMRT treatments are presented in the first part of the chapter. Measurements around 6 LINACs, of different manufacturers and nominal energies, that have been performed in the framework of the NEUTOR project are presented in the second part of the chapter. The third part is dedicated to the study of the neutron field around an unshielded PET cyclotron facility, in Pamplona (Spain). Finally, the results obtained around a self-shielded PET cyclotron facility in Keele (UK) are presented. Brief introductions about each facility characteristics are provided in each section.

7.1. Neutron fields measured in 3D and IMRT radiotherapy treatments

7.1.1. Radiotherapy

Cancer represents currently one of the most important diseases in developed societies. Around eleven million of new cancer cases were diagnosed during year 2002 [80], [81]. The World Health Organization predicts that around 15 million new patients will be diagnosed during year 2020 [82]. Radiotherapy represents one of the most useful tools available to cure cancer, together with surgery and chemotherapy. Usually these therapeutic modalities are used in combination, with an overall 65% fraction of total diagnoses undergoing radiation therapy. Although radiotherapy techniques are progressively more efficient for cancer cure, there is also a growing concern about the risk of secondary radiation induced tumours [83]. Epidemiologic studies

have shown that for radiation dose exposures above $50 - 100\,\mathrm{mSv}$ the secondary cancer risk for prostate and breast treatments is significantly higher in a 30 year interval after the therapy [84]. In a recent work, that includes a 40 year interval survey, it is indicated a significantly greater risk of secondary cancer for cervix tumour patients [85]. For this reason, it seems necessary to develop additional methods in order to provide an adequate radiation protection to the patient, that allow to evaluate the best strategy for the treatment and take into account the risk-benefit balance due to the peripheral dose delivered. ICRP publication 103 [20] makes recommendations about this subject. In many of the radiation therapy procedures the peripheral unwanted dose is due to photons and neutrons. Although photon doses have been deeply studied, following well known experimental procedures, the neutron contamination from high energy photon beams is still a subject of research and discussion.

Figure 7.1. Schematic diagram of a clinical linear electron accelerator (LINAC) showing the acceleration section, the rotating gantry, the collimator and the treatment couch.

When radiotherapy planning is done using X-rays. images of tumours in two dimensions (2D), width and height, are obtained. Treatments performed from this planning are usually called 2D tretments. With computer technology it's now possible to see the tumour in three dimensions (3D); width, height and depth, using scans from computer axial tomography or magnetic ressonance imaging. The information from these scans feeds directly into the radiotherapy planning computer, so the treatment area is seen in 3 dimensions. The computer programme then designs radiation beams that 'conform' more closely to the shape of the tumour and avoid healthy tissue as far as possible. This is called *3D conformal radiotherapy* (3D CRT). There is another type of conformal radiotherapy called *intensity modulated radiotherapy* (IMRT). Like 3D conformal radiotherapy, IMRT shapes the radiation beams to closely fit the area where the cancer is. But it also alters the radiotherapy dose depending on the shape of the tumour. This means that the central part of the cancer receives the highest dose of radiotherapy and a

surrounding area of tissue gets lower doses. Multileaf collimators, moving around the patient together with the LINAC head, shape the beams of radiotherapy to fit the tumour. IMRT can be static, if the LINAC gantry is fixed while the multileaf collimators are moving to conform the field, or dynamic, if the gantry rotates while the collimators move. Figure 7.1 shows a schematic representation of a LINAC.

Despite the capability of planning in radiotherapy and calculating doses accurately to within millimeters, it is not possible at to identify microscopic disease with such accuracy. The logistic difficulties of immobilizing a patient for the duration of an IMRT treatment (typically $15 - 30$ min) also limit the treatment accuracy. Patients and tumors move both as a result of voluntary movement and visceral motion such as respiration and digestion. Additionally, tumors shrink with treatment. Patients may lose weight over the course of the treatment, which will further alter their geometry and therefore dosimetry. The next direction in radiation oncology is to account for this movement, and this is being called *four-dimensional* (4D) *conformal radiotherapy* (CRT), a logical progression from 3D CRT [86].

In the isocenter of the linac for a reference IMRT treatment the neutron fluence can reach values of 0.55×10^6, 9.2×10^6 and 15×10^6 $\mathrm{cm}^{-2}\mathrm{Gy}^{-1}$ for 10, 15 and 18 MV respectively [87]. In terms of neutron ambient dose equivalent, an IMRT technique delivering 45 Gy could represent 300 mSv, while in a conventional treatment it can be reduced to approximately 100 mSv [88].

7.1.2. Measurement campaign at Hospital Plató, Barcelona

A measurement campaign took place at the Hospital Plató in Barcelona for comparing the neutron ambient dose equivalent delivered in realistic 3D and IMRT radiotherapy treatments. Two equivalent treatments for the same prostate tumour, one for 3D conformal radiotherapy and the other one for static IMRT, have been planned using an ECLIPSE Varian treatment planning system with an HELIOS IMRT module. These treatments have been delivered with a 18 MV Varian 2100CD LINAC, with a 120 Millenium multi-leaf collimator (figure 7.2). Figure 7.3 shows schematically how the multi-leaf collimator shapes the photon irradiation field. Exposures were made at rates of 600 cGy/min of photon irradiation measured in the isocenter (all 3D treatments and point at 135 cm in the IMRT treatment) and of 400 cGy/min (isocenter and point at 70 cm in the IMRT treatment).

Neutron ambient dose equivalent measurements have been performed using the UAB passive BSS, based on gold foil activation and described in this work, during the dummy application of the planned treatments. Three points are monitored: *i)* the LINAC isocenter, where the direct photon irradiation takes place; *ii)* a point at 70 cm from the isocenter, at its same height and in the "head" direction and *iii)* a point at 135 cm from the isocenter, also at its same height and in the "feet" direction. Photons and neutrons are present at the isocenter, while only neutrons are expected at points *ii* and *iii*. Monitoring these points allows to test the photon insensitivity of the passive BSS as well as to establish the variations of the neutron field as a function of the distance (and direction) from the isocenter. Figure 7.4 displays one of the BSS spheres situated on the LINAC couch, prepared for exposure at 135 cm from the isocenter.

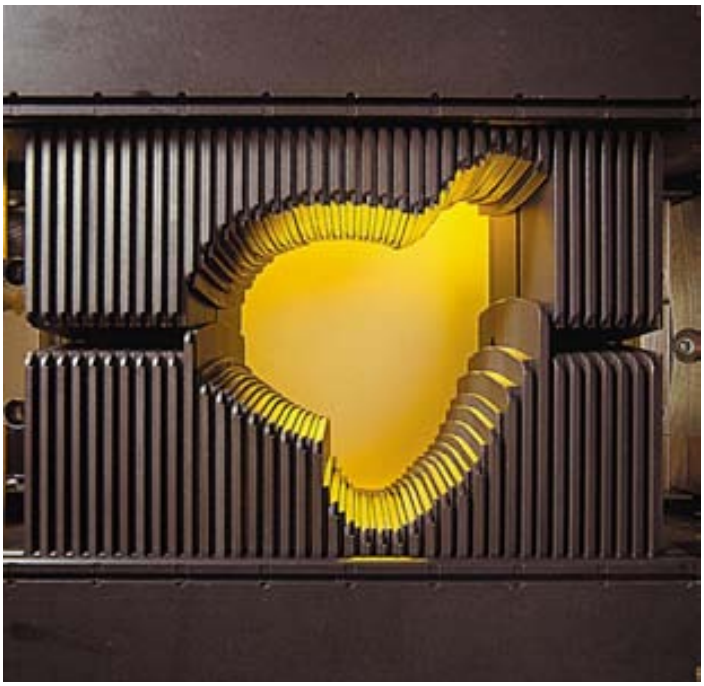

Figure 7.2. A 120 Millenium multi-leaf collimator from Varian (from the Varian webpage http://www.varian.com).

7.1.3. Results and discussion

The saturation activities induced in the gold foils used in both treatments in Hospital Plató, for each sphere-detector combination and each place of measurement, are presented in table 7.1. Neutron unit fluence spectra in terms of lethargy obtained from unfolding with FRUIT (section 3.3.) the saturation activities of the BSS gold foils exposed at the three measurement points for the 3D and IMRT treatments are displayed in figures 7.5 and 7.6 respectively. These graphs show how the fluence spreads over the entire energy range of interest, but do not allow comparing in absolute terms the neutron fields present at the different points. It becomes apparent from these graphs that the position of the evaporation peak (around a fraction of MeV) does not depend of the treatment performed nor from the position of the point of measurement, and that the relative contribution of the epithermal neutron component becomes more important when the distance from the isocenter increases. This was expected, as the amount of primary neutrons that scatter with the air in the treatment room and, therefore, loose energy, increases with distance (see section 1.2.1.). It is also obvious that the position of the thermal peak does not vary with treatment nor with position, as expected from the fact that this position is only dependent of the temperature of the irradiation room, to which thermal neutrons are in equilibrium.

Figures 7.7 and 7.8 show the unfolded absolute neutron fluence spectra in terms of lethargy, at the three measurement points, respectively for the 3D and IMRT treatments. Spectra are presented per unit photon absorbed dose (Gy) at the isocenter to allow comparison of

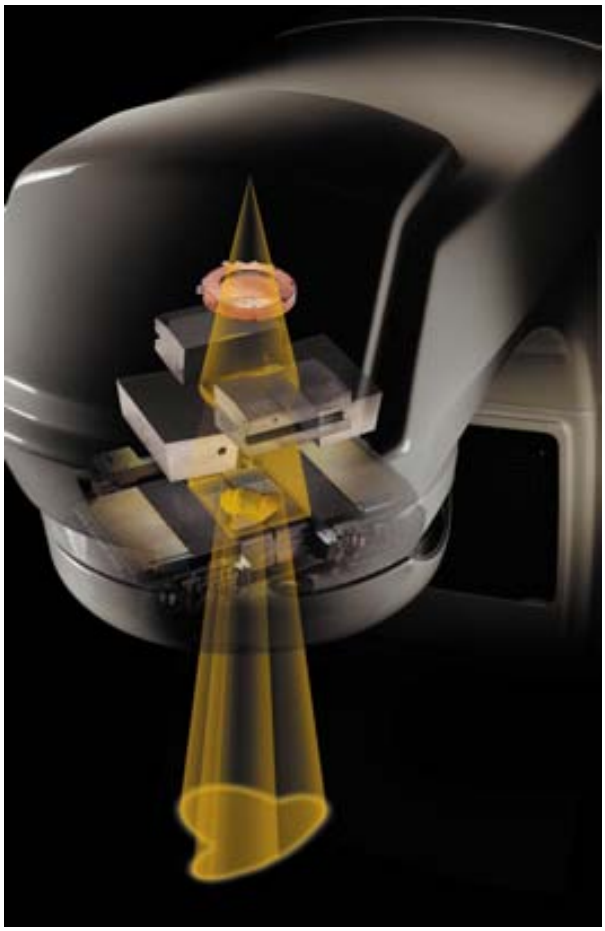

Figure 7.3. Schematic diagram of how a multi-leaf colliamtor shapes the photon field in a LINAC accelerator (from the Varian webpage http://www.varian.com).

Figure 7.4. The 10 in sphere of the UAB passive BSS on the LINAC couch, prepared for exposure at 135 cm from the isocenter.

Table 7.1. Summary of induced saturation activities for all sphere configurations, all points and all treatments in Hospital Plató

Sphere-detector combination	Saturation activities A^i_∞ $\left(\mathrm{Bq\,mg^{-1}}\right)$		
	3D treatment		
	Isocenter	**70** cm **from isocenter**	**135** cm **from isocenter**
2.5”	398 ± 20	323.3 ± 3.1	272.8 ± 1.8
3”	483 ± 23	397.3 ± 4.6	320.0 ± 3.2
4.2”	656 ± 35	470.5 ± 5.2	361.2 ± 4.1
5”	692 ± 59	494.7 ± 5.7	358.0 ± 3.2
6”	594 ± 35	433.1 ± 4.3	295.2 ± 2.5
8”	370 ± 29	265.9 ± 2.5	172.4 ± 1.8
10”	170 ± 12	124.4 ± 1.7	85.12 ± 0.75
12”	86.5 ± 6.3	23.75 ± 0.44	40.05 ± 0.31
2.5”+ Cd	–	266.6 ± 1.9	–
3”+ Cd	–	346.4 ± 3.5	–
4.2”+ Cd	–	455.3 ± 3.4	–
	IMRT treatment		
	Isocenter	**70** cm **from isocenter**	**135** cm **from isocenter**
2.5”	280.5 ± 4.6	216.6 ± 5.1	268.8 ± 2.3
3”	351 ± 15	264.2 ± 2.1	319.0 ± 3.3
4.2”	453 ± 37	325.9 ± 2.8	351.3 ± 4.0
5”	439 ± 38	317.3 ± 4.1	347.5 ± 5.9
6”	391 ± 46	284.6 ± 3.4	284.4 ± 3.7
8”	250 ± 12	174.0 ± 1.9	174.8 ± 1.7
10”	124.0 ± 9.6	89.2 ± 1.2	84.5 ± 1.5
12”	58.3 ± 2.0	39.57 ± 0.65	38.61 ± 0.72
2.5”+ Cd	192 ± 21	182.0 ± 1.2	
3”+ Cd	244 ± 30	231.1 ± 2.3	
4.2”+ Cd	262 ± 28	325.5 ± 4.4	

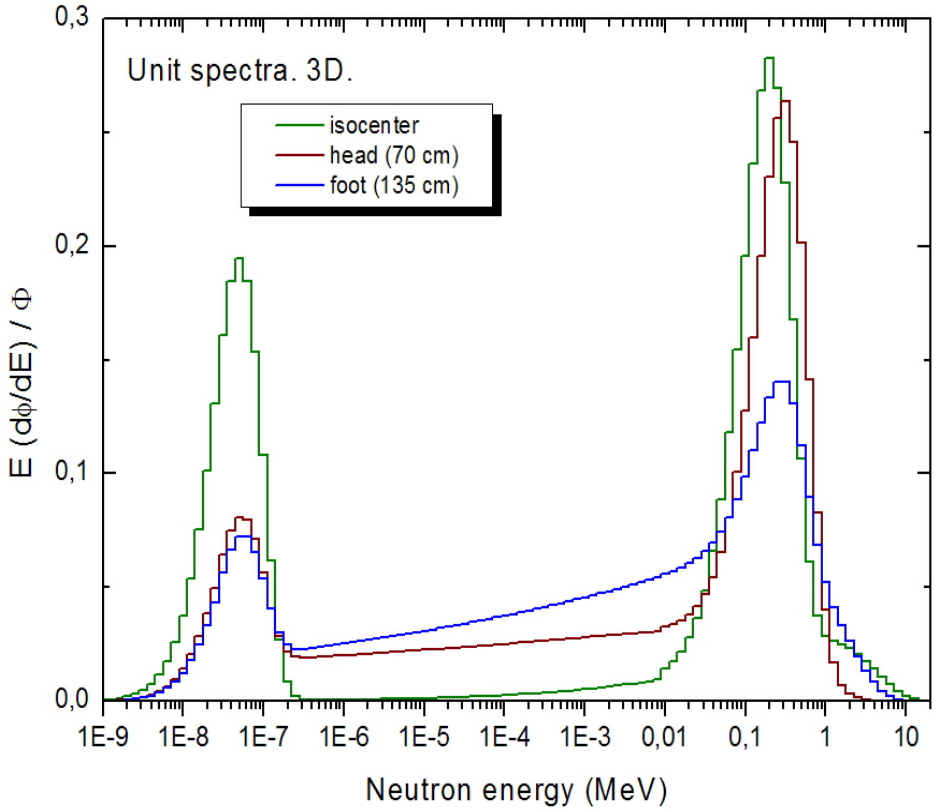

Figure 7.5. Unfolded neutron unit fluence spectra in terms of lethargy at the three measurement points for the 3D treatment.

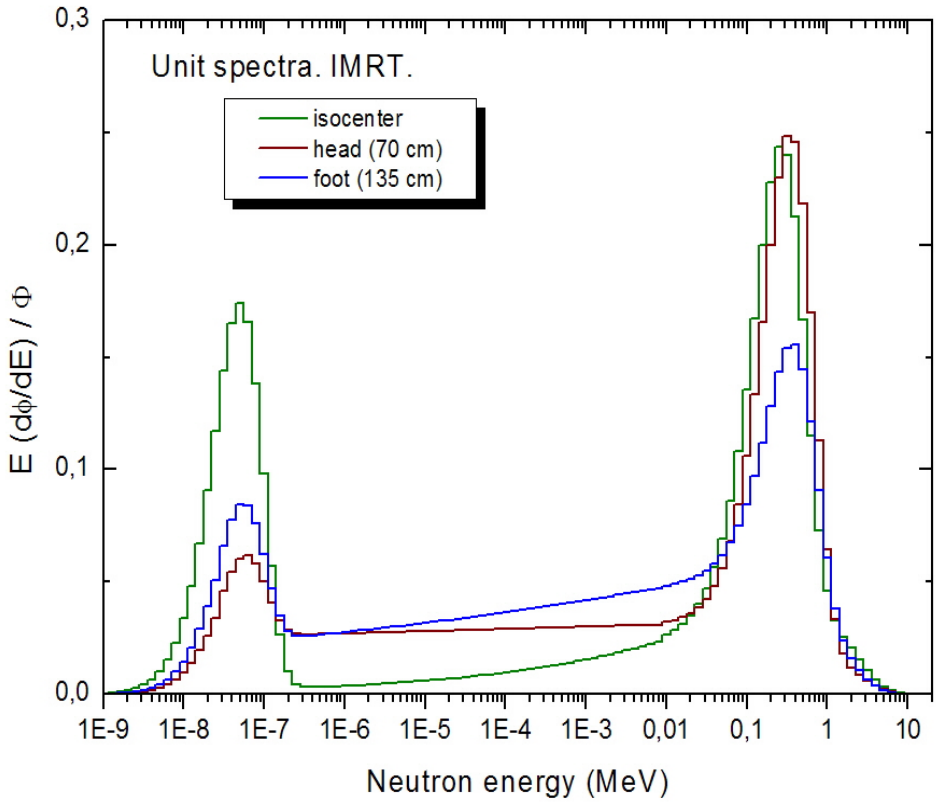

Figure 7.6. Unfolded neutron unit fluence spectra in terms of lethargy at the three measurement points for the IMRT treatment.

the effects of irradiations to different integral doses. It is appreciated, in both figures, that the most important amount of fast (direct) neutrons appears, as expected, at the isocenter, while this amount decreases as a function of the distance at the other points. This agrees with the fact that the direct neutron component, coming from the accelerator head, decraeses with the inverse square law of the distance to the production point. On the contrary, the thermal neutron component at 70 and 135 cm are similar (almost equal in the IMRT treatments), indicating that this component does not follow the inverse square law of the distance, as expected. The large thermal component found at the isocenter may be explained by the in situ thermalisation of fast neutrons that interact with the material located close to the isocenter (couch, ...).

Unfolded absolute neutron spectra in terms of lethargy and per unit delivered dose at the isocenter, at 70 cm from the isocenter (head) and at 135 cm from the isocenter (feet) are displayed, respectively, in figures 7.9, 7.10 and 7.11. Spectra obtained for the two treatments (3D and IMRT) are presented in each of these figures. In all cases, for a given measurement point, there is very small difference between the spectra obtained for the 3D and IMRT treatments. This result indicates that the neutron production processes in both situations are the same, and that the fraction of neutrons which may originate in the multi-leaf collimator does not depend in an appreciable way on the leaf's position (open in the 3D treatment, or closed, defining the geometry of the irradiation field, in the IMRT treatment). It is suggested that possible differences in neutron production between 3D and IMRT treatments may be due to the presence or absence of the multi-leaf collimator in different accelerator units rather than to the treatment itself and the usage or not of the IMRT technique. For studying this situation, new exposures should be planned allowing to compare results from IMRT treatments in accelerators having the multi-leaf collimators with these obtained from 3D treatments in accelerators not having the collimator units.

Table 7.2 shows the values of the global dosimetric quantities obtained at all irradiation points, for both treatments. For all measurement points, it is confirmed that the values of the global dosimetric quantities obtained for the 3D and IMRT treatments are indistinguishable one from each other. The values obtained for the neutron fluences and ambient dose equivalents per unit prescribed dose completely agree with those found by Howell et al [89].

7.2. Measured neutron fields at NEUTOR Project radiotherapy LINACs

7.2.1. The NEUTOR project

The NEUTOR project was set up in Spain by a group of about 20 scientists from different Spanish universities, institutions and hospitals, with the support of the Spanish National Nuclear Safety Council (CSN). The final goal of this project is to estimate the neutron equivalent doses that a patient subject to a given radiotherapy treatment has received in several relevant organs in a given session from the readings of a new digital device located inside the treatment room, in a place where it does not interfere with usual clinical procedures. The project started in 2007 and is still in development. The first task was developing a new digital neutron detector, based on the fact that Single Event Upsets (SEU) in digital SRAM memories occur when the device is placed inside a thermal neutron field [90], [91]. An anthropomorphic female phantom

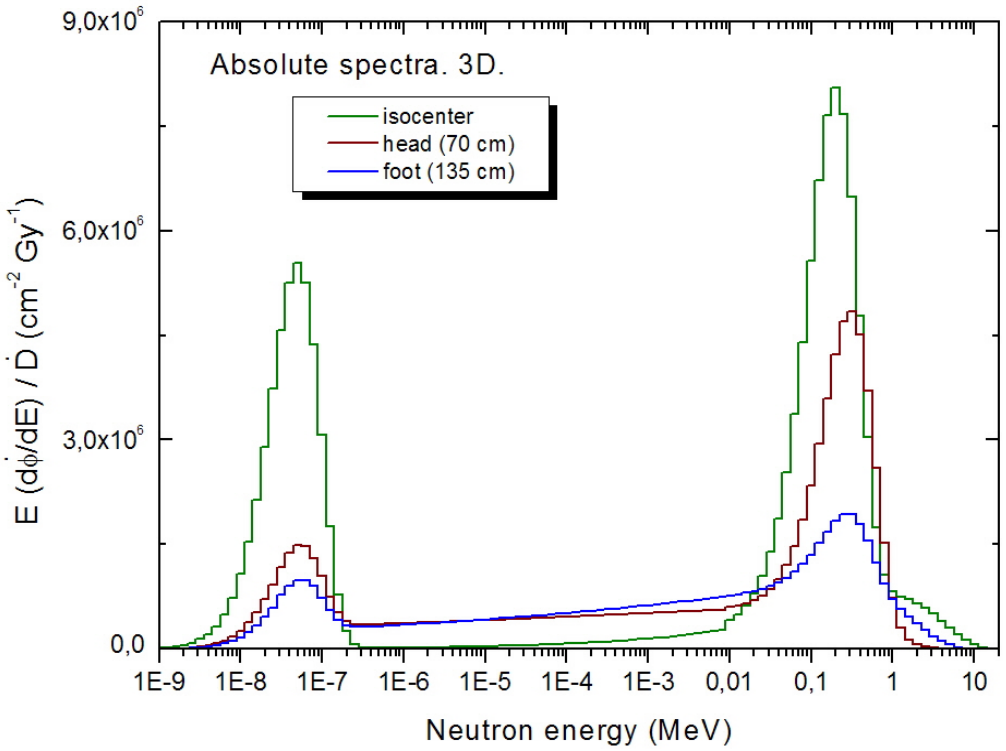

Figure 7.7. Unfolded neutron fluence spectra in terms of lethargy per unit delivered photon dose at the three measurement points for the 3D treatment.

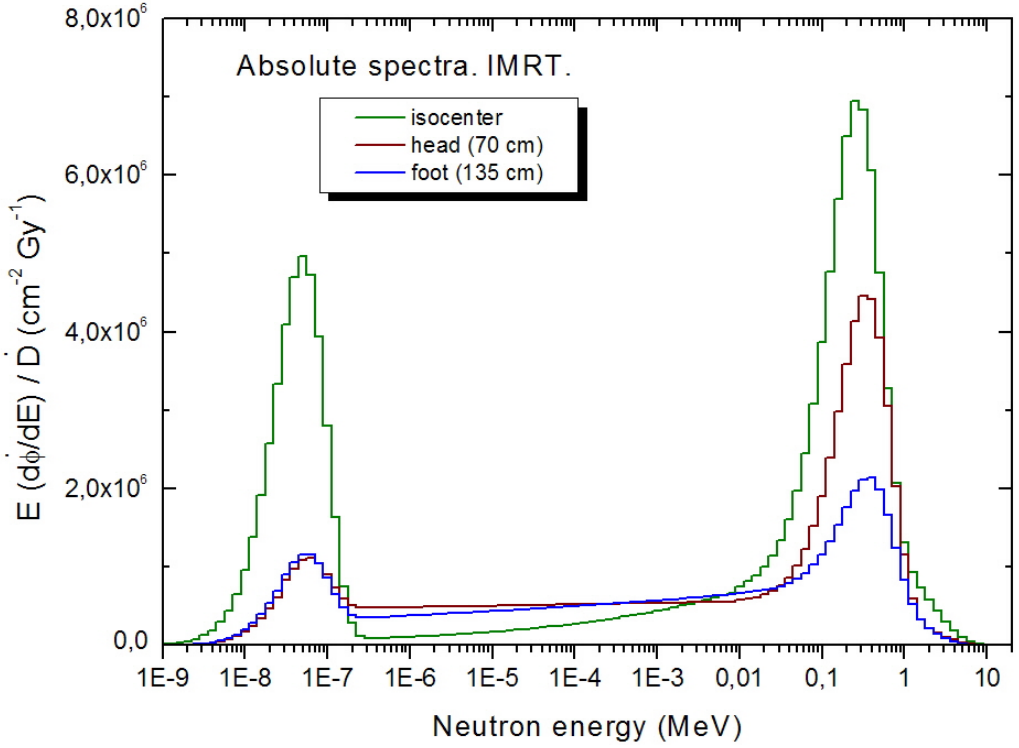

Figure 7.8. Unfolded neutron fluence spectra in terms of lethargy per unit delivered photon dose at the three measurement points for the IMRT treatment.

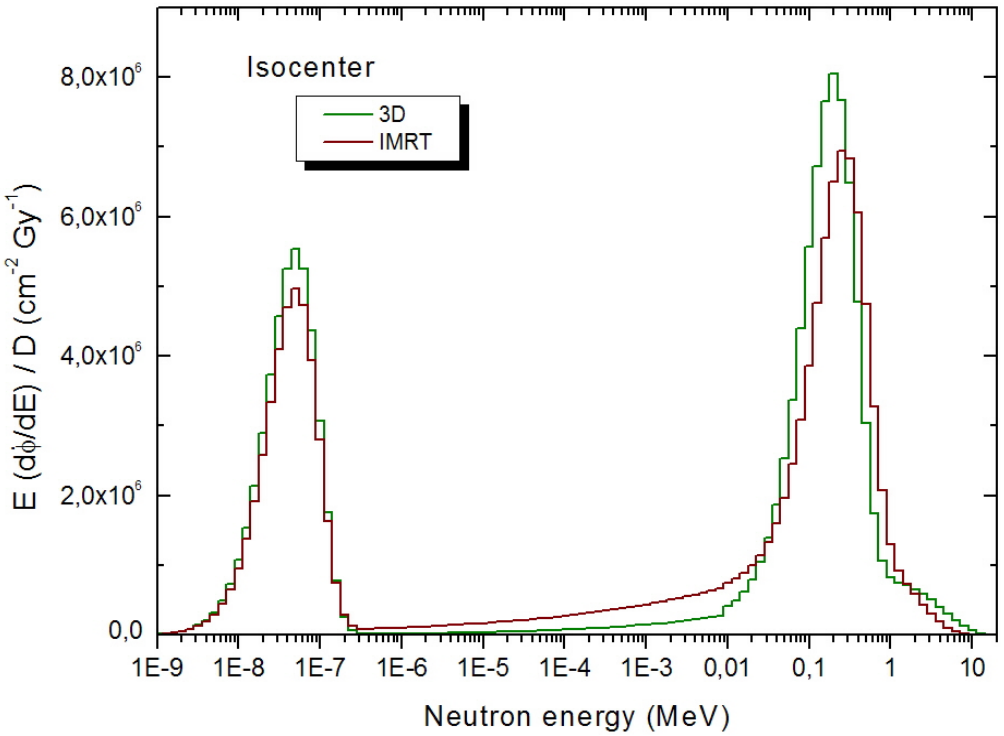

Figure 7.9. Unfolded neutron unit fluence spectra in terms of lethargy at the isocenter for the 3D and IMRT treatments.

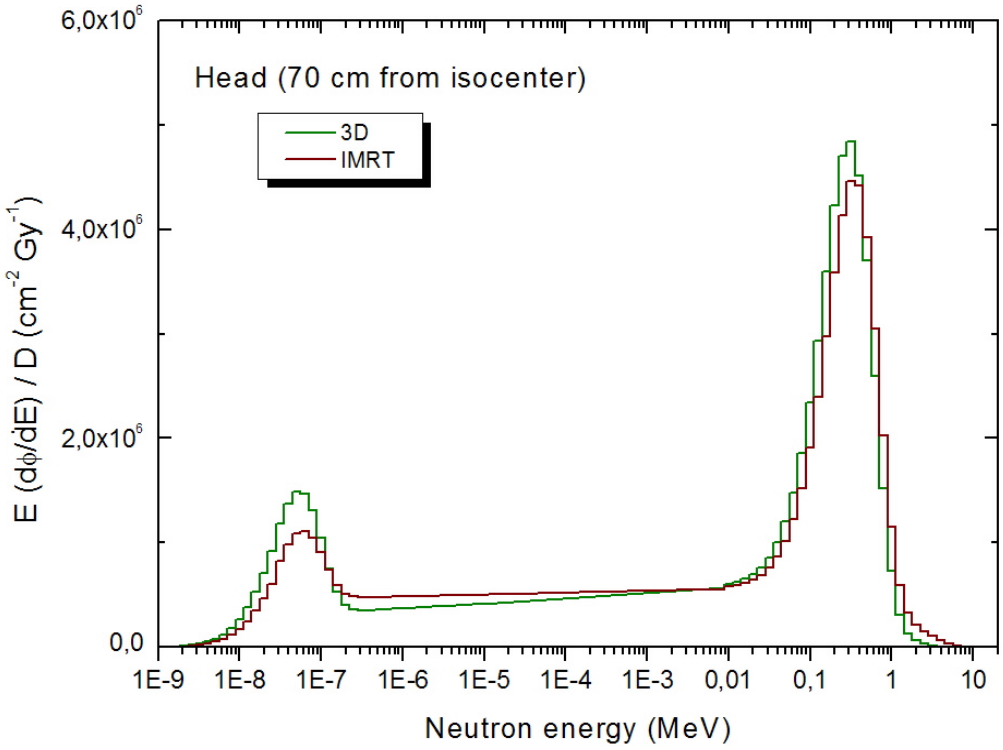

Figure 7.10. Unfolded neutron unit fluence spectra in terms of lethargy at 70 cm from the isocenter (head) for the 3D and IMRT treatments.

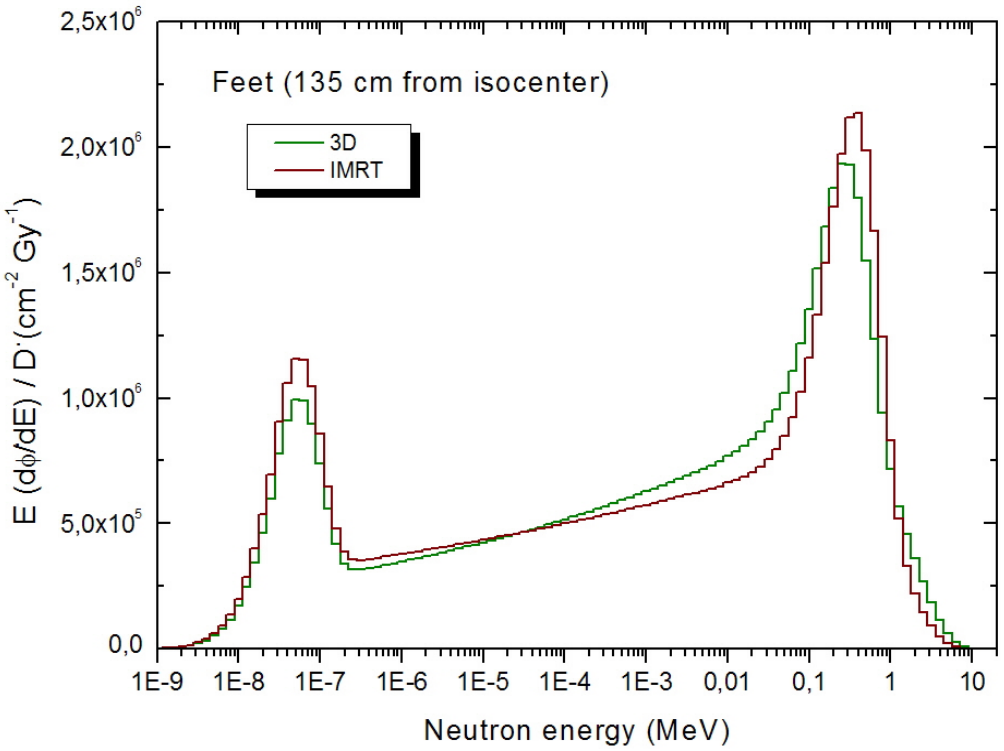

Figure 7.11. Unfolded neutron unit fluence spectra in terms of lethargy at 135 cm from the isocenter (feet) for the 3D and IMRT treatments.

Table 7.2. Global neutron dosimetric quantities for both 3D and IMRT treatments at the three points of measurement.

	3D treatment	**IMRT treatment**
Isocenter		
$\Phi\left(\mathrm{cm}^{-2}\mathrm{Gy}^{-1}\right)$	$(2.849 \pm 0.085) \times 10^7$	$(2.85 \pm 0.17) \times 10^7$
$H^*(10)\left(\mathrm{mSv\,Gy}^{-1}\right)$	3.14 ± 0.21	3.27 ± 0.22
$\bar{E}_\Phi$ (MeV)	0.23	0.20
$\bar{E}_{H^*}$ (MeV)	0.67	0.55
70 cm **from isocenter (head)**		
$\Phi\left(\mathrm{cm}^{-2}\mathrm{Gy}^{-1}\right)$	$(1.838 \pm 0.062) \times 10^7$	$(1.797 \pm 0.069) \times 10^7$
$H^*(10)\left(\mathrm{mSv\,Gy}^{-1}\right)$	2.11 ± 0.12	2.21 ± 0.12
$\bar{E}_\Phi$ (MeV)	0.16	0.20
$\bar{E}_{H^*}$ (MeV)	0.41	0.53
135 cm **from isocenter (head)**		
$\Phi\left(\mathrm{cm}^{-2}\mathrm{Gy}^{-1}\right)$	$(1.374 \pm 0.069) \times 10^7$	$(1.371 \pm 0.097) \times 10^7$
$H^*(10)\left(\mathrm{mSv\,Gy}^{-1}\right)$	1.224 ± 0.087	1.27 ± 0.11
$\bar{E}_\Phi$ (MeV)	0.18	0.16
$\bar{E}_{H^*}$ (MeV)	0.68	0.58

(NORMA), tissue equivalent for photon irradiation, has been constructed and filled with several types of passive neutron detectors (TLDs, PADCs, gold foils, ...) at 16 different places, see figure 7.12, and irradiated to several "standard" radiotherapy treatments at a number of LINAC accelerators of different energies (between 6 and 23 MV) and makes.

The neutron fields in the 16 measurement points inside NORMA have been evaluated from simulation for a large number of irradiation conditions (LINAC nominal energies, positions of the phantom, treatment conditions, room geometries,...) and published in [92]. These simulated neutron fields need to be experimentally validated. For this task, the UAB passive Bonner sphere spectrometer developed in this thesis has been chosen. The results obtained have been recently published in [93] and are one of the contributions of the UAB group to the NEUTOR project.

7.2.2. Irradiation conditions at NEUTOR LINACs

A set of irradiations has been performed at 6 LINAC accelerators, chosen to explore as many different makes, nominal energies, room (or bunker) geometries and sizes as possible:

- Two 15 MV Siemens Primus from the Hospital Universitario Virgen de la Macarena, located inside two geometrically distinct rooms. Bunker 1 is a relatively big bunker, while bunker 2 is a much smaller one. They have been selected to study the possible influence of the irradiation room size and geometry on the neutron field.
- One 18 MV Siemens Primus LINAC at the Hospital General Universitario in València.
- One 23 MV Siemens Mevatron LINAC at the Universitätsklinikum in Heidelberg.

Figure 7.12. The antropomorphic female phantom NORMA on the couch of a linac radiotherapy treatment room. On the upper right corner, the placement of detectors in points 7, 8 and 16 can be seen. On the bottom part, a scheme of the distribution of the 16 measurement points inside NORMA is given.

- One 15 MV Varian CLINAC 2100 from the Hospital Puerta de Hierro.
- One 15 MV Elekta Synergy LINAC from the Hospital Ramón y Cajal.

In all cases, the SEU-based digital detector was placed inside the treatment room in a point along the gantry rotation axis where it does not interfere with the patient or with the gantry movement. Typical distances from the isocenter to this location vary typically from 3 m to 6 m, depending on the room geometry and size. Spectrometric measurements have been performed employing a static $(10 \times 10)\,\mathrm{cm}^2$ field at $0\,^\circ$, in a reference point located at 50 cm from the isocenter, at its same height, without the presence of the anthropomorphic phantom at the couch, as well as the place where the digital device is located, with the phantom at the couch. All "standard treatments" have been set to 1000 "monitor units" (MU), as specified and measured in the control console. One monitor unit corresponds to a photon dose of 1 cGy measured at the depth of maximum dose (source to surface distance, SSD = 100 cm) in a water cube, along the photon beam axis. The dose rate, related to the accelerator beam intensity, has ranged from 300 to 600 MU/ min. Giving the results "per MU" or "per Gy" enables comparing neutron production from treatments and accelerators supplying different photon doses.

After irradiation, the activities induced in the irradiated gold foils have been measured with the UAB NaI(Tl) detectors. Both fixed and portable NaI(Tl) detectors have been used in parallel to reduce the elapsed time between irradiation and measurement. In the Heidelberg campaign only the portable NaI(Tl) has been used because of the timing of the campaign. Measuring times have been optimised to ensure a relative uncertainty as close to 1% as possible. The saturation activities have been calculated for each sphere-detector combination. The neutron energy distributions and their global dosimetric quantities have been obtained for all points by unfolding with the FRUIT code, using the LINAC enviroment option.

7.2.3. Experimental neutron fields at NEUTOR LINACs

The saturation activities induced in the gold foils, for each sphere-detector combination and each place of measurement, are presented in tables 7.3 and 7.4. The average relative uncertainty is 1.8%, with a maximum of 10.9% and a minimum of 0.6%. At 50 cm from the isocenter, the saturation activity smoothly increases with sphere diameter up to the 5" sphere, after which it decreases. For the Digital Device place a similar behaviour is observed. However, the sphere presenting a maximum in those cases is the 4.2". This is consistent with the energy dependence of the response matrix and with the fact that the neutron energy distribution is expected to be softer at the place where the Digital Device is located than at 50 cm from the isocenter.

The lethargy neutron spectra (per Gy of photon irradiation) at 50 cm from the isocenter, for the LINACs and rooms under study, are represented in figure 7.13 . In all cases the fast neutron component is dominant close to the isocenter, whereas the thermal component is relatively small. Of particular interest is the fact that for the Elekta accelerator no thermal component (or a very small one) is found at this measurement point, probably because the composition and geometry of its head differs significantly from the other LINACs. For the remaining accelerators, the presence of bigger thermal components is related to smaller treatment rooms.

The neutron fluence energy distributions obtained for the Siemens accelerators studied and operating at different energies are displayed in figure 7.14, for clarity. As expected, primary

Table 7.3. Summary of induced saturation activities for all sphere configurations and all points in the NEUTOR project 15 MeV LINACs

Sphere configuration	Saturation activity A^i_∞ $\left(\mathrm{Bq\,mg^{-1}}\right)$			
	Sevilla Bunker 1 (15 MV, **Siemens Primus**)		**Sevilla Bunker 2** (15 MV, **Siemens Primus**)	
	50 cm from ISO	Digital Device	50 cm from ISO	Digital Device
2.5"	29.19 ± 0.17	–	29.02 ± 0.35	12.35 ± 0.15
3"	38.01 ± 0.35	9.66 ± 0.16	38.57 ± 0.44	–
4.2"	50.83 ± 0.34	9.37 ± 0.20	50.53 ± 0.46	14.18 ± 0.26
5"	54.17 ± 0.39	7.58 ± 0.27	50.60 ± 0.64	13.17 ± 0.31
6"	49.03 ± 0.38	7.34 ± 0.14	47.32 ± 0.54	9.51 ± 0.15
8"	29.97 ± 0.26	3.16 ± 0.29	26.05 ± 0.40	5.52 ± 0.13
10"	15.88 ± 0.14	–	14.00 ± 0.22	2.243 ± 0.025
12"	7.345 ± 0.052	0.783 ± 0.054	7.10 ± 0.11	2.04 ± 0.22
2.5"+ Cd	24.75 ± 0.14	5.19 ± 0.17	24.87 ± 0.29	6.95 ± 0.18
3"+ Cd	33.39 ± 0.31	6.95 ± 0.20	33.25 ± 0.38	8.99 ± 0.14
4.2"+ Cd	48.57 ± 0.39	6.68 ± 0.33	45.97 ± 0.54	10.24 ± 0.17
	Puerta de Hierro (15 MV, **Varian Clinac 2100**)		**Ramón y Cajal** (15 MV, **Elekta Synergy**)	
	50 cm from ISO	Digital Device	50 cm from ISO	Digital Device
2.5"	76.2 ± 1.0	29.19 ± 0.32	29.58 ± 0.54	10.03 ± 0.11
3"	110.0 ± 1.2	32.39 ± 0.38	46.49 ± 0.46	12.26 ± 0.20
4.2"	146.6 ± 2.1	33.63 ± 0.52	62.26 ± 0.99	12.59 ± 0.14
5"	148.9 ± 1.9	30.38 ± 0.49	68.36 ± 0.95	10.32 ± 0.19
6"	138.1 ± 2.1	25.00 ± 0.40	62.12 ± 0.99	9.68 ± 0.11
8"	83.8 ± 1.3	12.16 ± 0.26	42.16 ± 0.70	4.944 ± 0.090
10"	33.48 ± 0.53	5.70 ± 0.19	22.80 ± 0.26	1.973 ± 0.056
12"	–	2.722 ± 0.060	11.41 ± 0.17	–
2.5"+ Cd	68.90 ± 0.92	11.08 ± 0.28	29.95 ± 0.33	7.589 ± 0.062
3"+ Cd	95.1 ± 1.4	21.24 ± 0.37	38.36 ± 0.47	9.56 ± 0.14
4.2"+ Cd	139.2 ± 1.2	25.84 ± 0.41	62.17 ± 0.75	10.61 ± 0.14

Table 7.4. Summary of induced saturation activities for all sphere configurations and all points in the València and Heidelberg NEUTOR project LINACs

Sphere configuration	Saturation activity $\mathbf{A}_{\infty,d} \pm \mathbf{\Delta A}_{\infty,d}$ $\left(\mathrm{Bq\,mg^{-1}}\right)$			
	València (18 MV, **Siemens Primus**)		**Heidelberg** (23 MV, **Siemens Mevatron**)	
	50 cm from ISO	Digital Device	50 cm from ISO	Digital Device
2.5"	62.77 ± 0.66	18.59 ± 0.50	97.2 ± 1.3	32.17 ± 0.47
3"	81.19 ± 0.76	27.88 ± 0.29	125.5 ± 1.7	32.45 ± 0.66
4.2"	105.9 ± 1.1	30.68 ± 0.30	176.5 ± 2.0	36.78 ± 0.62
5"	110.9 ± 1.2	23.20 ± 0.51	176.1 ± 2.2	34.56 ± 0.64
6"	100.6 ± 1.0	24.27 ± 0.33	168.6 ± 2.1	27.31 ± 0.60
8"	64.02 ± 0.42	11.26 ± 0.25	106.2 ± 1.4	11.35 ± 0.55
10"	34.21 ± 0.24	6.797 ± 0.093	51.86 ± 0.84	5.86 ± 0.035
12"	12.12 ± 0.14	2.951 ± 0.056	25.70 ± 0.40	3.85 ± 0.30
2.5"+ Cd	54.39 ± 0.58	17.70 ± 0.24	86.35 ± 0.76	23.71 ± 0.69
3"+ Cd	76.51 ± 0.70	18.80 ± 0.49	113.5 ± 1.6	25.17 ± 0.73
4.2"+ Cd	108.8 ± 1.0	25.87 ± 0.34	169.1 ± 2.2	29.39 ± 0.60

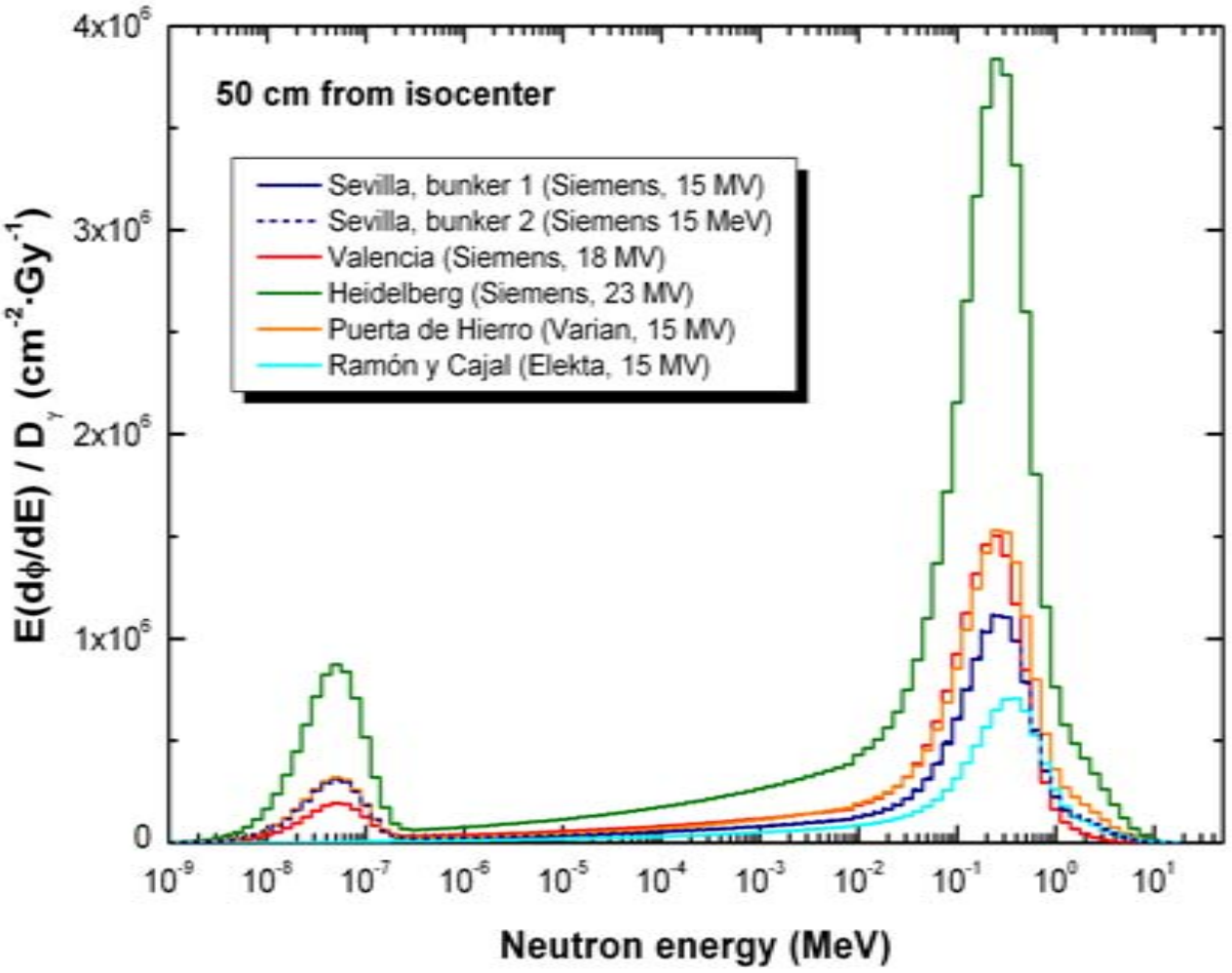

Figure 7.13. Experimental neutron spectra in lethargic representation, per Gy of photon irradiation, at $50cm$ from the isocenter for the different LINACs and rooms under study in the NEUTOR project

electron energy is the key parameter for neutron production when similar accelerators are compared. From the fact that spectra obtained for bunkers 1 and 2 in Sevilla are indistinguishable in practice, it is inferred that neutrons present at this measurement point (50 cm from isocenter) are mainly coming from the accelerator head, originated in the target or in materials surrounding it, and are not influenced by the geometry of the treatment room.

Conversely, shown in figure 7.15 are the neutron spectra obtained at 50 cm from the isocenter for the equal nominal energy (15 MV) LINACs studied. It results that the Varian Clinac accelerator is that originating more neutron contamination, followed by the Siemens Primus and the Elekta Synergy ones. These differences in neutron production arise from the structural disparities from one model to another and, in which respects the Elekta accelerator, are in agreement with the structure reported by [94].

Lethargy neutron spectra per unit fluence at 50 cm from the isocenter are presented in figure 7.16. The most prominent fact from this figure is that the spectra shown are almost independent on accelerator type and energy. All spectra display a maximum around 0.2 MeV, thus indicating that the neutron production mechanism is energy independent, confirming the prominence of an evaporation process in front of a direct neutron emission. Furthermore, this production mechanism does not depend on the specific geometry of the target irradiation nor on the primary electron energy. The small variation in the evaporation peak energy found for the Elekta LINAC in comparison to the others may also be explained as a consequence of the different target and surrounding material composition reported by [94].

Figure 7.17 represents the lethargy neutron spectra per Gy of photon irradiation at the place where the digital device stands, inside the different treatment rooms under study. In this place, the thermal component dominates over the less abundant fast component. However, distinct behaviours are observed for each of these components: while the fast component is more abundant when the accelerator nominal energy increases, as it was the case at 50 cm from the isocenter, the thermal component does not show this behaviour. Comparing spectra from Sevilla bunker 1 and bunker 2 irradiations it becomes clear that bunker size plays a prominent role on the neutron spectra at the place of the digital device. In fact, the fast component is bigger for the small bunker as the place of the digital device is closer to the accelerator target (distance inverse square law for the neutron direct component), and the thermal component is also bigger for the small bunker as bunker walls, where this component is mainly originated, are also closer to the accelerator target so that they receive a higher fluence of direct neutrons, which become then thermalised. The amount of thermal neutrons at the place of the digital device is, then, mainly affected by the irradiation room size, increasing for smaller rooms.

The unit lethargy neutron spectra at the Digital Device places are plotted in figure 7.18, where it is observed that these unit spectra are different one from each other, so that the contribution of thermal, intermediate and fast neutrons to the total fluence depends on the accelerator and room characteristics.

Finally, table 7.5 shows a summary of the global dosimetric quantities (neutron fluence, neutron dose equivalent, mean energy of the neutron spectrum, and effective energy of the spectrum, i.e. the energy averaged over dose) characterizing the neutron field at 50 cm from the isocenter and at the place of the digital device, obtained from the UAB passive Bonner sphere spectrometer measurements. It is apparent that both the neutron fluence and dose equivalent per monitor unit increase for increasing accelerator energies, indicating that neutron photoproduction rises with energy for constant photon production, as expected and in agreement

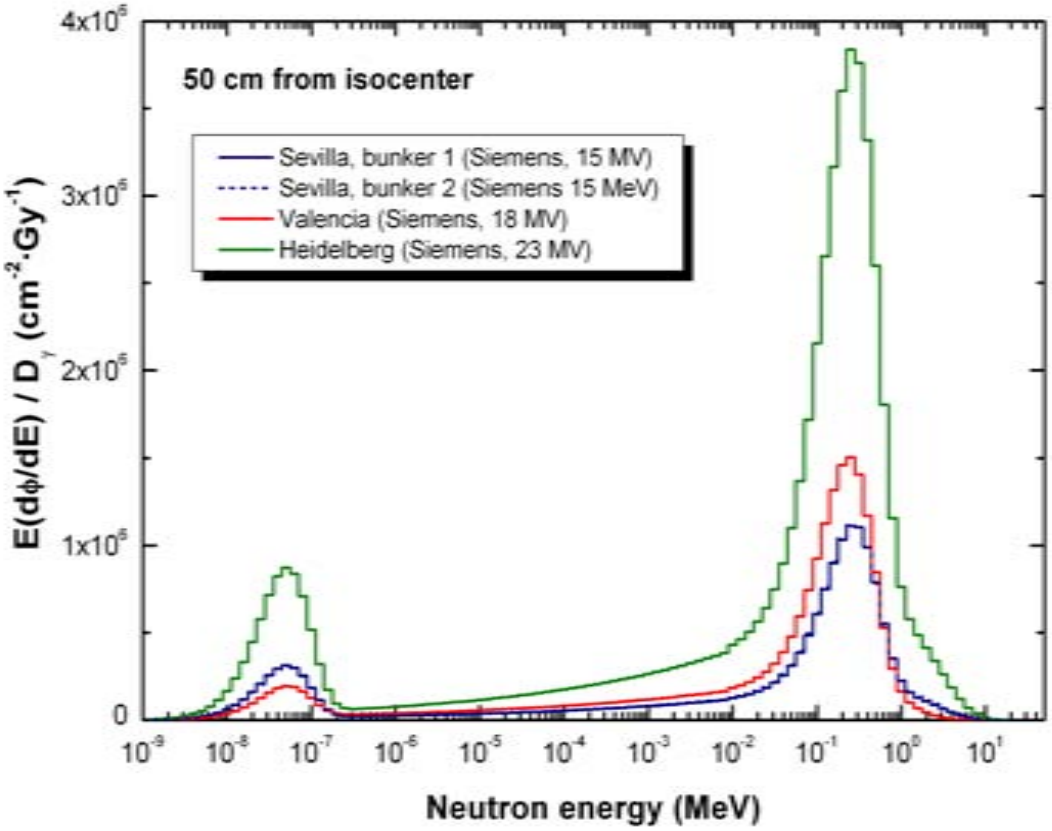

Figure 7.14. Experimental neutron spectra as in figure 7.13 for all Siemens LINACs under study to show the change in spectra as nominal energy varies

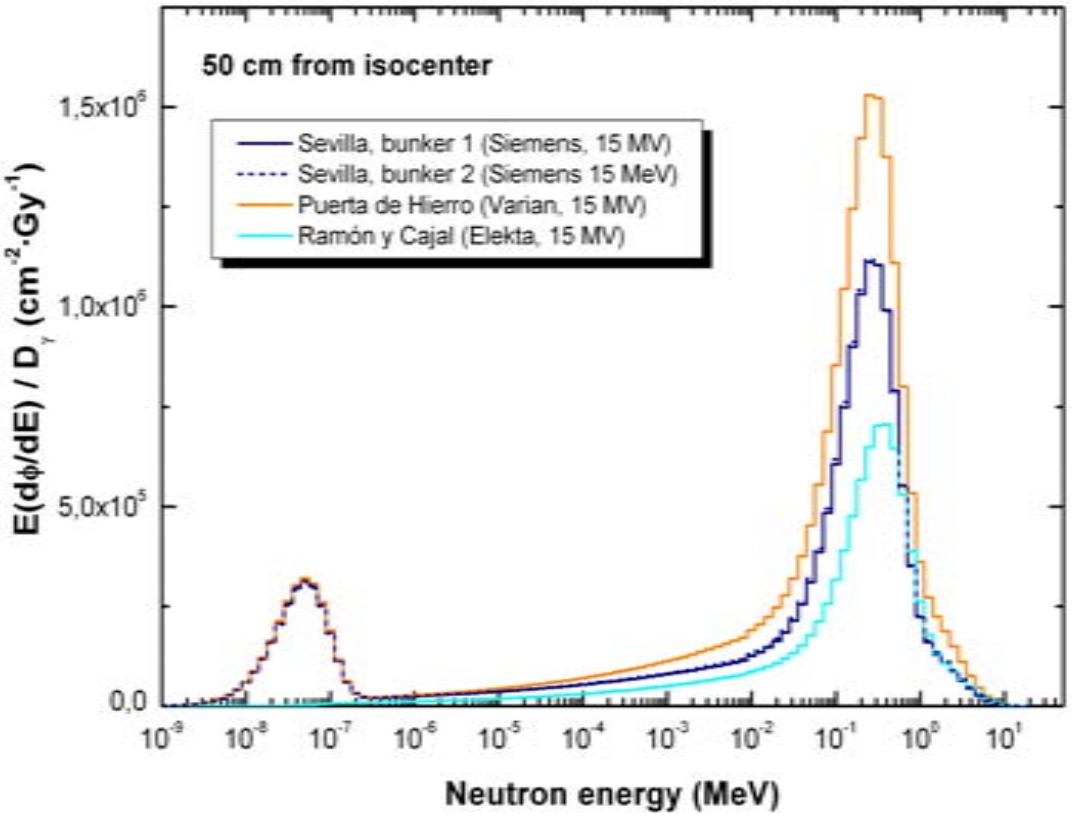

Figure 7.15. Experimental neutron spectra as in figure 7.13 for all LINACs under study with $15MV$ nominal energy, to see the effect in spectra of different makes

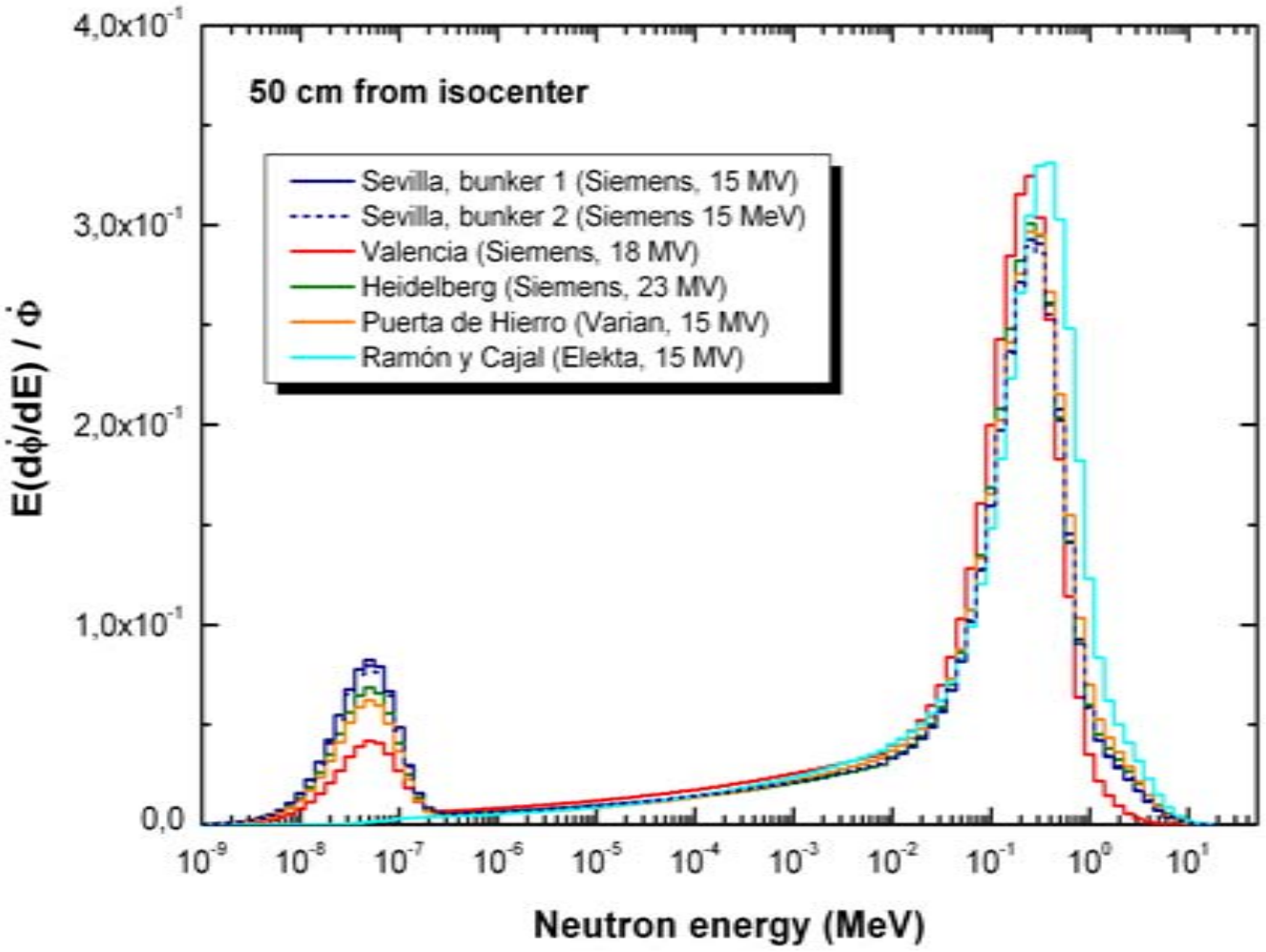

Figure 7.16. Experimental unit neutron spectra, in lethargic representation, at $50cm$ from the isocenter for the different LINACs and rooms under study in the NEUTOR project

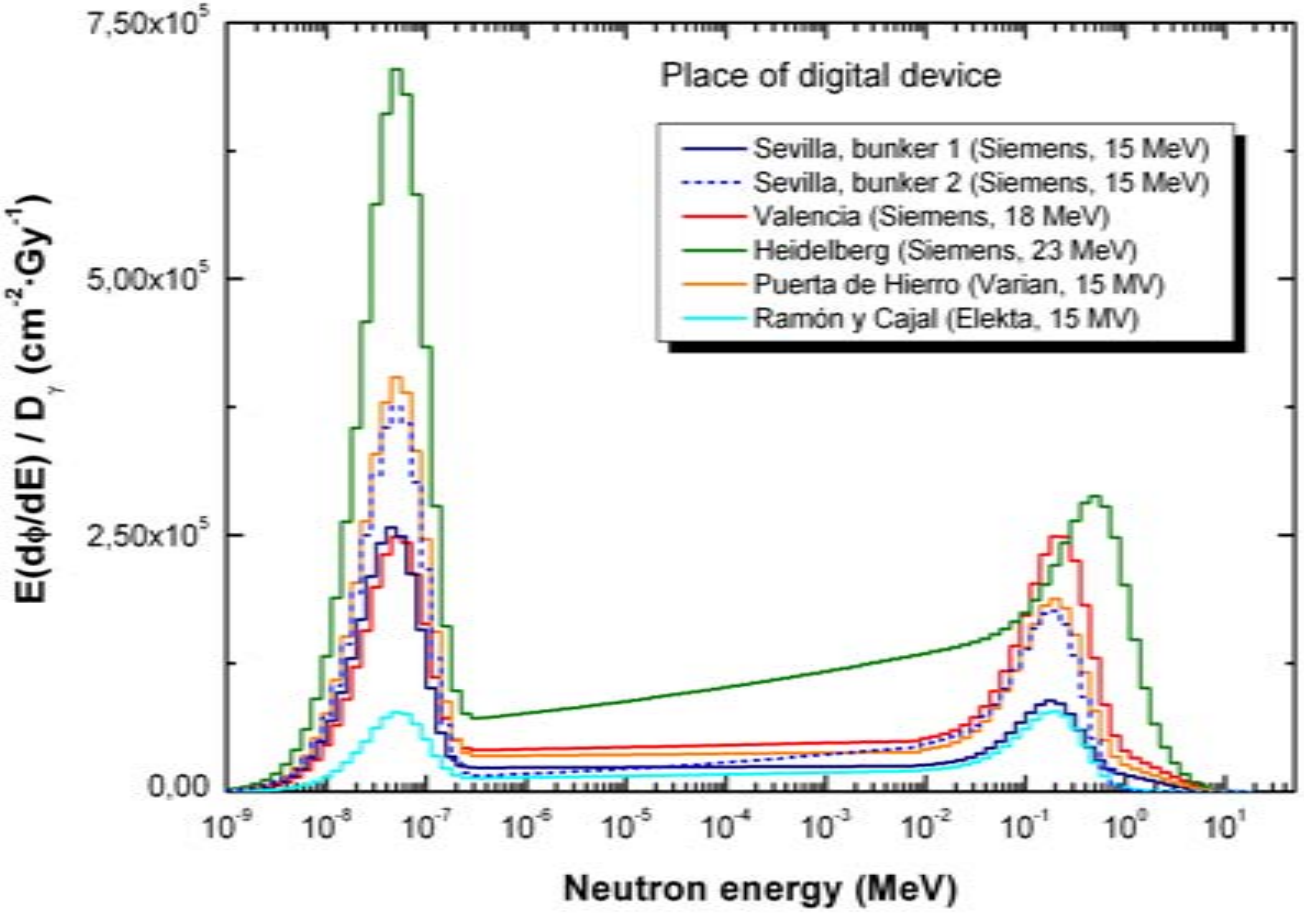

Figure 7.17. Experimental neutron spectra in lethargic representation, per Gy of photon irradiation, at the place of the digital device inside each LINAC treatment room studied

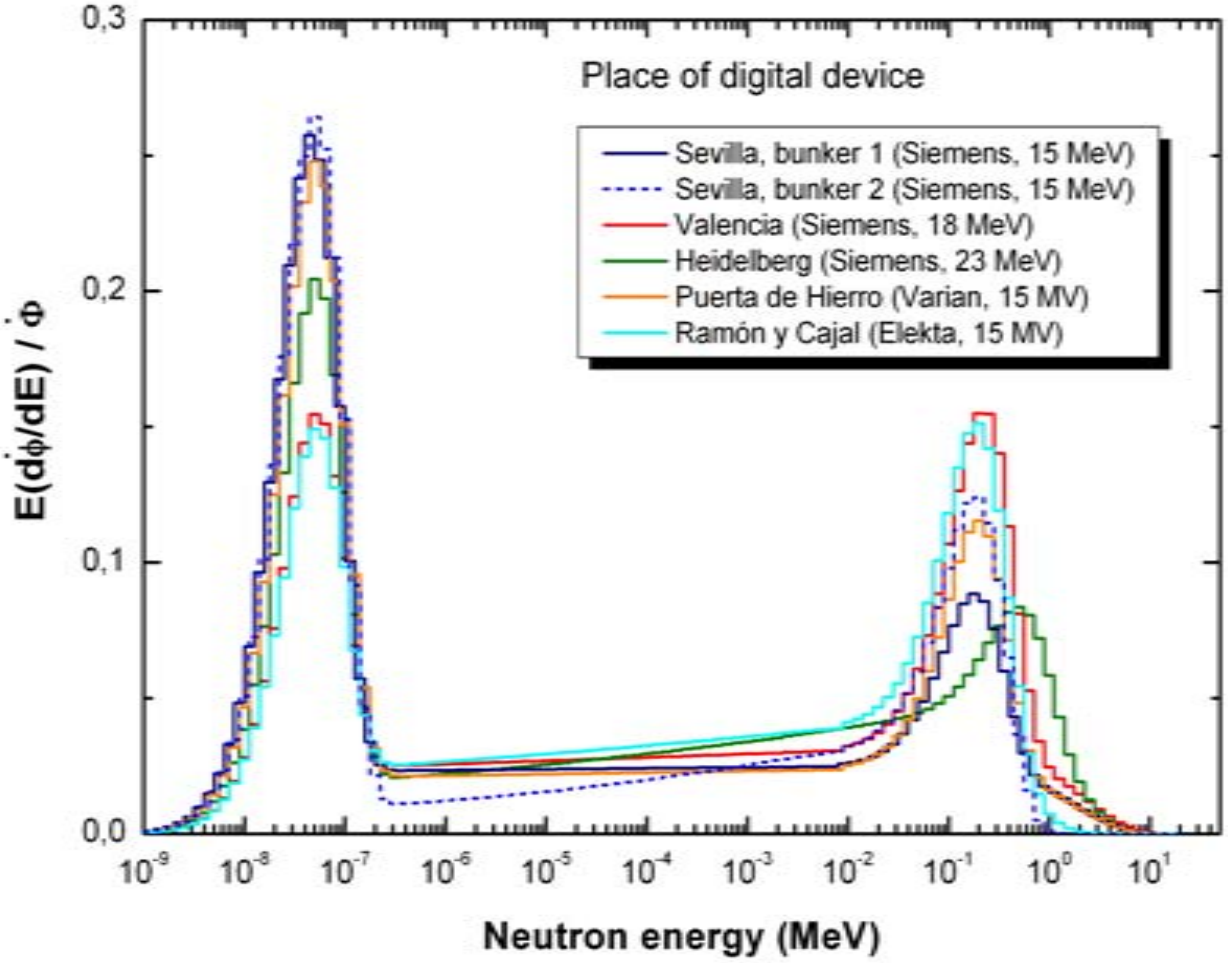

Figure 7.18. Experimental unit neutron spectra, in lethargic representation, at the place of the digital device place in each of the different LINAC rooms of the NEUTOR project

Table 7.5. Global dosimetric quantities obtained with the UAB passive BSS for the neutron fields at 50 cm from the isocenter (50 cm from ISO) and at the place of the digital device (Place of DD), for all the LINACs studied for the NEUTOR project. Fluence and ambient dose equivalent are normalised to unit prescribed dose. Also given are the mean energy and the effective energy of each neutron spectrum

	$\Phi\,(\mathrm{cm^{-2}Gy^{-1}})$	$H^*(10)\,(\mathrm{mSv\,Gy^{-1}})$	$\bar{E}_\Phi\,(\mathrm{MeV})$	$\bar{E}_{H^*}\,(\mathrm{MeV})$
Sevilla Bunker 1 (15 MV, **Siemens Primus**)				
50 cm from ISO	$(3.797 \pm 0.043) \times 10^6$	0.532 ± 0.019	0.27	0.61
Place of DD	$(1.001 \pm 0.015) \times 10^6$	0.0488 ± 0.0073	0.086	0.57
Sevilla Bunker 2 (15 MV, **Siemens Primus**)				
50 cm from ISO	$(3.864 \pm 0.038) \times 10^6$	0.539 ± 0.017	0.27	0.62
Place of DD	$(1.421 \pm 0.017) \times 10^6$	0.0640 ± 0.0075	0.048	0.22
València (18 MV, **Siemens Primus**)				
50 cm from ISO	$(4.632 \pm 0.044) \times 10^6$	0.595 ± 0.016	0.19	0.40
Place of DD	$(1.605 \pm 0.020) \times 10^6$	0.1188 ± 0.0015	0.14	0.57
Heidelberg (23 MV, **Siemens Mevatron**)				
50 cm from ISO	$(1.277 \pm 0.013) \times 10^7$	1.846 ± 0.053	0.29	0.66
Place of DD	$(3.446 \pm 0.044) \times 10^6$	0.2323 ± 0.0030	0.13	0.70
Puerta de Hierro (15 MV, **Varian Clinac 2100**)				
50 cm from ISO	$(5.157 \pm 0.15) \times 10^6$	0.769 ± 0.040	0.30	0.67
Place of DD	$(1.630 \pm 0.068) \times 10^6$	0.0873 ± 0.0067	0.086	0.48
Ramón y Cajal (15 MV, **Elekta Synergy**)				
50 cm from ISO	$(2.131 \pm 0.028) \times 10^6$	0.403 ± 0.012	0.42	0.77
Place of DD	$(0.518 \pm 0.028) \times 10^6$	0.0292 ± 0.0028	0.067	0.27

with the plot in figure 7.13. Nevertheless, the fact that unit spectra close to the isocenter are machine independent, with a maximum around 0.2 MeV, indicate that the neutron production mechanism is energy independent, confirming the prominence of an evaporation process in front of a direct neutron emission. In addition, the fact that effective energies are always bigger than mean energies puts into evidence that the dose contribution of low energy neutrons is small in front of that of higher energy neutrons, as inferred from the values of the fluence to dose conversion coefficients.

7.3. Measured neutron field around an unshielded PET cyclotron

7.3.1. Irradiation conditions

The study of the neutron field of an unshielded PET cyclotron has been performed in a cyclotron facility at the Clínica Universitaria de Navarra in Pamplona, Spain. The cyclotron, shown in figure 7.19, is a negative ion accelerator by Ion Beam Application Radioisotopes (IBA), model Cyclone 18/9, able to accelerate protons and deuterons up to 18 MeV and 9 MeV, respectively. The maximum charged particle current is 60 μA, with approximate extraction efficiencies

Table 7.6. Saturation activities for all sphere configurations irradiated in Point C inside the PET cyclotron vault, at the Clínica Universitaria de Navarra

Sphere configuration	Saturation activities in Point C A^i_∞ $\left(\mathrm{Bq\,mg^{-1}}\right)$
2.5”	2040 ± 14
3”	2559 ± 18
4.2”	3771 ± 27
5”	4160 ± 27
6”	3812 ± 25
8”	3052 ± 21
10”	1944 ± 14
12”	1271 ± 11
2.5”+ Cd	1828 ± 15
3”+ Cd	2452 ± 18
4.2”+ Cd	3472 ± 24

of 80% for protons and 60% for deuterons.

The cyclotron is located in the hospital basement and housed in a concrete vault ($480 \times 400 \times 363\,\mathrm{cm}^3$) with wall thicknesses ranging from 180 cm to 200 cm. The ceiling is 100 cm thick and the cyclotron vault is accessed through a 140 cm thick motor-driven concrete door. A floor plan of the bunker is given in figure 7.20. The sample preparation room next to the cyclotron vault where staff usually works while cyclotron operation is also shown in this figure.

In order to study the neutron field produced with this cyclotron, all the sphere configurations of the UAB passive BSS have been sequentially irradiated at a specific point (Point C in figure 7.19) inside the cyclotron vault, located 1 m away from the target in the same direction of the proton incident beam. All measurements have been performed while the cyclotron was producing ^{18}F by bombarding a water target enriched with ^{18}O, using a beam of 18 MeV protons with nominal current 30 μA. Each sphere has been irradiated until an integrated current of 5 μA h has reached the target, so irradiation times have been around 10 min. After irradiation, saturation activities have been measured and the neutron spectrum at Point C has been obtained through unfolding with FRUIT, using the PET radiation environment. Points A and B in figure 7.20 refer to measurement points outside the cyclotron vault where neutron spectra have been also determined with the UAB active BSS. The results obtained in these two out-vault points are beyond the scope of this work. More details can be found in [95].

7.3.2. Results

A summary of the induced saturation activities obtained from measurements at Point C is provided in table 7.6.

The neutron fluence spectrum obtained by unfolding these saturation activities is shown in figure 7.21, in lethargic representation. The spectrum displays a large peak around 1 MeV plus a thermal component and an important epithermal contribution, which combined with the 1 MeV peak results in the quite asymetric form of the spectrum. As it was expected, the shape of the spectrum is compatible with an evaporation model producing fast neutrons that are moderated by the cyclotron structures and the vault walls. Fast neutrons (above 100 k eV) are the major contribution to fluence, 56.9%, followed by the epithermal component, 34.2%,

Figure 7.19. The PET cyclotron in use at Clínica Universitaria de Navarra in Pamplona, Spain. It is a Cyclone 18/9 from the IBA company. The UAB passive Bonner spectrometer at the place of measurement can also be seen. On the left upper corner, a closer view of the irradiation geometry is displayed.

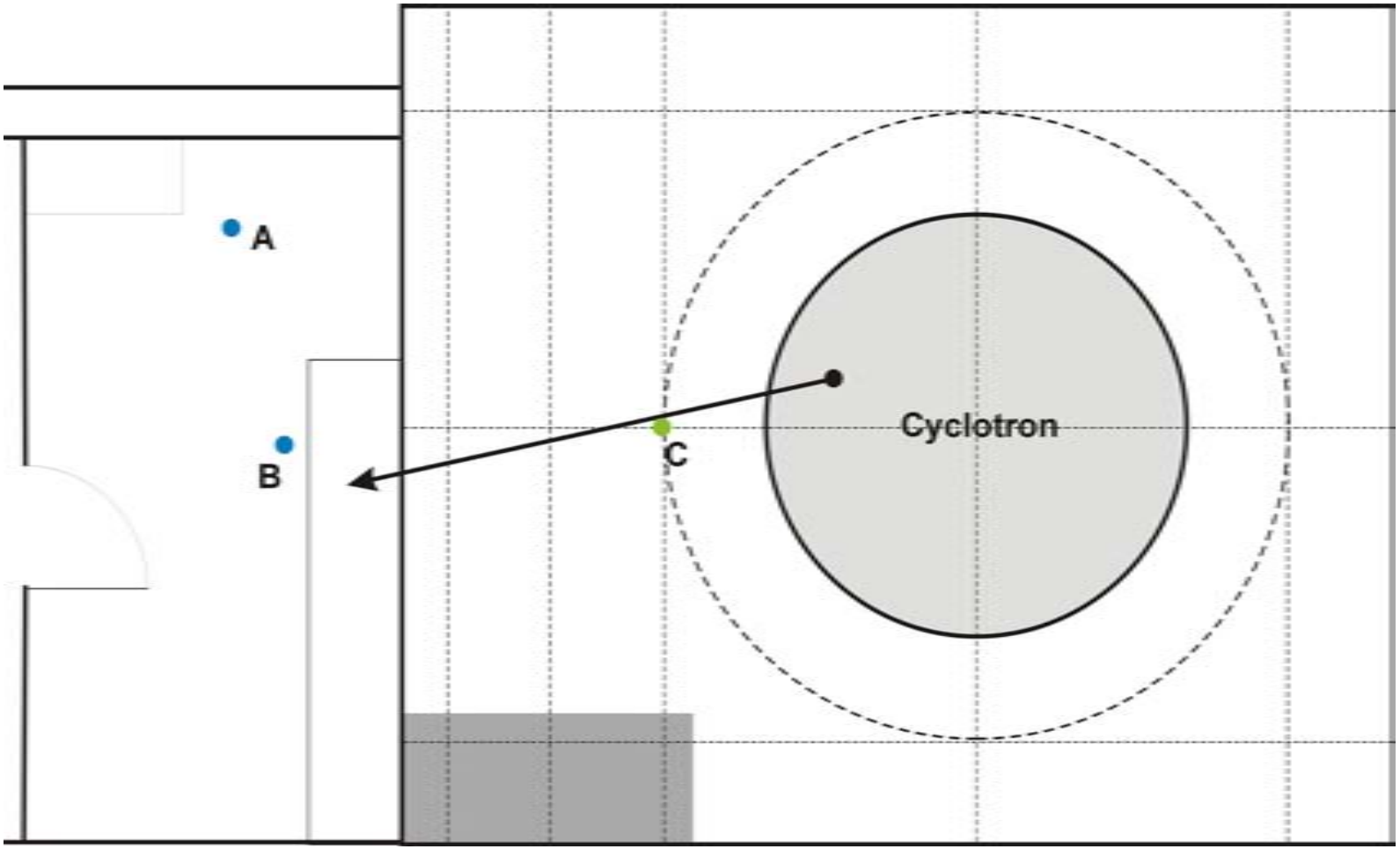

Figure 7.20. Floor plan of the PET cyclotron in use at Clínica Universitaria de Navarra in Pamplona, Spain.

Table 7.7. Global magnitudes of the neutron spectrum at Point C for the PET cyclotron in Clínica Universitaria de Navarra. Fluence and ambient dose equivalent are provided per second and per target integrated charge.

	Point C
$\Phi\left(\mathrm{cm}^{-2}\,\mathrm{s}^{-1}\right)$	$(1527 \pm 43) \times 10^4$
$\Phi\left(\mathrm{cm}^{-2}/\,\mu\mathrm{A}\cdot\mathrm{h}\right)$	$(1769 \pm 50) \times 10^6$
$H^*(10)\ \left(\mathrm{Sv\ h}^{-1}\right)$	10.96 ± 0.45
$H^*(10)\ \left(\mathrm{mSv}/\,\mu\mathrm{A}\cdot\mathrm{h}\right)$	353 ± 15
$\bar{E}_\Phi\ (\mathrm{MeV})$	1.0
$\bar{E}_{H^*}\ (\mathrm{MeV})$	2.0

and $\sim$ 9% thermal component. In terms of dose, 96% of it is delivered by the fast neutron component, explaining the hardness of the neutron spectrum at Point C.

The global dosimetric quantities associated to the measured neutron spectrum are provided in table 7.7. Fluence and ambient dose equivalent are also given in terms of charge integrated in the target. The values encountered are in agreement with those published by other authors ([96], [11], [97]).

7.4. Measured neutron field around a self-shielded PET cyclotron

7.4.1. Irradiation conditions

The cyclotron employed in the study of a self-shielded machine is a GE Medical System PETtrace cyclotron located at the Molecular Imaging Institute (M2i) in Keele, UK. To date, the cyclotron has been exclusively employed for the production of ^{18}F, used in the synthesis of [^{18}F]FDG for PET studies. On a typical run, around $1.4 - 2.2$ ml of ^{18}O enriched H_2O are irradiated for 90 min with 16 MeV protons (on target) and an average beam current of 50 mA, producing 150 G Bq of ^{18}F. The PETtrace cyclotron and its self-shielding, consisting of a series of polyethylene blocks (5 cm thick each one) placed around the target, can be seen in figure 7.22. These polyethylene blocks were not present in the unshielded PET cyclotron described in section 7.3..

The M2i self-shielded cyclotron is housed in a ($390 \times 486 \times 285\,\mathrm{cm}^3$) concrete vault with wall thicknesses between 30 cm and 179 cm and it is accessed through a maze with 2 bends, 81.5 cm wide. Three points inside the cyclotron vault have been selected to determine the associated neutron spectra, see figure 7.23 for clarity. The first place, labelled Point 1, can be seen in figure 7.24 and it is in direct sight from the target; Point 2 is close to the target but behind the polyethylene shielding, see figure 7.25; finally Point 3 is in the maze and shown in figure 7.26. The whole set of spheres of the UAB passive BSS have been irradiated in each point in dedicated exposures, so the activity of a total of 33 gold foils have been counted to determine their saturation activities. In each irradiation a proton beam of 15 MeV with a nominal current of 40 μA hitting the target during 10 min. On-target average integrated current has been 6.7 μA h. Neutron spectra at each point have been obtained by unfolding the saturation activities induced in the gold foils using the PET environment of the FRUIT code.

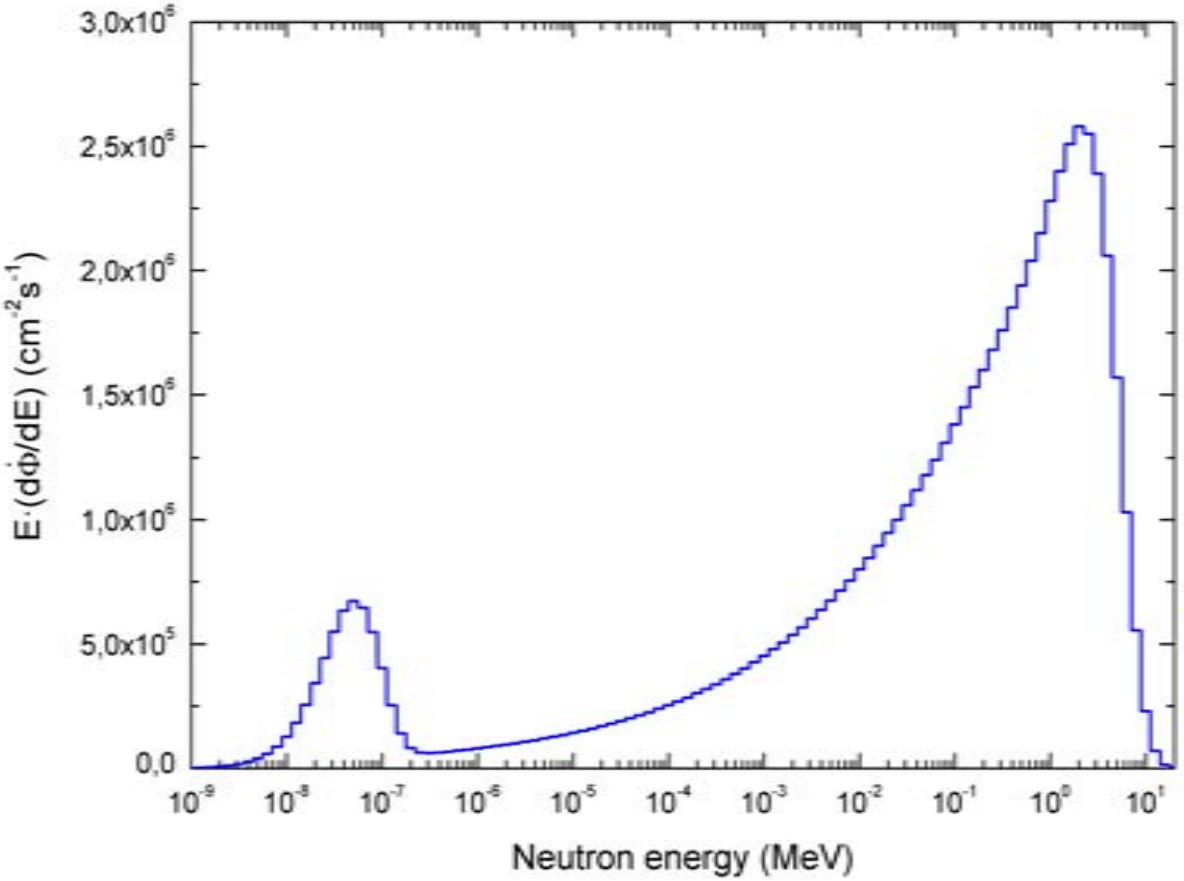

Figure 7.21. Experimental neutron spectra in lethargic representation at Point C place inside the cyclotron vault of Clínica Universitaria de Navarra

Figure 7.22. The GE medical PETtrace cyclotron of the M2i institute in Keele, UK. Enlarged views of the injection system and of the target are shown on the right, top and bottom, respectively.

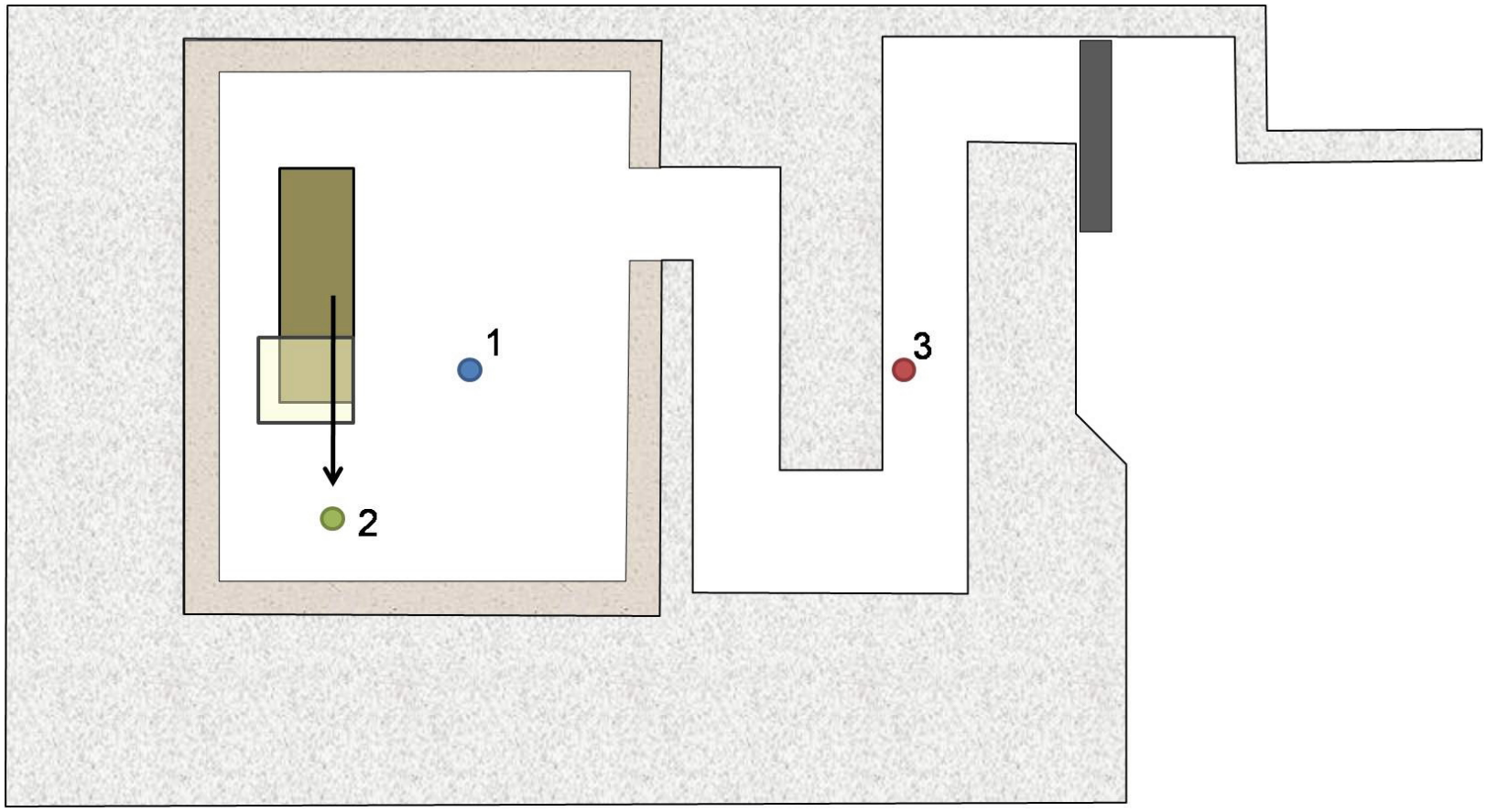

Figure 7.23. Schematic floor plan of the PETtrace cyclotron vault in the M2i Institute, Keele, UK. The arrow indicates the proton beam incidence direction. The white box overimposed on a brown box indicate the polyethylene shielding around the cyclotron, respectively.

Figure 7.24. View of the GE medical system PETtrace cyclotron and of the irradiation place Point 1, situated in direct view of the target with no polyethylene shielding.

Figure 7.25. View of the GE medical system PETtrace cyclotron and of the irradiation place Point 2, situated behind the polyethylene shielding and next to target.

Figure 7.26. View of the GE medical system PETtrace cyclotron and of the irradiation place Point 3, in the maze.

Table 7.8. Saturation activities for all sphere configurations irradiated in Points 1&2 inside the PETtrace cyclotron vault, at M2i Institute in Keele (UK)

Sphere configuration	A^i_∞ $\left(\mathrm{Bq\,mg^{-1}}\right)$ Point 1	Point 2
2.5”	2140 ± 18	880.7 ± 7.1
3”	2623 ± 20	972.7 ± 7.8
4.2”	3724 ± 29	1056.3 ± 8.2
5”	4003 ± 33	952.0 ± 6.1
6”	4129 ± 25	823.0 ± 7.4
8”	3417 ± 24	510.4 ± 4.4
10”	2322 ± 18	284.3 ± 2.3
12”	1542 ± 13	149.5 ± 1.3
2.5”+ Cd	1701 ± 12	565.3 ± 3.3
3”+ Cd	2310 ± 15	692.0 ± 5.9
4.2”+ Cd	3442 ± 24	852.2 ± 5.3

7.4.2. Results

The saturation activities measured for Points 1 and 2 around the PETtrace are shown in table 7.8. The saturation activities for Point 3 are not displayed as they are below the detection limit of the NaI(Tl) portable detector, which has been the only one used in this experimental campaign.

Table 7.9 summarizes the global dosimetric quantitys of the spectra found for the in-vault PETtrace places, Points 1 and 2. Results obtained for Point 1 are comparable to those encountered inside the vault at the Clínica Universitaria the Navarra, Point C, as both irradiation places are in direct view of the target with no further shielding. It should be noticed that the mean and effective energy obtained in Point 1 are almost the same than those obtained for the Clínica de Navarra unit. On the other hand, the values in Point 2, being smaller than in Point 1, confirm the effect of the polyethylene shielding. The decrease found in the total fluence and ambient dose equivalent, together with the lower values for the mean and effective energies when compared with Point 1, is a consequence of a degraded and softer neutron spectrum with smaller total fluence. For the third point under study, Point 3 placed in the maze, the total neutron fluence was below the detection limit of the UAB passive BSS. According to the procedure indicated in section 6.4., it is found that the neutron fluence in Point 3 is $\Phi^{\mathrm{P3}} \leq 8.6 \times 10^3\,\mathrm{cm^{-2}\,s^{-1}}$.

Neutron spectra obtained for Points 1 and 2 are presented in figure 7.27 in terms of lethargy and normalised to unit fluence rate. It can be observed that an important thermalisation of neutrons occur at Point 2 with respect to Point 1 due to the presence of the polyethylene shielding. This thermalisation was expected and it is indicated by the change in their mean and effective energies. In addition, spectra at both points display a main peak around 1 MeV, independently of the presence of shielding, confirming that neutrons are produced in the evaporation of the compound nuclei formed during irradiation.

Figure 7.28 displays the absolute value of the neutron fluence energy spectra (also in terms of lethargy) at Points 1 and 2. Again, the influence of the polyethylene shield is clear as, although the thermal component remains almost invariable for both points, the fast neutron component present at Point 1 has almost disappeared at Point 2. The fact that measurements obtained in Point 3 are below the detection limit confirms that both the polyethylene blocks

Table 7.9. Global magnitudes of the neutron spectrum at Points 1 and 2 for the PETtrace cyclotron in M2i Keele. Fluence and ambient dose equivalent are provided per second and per target integrated charge.

	Point P1	**Point P2**
$\Phi\left(\mathrm{cm}^{-2}\,\mathrm{s}^{-1}\right)$	$(1707 \pm 20) \times 10^4$	$(5063 \pm 56) \times 10^3$
$\Phi\left(\mathrm{cm}^{-2}/\,\mu\mathrm{A}\cdot\mathrm{h}\right)$	$(1529 \pm 18) \times 10^6$	$(4534 \pm 50) \times 10^5$
$H^*\,(10)\ \left(\mathrm{Sv\ h}^{-1}\right)$	13.53 ± 0.42	1.563 ± 0.075
$H^*\,(10)\ (\mathrm{mSv}/\,\mu\mathrm{A}\cdot\mathrm{h})$	337 ± 10	38.9 ± 1.9
$\bar{E}_\Phi\ (\mathrm{MeV})$	0.98	0.21
$\bar{E}_{H^*}\ (\mathrm{MeV})$	1.81	0.97

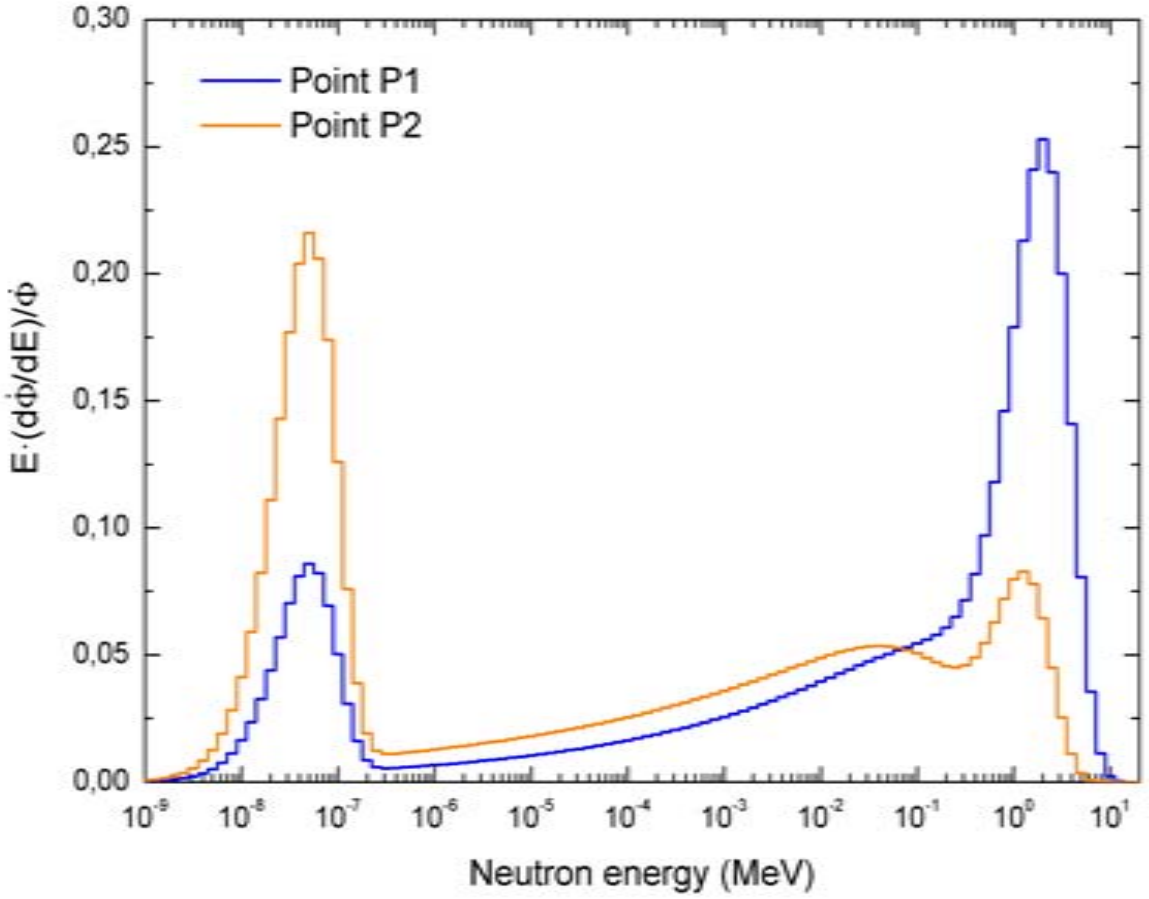

Figure 7.27. Experimental unit neutron spectra, in lethargic representation, at Points 1 and 2 inside the PETtrace cyclotron vault of the M2i Institute in Keele, UK.

and the maze geometry act as very good neutron shielding, as expected.

7.5. Conclusions

The UAB passive Bonner sphere spectrometer has been used in a measurement campaign that took place at the Hospital Plató in Barcelona for comparing the neutron ambient dose equivalent delivered in realistic 3D and IMRT radiotherapy treatments. Three points inside the treatment room have been monitored for the two treatment techniques:. It was found that, in a given measurement point, there is very small difference between the neutron spectra obtained for the 3D and IMRT treatments. This result indicates that the neutron production processes in both situations are the same and that the fraction of neutrons, which may originate in the multi-leaf collimator, does not depend in an appreciable way on the leaf's position.

The UAB passive BSS has also been chosen to measure the neutron spectra at several LINACs under different irradiation conditions, in two points inside the treatment room: at 50 cm from the isocenter and at the place where the digital device from the NEUTOR project is located. Global dosimetric quantities (fluence and ambient dose equivalent) have been obtained from these measurements. It has been found that unit neutron spectra near the isocenter do not depend on the accelerator energy, having a maximum around 0.2 MeV, and that neutron photoproduction increases with energy, as expected. In addition, it was found that, for LINACs operating at the same energy (15 MV) and in similar treatment rooms, the smallest neutron production was measured for the Elekta Synergy LINAC followed by the Siemens Primus and by the Varian Clinac 2100C. On the other hand, spectra at the place of the digital device are much dependent on the treatment room geometry and size, in addition to the characteristics of the accelerator. The UAB passive BSS has proved a good performance in the mixed photon/neutron fields present in LINAC facilities.

Cyclotrons dedicated to the production of short-lived radioisotopes for Positron Emission Tomography are usually installed in dedicated facilities near or inside medical imaging units. They produce complex workplace radiation fields with high intensities and mixing of different components, whose main contribution comes from neutrons. The complexity of the radiation fields discards the usage of active systems for the determination of the neutron fluence energy spectra and their associated magnitudes. The UAB passive BSS has been used to measure the neutron spectra present at different points around 2 PET cyclotrons, the first an unshielded cyclotron and, the second, a self-shielded one. Spectra and their global dosimetric quantities have been obtained for both PET cyclotrons consistently obtaining a harder spectrum for the unshielded cyclotron. The effect of the polyethylene shielding in the M2i Institute machine has also been clearly identified by the softer spectrum found in its Point 2. The high neutron fluence and ambient dose equivalent values found inside both vaults indicate that measurements with usual neutron monitors may not perform well in these environments due to saturation effects. In the self-shielded PET cyclotron facility, the total neutron fluence measured in the maze was below the detection limit of the UAB passive BSS ($8.6 \times 10^3\,\mathrm{cm^{-2}\,s^{-1}}$), indicating the adequacy of the facility design for radioprotection purposes.

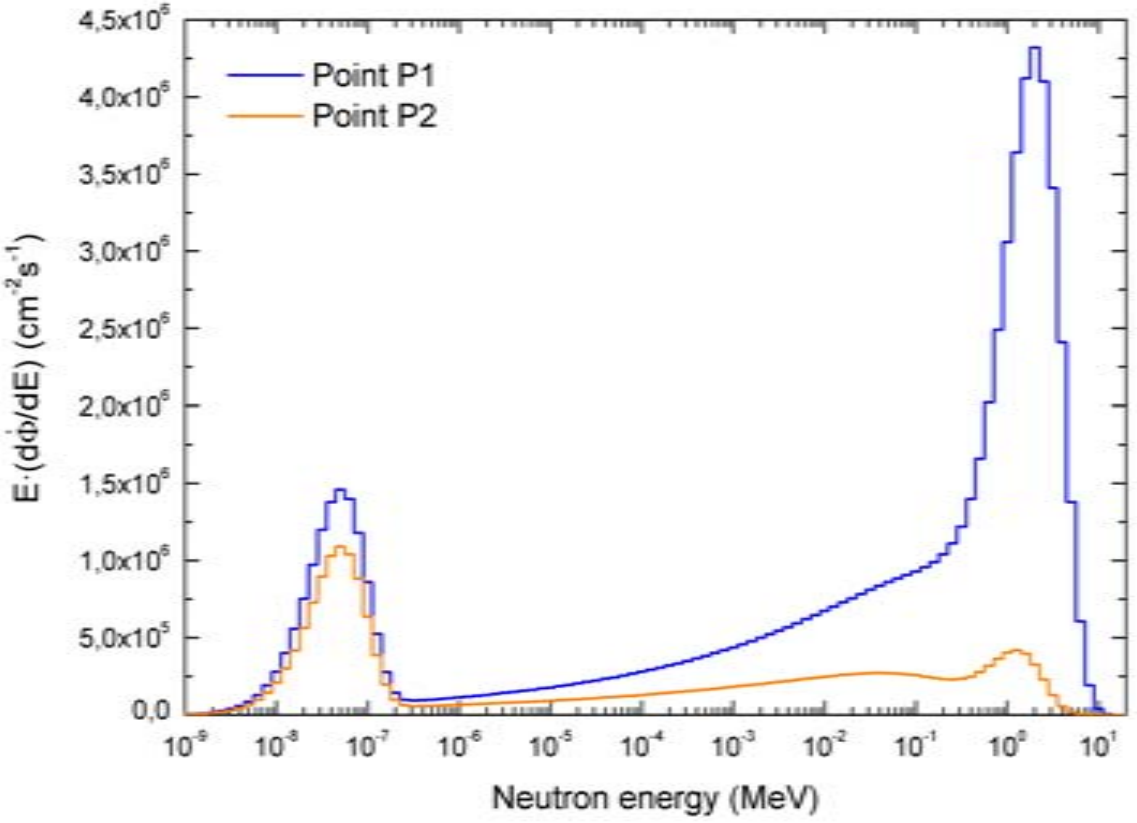

Figure 7.28. Experimental neutron spectra, in lethargic representation, at Points 1 and 2 inside the PETtrace cyclotron vault of the M2i Institute in Keele, UK.

CHAPTER 8.

Conclusions & Perspectives

8.1. Conclusions

The present work describes the design, characterisation and application of the new UAB neutron passive Bonner sphere spectrometer. This spectrometer is useful to perform experimental characterizations of complex and/or pulsed neutron fields in workplaces, where in addition they can be mixed with photons and where active detectors cannot be used. These fields include those generated in LINAC and PET medical facitilities as well as those generated in high energy research or industry accelerators. The main conclusions of this work are:

1. The response functions of the UAB passive Bonner sphere spectrometer, which has been completely designed and characterised in this work, have been simulated with the MCNPX^{TM} code using a realistic geometry and the most updated cross-sections.

2. The UAB passive BSS response functions do not depend on the irradiation geometry of the incident neutron beam and present an isotropic behaviour as no appreciable difference is found between the results for the three irradiation geometries (*isotropic*, *normal beam* and *parallel beam*) tested.

3. It was found from MCNPX simulations that the 0.4% relative uncertainty in the nominal polyethylene density value of the passive BSS spheres as provided by the manufacturer could be considered negligible. However, mass and dimensions of each gold foil used should always be well controlled for reducing measurement uncertainties.

4. The response functions have been tested experimentally and the best estimation of the calibration factor is $f_{\text{best}} = 0.988 \pm 0.033$, calculated from exposure of all the sphere-detector combinations of the UAB passive BSS to a reference ^{252}Cf ISO standard source at IRSN Cadarache (France).

5. The uncertainty of the response function matrix for the UAB passive BSS was estimated to be $\pm 3.2\%$. To do this, the accuracy of the response factors, $r_{i,\text{ref}}$, were calculated from the

measurements of the ISO ^{252}Cf neutron field at IRSN Cadarache for each sphere-detector combination. An average value 1.000 ± 0.032 was derived for all of them and its standard deviation is assumed to be the uncertainty associated to the contribution of the response matrix of the UAB passive BSS.

6. The monoenergetic neutron beams available at the AMANDE facility (IRSN Cadarache, France) were used to validate the UAB passive BSS response matrix. A total of 4 different energy beams were tested: 144 keV, 565 keV, 1.2 MeV and 5 MeV. The experimental results obtained with our spectrometer agree with the reference spectra provided by AMANDE for all sphere configurations and neutron energies.

7. A procedure to obtain this detection limit was defined taking into account the complex procedure, involving unfolding, required to obtain fluence rate estimations from the BSS measurements. Three different scenarios reflecting different irradiation, elapsed and measurement times were considered. The minimum detectable fluence rate, $\dot{\Phi}^{\mathrm{MD}}$, obtained for the average scenario condition is $3.3 \times 10^3\,\mathrm{cm^{-2}\,s^{-1}}$ for fixed NaI(Tl) detector and $8.3 \times 10^3\,\mathrm{cm^{-2}\,s^{-1}}$ for the portable one. The independence of these minimum detectable fluence rates from the physical model used for unfolding has been proved.

8. Several measurement campaigns were undertaken to determine the neutron spectra present at LINAC and PET facilities using the UAB passive Bonner sphere spectrometer. In one of these campaigns (Hospital Plató in Barcelona) it was found that, in a given measurement point, there is very small difference between the spectra and the global dosimetric quantities obtained for the 3D and IMRT radiotherapy treatments studied. This result indicates that the neutron production processes in both situations are the same, and that the fraction of neutrons which may originate in the multi-leaf collimator does not depend in an appreciable way on the leaf's position.

9. In another campaign, the neutron spectra at 6 LINACs of different makes, nominal energies, room (or bunker) geometries and sizes were measured with the UAB passive BSS. It has been found that unit neutron spectra near the isocenter do not depend on the accelerator energy, having a maximum around 0.2 MeV, and that neutron photoproduction increases with energy, as expected.

10. Spectra measured at the place of the digital device are much dependent on the treatment room geometry and size, in addition to the characteristics of the accelerator.

11. In the same campaign, it was found that, for LINACs operating at the same energy (15 MV) and in similar treatment rooms, the smallest neutron production was measured for the Elekta Synergy LINAC followed by the Siemens Primus and by the Varian Clinac 2100C.

12. The neutron spectra were measured at different points around 2 PET cyclotrons, one unshielded and another one self-shielded, showing that the effect of the polyethylene shielding of the second machine leads to a softer neutron spectrum, whereas a harder neutron spectrum was measured for the unshielded cyclotron.

13. The UAB passive BSS has proved a good performance in the PET cyclotron facilities, where active instruments cannot be used because of saturation and pulse pile-up effects given the extremely high neutron fluence rates present inside the vaults of the these facilities.

14. In the self-shielded PET cyclotron facility, the total neutron fluence measured in the maze was below the detection limit of the UAB passive BSS ($8.6 \times 10^3\,\mathrm{cm^{-2}\,s^{-1}}$), indicating the adequacy of the facility design for radioprotection purposes.

8.2. Perspectives

As commented in section 3.2. the range of application of any Bonner sphere spectrometer can be extended into the high-energy region (above 20 MeV) by adding several spheres with inner metallic shells. Following this procedure, two new configurations have been designed and constructed by our group which are based on a 7 in polyethylene sphere which can incorporate lead and copper shells, 1 in thick, inside. An important difficulty is that no reference high energy neutron field, allowing to validate the response functions of the new configurations, is yet defined. In fact, high-energy fields available are not fully characterised, although important international efforts are in progress in order to establish standards for high-energy neutron spectra evaluation. Our group is participating in this field through the EURADOS organisation. The extended range UAB Bonner sphere spectrometers will be of great utility to characterize the neutron spectra induced by cosmic rays in the atmosphere, i.e. at different altitudes or during large duration transoceanic flights, as well as those produced at high-energy particle accelerators, syncrotrons and cyclotrons. In addition, proton- and hadron-therapy beams produce complex neutron fields with an important high energy component. Extension of the range of validity of our Bonner sphere spectrometers to high energy neutrons will allow them to be used in these fields. Characterising all these types of neutron spectra is of key importance to study the possible operating failures and defects induced by these neutrons in electronic circuits and to quantify the subsequent potential radiological risk for the working staff and for the patients.

References

[1] NCRP, Neutron Contamination from Medical Electron Accelerators, National Council on Radiation Protection and Measurements, Bethesda, MD (1984).

[2] N. Bohr, Neutron capture and nuclear constitution, Nature 137 (1936) 344–348.

[3] V. Weisskopf, Statistics and nuclear reactions, Physical Review (52) (1937) 295–303.

[4] K. Schmidt, Deexcitation mechanisms in compound nucleus reactions. http://fpsalmon.usc.es/genp/doc/escuela230309/Compound-Nucleus.pdf.

[5] R. McCall, T. Jenkins, R. Shore, Transport of accelerator produced neutrons in a concrete room, IEEE Transactions on Nuclear Science NS-26 (1) (1979) 1593–1602.

[6] C. M. Eisenhauer, R. B. Schwartz, T. Johnson, Measurement of neutrons reflected from the surfaces of a calibration room, Health Physics 42 (4) (1982) 489.

[7] D. S. Followil, M. S. Stovall, S. F. Kry, G. S. Ibbott, Neutron source strength measurements for varian, siemens, elekta, and general electric linear accelerators, J. Appl. Cli. Med. Phys. 4 (3) (2003) 189–194.

[8] IAEA, Cyclotron Produced Radionuclides: Physical Characteristics and Production Methods, International Atomic Energy Agency, Vienna, Austria (2009).

[9] IAEA, Directory of Cyclotrons Used for Radionuclide Production in Member States: 2006 Update, International Atomic Energy Agency, Vienna, http://www-naweb.iaea.org/napc/iachem/cyclotrons/PDF/DCRP.pdf (2006).

[10] S. Qaim, Nuclear data relevant to the production and application of diagnostic radionuclides, Radiochim. Acta 89 (2001) 223–232.

[11] R. Gallerani, G. Cicoria, E. Fantuzzi, M. Marengo, D. Mostacci, Neutron production in the operation of a 16.5 MeV PETrace cyclotron, Progress in Nuclear Energy 50 (2008) 939–943.

[12] J. Chadwick, The existence of a neutron, Proceedings of the Royal Society A 136 (1932) 692–708.

[13] J. Turner, Atoms, Radiation and Radiation Protection, 2nd Edition, John Wiley and Sons, 1995.

[14] G. Knoll, Radiation Detection and Measurement, 3rd Edition, John Wiley Sons, Inc., Michigan, USA, 1999.

[15] P. Coll, Fundamentos de Dosimetría Teórica Y Protección Radiológica, Vol. II, Edicions UPC, 1990.

[16] E. Segré, Nuclei and Particles an Introduction to Nuclear and Subnuclear Physics, 2nd Edition, Addison-Wesley, 1982.

[17] D. Blanc, Les Rayonnements Ionisants; Détection, Spectrométrie, Dosimétrie, Physique Fondamentale et Appliquée, Masson, 1990.

[18] D. Thomas, H. Klein, Introduction, Radiation Protection Dosimetry 107 (1-3) (2003) 13–21.

[19] ICRP, 1990 recommendations of the international commission on radiological protection, Publication 60 (1991) .

[20] ICRP, The 2007 recommendations of the international commission on radiological protection, Publication 103 (2007) .

[21] ICRP, Conversion coefficients for use in radiological protection against external radiation, Publication 74 (1995) .

[22] ICRU, Quantities and units in radiation protection dosimetry, Report 51 (1993) .

[23] ICRU, Conversion coefficients for use in radiological protection against external radiation, Report 57 (1998) .

[24] ICRU, Determination of operational dose equivalent quantities for neutrons, Report 66 (2001) .

[25] R. Tanner, C. Molinos, N. Roberts, D. Bartlett, L.G.Hager, L. Jones, G. Taylor, D. Thomas, Practical implications of neutron survey instrument performance, Tech. Rep. HPA-RPD-016, Health Protection Agency, Radiation Protection Division (2006).

[26] A. Alevra, Neutron spectrometry, Radioprotection 34 (3) (1999) 305–333.

[27] J. Chadwick, Adventures in Experimental Physics, World Science Education, Princeton, 1972.

[28] F. Brooks, H. Klein, Neutron spectrometry - historical review and present status, Nuclear Instruments and Methods in Physics Research A 476 (476) (2002) 1–11.

[29] H. Tagziria, W. Hansen, Neutron spectrometry in mixed fields: Proportional counters spectrometers, Radiation Protection Dosimetry 107 (1-3) (2003) 73–93.

[30] H. Klein, Neutron spectrometry in mixed fields: NE213/BC501A liquid scintillation spectrometers, Radiation Protection Dosimetry 107 (1-3) (2003) 95–109.

[31] M. Bakali, Espectrometría neutrónica en las centrales nucleares mediante un sistema de esferas bonner, Ph.D. thesis, Universitat Autònoma de Barcelona, (In spanish) (2001).

[32] F. D'Errico, M. Matzke, Neutron spectrometry in mixed fields: Superheated drop (bubble) detectors, Radiation Protection Dosimetry 107 (1-3) (2003) 111–124.

[33] E.-V. R. . Data, Http://www.nndc.bnl.gov/point2004/.

[34] R. Bramblett, R. Ewing, T. Bonner, A new type of neutron spectrometer, Nuclear Instruments and Methods 9 (1960) 1–12.

[35] D. Thomas, A. Alevra, Bonner sphere spectrometers - a critical review, Nuclear Instruments and Methods in Physics Research A 476 (2002) 12–20.

[36] A. Alevra, D. Thomas, Handbook on neutron and photon spectrometry techniques for radiation protection, Radiation Protection Dosimetry 107 (1-3) (2003) 37–72.

[37] A. Alevra, V. Plostinaru, Characteristaion of the IPNE bonner sphere spectrometer by comparison with the PTB system, Nuclear Instruments and Methods in Physics Research A 476 (2002) 21–25.

[38] V. Lacoste, V. Gressier, J.-L. Pochat, F. Fernández, M. Bakali, T. Bouassoule, Characterisation of bonner sphere systems at monoenergetic and thermal neutron fields, Radiation Protection Dosimetry 110 (1-4) (2004) 529.

[39] D. Thomas, A. Bardell, E. Macaulay, Characterisation of a gold foil-based bonner sphere set and measurements of a neutron spectra at a medical accelerator, Nuclear Instruments and Methods in Physics Research A 476 (2002) 31–35.

[40] R. Bedogni, Neutron spectrometry and dosimetry for radiation protection around a high energy electron/positron collider, Ph.D. thesis, Universitat Autònoma de Barcelona (July 2006).

[41] C. Wang, T. Blue, A neutron spectrometer for neutrons with energies between 1eV and 10keV, Nuclear Instruments and Methods A 290 (1990) 237–241.

[42] A. Aroua, M. Grecescu, S. Prêtre, J.-F. Valley, Improved neutron spectrometer based on bonner spheres, Radiation Protection Dosimetry 70 (1-4) (1997) 285–289.

[43] B. Wiegel, A. Alevra, NEMUS - the PTB NEutron MUltisphere spectrometer: Bonner spheres and more, Nuclear Instruments and Methods 476 (1-2) (2002) 36–41.

[44] V. Kryuchkov, G. Semenova, Neutron responses for sphere spectrometer, IHEP Preprint, in Russian (1987).

[45] H. Hsu, K. Alvar, D. Vasilik, A new bonner-sphere set for high energy neutron measurements - monte carlo simulation, IEEE Transactions on Nuclear Science 41 (1994) 938–940.

[46] C. Birattari, A. Esposito, A. Ferrari, M. Pelliccioni, T. Rancati, M. Silari, The extended range neutron rem counter LINUS: Overview and latest developments, Radiation Protection Dosimetry 76 (1998) 135–148.

[47] M. Matzke, Unfolding of Pulse Height Spectra: The HEPRO Program System, Braunschweig: Physikalisch-Technische Bundesanstalt (1994).

[48] M. Matzke, Unfolding procedures, Radiation Protection Dosimetry 107 (1-3) (2003) 155–174.

[49] M. Reginatto, Bayesian approach for quantifying the uncertainty of neutron doses derived from spectrometric measurements, Radiation Protection Dosimetry 121 (1) (2006) 64–69.

[50] M. Reginatto, P. Goldhagen, MAXED, a computer code for maximum entropy deconvolution of multisphere neutron spectrometer data, Health Physics 77 (5) (1999) 583–589.

[51] E. Cordes, G. Fehrenbacher, R. Schutz, M. Sprunck, K. Hahn, R. Hofmann, W. Biersack, J. P.and Wahl, An approach to unfold the response of a multi-element system using an artificial neural network, IEEE Transactions on Nuclear Science 45 (3) (1998) 1464–1469.

[52] D. W. Freeman, D. R. Edwards, A. E. Bolon, Genetic algorithms - a new technique for solving the neutron spectrum unfolding problem, Nuclear Instruments and Methods A 425 (3) (1999) 549–576.

[53] S. Avdic, S. A. Pozzi, V. Protopopescu, Detector response unfolding using artificial neural networks, Nuclear Instruments and Methods A 565 (2) (2006) 742–752.

[54] B. Mukherjee, BONDI-97: A novel neutron energy spectrum unfolding tool using a genetic algorithm, Nuclear Instruments and Methods A 432 (2-3) (1999) 305–312.

[55] M. Tomás, F. Fernández, M. Bakali, , H. Muller, MITOM: A new unfolding code based on a spectra model method applied to neutron spectrometry, Radiation Protection Dosimetry 110 (1-4) (2004) 545–548.

[56] F. Fernández, C. Domingo, K. Amgarou, J. Castelo, T. Bouassoule, M. Garcia, E. Luguera, Neutron measurements in a varian 2100c LINAC facility using a bonner sphere system based on passive gold activation detectors, Radiation Protection Dosimetry 126 (1-4) (2007) 361–365.

[57] R. Bedogni, C. Domingo, E. Esposito, F. Fernández, FRUIT: An operational tool for multisphere neutron spectrometry in workplaces, Nuclear Instruments and Methods A 580 (3) (2007) 1301–1309.

[58] R. Bedogni, C. Domingo, A. Esposito, M. Chiti, M. García-Fusté, G. Lovestam, Testing bonner sphere spectrometers in the JRC-IRMM mono-energetic neutron beams, Nuclear Instruments and Methods A in press (doi:10:1016/j.nima.2010.04.019).

[59] ISO, Reference neutron radiations - part 2: Calibration fundamentals of radiation protection devices related to the basic quantities characterizing the radiation field, Guide 8529-2 (2000) .

[60] F. Fernández, M. Bakali, M. Tomás, H. Muller, J. L. Pochat, Neutron measurements in the vandellòs II nuclear power plant with a bonner sphere system, Radiation Protection Dosimetry 110 (1-4) (2004) 517–521.

[61] F. Fernández, C. Domingo, K. Amgarou, T. Bouassoule, M. J. García, Neutron measurements in spanish nuclear power plants with a bonner sphere spectrometer system, Radiation Protection Dosimetry 126 (1-4) (2007) 355–360.

[62] E. Measures, Compteur he-3 notice technique, Tech. rep., Eurysis Measures (1998).

[63] R. Caizergues, G. Poullot, Calcul de la reponse de sphères de bonner pour les détecteurs LiI, he et mn, Tech. Rep. CEA-R-4400, Commissariat a lŠEnergie Atomique, Centre dŠEtudes Nucleaires de Saclay, Gif-sur-Yvette (1972).

[64] Los Alamos National Laboratory, New Mexico, MCNP-B. A General Monte Carlo N-Particle Transport Code Version 4B (1997).

[65] F. D'Errico, A. Bos, Passive detectors for neutron personal dosimetry: State of the art, Radiat. Prot. Dosim. 110 (1-4) (2004) 195–200.

[66] K. Amgarou, Study of thermal neutron activation materials, Tech. Rep. DRPH/SDE 2006-09, Institut de Radioprotection et de Sûreté Nucléaire (2006).

[67] K. Amgarou, C. Domingo, T. Bouassoule, F. Fernández, Monte carlo simulation of the NaI(Tl) detector response to measure gold activated foils, Nuclear Instruments and Methods B 267 (17) (2009) 2944–2951.

[68] J. Castelo, Flujo neutrónico en los aceleradores lineales de electrones para radioterapia, Ph.D. thesis, Universitat Autònoma de Barcelona (2010).

[69] K. Lowry, T. Johnson, The effect of the choice of response matrix on neutron spectra unfolded from bonner sphere data, Health Physics 50 (4) (1986) 543–547.

[70] L. Waters, MCNPXTM Users Manual, ECI, Version 2.4.0, Los Alamos National Laboratory (2002).

[71] W. Engle, User Manual for ANISN, a One Dimensional Discrete Ordinates Transport Code with Anisotropic Scattering, AEC Research and Development (1967).

[72] Los Alamos National Laboratory, MCNP-A. A General Monte Carlo Code N-Particle Transport Code Version 4A (1993).

[73] K. Amgarou, MCNPX response matrix calculations of the IRSN passive bonner sphere system, Tech. Rep. DRPH/SDE nž2007-24, Institut de Radioprotection et de Sûreté Nucléaire (2007).

[74] H. Klein, Results of a large scale neutron spectrometry and dosimetry comparison exercise at the cadarache moderator assembly, Radiation Protection Dosimetry 70 (1-4) (1997) 313–322.

[75] A. Alevra, B. Siebert, Influence of Neutron Spectra and Fluence Response Data on the Determination of Dose Equivalent with Bonner Spheres, Braunschweig: Physikalisch-Technische Bundesanstalt (1986).

[76] ISO, Reference neutron radiations - part 1: Characteristics and methods of production, Guide 8529 (2001) .

[77] N. Magalotti, Modelling of the Neutron Source of the IRSN Van Gogh Irradiator: Cf-252 Source, IRSN (2005).

[78] L. Currie, Limits for qualitative detection and quantitative determination. application to radiochemistry, Analytical Chemistry 40 (3) (1968) 586–593.

[79] I. Zvara, P.Povinec, I. Sykora, Determination of very low levels of radioactivity, Tech. Rep. 12, International Union of Pure and Applied Chemistry (IUPAC) (1994).

[80] F. Kamangar, G. Dores, W. Anderson, Patterns of cancer incidence, mortality, and prevalence across five continents: Defining priorities to reduce cancer disparities in different geographic regions of the world, J. Clin. Oncol. 24 (2006) 2137–2150.

[81] D. M. Parkin, F. Bray, J. Ferlay, P. Pisani, Global cancer statistics, 2002, CA Cancer J. Clin. 55 (2) (2005) 74–108.

[82] H. Frankish, 15 million new cancer cases per year by 2020, says WHO, The Lancet 361 (9365) (2003) 1278–1278.

[83] X. Xu, B. Bednarz, H. Paganetti, A review of dosimetry studies on external-beam radiation treatment with respect to second cancer induction, Phys. Med. Biol. 53 (2008) R193–R241.

[84] L. Travis, D. Hill, G. Dores, M. Gospodarowicz, F. Van Leeuwen, E. Holowaty, B. Glimelius, M. Andersson, T. Wiklund, C. Lynch, M. Van't Veer, I. Glimelius, H. Storm, E. Pukkala, M. Stovall, R. Curtis, J. Boice, E. Gilbert, Breast cancer following radiotherapy and chemotherapy among young women with hodgkin disease, JAMA 290 (2003) 465–475.

[85] A. Chaturvedi, E. Engels, E. Gilbert, B. Chen, H. Storm, C. Lynch, P. Hall, F. Langmark, E. Pukkala, M. Kaijser, M. Andersson, S. Fosså, H. Joensuu, J. Boice, R. Kleinerman, L. Travis, Second cancers among 104760 survivors of cervical cancer: Evaluation of long term risk, JCNI 99 (2007) 1634–1643.

[86] M. Kara Bucci, A. Bevan, M. Roach, Advances in radiation therapy: Conventional to 3d, to IMRT, to 4d and beyond, CA Cancer J. Clin 55 (2005) 117–134.

[87] S. Kry, M. Salehpour, D. Followill, M. Stovall, D. Kuban, R. White, I. Rosen, Out-of-field photon and neutron dose equivalents from step-and-shoot intensity-modulated radiation therapy, Int. J. Radiat. Oncol. Biol. Phys. 62 (2005) 1204–1216.

[88] R. Howell, M. Ferenci, N. Hertel, G. Fullerton, Investigation of secondary neutron dose for 18 MV dynamic MLC IMRT delivery, Med. Phys. 32 (3) (2005) 786–793.

[89] R. Howell, N. Hertel, Z. Wang, J. Hutchinson, G. Fullerton, Calculation of effective dose from measurements of secondary neutron spectra and scattered photon dose from dynamic MLC IMRT for 6 MV, 15 MV, and 18 MV beam energies, Med. Phys. 33 (2006) 360–368.

[90] F. Gómez, A. Iglesias, F. Sánchez-Doblado, A new active method for in-room measurement of neutron fluence in modern radiotherapy, Nuclear Instruments and Methods in Physics Research Section A (2010) submitted.

[91] F. Gómez, A. Iglesias, F. Sánchez-Doblado, C. Domingo, Active on-line detector for in-room radiotherapy neutron measurements, Radiation Measurements (2010) submitted.

[92] J. Pena, L. Franco, F. Gómez, A. Iglesias, J. Pardo, M. Pombar, Monte carlo study of siemens PRIMUS photoneutron production, Physics in Medicine and Biology 50 (2005) 5921–5933.

[93] C. Domingo, M. García-Fusté, E. Morales, K. Amgarou, J. Terrón, J. Roselló, L. Brualla, L. Nuñez, R. Colmenares, F. Gómez, G. Hartmann, F. Sánchez-Doblado, F. Fernández, Neutron spectrometry and determination of neutron ambient dose equivalents in different LINAC radiotherapy rooms, Radiation Measurements (2009) submitted.

[94] S. Martínez, R. Barquero, F. Sánchez-Doblado, C. Domingo, M. Romero, J. Gómez-Ros, A. Lallena, Reduction of neutron production in new accelerators for radiotherapy, Radiation Measurements (2010) submitted.

[95] F. Fernández, K. Amgarou, C. Domingo, M. García, G. Quincoces, J. Martí-Climent, R. Méndez, R. Barquero, Neutron spectrometry in a PET cyclotron with a bonner sphere system, Radiation Protection Dosimetry 126 (1-4) (2007) 371–375.

[96] R. Méndez, M. Iñiguez, J. Martí-Climent, I. Peñuelas, H. Vega-Carrillo, R. Barquero, Study of the neutron field in the vicinity of an unshielded PET cyclotron, Physics in Medicine and Biology 50 (2005) 5141–5152.

[97] H. Vega-Carrillo, Neutron energy spectra inside a PET cyclotron vault room, Nuclear Instruments and Methods in Physics Research A 463 (2001) 375–386.

APPENDIX A

Manufacturing control parameters for the Bonner spheres set

The polyethylene used for the Bonner spheres has a nominal density value of $0.920\,\mathrm{g\,cm^{-3}}$. The manufacturing parameters Ø and F are defined in figure A1. Their nominal values and manufacturing tolerances, together with the measured values obtained after production at our laboratory, are provided in tables A1 and A2.

Maximum and minimum values of the mass of each sphere have been calculated from the polyethylene density value and the nominal parameters Ø, F and their tolerances for each sphere. These calculated masses and the measured values obtained at our laboratory after production are presented in table A3.

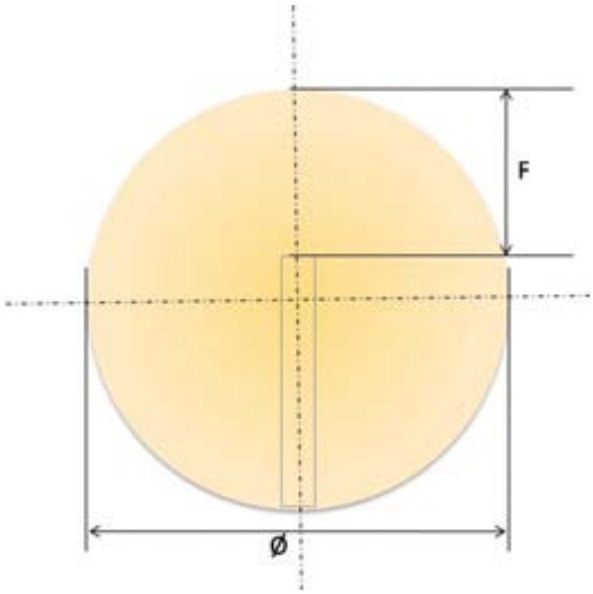

Figure A1. The parameters Ø and F used for manufacturing the polyethylene spheres.

Table A1. Nominal and tolerance values of the parameter Ø of the manufactured polyethylene spheres together with their corresponding measured values.

Diameter Ø (mm)			
Nominal value (in)	Nominal value (mm)	Tolerance	Measured
2.5	63.50	0.05	63.50
3	76.20	0.10	76.15
4.2	106.68	0.10	106.67
5	127.00	0.10	126.80
6	152.40	0.15	152.40
8	203.20	0.20	203.50
10	254.00	0.25	254.20
12	304.08	0.30	305.08

Table A2. Nominal and tolerance values of the F parameter for all the manufactured polyethylene spheres together with their corresponding measured values.

Sphere diameter Ø	F (mm)		
Nominal value (in)	Nominal value	Tolerance	Measured
2.5	21.70	0.06	21.67
3	28.03	0.08	27.86
4.2	43.29	0.11	43.28
5	53.35	0.13	53.24
6	66.15	0.15	66.12
8	91.70	0.20	91.64
10	117.05	0.25	117.02
12	142.49	0.30	142.48

Table A3. Maximum and minimum values of the mass of each sphere calculated from the polyethylene density value, the nominal values of parameters Ø, F and their tolerances. The measured values obtained at our laboratory after production are also presented.

Sphere diameter Ø	Calculated mass (g)		Measured mass (g)
Nominal value (in)	Max	Min	
2.5	113.13	108.44	110
3	199.00	197.16	200
4.2	583.84	580.22	579
5	964.85	959.85	961
6	1681.43	1671.00	1670
8	3994.11	3970.22	4000
10	7839.02	7792.34	7850
12	13620.86	13539.85	13659

APPENDIX B

Input simulation files for MCNPX

Input files for simulation of the response functions of the UAB passive BSS. Incident neutron energy is set to E MeV and the number of (n, γ) reaction rate producing ^{198}Au, per unit of gold foil mass and incident neutron fluence, is tallied.

```
RESPONSE SIMULATION FOR 2.5in CONFIGURATION
C
C — CELL DEFINITIONS —
1 0 1 -2 3 -4 5 -6 #2 #3 #4 #5 #6          $ UNIVERSE: A void cube
2 2 -0.920000 -7 #3 #4 #5 #6               $ Polyethylene sphere cell
3 3 -7.960000 (-16 15 13 -9):(-17 16 -12 5):&
 (-16 9 -8):(-16 -14 5) #6                 $ Cell defining the steel support
4 4 -19.30000 -18 -10 11                   $ Gold foil cell
5 1 -0.001293 (-17 16 12 -8)               $ Air cell between sphere and support
6 1 -0.001293 (-15 -9 14):(-16 15 -13 14)  $ Air cavity cell inside support
10 0 -1:2:-3:4:-5:6                        $ Outside universe
C End of cell definiton
C
C — SURFACES —
1 py -18.000                               $ Void cube face at -Y
2 py 18.000                                $ Void cube face at +Y
3 px -18.000                               $ Void cube face at -X
4 px 18.000                                $ Void cube face at +X
5 pz -18.000                               $ Void cube face at -Z
6 pz 18.000                                $ Void cube face at +Z
7 so 3.1750                                $ surface of the 2.5in polyethylene sphere
8 pz -1.4000                               $ Support's top plane external surface
9 pz -1.5000                               $ Upper surface of support's air cavity
10 pz 0.0055                               $ Gold foil's upper plane surface
11 pz -0.0055                              $ Gold foil's lower plane surface
12 pz -6.4000                              $ Surface connecting support's top and bottom parts
13 pz -6.5000                              $ Surface connecting top and bottom parts of support's air cavity
14 pz -12.000                              $ Lower surface of support's air cavity
15 cz 0.5000                               $ Lateral surface for support's air cavity, upper part
16 cz 0.6000                               $ Lateral surface for the lower part of the support's air cavity
C                                            and for support's top part
17 cz 0.7000                               $ Lateral surface for support's bottom part
18 cz 0.7500                               $ Lateral surface of the gold foil
C End of surface definition
C Following line must be a blank line
```

```
MODE N                                                          $ Only neutrons will be transported
IMP:N 1 1 1 1 1 1 0                                             $ Neutron importances in each cell
C
C — SOURCE DEFINITION —
C
sdef sur=1 pos=0 -18 0 rad=d1 dir=1 vec=0 1 0 &                 $ A plane disc neutron source of EMeV energy centered
erg=EMeV par=1 wgt=1                                            $ at (0,-18,0)cm with radius defined on si1
si1 0 3.810                                                     $ Source radius
C
C — TALLY DEFINITION —
C
F4:N 4                                                          $ Neutron flux averaged over cell 4 tally (part/cm^2)
FQ4 e m                                                         $ Print hierarchy, e=energy, m=multiplier
FM4 (1.394E-04 4 102)                                           $ Multiplication factor for material 4 and 102
C                                                                 cross section, detailed in section 5.2.3.
CFC4 'reaction rate per unit of gold foil mass and neutron fluence'  $ Comment to be printed with tally F4 results
C
C — MATERIAL DEFINITION —
C
m1 8016.60c -0.2421 7014.60c -0.7553 6012.50c -0.0021&
18000.35c -0.0005                                               $ Air
m2 1001.60c 0.67 6012.50c 0.33                                  $ Polyethylene (CH2)n
mt2 poly.01t                                                    $ Identifier for S(α,β) thermal neutron treatment
m3 24050.60c -0.008 24052.60c -0.151 24053.60c -0.017 &
24054.60c -0.004 26054.60c -0.039 26056.60c -0.634 &
26057.60c -0.015 26058.60c -0.002 28058.60c -0.067 &
28060.60c -0.027 28061.60c -0.001 28062.60c -0.004 &
28064.60c -0.001 42000.60c -0.03                                $ Steel
m4 79197.60c 1                                                  $ Pure gold
C
C — OTHER PARAMETERS —
C
PHYS:N 20.0 0.0                                                 $ Upper limit for neutron energy is 20.0 MeV
CUT:N 1E+34
C
NPS 1500000                                                     $ History number
PRDMP 1500000 -120 1 1 0                                        $ Plotting card
PRINT 40 50 100 110 120 126 130 140 160 200                     $ List of information tables to be plotted
```

```
RESPONSE SIMULATION FOR 3.0in CONFIGURATION
C
C — CELL DEFINITIONS —
1 0 1 -2 3 -4 5 -6 #2 #3 #4 #5 #6          $ UNIVERSE: A void cube
2 2 -0.920000 -7 #3 #4 #5 #6               $ Polyethylene sphere cell
3 3 -7.960000 (-16 15 13 -9):(-17 16 -12 5):&
 (-16 9 -8):(-16 -14 5) #6                 $ Cell defining the steel support
4 4 -19.30000 -18 -10 11                   $ Gold foil cell
5 1 -0.001293 (-17 16 12 -8)               $ Air cell between sphere and support
6 1 -0.001293 (-15 -9 14):(-16 15 -13 14)  $ Air cavity cell inside support
10 0 -1:2:-3:4:-5:6                        $ Outside universe
C End of cell definiton
C
C — SURFACES —
1 py -18.000                               $ Void cube face at -Y
2 py 18.000                                $ Void cube face at +Y
3 px -18.000                               $ Void cube face at -X
4 px 18.000                                $ Void cube face at +X
5 pz -18.000                               $ Void cube face at -Z
6 pz 18.000                                $ Void cube face at +Z
7 so 3.810                                 $ surface of the 3.0in polyethylene sphere
8 pz -1.4000                               $ Support's top plane external surface
9 pz -1.5000                               $ Upper surface of support's air cavity
10 pz 0.0055                               $ Gold foil's upper plane surface
11 pz -0.0055                              $ Gold foil's lower plane surface
12 pz -6.4000                              $ Surface connecting support's top and bottom parts
13 pz -6.5000                              $ Surface connecting top and bottom parts of support's air cavity
14 pz -12.000                              $ Lower surface of support's air cavity
15 cz 0.5000                               $ Lateral surface for support's air cavity, upper part
16 cz 0.6000                               $ Lateral surface for the lower part of the support's air cavity
C                                            and for support's top part
17 cz 0.7000                               $ Lateral surface for support's bottom part
18 cz 0.7500                               $ Lateral surface of the gold foil
C End of surface definition
C Following line must be a blank line
```

```
MODE N                                                          $ Only neutrons will be transported
IMP:N 1 1 1 1 1 1 0                                             $ Neutron importances in each cell
C
C — SOURCE DEFINITION —
C
sdef sur=1 pos=0 -18 0 rad=d1 dir=1 vec=0 1 0 &                 $ A plane disc neutron source of EMeV energy centered
erg=EMeV par=1 wgt=1                                            $ at (0,-18,0)cm with radius defined on si1
si1 0 3.175                                                     $ Source radius
C
C — TALLY DEFINITION —
C
F4:N 4                                                          $ Neutron flux averaged over cell 4 tally (part/cm^2)
FQ4 e m                                                         $ Print hierarchy, e=energy, m=multiplier
FM4 (9.683E-05 4 102)                                           $ Multiplication factor for material 4 and 102
C                                                                 cross section, detailed in section 5.2.3.
CFC4 'reaction rate per unit of gold foil mass and neutron fluence'  $ Comment to be printed with tally F4 results
C
C — MATERIAL DEFINITION —
C
m1 8016.60c -0.2421 7014.60c -0.7553 6012.50c -0.0021&
18000.35c -0.0005                                               $ Air
m2 1001.60c 0.67 6012.50c 0.33                                  $ Polyethylene (CH2)n
mt2 poly.01t                                                    $ Identifier for S(α,β) thermal neutron treatment
m3 24050.60c -0.008 24052.60c -0.151 24053.60c -0.017 &
24054.60c -0.004 26054.60c -0.039 26056.60c -0.634 &
26057.60c -0.015 26058.60c -0.002 28058.60c -0.067 &
28060.60c -0.027 28061.60c -0.001 28062.60c -0.004 &
28064.60c -0.001 42000.60c -0.03                                $ Steel
m4 79197.60c 1                                                  $ Pure gold
C
C — OTHER PARAMETERS —
C
PHYS:N 20.0 0.0                                                 $ Upper limit for neutron energy is 20.0 MeV
CUT:N 1E+34
C
NPS 1500000                                                     $ History number
PRDMP 1500000 -120 1 1 0                                        $ Plotting card
PRINT 40 50 100 110 120 126 130 140 160 200                     $ List of information tables to be plotted
```

```
RESPONSE SIMULATION FOR 4.2in CONFIGURATION
C
C — CELL DEFINITIONS —
1 0 1 -2 3 -4 5 -6 #2 #3 #4 #5 #6          $ UNIVERSE: A void cube
2 2 -0.920000 -7 #3 #4 #5 #6               $ Polyethylene sphere cell
3 3 -7.960000 (-16 15 13 -9):(-17 16 -12 5):&
 (-16 9 -8):(-16 -14 5) #6                 $ Cell defining the steel support
4 4 -19.30000 -18 -10 11                   $ Gold foil cell
5 1 -0.001293 (-17 16 12 -8)               $ Air cell between sphere and support
6 1 -0.001293 (-15 -9 14):(-16 15 -13 14)  $ Air cavity cell inside support
10 0 -1:2:-3:4:-5:6                        $ Outside universe
C End of cell definiton
C
C — SURFACES —
1 py -18.000                               $ Void cube face at -Y
2 py 18.000                                $ Void cube face at +Y
3 px -18.000                               $ Void cube face at -X
4 px 18.000                                $ Void cube face at +X
5 pz -18.000                               $ Void cube face at -Z
6 pz 18.000                                $ Void cube face at +Z
7 so 5.334                                 $ surface of the 4.2in polyethylene sphere
8 pz -1.4000                               $ Support's top plane external surface
9 pz -1.5000                               $ Upper surface of support's air cavity
10 pz 0.0055                               $ Gold foil's upper plane surface
11 pz -0.0055                              $ Gold foil's lower plane surface
12 pz -6.4000                              $ Surface connecting support's top and bottom parts
13 pz -6.5000                              $ Surface connecting top and bottom parts of support's air cavity
14 pz -12.000                              $ Lower surface of support's air cavity
15 cz 0.5000                               $ Lateral surface for support's air cavity, upper part
16 cz 0.6000                               $ Lateral surface for the lower part of the support's air cavity
C                                            and for support's top part
17 cz 0.7000                               $ Lateral surface for support's bottom part
18 cz 0.7500                               $ Lateral surface of the gold foil
C End of surface definition
C Following line must be a blank line
```

```
MODE N                                                          $ Only neutrons will be transported
IMP:N 1 1 1 1 1 1 0                                             $ Neutron importances in each cell
C
C — SOURCE DEFINITION —
C
sdef sur=1 pos=0 -18 0 rad=d1 dir=1 vec=0 1 0 &                 $ A plane disc neutron source of EMeV energy centered
erg=EMeV par=1 wgt=1                                            $ at (0,-18,0)cm with radius defined on si1
si1 0 5.334                                                     $ Source radius
C
C — TALLY DEFINITION —
C
F4:N 4                                                          $ Neutron flux averaged over cell 4 tally (part/cm^2)
FQ4 e m                                                         $ Print hierarchy, e=energy, m=multiplier
FM4 (2.733E-04 4 102)                                           $ Multiplication factor for material 4 and 102
C                                                                 cross section, detailed in section 5.2.3.
CFC4 'reaction rate per unit of gold foil mass and neutron fluence'  $ Comment to be printed with tally F4 results
C
C — MATERIAL DEFINITION —
C
m1 8016.60c -0.2421 7014.60c -0.7553 6012.50c -0.0021&
18000.35c -0.0005                                               $ Air
m2 1001.60c 0.67 6012.50c 0.33                                  $ Polyethylene (CH2)n
mt2 poly.01t                                                    $ Identifier for S(α,β) thermal neutron treatment
m3 24050.60c -0.008 24052.60c -0.151 24053.60c -0.017 &
24054.60c -0.004 26054.60c -0.039 26056.60c -0.634 &
26057.60c -0.015 26058.60c -0.002 28058.60c -0.067 &
28060.60c -0.027 28061.60c -0.001 28062.60c -0.004 &
28064.60c -0.001 42000.60c -0.03                                $ Steel
m4 79197.60c 1                                                  $ Pure gold
C
C — OTHER PARAMETERS —
C
PHYS:N 20.0 0.0                                                 $ Upper limit for neutron energy is 20.0 MeV
CUT:N 1E+34
C
NPS 1500000                                                     $ History number
PRDMP 1500000 -120 1 1 0                                        $ Plotting card
PRINT 40 50 100 110 120 126 130 140 160 200                     $ List of information tables to be plotted
```

```
RESPONSE SIMULATION FOR 5.0in CONFIGURATION
C
C — CELL DEFINITIONS —
1 0 1 -2 3 -4 5 -6 #2 #3 #4 #5 #6          $ UNIVERSE: A void cube
2 2 -0.920000 -7 #3 #4 #5 #6               $ Polyethylene sphere cell
3 3 -7.960000 (-16 15 13 -9):(-17 16 -12 5):&
 (-16 9 -8):(-16 -14 5) #6                 $ Cell defining the steel support
4 4 -19.30000 -18 -10 11                   $ Gold foil cell
5 1 -0.001293 (-17 16 12 -8)               $ Air cell between sphere and support
6 1 -0.001293 (-15 -9 14):(-16 15 -13 14)  $ Air cavity cell inside support
10 0 -1:2:-3:4:-5:6                        $ Outside universe
C End of cell definiton
C
C — SURFACES —
1 py -18.000                               $ Void cube face at -Y
2 py 18.000                                $ Void cube face at +Y
3 px -18.000                               $ Void cube face at -X
4 px 18.000                                $ Void cube face at +X
5 pz -18.000                               $ Void cube face at -Z
6 pz 18.000                                $ Void cube face at +Z
7 so 6.350                                 $ surface of the 5.0in polyethylene sphere
8 pz -1.4000                               $ Support's top plane external surface
9 pz -1.5000                               $ Upper surface of support's air cavity
10 pz 0.0055                               $ Gold foil's upper plane surface
11 pz -0.0055                              $ Gold foil's lower plane surface
12 pz -6.4000                              $ Surface connecting support's top and bottom parts
13 pz -6.5000                              $ Surface connecting top and bottom parts of support's air cavity
14 pz -12.000                              $ Lower surface of support's air cavity
15 cz 0.5000                               $ Lateral surface for support's air cavity, upper part
16 cz 0.6000                               $ Lateral surface for the lower part of the support's air cavity
C                                            and for support's top part
17 cz 0.7000                               $ Lateral surface for support's bottom part
18 cz 0.7500                               $ Lateral surface of the gold foil
C End of surface definition
C Following line must be a blank line
```

```
MODE N                                                          $ Only neutrons will be transported
IMP:N 1 1 1 1 1 1 0                                             $ Neutron importances in each cell
C
C — SOURCE DEFINITION —
C
sdef sur=1 pos=0 -18 0 rad=d1 dir=1 vec=0 1 0 &                 $ A plane disc neutron source of EMeV energy centered
erg=EMeV par=1 wgt=1                                            $ at (0,-18,0)cm with radius defined on si1
si1 0 6.350                                                     $ Source radius
C
C — TALLY DEFINITION —
C
F4:N 4                                                          $ Neutron flux averaged over cell 4 tally (part/cm^2)
FQ4 e m                                                         $ Print hierarchy, e=energy, m=multiplier
FM4 (3.873E-04 4 102)                                           $ Multiplication factor for material 4 and 102
C                                                                 cross section, detailed in section 5.2.3.
CFC4 'reaction rate per unit of gold foil mass and neutron fluence'  $ Comment to be printed with tally F4 results
C
C — MATERIAL DEFINITION —
C
m1 8016.60c -0.2421 7014.60c -0.7553 6012.50c -0.0021&
18000.35c -0.0005                                               $ Air
m2 1001.60c 0.67 6012.50c 0.33                                  $ Polyethylene (CH2)n
mt2 poly.01t                                                    $ Identifier for S(α,β) thermal neutron treatment
m3 24050.60c -0.008 24052.60c -0.151 24053.60c -0.017 &
24054.60c -0.004 26054.60c -0.039 26056.60c -0.634 &
26057.60c -0.015 26058.60c -0.002 28058.60c -0.067 &
28060.60c -0.027 28061.60c -0.001 28062.60c -0.004 &
28064.60c -0.001 42000.60c -0.03                                $ Steel
m4 79197.60c 1                                                  $ Pure gold
C
C — OTHER PARAMETERS —
C
PHYS:N 20.0 0.0                                                 $ Upper limit for neutron energy is 20.0 MeV
CUT:N 1E+34
C
NPS 1500000                                                     $ History number
PRDMP 1500000 -120 1 1 0                                        $ Plotting card
PRINT 40 50 100 110 120 126 130 140 160 200                     $ List of information tables to be plotted
```

```
RESPONSE SIMULATION FOR 6.0in CONFIGURATION
C
C — CELL DEFINITIONS —
1 0 1 -2 3 -4 5 -6 #2 #3 #4 #5 #6          $ UNIVERSE: A void cube
2 2 -0.920000 -7 #3 #4 #5 #6               $ Polyethylene sphere cell
3 3 -7.960000 (-16 15 13 -9):(-17 16 -12 5):&
 (-16 9 -8):(-16 -14 5) #6                 $ Cell defining the steel support
4 4 -19.30000 -18 -10 11                   $ Gold foil cell
5 1 -0.001293 (-17 16 12 -8)               $ Air cell between sphere and support
6 1 -0.001293 (-15 -9 14):(-16 15 -13 14)  $ Air cavity cell inside support
10 0 -1:2:-3:4:-5:6                        $ Outside universe
C End of cell definiton
C
C — SURFACES —
1 py -18.000                               $ Void cube face at -Y
2 py 18.000                                $ Void cube face at +Y
3 px -18.000                               $ Void cube face at -X
4 px 18.000                                $ Void cube face at +X
5 pz -18.000                               $ Void cube face at -Z
6 pz 18.000                                $ Void cube face at +Z
7 so 7.620                                 $ surface of the 6.0in polyethylene sphere
8 pz -1.4000                               $ Support's top plane external surface
9 pz -1.5000                               $ Upper surface of support's air cavity
10 pz 0.0055                               $ Gold foil's upper plane surface
11 pz -0.0055                              $ Gold foil's lower plane surface
12 pz -6.4000                              $ Surface connecting support's top and bottom parts
13 pz -6.5000                              $ Surface connecting top and bottom parts of support's air cavity
14 pz -12.000                              $ Lower surface of support's air cavity
15 cz 0.5000                               $ Lateral surface for support's air cavity, upper part
16 cz 0.6000                               $ Lateral surface for the lower part of the support's air cavity
C                                            and for support's top part
17 cz 0.7000                               $ Lateral surface for support's bottom part
18 cz 0.7500                               $ Lateral surface of the gold foil
C End of surface definition
C Following line must be a blank line
```

```
MODE N                                                          $ Only neutrons will be transported
IMP:N 1 1 1 1 1 1 0                                             $ Neutron importances in each cell
C
C — SOURCE DEFINITION —
C
sdef sur=1 pos=0 -18 0 rad=d1 dir=1 vec=0 1 0 &                 $ A plane disc neutron source of EMeV energy centered
erg=EMeV par=1 wgt=1                                            $ at (0,-18,0)cm with radius defined on si1
si1 0 7.620                                                     $ Source radius
C
C — TALLY DEFINITION —
C
F4:N 4                                                          $ Neutron flux averaged over cell 4 tally (part/cm^2)
FQ4 e m                                                         $ Print hierarchy, e=energy, m=multiplier
FM4 (5.577E-04 4 102)                                           $ Multiplication factor for material 4 and 102
C                                                                 cross section, detailed in section 5.2.3.
CFC4 'reaction rate per unit of gold foil mass and neutron fluence'  $ Comment to be printed with tally F4 results
C
C — MATERIAL DEFINITION —
C
m1 8016.60c -0.2421 7014.60c -0.7553 6012.50c -0.0021&
18000.35c -0.0005                                               $ Air
m2 1001.60c 0.67 6012.50c 0.33                                  $ Polyethylene (CH2)n
mt2 poly.01t                                                    $ Identifier for S(α,β) thermal neutron treatment
m3 24050.60c -0.008 24052.60c -0.151 24053.60c -0.017 &
24054.60c -0.004 26054.60c -0.039 26056.60c -0.634 &
26057.60c -0.015 26058.60c -0.002 28058.60c -0.067 &
28060.60c -0.027 28061.60c -0.001 28062.60c -0.004 &
28064.60c -0.001 42000.60c -0.03                                $ Steel
m4 79197.60c 1                                                  $ Pure gold
C
C — OTHER PARAMETERS —
C
PHYS:N 20.0 0.0                                                 $ Upper limit for neutron energy is 20.0 MeV
CUT:N 1E+34
C
NPS 1500000                                                     $ History number
PRDMP 1500000 -120 1 1 0                                        $ Plotting card
PRINT 40 50 100 110 120 126 130 140 160 200                     $ List of information tables to be plotted
```

```
RESPONSE SIMULATION FOR 8.0in CONFIGURATION
C
C — CELL DEFINITIONS —
1 0 1 -2 3 -4 5 -6 #2 #3 #4 #5 #6          $ UNIVERSE: A void cube
2 2 -0.920000 -7 #3 #4 #5 #6               $ Polyethylene sphere cell
3 3 -7.960000 (-16 15 13 -9):(-17 16 -12 5):&
 (-16 9 -8):(-16 -14 5) #6                 $ Cell defining the steel support
4 4 -19.30000 -18 -10 11                   $ Gold foil cell
5 1 -0.001293 (-17 16 12 -8)               $ Air cell between sphere and support
6 1 -0.001293 (-15 -9 14):(-16 15 -13 14)  $ Air cavity cell inside support
10 0 -1:2:-3:4:-5:6                        $ Outside universe
C End of cell definiton
C
C — SURFACES —
1 py -18.000                               $ Void cube face at -Y
2 py 18.000                                $ Void cube face at +Y
3 px -18.000                               $ Void cube face at -X
4 px 18.000                                $ Void cube face at +X
5 pz -18.000                               $ Void cube face at -Z
6 pz 18.000                                $ Void cube face at +Z
7 so 10.160                                $ surface of the 8.0in polyethylene sphere
8 pz -1.4000                               $ Support's top plane external surface
9 pz -1.5000                               $ Upper surface of support's air cavity
10 pz 0.0055                               $ Gold foil's upper plane surface
11 pz -0.0055                              $ Gold foil's lower plane surface
12 pz -6.4000                              $ Surface connecting support's top and bottom parts
13 pz -6.5000                              $ Surface connecting top and bottom parts of support's air cavity
14 pz -12.000                              $ Lower surface of support's air cavity
15 cz 0.5000                               $ Lateral surface for support's air cavity, upper part
16 cz 0.6000                               $ Lateral surface for the lower part of the support's air cavity
C                                            and for support's top part
17 cz 0.7000                               $ Lateral surface for support's bottom part
18 cz 0.7500                               $ Lateral surface of the gold foil
C End of surface definition
C Following line must be a blank line
```

```
MODE N                                                          $ Only neutrons will be transported
IMP:N 1 1 1 1 1 1 0                                             $ Neutron importances in each cell
C
C — SOURCE DEFINITION —
C
sdef sur=1 pos=0 -18 0 rad=d1 dir=1 vec=0 1 0 &                 $ A plane disc neutron source of EMeV energy centered
erg=EMeV par=1 wgt=1                                            $ at (0,-18,0)cm with radius defined on si1
si1 0 10.160                                                    $ Source radius
C
C — TALLY DEFINITION —
C
F4:N 4                                                          $ Neutron flux averaged over cell 4 tally (part/cm^2)
FQ4 e m                                                         $ Print hierarchy, e=energy, m=multiplier
FM4 (9.915E-04 4 102)                                           $ Multiplication factor for material 4 and 102
C                                                                 cross section, detailed in section 5.2.3.
CFC4 'reaction rate per unit of gold foil mass and neutron fluence'  $ Comment to be printed with tally F4 results
C
C — MATERIAL DEFINITION —
C
m1 8016.60c -0.2421 7014.60c -0.7553 6012.50c -0.0021&
18000.35c -0.0005                                               $ Air
m2 1001.60c 0.67 6012.50c 0.33                                  $ Polyethylene (CH2)n
mt2 poly.01t                                                    $ Identifier for S(α,β) thermal neutron treatment
m3 24050.60c -0.008 24052.60c -0.151 24053.60c -0.017 &
24054.60c -0.004 26054.60c -0.039 26056.60c -0.634 &
26057.60c -0.015 26058.60c -0.002 28058.60c -0.067 &
28060.60c -0.027 28061.60c -0.001 28062.60c -0.004 &
28064.60c -0.001 42000.60c -0.03                                $ Steel
m4 79197.60c 1                                                  $ Pure gold
C
C — OTHER PARAMETERS —
C
PHYS:N 20.0 0.0                                                 $ Upper limit for neutron energy is 20.0 MeV
CUT:N 1E+34
C
NPS 1500000                                                     $ History number
PRDMP 1500000 -120 1 1 0                                        $ Plotting card
PRINT 40 50 100 110 120 126 130 140 160 200                     $ List of information tables to be plotted
```

```
RESPONSE SIMULATION FOR 10in CONFIGURATION
C
C — CELL DEFINITIONS —
1 0 1 -2 3 -4 5 -6 #2 #3 #4 #5 #6          $ UNIVERSE: A void cube
2 2 -0.920000 -7 #3 #4 #5 #6               $ Polyethylene sphere cell
3 3 -7.960000 (-16 15 13 -9):(-17 16 -12 5):&
 (-16 9 -8):(-16 -14 5) #6                 $ Cell defining the steel support
4 4 -19.30000 -18 -10 11                   $ Gold foil cell
5 1 -0.001293 (-17 16 12 -8)               $ Air cell between sphere and support
6 1 -0.001293 (-15 -9 14):(-16 15 -13 14)  $ Air cavity cell inside support
10 0 -1:2:-3:4:-5:6                        $ Outside universe
C End of cell definiton
C
C — SURFACES —
1 py -18.000                               $ Void cube face at -Y
2 py 18.000                                $ Void cube face at +Y
3 px -18.000                               $ Void cube face at -X
4 px 18.000                                $ Void cube face at +X
5 pz -18.000                               $ Void cube face at -Z
6 pz 18.000                                $ Void cube face at +Z
7 so 12.700                                $ surface of the 10in polyethylene sphere
8 pz -1.4000                               $ Support's top plane external surface
9 pz -1.5000                               $ Upper surface of support's air cavity
10 pz 0.0055                               $ Gold foil's upper plane surface
11 pz -0.0055                              $ Gold foil's lower plane surface
12 pz -6.4000                              $ Surface connecting support's top and bottom parts
13 pz -6.5000                              $ Surface connecting top and bottom parts of support's air cavity
14 pz -12.000                              $ Lower surface of support's air cavity
15 cz 0.5000                               $ Lateral surface for support's air cavity, upper part
16 cz 0.6000                               $ Lateral surface for the lower part of the support's air cavity
C                                            and for support's top part
17 cz 0.7000                               $ Lateral surface for support's bottom part
18 cz 0.7500                               $ Lateral surface of the gold foil
C End of surface definition
C Following line must be a blank line
```

```
MODE N                                                          $ Only neutrons will be transported
IMP:N 1 1 1 1 1 1 0                                             $ Neutron importances in each cell
C
C — SOURCE DEFINITION —
C
sdef sur=1 pos=0 -18 0 rad=d1 dir=1 vec=0 1 0 &                 $ A plane disc neutron source of EMeV energy centered
erg=EMeV par=1 wgt=1                                            $ at (0,-18,0)cm with radius defined on si1
si1 0 12.700                                                    $ Source radius
C
C — TALLY DEFINITION —
C
F4:N 4                                                          $ Neutron flux averaged over cell 4 tally (part/cm^2)
FQ4 e m                                                         $ Print hierarchy, e=energy, m=multiplier
FM4 (1.549E-03 4 102)                                           $ Multiplication factor for material 4 and 102
C                                                                 cross section, detailed in section 5.2.3.
CFC4 'reaction rate per unit of gold foil mass and neutron fluence'  $ Comment to be printed with tally F4 results
C
C — MATERIAL DEFINITION —
C
m1 8016.60c -0.2421 7014.60c -0.7553 6012.50c -0.0021&
18000.35c -0.0005                                               $ Air
m2 1001.60c 0.67 6012.50c 0.33                                  $ Polyethylene (CH2)n
mt2 poly.01t                                                    $ Identifier for S(α,β) thermal neutron treatment
m3 24050.60c -0.008 24052.60c -0.151 24053.60c -0.017 &
24054.60c -0.004 26054.60c -0.039 26056.60c -0.634 &
26057.60c -0.015 26058.60c -0.002 28058.60c -0.067 &
28060.60c -0.027 28061.60c -0.001 28062.60c -0.004 &
28064.60c -0.001 42000.60c -0.03                                $ Steel
m4 79197.60c 1                                                  $ Pure gold
C
C — OTHER PARAMETERS —
C
PHYS:N 20.0 0.0                                                 $ Upper limit for neutron energy is 20.0 MeV
CUT:N 1E+34
C
NPS 1500000                                                     $ History number
PRDMP 1500000 -120 1 1 0                                        $ Plotting card
PRINT 40 50 100 110 120 126 130 140 160 200                     $ List of information tables to be plotted
```

```
RESPONSE SIMULATION FOR 12in CONFIGURATION
C
C — CELL DEFINITIONS —
1 0 1 -2 3 -4 5 -6 #2 #3 #4 #5 #6          $ UNIVERSE: A void cube
2 2 -0.920000 -7 #3 #4 #5 #6               $ Polyethylene sphere cell
3 3 -7.960000 (-16 15 13 -9):(-17 16 -12 5):&
 (-16 9 -8):(-16 -14 5) #6                 $ Cell defining the steel support
4 4 -19.30000 -18 -10 11                   $ Gold foil cell
5 1 -0.001293 (-17 16 12 -8)               $ Air cell between sphere and support
6 1 -0.001293 (-15 -9 14):(-16 15 -13 14)  $ Air cavity cell inside support
10 0 -1:2:-3:4:-5:6                        $ Outside universe
C End of cell definiton
C
C — SURFACES —
1 py -18.000                               $ Void cube face at -Y
2 py 18.000                                $ Void cube face at +Y
3 px -18.000                               $ Void cube face at -X
4 px 18.000                                $ Void cube face at +X
5 pz -18.000                               $ Void cube face at -Z
6 pz 18.000                                $ Void cube face at +Z
7 so 15.240                                $ surface of the 12in polyethylene sphere
8 pz -1.4000                               $ Support's top plane external surface
9 pz -1.5000                               $ Upper surface of support's air cavity
10 pz 0.0055                               $ Gold foil's upper plane surface
11 pz -0.0055                              $ Gold foil's lower plane surface
12 pz -6.4000                              $ Surface connecting support's top and bottom parts
13 pz -6.5000                              $ Surface connecting top and bottom parts of support's air cavity
14 pz -12.000                              $ Lower surface of support's air cavity
15 cz 0.5000                               $ Lateral surface for support's air cavity, upper part
16 cz 0.6000                               $ Lateral surface for the lower part of the support's air cavity
C                                            and for support's top part
17 cz 0.7000                               $ Lateral surface for support's bottom part
18 cz 0.7500                               $ Lateral surface of the gold foil
C End of surface definition
C Following line must be a blank line
```

```
MODE N                                                          $ Only neutrons will be transported
IMP:N 1 1 1 1 1 1 0                                             $ Neutron importances in each cell
C
C — SOURCE DEFINITION —
C
sdef sur=1 pos=0 -18 0 rad=d1 dir=1 vec=0 1 0 &                 $ A plane disc neutron source of EMeV energy centered
erg=EMeV par=1 wgt=1                                            $ at (0,-18,0)cm with radius defined on si1
si1 0 15.240                                                    $ Source radius
C
C — TALLY DEFINITION —
C
F4:N 4                                                          $ Neutron flux averaged over cell 4 tally (part/cm^2)
FQ4 e m                                                         $ Print hierarchy, e=energy, m=multiplier
FM4 (2.231E-03 4 102)                                           $ Multiplication factor for material 4 and 102
C                                                                 cross section, detailed in section 5.2.3.
CFC4 'reaction rate per unit of gold foil mass and neutron fluence'  $ Comment to be printed with tally F4 results
C
C — MATERIAL DEFINITION —
C
m1 8016.60c -0.2421 7014.60c -0.7553 6012.50c -0.0021&
18000.35c -0.0005                                               $ Air
m2 1001.60c 0.67 6012.50c 0.33                                  $ Polyethylene (CH2)n
mt2 poly.01t                                                    $ Identifier for S(α,β) thermal neutron treatment
m3 24050.60c -0.008 24052.60c -0.151 24053.60c -0.017 &
24054.60c -0.004 26054.60c -0.039 26056.60c -0.634 &
26057.60c -0.015 26058.60c -0.002 28058.60c -0.067 &
28060.60c -0.027 28061.60c -0.001 28062.60c -0.004 &
28064.60c -0.001 42000.60c -0.03                                $ Steel
m4 79197.60c 1                                                  $ Pure gold
C
C — OTHER PARAMETERS —
C
PHYS:N 20.0 0.0                                                 $ Upper limit for neutron energy is 20.0 MeV
CUT:N 1E+34
C
NPS 1500000                                                     $ History number
PRDMP 1500000 -120 1 1 0                                        $ Plotting card
PRINT 40 50 100 110 120 126 130 140 160 200                     $ List of information tables to be plotted
```

```
RESPONSE SIMULATION FOR 2.5in + Cd CONFIGURATION
C
C — CELL DEFINITIONS —
1 0 1 -2 3 -4 5 -6 #2 #3 #4 #5 #6 #7 #8 #9 #11 #12   $ UNIVERSE: A void cube
2 2 -0.920000 -7 #3 #4 #5 #6                          $ Polyethylene sphere cell
3 3 -7.960000 (-16 15 13 -9):(-17 16 -12 5):&
 (-16 9 -8):(-16 -14 5) #6                            $ Cell defining the steel support
4 4 -19.30000 -18 -10 11                              $ Gold foil cell
5 1 -0.001293 (-17 16 12 -8)                          $ Air cell between sphere and support
6 1 -0.001293 (-15 -9 14):(-16 15 -13 14)             $ Air cavity cell inside support
7 5 -8.640000 -20 19 #2 #3 #4 #5 #6                   $ Cadmium shell
8 5 -8.640000 -22 17 5 -24 #3 #5                      $ Cadmium shell support
9 6 -2.702000 -21 20 #2 #3 #4 #5 #6 #8                $ Aluminium cover for Cd shell
11 6 -2.702000 -23 22 5 -25 #3 #5 #8                  $ Aluminium cover support
12 1 -0.001293 -19 7 #2 #3 #4 #5 #6                   $ Air between Cd shell and sphere
10 0 -1:2:-3:4:-5:6                                   $ Outside universe
C End of cell definiton
C
    C — SURFACES —
    1 py -18.000          $ Void cube face at -Y
    2 py 18.000           $ Void cube face at +Y
    3 px -18.000          $ Void cube face at -X
    4 px 18.000           $ Void cube face at +X
    5 pz -18.000          $ Void cube face at -Z
    6 pz 18.000           $ Void cube face at +Z
    7 so 3.1750           $ surface of the 2.5in polyethylene sphere
    8 pz -1.4000          $ Support's top plane external surface
    9 pz -1.5000          $ Upper surface of support's air cavity
    10 pz 0.0055          $ Gold foil's upper plane surface
    11 pz -0.0055         $ Gold foil's lower plane surface
    12 pz -6.4000         $ Surface connecting support's top and bottom parts
    13 pz -6.5000         $ Surface connecting top and bottom parts of support's air cavity
    14 pz -12.000         $ Lower surface of support's air cavity
    15 cz 0.5000          $ Lateral surface for support's air cavity, upper part
    16 cz 0.6000          $ Lateral surface for the lower part of the support's air cavity
    C                       and for support's top part
```

```
17 cz 0.7000                    $ Lateral surface for support's bottom part
18 cz 0.7500                    $ Lateral surface of the gold foil
19 so 6.5000                    $ Inner limit of the Cd shell
20 so 6.6500                    $ Outer limit of the Cd shell
21 so 6.8000                    $ Outer limit of the Al cover
22 cz 0.8500                    $ Inner limit of the Cd shell support
23 cz 1.0000                    $ Outer limit of the Cd shell support
24 pz -6.6150                   $ Upper limit of the Cd shell support
25 pz -6.7500                   $ Lower limit of the Cd shell support
C End of surface definition
C Following line must be a blank line

MODE N                          $ Only neutrons will be transported
IMP:N 1 1 1 1 1 1 1 1 1 1 0     $ Neutron importances in each cell
C
C — SOURCE DEFINITION —
C
sdef sur=1 pos=0 -18 0 rad=d1 dir=1 vec=0 1 0 &   $ A plane disc neutron source of EMeV energy centered
erg=EMeV par=1 wgt=1            $ at (0,-18,0)cm with radius defined on si1
si1 0 6.800                     $ Source radius
C
C — TALLY DEFINITION —
C
F4:N 4                          $ Neutron flux averaged over cell 4 tally (part/cm^2)
FQ4 e m                         $ Print hierarchy, e=energy, m=multiplier
FM4 (4.441E-04 4 102)           $ Multiplication factor for material 4 and 102
C                                   cross section, detailed in section 5.2.3.
CFC4 'reaction rate per unit of gold foil mass and neutron fluence'   $ Comment to be printed with tally F4 results
C
```

```
C --- MATERIAL DEFINITION ---
C
m1 8016.60c -0.2421 7014.60c -0.7553 6012.50c -0.0021&
18000.35c -0.0005                                      $ Air
m2 1001.60c 0.67 6012.50c 0.33                         $ Polyethylene (CH2)n
mt2 poly.01t                                           $ Identifier for S(α,β) thermal neutron treatment
m3 24050.60c -0.008 24052.60c -0.151 24053.60c -0.017 &
24054.60c -0.004 26054.60c -0.039 26056.60c -0.634 &
26057.60c -0.015 26058.60c -0.002 28058.60c -0.067 &
28060.60c -0.027 28061.60c -0.001 28062.60c -0.004 &
28064.60c -0.001 42000.60c -0.03                       $ Steel
m4 79197.60c 1                                         $ Pure gold
m5 48000.51c 1                                         $ Cadmium
m6 13027.60c 1                                         $ Aluminium
C
C --- OTHER PARAMETERS ---
C
PHYS:N 20.0 0.0                                        $ Upper limit for neutron energy is 20.0 MeV
CUT:N 1E+34
C
NPS 1500000                                            $ History number
PRDMP 1500000 -120 1 1 0                               $ Plotting card
PRINT 40 50 100 110 120 126 130 140 160 200            $ List of information tables to be plotted
```

```
RESPONSE SIMULATION FOR 3.0in + Cd CONFIGURATION
C
C — CELL DEFINITIONS —
1 0 1 -2 3 -4 5 -6 #2 #3 #4 #5 #6 #7 #8 #9 #11 #12   $ UNIVERSE: A void cube
2 2 -0.920000 -7 #3 #4 #5 #6                          $ Polyethylene sphere cell
3 3 -7.960000 (-16 15 13 -9):(-17 16 -12 5):&
 (-16 9 -8):(-16 -14 5) #6                            $ Cell defining the steel support
4 4 -19.30000 -18 -10 11                              $ Gold foil cell
5 1 -0.001293 (-17 16 12 -8)                          $ Air cell between sphere and support
6 1 -0.001293 (-15 -9 14):(-16 15 -13 14)             $ Air cavity cell inside support
7 5 -8.640000 -20 19 #2 #3 #4 #5 #6                   $ Cadmium shell
8 5 -8.640000 -22 17 5 -24 #3 #5                      $ Cadmium shell support
9 6 -2.702000 -21 20 #2 #3 #4 #5 #6 #8                $ Aluminium cover for Cd shell
11 6 -2.702000 -23 22 5 -25 #3 #5 #8                  $ Aluminium cover support
12 1 -0.001293 -19 7 #2 #3 #4 #5 #6                   $ Air between Cd shell and sphere
10 0 -1:2:-3:4:-5:6                                   $ Outside universe
C End of cell definiton
C
    C — SURFACES —
    1 py -18.000          $ Void cube face at -Y
    2 py 18.000           $ Void cube face at +Y
    3 px -18.000          $ Void cube face at -X
    4 px 18.000           $ Void cube face at +X
    5 pz -18.000          $ Void cube face at -Z
    6 pz 18.000           $ Void cube face at +Z
    7 so 3.810            $ surface of the 3.0in polyethylene sphere
    8 pz -1.4000          $ Support's top plane external surface
    9 pz -1.5000          $ Upper surface of support's air cavity
    10 pz 0.0055          $ Gold foil's upper plane surface
    11 pz -0.0055         $ Gold foil's lower plane surface
    12 pz -6.4000         $ Surface connecting support's top and bottom parts
    13 pz -6.5000         $ Surface connecting top and bottom parts of support's air cavity
    14 pz -12.000         $ Lower surface of support's air cavity
    15 cz 0.5000          $ Lateral surface for support's air cavity, upper part
    16 cz 0.6000          $ Lateral surface for the lower part of the support's air cavity
    C                       and for support's top part
```

```
17 cz 0.7000                $ Lateral surface for support's bottom part
18 cz 0.7500                $ Lateral surface of the gold foil
19 so 6.5000                $ Inner limit of the Cd shell
20 so 6.6500                $ Outer limit of the Cd shell
21 so 6.8000                $ Outer limit of the Al cover
22 cz 0.8500                $ Inner limit of the Cd shell support
23 cz 1.0000                $ Outer limit of the Cd shell support
24 pz -6.6150               $ Upper limit of the Cd shell support
25 pz -6.7500               $ Lower limit of the Cd shell support
C End of surface definition
C Following line must be a blank line

MODE N                      $ Only neutrons will be transported
IMP:N 1 1 1 1 1 1 1 1 1 1 0 $ Neutron importances in each cell
C
C — SOURCE DEFINITION —
C
sdef sur=1 pos=0 -18 0 rad=d1 dir=1 vec=0 1 0 &
                            $ A plane disc neutron source of EMeV energy centered
erg=EMeV par=1 wgt=1        $ at (0,-18,0)cm with radius defined on si1
si1 0 6.800                 $ Source radius
C
C — TALLY DEFINITION —
C
F4:N 4                      $ Neutron flux averaged over cell 4 tally (part/cm^2)
FQ4 e m                     $ Print hierarchy, e=energy, m=multiplier
FM4 (4.441E-04 4 102)       $ Multiplication factor for material 4 and 102
                              cross section, detailed in section 5.2.3.
C
CFC4 'reaction rate per unit of gold foil mass and neutron fluence'
                            $ Comment to be printed with tally F4 results
C
```

```
C --- MATERIAL DEFINITION ---
C
m1 8016.60c -0.2421 7014.60c -0.7553 6012.50c -0.0021&
18000.35c -0.0005                                        $ Air
m2 1001.60c 0.67 6012.50c 0.33                           $ Polyethylene (CH2)n
mt2 poly.01t                                             $ Identifier for S(α,β) thermal neutron treatment
m3 24050.60c -0.008 24052.60c -0.151 24053.60c -0.017 &
24054.60c -0.004 26054.60c -0.039 26056.60c -0.634 &
26057.60c -0.015 26058.60c -0.002 28058.60c -0.067 &
28060.60c -0.027 28061.60c -0.001 28062.60c -0.004 &
28064.60c -0.001 42000.60c -0.03                         $ Steel
m4 79197.60c 1                                           $ Pure gold
m5 48000.51c 1                                           $ Cadmium
m6 13027.60c 1                                           $ Aluminium
C
C --- OTHER PARAMETERS ---
C
PHYS:N 20.0 0.0                                          $ Upper limit for neutron energy is 20.0 MeV
CUT:N 1E+34
C
NPS 1500000                                              $ History number
PRDMP 1500000 -120 1 1 0                                 $ Plotting card
PRINT 40 50 100 110 120 126 130 140 160 200              $ List of information tables to be plotted
```

```
RESPONSE SIMULATION FOR 4.2in + Cd CONFIGURATION
C
C — CELL DEFINITIONS —
1 0 1 -2 3 -4 5 -6 #2 #3 #4 #5 #6 #7 #8 #9 #11 #12   $ UNIVERSE: A void cube
2 2 -0.920000 -7 #3 #4 #5 #6                          $ Polyethylene sphere cell
3 3 -7.960000 (-16 15 13 -9):(-17 16 -12 5):&
 (-16 9 -8):(-16 -14 5) #6                            $ Cell defining the steel support
4 4 -19.30000 -18 -10 11                              $ Gold foil cell
5 1 -0.001293 (-17 16 12 -8)                          $ Air cell between sphere and support
6 1 -0.001293 (-15 -9 14):(-16 15 -13 14)             $ Air cavity cell inside support
7 5 -8.640000 -20 19 #2 #3 #4 #5 #6                   $ Cadmium shell
8 5 -8.640000 -22 17 5 -24 #3 #5                      $ Cadmium shell support
9 6 -2.702000 -21 20 #2 #3 #4 #5 #6 #8                $ Aluminium cover for Cd shell
11 6 -2.702000 -23 22 5 -25 #3 #5 #8                  $ Aluminium cover support
12 1 -0.001293 -19 7 #2 #3 #4 #5 #6                   $ Air between Cd shell and sphere
10 0 -1:2:-3:4:-5:6                                   $ Outside universe
C End of cell definiton
C
    C — SURFACES —
    1 py -18.000          $ Void cube face at -Y
    2 py 18.000           $ Void cube face at +Y
    3 px -18.000          $ Void cube face at -X
    4 px 18.000           $ Void cube face at +X
    5 pz -18.000          $ Void cube face at -Z
    6 pz 18.000           $ Void cube face at +Z
    7 so 5.334            $ surface of the 4.2in polyethylene sphere
    8 pz -1.4000          $ Support's top plane external surface
    9 pz -1.5000          $ Upper surface of support's air cavity
    10 pz 0.0055          $ Gold foil's upper plane surface
    11 pz -0.0055         $ Gold foil's lower plane surface
    12 pz -6.4000         $ Surface connecting support's top and bottom parts
    13 pz -6.5000         $ Surface connecting top and bottom parts of support's air cavity
    14 pz -12.000         $ Lower surface of support's air cavity
    15 cz 0.5000          $ Lateral surface for support's air cavity, upper part
    16 cz 0.6000          $ Lateral surface for the lower part of the support's air cavity
    C                       and for support's top part
```

```
17 cz 0.7000                $ Lateral surface for support's bottom part
18 cz 0.7500                $ Lateral surface of the gold foil
19 so 6.5000                $ Inner limit of the Cd shell
20 so 6.6500                $ Outer limit of the Cd shell
21 so 6.8000                $ Outer limit of the Al cover
22 cz 0.8500                $ Inner limit of the Cd shell support
23 cz 1.0000                $ Outer limit of the Cd shell support
24 pz -6.6150               $ Upper limit of the Cd shell support
25 pz -6.7500               $ Lower limit of the Cd shell support
C End of surface definition
C Following line must be a blank line

MODE N                      $ Only neutrons will be transported
IMP:N 1 1 1 1 1 1 1 1 1 1 0 $ Neutron importances in each cell
C
C — SOURCE DEFINITION —
C
sdef sur=1 pos=0 -18 0 rad=d1 dir=1 vec=0 1 0 &  $ A plane disc neutron source of EMeV energy centered
erg=EMeV par=1 wgt=1                             $ at (0,-18,0)cm with radius defined on si1
si1 0 6.800                 $ Source radius
C
C — TALLY DEFINITION —
C
F4:N 4                      $ Neutron flux averaged over cell 4 tally (part/cm^2)
FQ4 e m                     $ Print hierarchy, e=energy, m=multiplier
FM4 (4.441E-04 4 102)       $ Multiplication factor for material 4 and 102
C                             cross section, detailed in section 5.2.3.
CFC4 'reaction rate per unit of gold foil mass and neutron fluence'  $ Comment to be printed with tally F4 results
C
```

```
C — MATERIAL DEFINITION —
C
m1 8016.60c -0.2421 7014.60c -0.7553 6012.50c -0.0021&
18000.35c -0.0005                                          $ Air
m2 1001.60c 0.67 6012.50c 0.33                             $ Polyethylene (CH2)n
mt2 poly.01t                                               $ Identifier for S(α,β) thermal neutron treatment
m3 24050.60c -0.008 24052.60c -0.151 24053.60c -0.017 &
24054.60c -0.004 26054.60c -0.039 26056.60c -0.634 &
26057.60c -0.015 26058.60c -0.002 28058.60c -0.067 &
28060.60c -0.027 28061.60c -0.001 28062.60c -0.004 &
28064.60c -0.001 42000.60c -0.03                           $ Steel
m4 79197.60c 1                                             $ Pure gold
m5 48000.51c 1                                             $ Cadmium
m6 13027.60c 1                                             $ Aluminium
C
C — OTHER PARAMETERS —
C
PHYS:N 20.0 0.0                                            $ Upper limit for neutron energy is 20.0 MeV
CUT:N 1E+34
C
NPS 1500000                                                $ History number
PRDMP 1500000 -120 1 1 0                                   $ Plotting card
PRINT 40 50 100 110 120 126 130 140 160 200                $ List of information tables to be plotted
```

APPENDIX C

Response function matrix for the UAB BSS passive spectrometer

E (MeV)	2.5"	3"	4.2"	5"	6"	8"	10"	12"	2.5" + Cd	3" + Cd	4.2" + Cd
1.000E-09	6.530E-05	5.683E-05	3.875E-05	2.883E-05	1.904E-05	8.088E-06	3.141E-06	1.263E-06	0.000E+00	0.000E+00	0.000E+00
1.259E-09	6.643E-05	5.775E-05	3.940E-05	2.928E-05	1.951E-05	8.223E-06	3.217E-06	1.279E-06	0.000E+00	0.000E+00	0.000E+00
1.585E-09	6.769E-05	5.878E-05	4.012E-05	2.978E-05	1.999E-05	8.375E-06	3.296E-06	1.296E-06	0.000E+00	0.000E+00	0.000E+00
1.995E-09	6.923E-05	5.997E-05	4.097E-05	3.036E-05	2.050E-05	8.561E-06	3.378E-06	1.316E-06	0.000E+00	0.000E+00	0.000E+00
2.512E-09	7.118E-05	6.142E-05	4.203E-05	3.109E-05	2.107E-05	8.797E-06	3.466E-06	1.340E-06	0.000E+00	0.000E+00	0.000E+00
3.162E-09	7.356E-05	6.320E-05	4.332E-05	3.200E-05	2.172E-05	9.083E-06	3.565E-06	1.375E-06	0.000E+00	0.000E+00	0.000E+00
3.981E-09	7.632E-05	6.538E-05	4.490E-05	3.315E-05	2.251E-05	9.411E-06	3.683E-06	1.433E-06	0.000E+00	0.000E+00	0.000E+00
5.012E-09	7.946E-05	6.803E-05	4.678E-05	3.460E-05	2.346E-05	9.772E-06	3.826E-06	1.523E-06	0.000E+00	0.000E+00	0.000E+00
6.310E-09	8.298E-05	7.117E-05	4.898E-05	3.634E-05	2.459E-05	1.018E-05	3.998E-06	1.638E-06	0.000E+00	0.000E+00	0.000E+00
7.943E-09	8.698E-05	7.482E-05	5.152E-05	3.828E-05	2.588E-05	1.065E-05	4.202E-06	1.739E-06	0.000E+00	0.000E+00	0.000E+00
1.000E-08	9.156E-05	7.900E-05	5.441E-05	4.032E-05	2.731E-05	1.124E-05	4.439E-06	1.787E-06	0.000E+00	0.000E+00	0.000E+00
1.259E-08	9.681E-05	8.369E-05	5.762E-05	4.240E-05	2.884E-05	1.196E-05	4.708E-06	1.767E-06	0.000E+00	0.000E+00	0.000E+00
1.585E-08	1.027E-04	8.885E-05	6.089E-05	4.468E-05	3.048E-05	1.272E-05	4.995E-06	1.766E-06	0.000E+00	0.000E+00	0.000E+00
1.995E-08	1.091E-04	9.444E-05	6.394E-05	4.734E-05	3.221E-05	1.342E-05	5.283E-06	1.886E-06	0.000E+00	0.000E+00	0.000E+00
2.512E-08	1.160E-04	1.004E-04	6.658E-05	5.056E-05	3.407E-05	1.399E-05	5.560E-06	2.245E-06	0.000E+00	0.000E+00	0.000E+00
3.162E-08	1.237E-04	1.070E-04	6.974E-05	5.419E-05	3.611E-05	1.460E-05	5.870E-06	2.662E-06	0.000E+00	0.000E+00	0.000E+00
3.981E-08	1.327E-04	1.147E-04	7.507E-05	5.794E-05	3.847E-05	1.560E-05	6.297E-06	2.840E-06	0.000E+00	0.000E+00	0.000E+00
5.012E-08	1.435E-04	1.238E-04	8.412E-05	6.157E-05	4.130E-05	1.730E-05	6.916E-06	2.501E-06	0.000E+00	0.000E+00	0.000E+00
6.310E-08	1.561E-04	1.363E-04	9.451E-05	6.743E-05	4.540E-05	1.936E-05	7.620E-06	2.478E-06	0.000E+00	0.000E+00	0.000E+00
7.943E-08	1.756E-04	1.517E-04	1.047E-04	7.576E-05	5.067E-05	2.145E-05	8.353E-06	2.996E-06	0.000E+00	0.000E+00	0.000E+00
1.000E-07	1.939E-04	1.684E-04	1.150E-04	8.505E-05	5.643E-05	2.358E-05	9.150E-06	3.621E-06	0.000E+00	0.000E+00	0.000E+00
1.259E-07	2.110E-04	1.850E-04	1.256E-04	9.404E-05	6.212E-05	2.574E-05	1.003E-05	4.020E-06	0.000E+00	0.000E+00	4.609E-08
1.585E-07	2.268E-04	2.012E-04	1.366E-04	1.026E-04	6.765E-05	2.794E-05	1.097E-05	4.237E-06	0.000E+00	0.000E+00	7.823E-08
1.995E-07	2.417E-04	2.166E-04	1.478E-04	1.110E-04	7.305E-05	3.020E-05	1.191E-05	4.414E-06	0.000E+00	0.000E+00	3.897E-08
2.512E-07	2.569E-04	2.312E-04	1.591E-04	1.192E-04	7.836E-05	3.252E-05	1.282E-05	4.681E-06	2.598E-06	1.977E-06	1.863E-07
3.162E-07	2.694E-04	2.448E-04	1.704E-04	1.274E-04	8.368E-05	3.488E-05	1.369E-05	5.048E-06	1.352E-05	1.128E-05	4.441E-06
3.981E-07	2.818E-04	2.577E-04	1.814E-04	1.354E-04	8.870E-05	3.724E-05	1.452E-05	5.448E-06	3.955E-05	3.474E-05	1.910E-06
5.012E-07	2.929E-04	2.698E-04	1.919E-04	1.431E-04	9.370E-05	3.955E-05	1.533E-05	5.812E-06	8.803E-05	7.957E-05	5.037E-06
6.310E-07	3.025E-04	2.812E-04	2.018E-04	1.503E-04	9.863E-05	4.178E-05	1.613E-05	6.109E-06	1.565E-04	1.437E-04	9.730E-06
7.943E-07	3.103E-04	2.916E-04	2.109E-04	1.573E-04	1.036E-04	4.389E-05	1.691E-05	6.365E-06	2.275E-04	2.107E-04	1.478E-04
1.000E-06	3.163E-04	3.005E-04	2.196E-04	1.639E-04	1.087E-04	4.587E-05	1.767E-05	6.612E-06	2.823E-04	2.630E-04	1.888E-04

E (MeV)	2.5"	3"	4.2"	5"	6"	8"	10"	12"	2.5" + Cd	3" + Cd	4.2" + Cd
1.259E-06	3.206E-04	3.079E-04	2.278E-04	1.704E-04	1.141E-04	4.770E-05	1.840E-05	6.873E-06	3.083E-04	2.888E-04	2.116E-04
1.585E-06	3.264E-04	3.143E-04	2.360E-04	1.770E-04	1.197E-04	4.944E-05	1.913E-05	7.151E-06	3.163E-04	3.002E-04	2.243E-04
1.995E-06	3.285E-04	3.202E-04	2.442E-04	1.839E-04	1.253E-04	5.117E-05	1.986E-05	7.443E-06	3.273E-04	3.113E-04	2.366E-04
2.512E-06	3.317E-04	3.254E-04	2.514E-04	1.908E-04	1.306E-04	5.298E-05	2.063E-05	7.746E-06	3.339E-04	3.213E-04	2.470E-04
3.162E-06	3.331E-04	3.296E-04	2.586E-04	1.973E-04	1.351E-04	5.490E-05	2.144E-05	8.053E-06	3.347E-04	3.269E-04	2.529E-04
3.981E-06	3.365E-04	3.347E-04	2.622E-04	2.036E-04	1.393E-04	5.687E-05	2.227E-05	8.355E-06	3.365E-04	3.325E-04	2.580E-04
5.012E-06	3.449E-04	3.421E-04	2.701E-04	2.097E-04	1.403E-04	5.875E-05	2.309E-05	8.637E-06	3.455E-04	3.422E-04	2.662E-04
6.310E-06	3.534E-04	3.492E-04	2.777E-04	2.150E-04	1.429E-04	6.043E-05	2.386E-05	8.887E-06	3.552E-04	3.516E-04	2.746E-04
7.943E-06	3.568E-04	3.535E-04	2.822E-04	2.189E-04	1.477E-04	6.188E-05	2.456E-05	9.102E-06	3.566E-04	3.558E-04	2.799E-04
1.000E-05	3.568E-04	3.561E-04	2.853E-04	2.221E-04	1.527E-04	6.333E-05	2.518E-05	9.322E-06	3.585E-04	3.576E-04	2.833E-04
1.259E-05	3.563E-04	3.585E-04	2.892E-04	2.255E-04	1.558E-04	6.503E-05	2.572E-05	9.584E-06	3.588E-04	3.602E-04	2.868E-04
1.585E-05	3.554E-04	3.604E-04	2.942E-04	2.295E-04	1.580E-04	6.693E-05	2.621E-05	9.873E-06	3.586E-04	3.621E-04	2.908E-04
1.995E-05	3.536E-04	3.612E-04	2.998E-04	2.345E-04	1.610E-04	6.885E-05	2.669E-05	1.016E-05	3.566E-04	3.616E-04	2.954E-04
2.512E-05	3.510E-04	3.615E-04	3.045E-04	2.392E-04	1.644E-04	7.070E-05	2.722E-05	1.041E-05	3.547E-04	3.611E-04	3.006E-04
3.162E-05	3.480E-04	3.620E-04	3.071E-04	2.425E-04	1.677E-04	7.232E-05	2.781E-05	1.061E-05	3.544E-04	3.625E-04	3.057E-04
3.981E-05	3.448E-04	3.619E-04	3.090E-04	2.453E-04	1.704E-04	7.373E-05	2.845E-05	1.079E-05	3.512E-04	3.630E-04	3.080E-04
5.012E-05	3.418E-04	3.606E-04	3.117E-04	2.488E-04	1.728E-04	7.493E-05	2.907E-05	1.099E-05	3.410E-04	3.588E-04	3.047E-04
6.310E-05	3.385E-04	3.589E-04	3.141E-04	2.526E-04	1.758E-04	7.595E-05	2.964E-05	1.125E-05	3.253E-04	3.476E-04	2.968E-04
7.943E-05	3.345E-04	3.575E-04	3.154E-04	2.562E-04	1.801E-04	7.684E-05	3.011E-05	1.158E-05	3.080E-04	3.299E-04	2.836E-04
1.000E-04	3.299E-04	3.554E-04	3.166E-04	2.594E-04	1.841E-04	7.773E-05	3.051E-05	1.190E-05	2.954E-04	3.157E-04	2.755E-04
1.259E-04	3.249E-04	3.519E-04	3.167E-04	2.624E-04	1.881E-04	7.875E-05	3.086E-05	1.214E-05	2.938E-04	3.154E-04	2.792E-04
1.585E-04	3.202E-04	3.482E-04	3.209E-04	2.653E-04	1.877E-04	7.999E-05	3.124E-05	1.228E-05	3.055E-04	3.310E-04	2.968E-04
1.995E-04	3.162E-04	3.457E-04	3.223E-04	2.682E-04	1.906E-04	8.145E-05	3.174E-05	1.235E-05	3.244E-04	3.540E-04	3.273E-04
2.512E-04	3.117E-04	3.435E-04	3.236E-04	2.708E-04	1.940E-04	8.321E-05	3.243E-05	1.239E-05	3.143E-04	3.437E-04	3.200E-04
3.162E-04	3.059E-04	3.406E-04	3.254E-04	2.728E-04	1.968E-04	8.521E-05	3.336E-05	1.241E-05	2.533E-04	2.761E-04	2.500E-04
3.981E-04	2.997E-04	3.371E-04	3.269E-04	2.734E-04	1.988E-04	8.721E-05	3.439E-05	1.249E-05	2.081E-04	2.274E-04	2.019E-04
5.012E-04	2.943E-04	3.334E-04	3.269E-04	2.727E-04	1.998E-04	8.886E-05	3.535E-05	1.268E-05	2.390E-04	2.658E-04	2.512E-04
6.310E-04	2.891E-04	3.294E-04	3.261E-04	2.727E-04	2.016E-04	8.985E-05	3.606E-05	1.306E-05	2.895E-04	3.265E-04	3.246E-04
7.943E-04	2.831E-04	3.248E-04	3.256E-04	2.753E-04	2.044E-04	9.026E-05	3.640E-05	1.361E-05	2.957E-04	3.360E-04	3.394E-04
1.000E-03	2.771E-04	3.211E-04	3.262E-04	2.787E-04	2.075E-04	9.176E-05	3.660E-05	1.396E-05	2.786E-04	3.183E-04	3.246E-04
1.260E-03	2.714E-04	3.184E-04	3.277E-04	2.807E-04	2.096E-04	9.477E-05	3.703E-05	1.403E-05	2.690E-04	3.094E-04	3.209E-04

E (MeV)	2.5°	3°	4.2°	5°	6°	8°	10°	12°	2.5° + Cd	3° + Cd	4.2° + Cd
1.590E-03	2.657E-04	3.136E-04	3.284E-04	2.817E-04	2.113E-04	9.622E-05	3.803E-05	1.433E-05	2.619E-04	3.044E-04	3.202E-04
2.000E-03	2.599E-04	3.081E-04	3.286E-04	2.829E-04	2.128E-04	9.702E-05	3.914E-05	1.474E-05	2.555E-04	3.012E-04	3.202E-04
2.510E-03	2.541E-04	3.037E-04	3.296E-04	2.853E-04	2.152E-04	9.849E-05	3.989E-05	1.506E-05	2.498E-04	2.992E-04	3.210E-04
3.160E-03	2.484E-04	3.001E-04	3.285E-04	2.887E-04	2.186E-04	1.007E-04	4.026E-05	1.524E-05	2.444E-04	2.975E-04	3.221E-04
3.980E-03	2.427E-04	2.963E-04	3.279E-04	2.920E-04	2.218E-04	1.028E-04	4.060E-05	1.543E-05	2.395E-04	2.952E-04	3.228E-04
5.010E-03	2.371E-04	2.912E-04	3.266E-04	2.941E-04	2.243E-04	1.040E-04	4.088E-05	1.573E-05	2.351E-04	2.915E-04	3.224E-04
6.310E-03	2.315E-04	2.851E-04	3.249E-04	2.947E-04	2.258E-04	1.045E-04	4.153E-05	1.615E-05	2.306E-04	2.865E-04	3.211E-04
7.940E-03	2.255E-04	2.805E-04	3.246E-04	2.951E-04	2.275E-04	1.058E-04	4.258E-05	1.649E-05	2.247E-04	2.821E-04	3.201E-04
1.000E-02	2.190E-04	2.787E-04	3.263E-04	2.967E-04	2.296E-04	1.091E-04	4.399E-05	1.664E-05	2.167E-04	2.791E-04	3.205E-04
1.259E-02	2.135E-04	2.752E-04	3.267E-04	2.985E-04	2.324E-04	1.124E-04	4.532E-05	1.687E-05	2.104E-04	2.738E-04	3.215E-04
1.585E-02	2.086E-04	2.696E-04	3.258E-04	3.003E-04	2.354E-04	1.151E-04	4.655E-05	1.725E-05	2.058E-04	2.672E-04	3.222E-04
1.995E-02	2.032E-04	2.630E-04	3.245E-04	3.022E-04	2.396E-04	1.175E-04	4.780E-05	1.774E-05	2.020E-04	2.619E-04	3.229E-04
2.512E-02	1.965E-04	2.568E-04	3.237E-04	3.042E-04	2.453E-04	1.199E-04	4.920E-05	1.832E-05	1.976E-04	2.599E-04	3.234E-04
3.162E-02	1.899E-04	2.520E-04	3.244E-04	3.070E-04	2.518E-04	1.227E-04	5.085E-05	1.898E-05	1.911E-04	2.561E-04	3.243E-04
3.981E-02	1.840E-04	2.485E-04	3.262E-04	3.109E-04	2.577E-04	1.259E-04	5.283E-05	1.977E-05	1.831E-04	2.490E-04	3.253E-04
5.012E-02	1.783E-04	2.449E-04	3.277E-04	3.162E-04	2.622E-04	1.297E-04	5.517E-05	2.062E-05	1.763E-04	2.427E-04	3.250E-04
6.310E-02	1.721E-04	2.400E-04	3.285E-04	3.224E-04	2.663E-04	1.349E-04	5.807E-05	2.213E-05	1.714E-04	2.391E-04	3.241E-04
7.943E-02	1.649E-04	2.336E-04	3.295E-04	3.282E-04	2.741E-04	1.434E-04	6.194E-05	2.353E-05	1.654E-04	2.358E-04	3.265E-04
1.000E-01	1.570E-04	2.261E-04	3.308E-04	3.338E-04	2.856E-04	1.542E-04	6.684E-05	2.517E-05	1.576E-04	2.299E-04	3.285E-04
1.259E-01	1.496E-04	2.185E-04	3.315E-04	3.403E-04	2.980E-04	1.647E-04	7.251E-05	2.745E-05	1.494E-04	2.196E-04	3.228E-04
1.585E-01	1.417E-04	2.104E-04	3.309E-04	3.472E-04	3.108E-04	1.770E-04	7.918E-05	3.054E-05	1.411E-04	2.087E-04	3.197E-04
1.995E-01	1.325E-04	2.012E-04	3.288E-04	3.533E-04	3.238E-04	1.924E-04	8.740E-05	3.466E-05	1.326E-04	1.996E-04	3.235E-04
2.512E-01	1.224E-04	1.908E-04	3.255E-04	3.574E-04	3.363E-04	2.093E-04	9.806E-05	4.019E-05	1.236E-04	1.907E-04	3.263E-04
3.162E-01	1.117E-04	1.792E-04	3.208E-04	3.587E-04	3.476E-04	2.266E-04	1.119E-04	4.754E-05	1.137E-04	1.806E-04	3.209E-04
3.981E-01	1.007E-04	1.669E-04	3.126E-04	3.586E-04	3.587E-04	2.471E-04	1.292E-04	5.712E-05	1.029E-04	1.682E-04	3.099E-04
5.012E-01	8.956E-05	1.508E-04	2.992E-04	3.581E-04	3.704E-04	2.731E-04	1.501E-04	6.942E-05	9.097E-05	1.530E-04	2.973E-04
6.310E-01	7.866E-05	1.348E-04	2.828E-04	3.520E-04	3.766E-04	2.975E-04	1.741E-04	8.590E-05	7.901E-05	1.364E-04	2.833E-04
7.943E-01	6.800E-05	1.192E-04	2.653E-04	3.383E-04	3.745E-04	3.161E-04	1.998E-04	1.067E-04	6.786E-05	1.204E-04	2.679E-04
1.000E+00	5.748E-05	1.038E-04	2.455E-04	3.221E-04	3.692E-04	3.336E-04	2.255E-04	1.300E-04	5.786E-05	1.057E-04	2.475E-04
1.259E+00	4.754E-05	8.881E-05	2.216E-04	3.029E-04	3.618E-04	3.504E-04	2.518E-04	1.556E-04	4.875E-05	9.202E-05	2.226E-04
1.585E+00	3.925E-05	7.447E-05	1.948E-04	2.723E-04	3.436E-04	3.552E-04	2.799E-04	1.867E-04	4.106E-05	7.776E-05	1.973E-04

E (MeV)	2.5"	3"	4.25"	5"	6"	8"	10"	12"	2.5" + Cd	3" + Cd	4.25" + Cd
1.995E+00	3.176E-05	6.180E-05	1.691E-04	2.425E-04	3.162E-04	3.526E-04	3.012E-04	2.133E-04	3.340E-06	6.435E-05	1.723E-04
2.512E+00	2.520E-05	5.067E-05	1.451E-04	2.140E-04	2.842E-04	3.418E-04	3.034E-04	2.336E-04	2.644E-06	5.264E-05	1.482E-04
3.162E+00	1.983E-05	4.088E-05	1.224E-04	1.856E-04	2.514E-04	3.176E-04	2.947E-04	2.354E-04	2.094E-06	4.311E-05	1.257E-04
3.981E+00	1.545E-05	3.234E-05	1.013E-04	1.577E-04	2.191E-04	2.885E-04	2.901E-04	2.419E-04	1.667E-06	3.522E-05	1.051E-04
5.012E+00	1.186E-05	2.501E-05	8.182E-05	1.307E-04	1.881E-04	2.593E-04	2.902E-04	2.671E-04	1.315E-06	2.818E-05	8.628E-05
6.310E+00	8.820E-06	1.885E-05	6.417E-05	1.052E-04	1.584E-04	2.305E-04	2.819E-04	2.410E-04	1.005E-06	2.155E-05	6.929E-05
7.943E+00	6.299E-06	1.381E-05	4.834E-05	8.124E-05	1.271E-04	1.985E-04	2.323E-04	2.320E-04	7.424E-06	1.604E-05	5.350E-05
1.000E+01	4.543E-06	1.026E-05	3.626E-05	6.221E-05	9.925E-05	1.619E-04	1.994E-04	2.141E-04	5.917E-06	1.269E-05	4.177E-05
1.259E+01	3.758E-06	8.514E-06	3.006E-05	5.203E-05	8.307E-05	1.402E-04	1.756E-04	1.917E-04	6.147E-06	1.200E-05	3.775E-05
1.585E+01	3.165E-06	7.109E-06	2.530E-05	4.376E-05	6.992E-05	1.241E-04	1.585E-04	1.729E-04	6.839E-06	1.220E-05	3.550E-05
1.995E+01	2.237E-06	5.073E-06	1.882E-05	3.244E-05	5.303E-05	9.363E-05	1.268E-04	1.418E-04	7.059E-06	1.198E-05	3.067E-05

APPENDIX D

Publications and contributions

D1. List of publications directly related to the Ph.D. work

- F. Fernández, C. Domingo, K. Amgarou, J. Castelo, T. Bouassoule, M.J. García, E. Luguera (2007)

  "Neutron measurements in a Varian 2100C LINAC faciltiy using a Bonner sphere system based on passive gold activation detectors"

  Radiation Protection Dosimetry, 126, 361-365

- F. Fernández, T. Bouassoule, K. Amgarou, C. Domingo, M.J. García, V. Lacoste, V. Gressier, H. Muller. (2007)

  "Monte Carlo calculations and validation of a gold-foil based Bonner sphere system"

  Radiation Protection Dosimetry, 126, 366-370

- F. Fernández, K. Amgarou, C. Domingo, M.J. García, G. Quincoces, J.M. Martí-Climent, R. Méndez, R. Barquero (2007)

  "Neutron spectrometry in a PET cyclotron by means of Bonner sphere system"

  Radiation Protection Dosimetry, 126, 371-375

- F. Fernández, T. Bouassoule, M. Tomás, K. Amgarou, C. Domingo, M.J. García, (2007)

  "La dosimetrie et spectrométrie neutronique: la contribution de l'Université Autonome de Barcelone"

  Radioprotection, 41, S71-S85

- C. Domingo, K. Amgarou, T. Bouassoule, J. Castelo, M.J. García, F. Fernández (2007)

  "La contribución del Grup de Física de Radiacions de la Universitat Autònoma de Barcelona a la dosimetría y espectrometría de neutrones: instrumentación"

  XXXI Reunión bienal de la Real Sociedad Española de Física y 17^o Encuentro Ibérico para la Enseñanza de la Física. Comunicaciones Científicas ISBN: 978-84-690-7298-1 Ed.: Eduardo Gutiérrez Marí, S.R.L.U.

- C. Domingo, K. Amgarou, J. Castelo, T. Bouassoule, M. J. García, E. Luguera, F. Fernández (2007)

  Determinación de la componente neutrónica en un LINAC Varian 2100C mediante un sistema de esferas Bonner basado en detectores pasivos por activación de oro".

  XXXI Reunión bienal de la Real Sociedad Española de Física y 17^o Encuentro Ibérico para la Enseñanza de la Física. Comunicaciones Científicas ISBN: 978-84-690-7298-1 Ed.: Eduardo Gutiérrez Marí, S.R.L.U.

- M.J. García-Fusté, A. Sánchez-Reyes, C. Domingo, K. Amgarou, E. Morales, J. Castelo (2008)

  "Differences on the neuton field in a VARIAN 2100CD linac facility due to IMRT or non-IMRT treatments"

  Radiotherapy & Oncology, 88, S397

- C. Domingo, F. Fernández, M.J. García, G. Lövenstam (2008)

  "Validation of the response functions of the active (^{3}He detector) and passive (^{197}Au foils activation) UAB Bonner Sphere Spectrometers"

  Neutron Physics Unit Scientific Report. EUR 23440 EN, 76-77

  ISBN: 978-92-79-09532-0

  Office for Official Publications of the European Communities

- C. Domingo, M.J. García-Fusté, E. Morales, K. Amgarou, J.A. Terrón, J. Roselló, L. Brualla, L. Núñez, R. Colmenares, F. Gómez, G.H. Hartmann, F. Sánchez-Doblado, F. Fernández. (2010)

  "Neutron spectrometry and determination of neutron ambient doses in different linac treatment rooms"

  Radiation Measurements, doi: doi: 10.1016/j.radmeas.2010.05.023

D2. Other publications related to neutron measurements, dosimetry and spectrometry

- F. Fernández, K. Amgarou, C. Domingo, M.J. García, A. Nourreddine, D. Mouhssine, A. Belafrites, I. Ribaud (2005)

  "A joint UAB-IReS-IPNO neutron comparison exercise with nuclear track detectors"

  Radiation Measurements, 40, 601-606

  M.J. García, K. Amgarou, C. Domingo, F. Fernández (2005)

  "Neutron response study of two CR-39 personal dosemeters with air and Nylon converters"

  Radiation Measurements, 40, 607-611

- F. Fernández, C. Domingo, J. Castelo, M.J. García, R. Bedogni, A. Esposito, M. Chiti. (2007)

  "Performance of the UAB and the INFN-LNF Bonner sphere spectrometers in quasi-monoenergetic neutron fields"

  Radiation Protection Dosimetry, 126, 342-345

- F. Fernández, C. Domingo, K. Amgarou, T. Bouassoule, M.J. García (2007)

  "Neutron measurements in Spanish nuclear power plants with an active Bonner sphere spectrometer"

  Radiation Protection Dosimetry, 126, 355-360

- M. Silari, S. Agosteo, P. Beck, R. Bedogni, E. Cale, M. Caresana, C. Domingo, L. Donadille, N. Dubourg, A. Esposito, G. Fehrenbacher, F. Fernández, M. Ferrarini, A. Fiechtner, A. Fuchs, M. J. García, N. Golnik, F. Gutermuth, S. Khurana, Th. Klages, M. Latocha, V. Mares, S. Mayer, T. Radon, H. Reithmeier), S. Rollet), H. Roos, W. Rühm, S. Sandri, D. Schardt, G. Simmer, F. Spurný, F. Trompier, C. Villa-Grasa, B. Wiegel, M. Wielunski, F. Wissmann, A. Zechner, M. Zielczyński (2009)

  "Intercomparison of radiation protection devices in a high-energy stray neutron field. Part III: Instrument response."

  Radiation Measurements, 44, 673-691

- C. Domingo, M.J. García-Fusté, E. Morales, K. Amgarou, J. Castelo, F. Sánchez-Doblado (2009)

  "Evaluation of neutron doses received at different organs in radiotherapy treatments using the UAB PADC based dosemeters in an antropomorphic phantom"

  Radiation Measurements, 44, 1073-1076

- M.J. García-Fusté, C. Domingo, K. Amgarou, T. Bouassoule, J. Castelo (2009)

  "Neutron dosimetry inside the contaiment building of spanish nuclear power plants with PADC based dosemetrs"

  Radiation Measurements, 44, 999-1001

- C. Domingo, T. Bouassoule, M.J. García-Fusté, J. García-Orellana, E. Morales. K. Amgarou, J. Castelo, F. Fernández. (2009)

  "Neutron dosimetric studies of density/moisture gauge operators during transport and usage"

  Radiation Measurements, 44, 1002-1005

- C. Domingo, M.J. García-Fusté, K. Amgarou, J. Castelo, E. Morales (2009)

  "Measurements in quasi-monoenergetic neutron beams at the EC-IRMM Van-der-Graaf accelerator for calibration of the UAB PADC based neutron dosimeter"

  Radiation Measurements, 44, 981-984

- A. Esposito, R. Bedogni, C. Domingo, M.J. García-Fusté, K. Amgarou (2010)

  "Measurements of leakage neutron spectra from a high-energy accumulation ring using Extended Range Bonner Sphere Spectrometers"

  Radiation Measurements, doi: 10.1016/j.radmeas.2010.04.008

- R. Bedogni, C. Domingo, A. Esposito, M. Chiti, M.J. García-Fusté, G. Lovestam. (2010)

  "Testing Bonner sphere spectrometers in the JRC-IRMM monoenergetic neutron beams"

  Nucl. Instr. Meth. Phys. Res. A, doi:10.1016/j.nima.2010.04.019

- C. Domingo, F. Gómez, F. Sánchez-Doblado, G.H. Hartmann, K. Amgarou, M.J. García-Fusté, M.T. Romero, R. Böttger, F. Wissmann, H. Schuhmacher. (2009)

  "Calibration of a neutron detector based on single event upset of SRAM memories"

  Radiation Measurements, submitted RADMEAS-S-09-00878

- M.J. García-Fusté, K. Amgarou, J. García-Orellana, C. Domingo (2009)

  "Neutron ambient dose equivalent levels at storage bunkers of density/moisture gauges"

  Radiation Measurements, submitted RADMEAS-S-09-00850

- C. Domingo, R. Bedogni, K. Amgarou, M.J. García-Fusté, A. Esposito (2009)

  "Comparing the dosimetric characteristics of Americium-Berillium neutron sources through Bonner sphere spectrometry"

  Radiation Measurements, submitted RADMEAS-S-09-00867

D3. Contributions to conferences related directly to the Ph.D. work

- C. Domingo, T. Bouassoule, K. Amgarou, M.J. García, J. Castelo, E. Morales, F. Fernández (2007)

  "Bonner Sphere Spectrometer. CONRAD WP4 problem P2"

  CONRAD WP4 workshop on Uncertainty Assesment in Computational Dosimetry: A Comparison of Approaches. Bologna (Italy), 8-10 October 2007

- C. Domingo, K. Amgarou, T. Bouassoule, J. Castelo, M.J. García-Fusté, E. Morales, F. Fernández.

  "Contribution of the GFR-UAB group to neutron dosimetry and spectrometry""

  24th International Conference on Nuclear Tracks in Solids, Bologna (Italy), 1-5 September 2008

- C. Domingo, M.J. García-Fusté, E. Morales, K. Amgarou, J.A. Terrón, J. Roselló, L. Brualla, L. Núñez, R. Colmenares, F :Gómez, G.H. Hartmann, F. Sánchez-Doblado, F. Fernández.

  "Medida de los espectros neutrónicos en las salas de tratamiento de diversos aceleradores lineales de electrones mediante un sistema de esferas Bonner con detectores de activación de Au"

  XVII Congreso nacional de la SEFM / XII Congreso nacional de la SEPR., Alicante (Spain), 2-5 June 2009

- M.J. García-Fusté, A. Sánchez-Reyes, C. Domingo, K. Amgarou, E. Morales, J. Castelo

  "Variación del campo de neutrones de un acelerador Varian 2100CD en función del tipo de tratamiento (IMRT ó 3DCRT)."

  Congreso: XVII Congreso nacional de la SEFM / XII Congreso nacional de la SEPR. Alicante (Spain), 2-5 June 2009

- C. Domingo, M.J. García-Fusté, E. Morales, K. Amgarou, J.A. Terrón, J. Roselló, L. Brualla, L. Núñez, R. Colmenares, F. Gómez, G.H. Hartmann, F. Sánchez-Doblado, F. Fernández.

  "Neutron spectrometry and determination of neutron ambient doses in radiotherapy under different exposure conditions"

  World Congress 2009. Medical Physics and Biomedical Engineering, Munich (Germany), 7-12 September 2009

D4. Other contributions to conferences

- F. Fernández, C. Domingo, K. Amgarou, T. Bouassoule, J. Castelo, M.J. García. (2006)

  "Problémes de radiprotection liés aux champs neutroniques présents dans les accelerateurs d'elèctrons »

  3ème édition des Jounées Scientifiques Francophones: Les codes de calcul en radioprotection, radiophysique et dosimétrie. Saclay (France), 28-29/nov./2006

- F. Sánchez-Doblado, C. Domingo, F. Gómez, J.L. Muñiz, R. Barquero, M.J. García-Fusté, G. Hartmann, J.A. Terrón, J. Pena, H. Schuhmacher, F. Wissmann, R. Böttger, A. Zimbal, F. Gutiérrez, F.X. Guerre, J. Roselló, L. Nuñez, L. Brualla, F. Manchado, A. Lorente, E. Gallego, M.T. Romero, R. Capote, D. Planes, J.I. Lagares, R. Arrans, R. Colmenares, K. Amgarou, E. Morales, J.P. Cano, F. Fernández

  "Dosimetría neutrónica de pacientes sometidos a radioterapia con haces de fotones."

  Congreso: XVII Congreso nacional de la SEFM / XII Congreso nacional de la SEPR. Alicante (Spain), 2-5 June 2009

- F. Sánchez-Doblado, C. Domingo, F. Gómez, J.L. Muñiz, R. Barquero, M.J. García-Fusté, G. Hartmann, M.T. Romero, J.A. Terrón, J. Pena, H. Schuhmacher, F. Wissmann, R. Böttger, A. Zimbal, F. Gutiérrez, F.X. Guerre, J. Roselló, L. Nuñez, L. Brualla, F. Manchado, A. Lorente, E. Gallego, R. Capote, D. Planes, J.I. Lagares, R. Arrans, R. Colmenares, K. Amgarou, E. Morales, J.P. Cano, F. Fernández

  "On line neutron dose evaluation in patients under radiotherapy"

  World Congress 2009. Medical Physics and Biomedical Engineering, Munich (Germany), 7-12 September 2009

- F. Sánchez-Doblado, C. Domingo, F. Gómez, J.L. Muñiz, R. Barquero, M.J. García-Fusté, G. Hartmann, M.T. Romero, J.A. Terrón, J. Pena, H. Schuhmacher, F. Wissmann, R. Böttger, A. Zimbal, F. Gutiérrez, F.X. Guerre, J. Roselló, L. Nuñez, L. Brualla, F. Manchado, A. Lorente, E. Gallego, R. Capote, D. Planes, J.I. Lagares, R. Arrans, R. Colmenares, K. Amgarou, E. Morales, J.P. Cano, F. Fernández

  "Neutron-induced second cancer risk estimation in patients under radiotherapy by means of an on-line in-vivo dosemeter"

  11th Neutron and ion dosimetry Symposium (NEUDOS-11), Cape Town (Southafrica), 12-16 October 2009